Astrophysics and Space Science Proceedings

Carlos Martins
Paolo Molaro *Editors*

From Varying Couplings to Fundamental Physics

Proceedings of Symposium 1 of JENAM 2010

Springer

Astrophysics and Space Science Proceedings

For further volumes:
http://www.springer.com/series/7395

From Varying Couplings to Fundamental Physics

Proceedings of Symposium 1
of JENAM 2010

Editors

Carlos Martins
Paolo Molaro

Springer

Editors
Carlos Martins
Centro de Astrofisica
Universidade do Porto
Rua das Estrelas
4150-762 Porto
Portugal
Carlos.Martins@astro.up.pt

Paolo Molaro
INAF-Osservatorio Astronomico
di Trieste
Via G.B. Tiepolo 11
34131 Trieste
Italy
molaro@oats.inaf.it

ISSN 1570-6591
e-ISSN 1570-6605
ISBN 978-3-642-19396-5
e-ISBN 978-3-642-19397-2
DOI 10.1007/978-3-642-19397-2
Springer Heidelberg Dordrecht London New York

Library of Congress Control Number: 2011928713

Cover design: eStudio Calamar S.L.

Printed on acid-free paper

Springer is part of Springer Science+Business Media (www.springer.com)

Preface

The concept that fundamental physical constants can change over time dates back to the late 1930s and has been a very fertile idea in several branches of theoretical physics so far. More recently it also evolved into a branch of observational astronomy. At present the detection of the smallest variations of coupling constants throughout the universal space-time is seen as an effective way to reveal the presence of light scalar fields foreseen in many cosmological and elementary particle theories.

The JENAM symposium entitled *From Varying Couplings to Fundamental Physics*, convened in Lisbon on the 6th and 7th September 2010, was the second JENAM symposium on this topic. Both symposia were held in Portugal. The first took place in Porto in 2002, and was one of the first in this field of research. To our knowledge the very first one was the discussion meeting on *The constants of physics* held on 25 and 26 May 1983 at the Royal Society and organized by William Hunter McCrea, Martin Rees, and Steven Weinberg.

Most of the presentations in those early days were theoretical, though in the 2002 JENAM first indications for α variation were presented by J.K. Webb and collaborators. At JENAM 2010 the majority of the talks were observational, reflecting the evolution of the field which also developed an active experimental character.

Actually, the JENAM 2010 symposium occurred at a particularly exciting time, only a few weeks after the first announcement on arXiv of the claim for a cosmological spatial dipole in the value of the fine-structure constant α. This prompted a press release and the symposium was the first forum for the formal presentation of these results. If confirmed, these observations will have dramatic implications for cosmology and fundamental physics. They were very lively debated at the meeting. In contrast, a number of astrophysical and atomic clocks measurements yield null results for variations of alpha and other constants. With an entirely different approach, evidence for a tiny variation of the electron-to-proton mass ratio in the Galaxy at the level of few parts per billion was also claimed. This could be the smoking gun of the presence of a chameleon scalar field.

The next few years bear the promise of being particularly exciting. While several groups will certainly use new and improved data to challenge the above claims, a quest for redundancy will also be undertaken, looking for new astrophysical techniques that may allow independent measurements. The prospects for future European facilities for this research area are particularly bright with several new spectrographs at ESO and other major observatories being built which will allow significant advances in the observational sensitivity leading eventually to a systematic mapping of the behaviour of the couplings throughout the cosmic history.

In our view the meeting was extremely successful, with plenty of opportunities for cross-disciplinary conversation. We wish to thank all participants for their presentations of unique quality and for sharing with us their most recent results. The more than one hundred registered participants from 32 countries revealed the great interest among the community, which goes far beyond the specialists of the sector.

We are pleased to acknowledge financial support from JENAM itself, the European Astronomical Society, Centro de Astrofísica da Universitade do Porto and Fundação para a Ciencia e a Tecnologia. We wish to warmly thank the Scientific Organizing Committee for their advice in preparing the scientific program and the JENAM local organizing committee for the assistance and for making the meeting very enjoyable.

Porto and Trieste *Carlos Martins*
November 2010 *Paolo Molaro*

Contents

Contributors

I.I. Agafonova Physical-Technical Institute, Polytekhnicheskaya Str. 26, 194021 St. Petersburg, Russia

L.G. Althaus Facultad de Ciencias Astronómicas y Geofísicas, Universidad Nacional de La Plata, Paseo del Bosque s/n, (1900) La Plata, Argentina

J. Bagdonaite Department of Astronomy, Vilnius University, Vilnius, Lithuania, and Institute for Lasers, Life and Biophotonics, VU University Amsterdam, de Boelelaan 1081, 1081 HV Amsterdam, The Netherlands

J.C. Berengut School of Physics, University of New South Wales, Sydney, NSW 2052, Australia

R. Buning Institute for Lasers, Life and Biophotonics, VU University Amsterdam, de Boelelaan 1081, 1081 HV Amsterdam, The Netherlands, and Leiden Institute of Physics, Leiden University, The Netherlands

M. Centurión INAF-Osservatorio Astronomico di Trieste, Via G.B. Tiepolo 11 Trieste, Italy

A.H. Córsico Facultad de Ciencias Astronómicas y Geofísicas, Universidad Nacional de La Plata, Paseo del Bosque s/n, (1900) La Plata, Argentina

S. di Serego Alighieri INAF - Osservatorio Astrofisico di Arcetri, Largo E. Fermi 5, Firenze, Italy, sperello@arcetri.astro.it

V.A. Dzuba School of Physics, University of New South Wales, Sydney, NSW 2052, Australia

V.V. Flambaum School of Physics, University of New South Wales, Sydney, NSW 2052, Australia

S. Galli Laboratoire APC, 10 rue Alice Domon et Leonie Duquet, 75205 Paris Cedex 13 and Physics Department and INFN, Università di Roma "La Sapienza", Ple Aldo Moro 2, 00185 Rome, Italy, galli@apc.univ-paris7.fr

E. García–Berro Departament de Física Aplicada, Universitat Politècnica de Catalunya, c/Esteve Terrades, 5, 08860 Castelldefels, Spain, and Institut d'Estudis Espacials de Catalunya, c/Gran Capità 2–4, Edif. Nexus 104, 08034 Barcelona, Spain, garcia@fa.upc.edu

N. Gupta ASTRON, Oude Hoogeveensedijk 4, 7991 PD, Dwingeloo, The Netherlands

C.M. Gutiérrez Instituto de Astrofísica de Canarias, 38205 La Laguna, Tenerife, Spain, cgc@iac.es

Ch. Henkel Max-Planck-Institut für Radioastronomie, Auf dem Hügel 69, D-53121 Bonn, Germany

J. Isern Institut de Ciències de l'Espai (CSIC), Campus UAB, 08193 Bellaterra, Spain, and Institut d'Estudis Espacials de Catalunya, c/Gran Capità 2–4, Edif. Nexus 104, 08034 Barcelona, Spain

L. Kaper Astronomical Institute Anton Pannekoek, Universiteit van Amsterdam, 1098 SJ Amsterdam, The Netherlands, and Institute for Lasers, Life and Biophotonics, VU University Amsterdam, de Boelelaan 1081, 1081 HV Amsterdam, The Netherlands

J.A. King School of Physics, University of New South Wales, Sydney, NSW 2052, Australia

M.G. Kozlov Petersburg Nuclear Physics Institute, Gatchina, 188300, Russia

L. Kraiselburd Grupo de Gravitación, Astrofísica y Cosmología, Facultad de Ciencias Astronómicas y Geofísicas, Universidad Nacional de La Plata, Paseo del Bosque s/n (1900) La Plata, Argentina, lkrai@fcaglp.fcaglp.unlp.edu.ar

A.V. Lapinov Institute for Applied Physics, Uljanov Str. 46, 603950 Nizhny Novgorod, Russia

C. Ledoux European Southern Observatory, Alonso de Córdova 3107, Casilla 19001, Vitacura, Santiago, Chile

S.A. Levshakov Physical-Technical Institute, Polytekhnicheskaya Str. 26, 194021 St. Petersburg, Russia, lev@astro.ioffe.rssu.ru

J. Liske ESO, Karl-Schwarzschild Strasse 2 85748 Garching, Munich, Germany

F. Lobo CAAUL/Departamento de Física, Faculdade de Ciências, Universidade de Lisboa, Campo Grande Ed. C8, 1749-016 Lisboa, Portugal

M. López-Corredoira Instituto de Astrofísica de Canarias, 38205 La Laguna, Tenerife, Spain

P. Lorén–Aguilar Departament de Física Aplicada, Universitat Politècnica de Catalunya, c/Esteve Terrades, 5, 08860 Castelldefels, Spain, and Institut d'Estudis Espacials de Catalunya, c/Gran Capità 2–4, Edif. Nexus 104, 08034 Barcelona, Spain

G. Maccaferri INAF-Istituto di Radio Astronomia, Via P. Gobetti 101, Bologna, Italy

C.J.A.P Martins Centro de Astrofísica, Universidade do Porto, Rua das Estrelas, 4150-762 Porto, Portugal, Carlos.Martins@astro.up.pt

A. Melchiorri Physics Department and INFN, Università di Roma “La Sapienza”, Ple Aldo Moro 2, 00185 Rome, Italy

E. Menegoni Physics Department and INFN, Università di Roma “La Sapienza”, Ple Aldo Moro 2, 00185 Rome, Italy

A. Mignano INAF-Istituto di Radio Astronomia, Via P. Gobetti 101, Bologna, Italy

M. Miller Bertolami Grupo de Evolución estelar y pulsaciones, Facultad de Ciencias Astronómicas y Geofísicas, Universidad Nacional de La Plata, Paseo del Bosque s/n (1900) La Plata, Argentina

J.P. Mimoso CAAUL/Departamento de Física, Faculdade de Ciências, Universidade de Lisboa, Campo Grande Ed. C8, 1749-016 Lisboa, Portugal, jpmimoso@cii.fc.ul.pt

P. Molaro INAF-Osservatorio Astronomico di Trieste, Via G. B. Tiepolo 11, 34143 Trieste, Italy, molaro@oats.inaf.it

S. Monai INAF-Osservatorio Astronomico di Trieste, Via G.B. Tiepolo 11 Trieste, Italy

M.T. Murphy Centre for Astrophysics and Supercomputing, Swinburne University of Technology, Victoria 3122, Australia

P. Noterdaeme Departamento de Astronomía, Universidad de Chile, Casilla 36-D, Santiago, Chile

P. Petitjean Institut d’Astrophysique de Paris, Université Paris 6 & CNRS, UMR7095, 98bis Boulevard Arago, 75014, Paris, France, petitjean@iap.fr

D. Reimers Hamburger Sternwarte, Universität Hamburg, Gojenbergsweg 112, D-21029 Hamburg, Germany

T. Sakai Institute of Astronomy, The University of Tokyo, Osawa, Mitaka, Tokyo 181-0015, Japan

P. Sisterna Facultad de Ciencias Exactas y Naturales, Universidad Nacional de Mar del Plata, Funes 3350 (7600) Mar del Plata, Argentina

R. Srianand IUCAA, Post Bag 4, Ganeshkhind, Pune 411 007, India

R.I. Thompson Steward Observatory, University of Arizona, Tucson, AZ 85721 USA, rit@email.arizona.edu

S. Torres Departament de Física Aplicada, Universitat Politècnica de Catalunya, c/Esteve Terrades, 5, 08860 Castelldefels, Spain, and Institut d’Estudis Espacials de Catalunya, c/Gran Capità 2–4, Edif. Nexus 104, 08034 Barcelona, Spain

W. Ubachs Institute for Lasers, Life and Biophotonics, VU University Amsterdam, de Boelelaan 1081, 1081 HV Amsterdam, The Netherlands, wimu@nat.vu.nl

H. Vucetich Grupo de Gravitación, Astrofísica y Cosmología, Facultad de Ciencias Astronómicas y Geofísicas, Universidad Nacional de La Plata, Paseo del Bosque s/n (1900) La Plata, Argentina

J.K. Webb School of Physics, University of New South Wales, Sydney, NSW 2052, Australia

M. Wendt Hamburger Sternwarte, Universität Hamburg, Gojenbergsweg 112, 21029 Hamburg, Germany, mwendt@hs.uni-hamburg.de

M. Zagermann Institute for Theoretical Physics & Center for Quantum Engineering and Spacetime Research (QUEST), Leibniz Universität Hannover, Appelstr. 2, D-30167 Hannover, Germany, Marco.Zagermann@itp.uni-hannover.de

Astrophysical Probes of Fundamental Physics

C.J.A.P. Martins

Abstract The dramatic confrontation between new observations and theories of the early and recent universe makes cosmology one of the most rapidly advancing fields in the physical sciences. The universe is a unique laboratory in which to probe fundamental physics, the rationale being to start from fundamental physics inspired models and explore their consequences in sufficient quantitative detail to be able to identify key astrophysical and cosmological tests of the underlying theory (or developing new tests when appropriate). An unprecedented number of such tests will be possible in the coming years, by exploiting the ever improving observational data. In this spirit I will highlight some open issues in cosmology and particle physics and provide some motivation for this symposium.

1 Scalar Fields

The deepest enigma of modern physics is whether or not there are fundamental scalar fields in nature. For over four decades the standard model of particle physics has been relying on one such field (the Higgs field) to give mass to all the other particles and make the theory gauge-invariant, but this hasn't yet been found. Finding it is the main science driver behind the LHC.

Despite the considerable success of the standard model of particle physics, there are at least three firmly established facts that it can't explain: neutrino masses, dark matter and the size of the baryon asymmetry of the universe. It's our confidence in the standard model that leads us to the expectation that there must be new physics beyond it. More importantly, all those three have obvious astrophysical and cosmological implications, so progress in fundamental particle physics will increasingly rely on progress in cosmology.

C.J.A.P. Martins
Centro de Astrofísica, Universidade do Porto, Rua das Estrelas, 4150-762 Porto, Portugal
and DAMTP/CTC, University of Cambridge, Wilberforce Road, Cambridge CB3 0WA, U.K.
e-mail: Carlos.Martins@astro.up.pt

C. Martins and P. Molaro (eds.), *From Varying Couplings to Fundamental Physics*,
Astrophysics and Space Science Proceedings, DOI 10.1007/978-3-642-19397-2_1,

In this context, it is remarkable that Einstein gravity has no scalar fields. Indeed this is exceptional, because almost any consistent gravitational theory one can think of will have one or more scalar fields. The fact that there is none is, to some extent, what defines Einstein gravity. Nevertheless recent developments suggest that scalar fields can be equally important in astrophysics and cosmology.

Scalar fields play a key role in most paradigms of modern cosmology. One reason for their popularity is that they can take a VEV while preserving Lorentz invariance, while vector fields or fermions would break Lorentz Invariance and lead to conflicts with Special Relativity. Among other things, scalar fields have been invoked to account for the exponential expansion of the early universe (inflation), cosmological phase transitions and their relics (cosmic defects), dynamical dark energy powering current acceleration phase, and the variation of nature's fundamental couplings.

Even more important than each of these paradigms is the fact that they usually don't occur alone. For example, in most realistic inflation models the inflationary epoch ends with a phase transition at which defects are produced. Another example, to which we shall return later, is that dynamical scalar fields coupling to the rest of the model (which they will do, in any realistic scenario [4]) will necessarily have significant variations of fundamental constants. These links will be crucial for future consistency tests.

2 Varying Constants

Nature is characterized by a set of physical laws and fundamental dimensionless couplings, which historically we have assumed to be spacetime-invariant. For the former this is a cornerstone of the scientific method, but for latter it is a simplifying assumption without further justification. Since it's these couplings that ultimately determine the properties of atoms, cells, planets and the universe as a whole, it's remarkable how little we know about them, and indeed that there is such a broad range of opinions on the subject [5, 7].

At one side of the divide there is the Russian school which tends to see constants as defining asymptotic states (for example the speed of light is the limit velocity of massive particle in flat space-time, and so forth). At the opposite end of the spectrum is the Eddington school, which sees them as simple conversion factors. You are subscribing to the Eddington school when you 'set constants to unity' in your calculations. However, this can't be pushed arbitrarily far. One is free to choose units in which $c = \hbar = G = 1$, but one can't choose units in which $c = \hbar = e = 1$, because in the latter case the fine-structure constant will also be unity, and in the real world it isn't.

From the point of view of current physics, three constants seem fundamental: one only needs to define units of length, time and energy to carry out any experiment one chooses. However, nobody knows what will happen in a more fundamental theory. Will we still have three, one or none at all? (To some extent one can argue that in string theory there are only two fundamental constants). Moreover, it is also unknown whether they will be fixed by consistency conditions, or remain arbitrary (with their evolution being driven by some dynamical attractor mechanism).

Although for model-building it makes sense to discuss variations of dimensional quantities, experimentally the situation is clear: one can only measure unambiguously dimensionless combinations of constants, and any such measurements are necessarily local. This is important if one wants to compare measurements at different cosmological epochs (searching for time variations) or even at different environments (searching for spatial variations). Face-value comparisons of measurements at different redshifts are too naive, and often manifestly incorrect. Most such comparisons are model-dependent, since a cosmological model must be assumed. In particular, assuming a constant rate of change (of the fine-structure constant say) is useless: no sensible particle physics model will ever have such dependence over any significant redshift range.

Thus speaking of variations of dimensional constants has no physical significance: one can concoct any variation by defining appropriate units of length, time and energy. Nevertheless, one is free to choose an arbitrary dimensionful unit as a standard and compare it with other quantities. A relevant example is the following. If one assumes particle masses to be constant, then constraints on the gravitational constant G are in fact constraining the (dimensionless) product of G and the nucleon mass squared. A better route is to compare the QCD interaction with the gravitational one: this can be done by assuming a fixed energy scale for QCD and allowing a varying G, or vice-versa. With these caveats, probes of a rolling G provide key information on the gravitational sector. Paradoxically, G was the first constant to be measured but is now the least well known, a consequence of the weakness of gravity.

If fundamental couplings are spacetime-varying, all the physics we know is incomplete and requires crucial revisions. Varying non-gravitational constants imply a violation of the Einstein Equivalence Principle, a fifth force of nature, and so on. Such a detection would therefore be revolutionary, but even improved null results are very important, and can provide constraints on anything from back-of-the-envelope toy models to string theory itself.

A simple way to illustrate the above point is as follows. If one imagines a cosmologically evolving scalar field that leads to varying fundamental couplings, then the natural timescale for their evolution would be the Hubble time. However, current local bounds from atomic clocks [13] are already six orders of magnitude stronger. Any such field must therefore be evolving much more slowly that one would naively expect, and this rules out many otherwise viable models.

3 Exciting Times

Searches for spacetime variations of fundamental constants mostly focus on the fine-structure constant α and the proton-to-electron mass ratio μ, as the rest of these proceedings illustrate. These are the only two dimensionless parameters needed for the description of the gross structure of atoms and molecules. Additionally, the gravitational constant G is interesting: although it has dimensions, one can construct dimensionless quantities involving it that probe the nature of the gravitational interaction (cf. Garcia-Berro's contribution in these proceedings).

It must be emphasized that in any sensible model where one of the couplings vary all the others should do as well, at some level. Different models predict very different relations for these variations; for example, in Grand-Unified Theories the variations of α and μ are related via

$$\frac{d\ln\mu}{dt} = R\frac{d\ln\alpha}{dt}\,, \tag{1}$$

where R is a constant free parameter. Not even its size is determined a priori, although the naive expectation (based on high-energy GUT scenarios) is that the modulus of R should be of order 30-50. (Having R of order unity would require fine-tuning.) Hence, simultaneous astrophysical measurements of α and μ, such as those in the radio band, provide an optimal way of probing GUTs and fundamental physics. Assuming the validity of the current claimed detections, measurements of α and μ with 10^{-6} accuracy can constrain R to 10% (or better, depending on its value).

Local (laboratory) bounds on the current rates of change can be obtained by looking at the frequency drift of two or more atomic clocks—see the contributions by Bize and Peik. These are currently consistent with no variation, and as has already been pointed out they note that these already restrict any variation to be many orders of magnitude weaker than the natural expectation for a cosmological process.

In coming years experiments such as μSCOPE, ACES, and possibly GG and STEP will carry out these measurements, as well as stringent Equivalence Principle tests, in microgravity conditions. These will improve on current sensitivities by several orders of magnitude, and if the current claims of astrophysical detections are correct they should find direct evidence for Equivalence Principle violations.

A nominally strong bound on α can be obtained from the Oklo natural nuclear reactor. However, this is obtained assuming that α is the only quantity that can change, which is a particularly poor assumption since it is known that the underlying chain or reactions is most sensitive to the coupling for the strong force (cf. Flambaum's contribution). The importance of this Oklo bound has therefore been grossly exaggerated.

Astrophysical measurements rely on precision spectroscopy, most often using absorption lines. Emission lines can also be used in principle, but with current means they are less sensitive—cf. the contribution by Gutierrez. Note however that although it's often claimed that another disadvantage of emission line measurements is that they can only be done at low redshift, this has been shown not to be the case [3].

For both α and μ there are few-sigma claims of detected variations [9, 12] at redshfits $z \sim 3$, but in both cases other studies find no variations. Recent months have seen the emergence of interesting new results, including evidence for a spatial dipole and further spatial variations within the Galaxy, and this symposium provided a timely opportunity for those involved to present and discuss them—cf. the contributions by Levshakov, Petitjean, Thompson, Webb, Wendt and Ubachs.

Bounds on α can be obtained at much higher redshift, in particular using the Cosmic Microwave Background [8]. WMAP data, when combined with other datasets, has recently led to constraining any such variation to be below the percent level—cf. Galli's contribution. There is no evidence for variation at this redshift. The bound is much weaker than the above (due to degeneracies with other cosmological parameters) but clean and model-independent. At even higher redshifts BBN can also be used (and also yields percent-level bounds), although with the caveat that in these case the bounds are necessarily model-dependent. The CMB data is also becoming good enough to constrain joint variations of α and other couplings. Such joint constraints will become increasingly important.

4 Redundancy and Further Tests

This field is perceived by outsiders as one plagued with controversy and haunted by concerns about systematics. Although this view is certainly unfair, it is true that improvements are needed—but it most also be emphasized that those active in the field are the first to admit this. Part of the problem stems from the fact that almost all the data that has been used so far was gathered for other purposes, and does not have the necessary quality to fully exploit the capabilities of modern spectrographs. Measurement of fundamental constants requires observing procedures beyond what is done in standard observations [16]. One needs customized data acquisition and wavelength calibration procedures beyond those supplied by standard pipelines, and ultimately one should calibrate with laser frequency combs. Fortunately, we are moving fast in this direction.

A new generation of high-resolution, ultra-stable spectrographs will be needed to resolve the issue. In the short term Maestro at the MMT and PEPSI at LBT will being significant improvements. Later on the prospects are even better with two ESO spectrographs, ESPRESSO for VLT (which has recently been approved by the ESO Council) and CODEX for the E-ELT. Both of these have searches for these variations as one of the key science drivers, and will improve on currently achievable sensitivities by one and two orders of magnitude, respectively.(Further details can be found in Molaro's contribution.) In the meantime, and ongoing VLT/UVES Large Programme will bring significant improvements.

With the anticipated gains if both statistical and systematic uncertainties, further tests will also become possible. For example, the ratio of the proton and electron masses μ is measured through molecular vibrational and rotational lines. If one uses H_2 then one is indeed measuring μ, but molecular Hydrogen is not easy to find, and therefore other molecules are also used, and in this case one needs to be more careful. Strictly speaking one is then probing an average nucleon mass containing both protons and neutrons. One can still write $m_{nuc}/m_e \sim F m_p/m_e$ (with F being a number of order a few), but only if there are no composition-dependent forces, or in other words if the scalar field has the same coupling to protons and neutrons. However, from a theoretical point of view this is highly unlikely. Nevertheless, this provides us with a golden opportunity to search for these couplings. All that needs to be done is to repeat the measurements with molecules containing different numbers of neutrons: H_2 has none, HD has one, and so forth. It should also be added that one can sometimes find these various molecules in the same system, so this need not be costly in terms of telescope time.

Moreover, given the extraordinary relevance of possible detections, it is especially important to have these confirmed by alternative and completely independent methods. Over the past decade or so a whole range of experimental and observational techniques have been used to search for temporal and spatial varying couplings throughout the cosmic history. Atomic clocks, geophysics (Oklo and meteorites), spectroscopy, the CMB and BBN have already been mentioned—they are the best known and more often used ones. But further astrophysical probes are also emerging, and they can play a key role in the coming years: examples are clusters (through the Sunyaev-Zel'dovich effect), helioseismology and strong gravity systems (white dwarfs and neutron stars).

Last but not least, complementary tests will be crucial to establish the robustness and consistency of the results. These are tests which do not measure varying constants directly but search for other non-standard effects that must be present if constants do vary. Equivalence Principle tests are the best known example. A second one that may well be crucial in the coming years are tests of the temperature-redshift relation. For example, in many models where photons are destroyed one can write

$$T(z) = T_0(1+z)^{1-\beta}\,, \tag{2}$$

where $\beta = 0$ in the standard model, and the current best constraint is $\beta < 0.08$ [11].

Measuring the CMB temperature at non-zero redshift is not trivial, but the systems where it can be done are also interesting for varying constants. At low redshifts $T(z)$ can be measured at SZ clusters [2], which can also be used to measure α, and at intermediate redshifts it can be measured spectroscopically using molecular rotational transitions [15], which can also be used to measure μ. The prospect of simultaneous measurements of $T(z)$, μ and possibly also α in the same system, with ESPRESSO or CODEX, is a particularly exciting one.

5 Dynamical Dark Energy

Observations suggest that the universe dominated by component whose gravitational behavior is similar to that of a cosmological constant. The required cosmological constant value is so small that a dynamical scalar field is arguably more likely. The fact that it must be slow-rolling in recent times (which is mandatory for $p < 0$) and dominating the energy budget are sufficient to ensure [4] that couplings of this field lead to observable long-range forces and time dependence of the constants of nature. It should be kept in mind that in any sensible theory scalars will couple to the rest of the world in any manner not prevented by symmetry principles.

Standard methods (SNe, Lensing, etc) are know to be of limited use as dark energy probes [6]. One reason for this is that what one observes and what one wants to measure are related by second derivatives. A clear detection of varying dark energy equation of state $w(z)$ is key to a convincing result. Since $w_0 \sim -1$ and since the field is slow-rolling when dynamically important, a convincing detection of $w(z)$ is quite unlikely even with EUCLID or WFIRST.

Since a scalar field yielding dark energy also yields varying couplings, they can be used to reconstruct $w(z)$ [10]. The procedure is analogous to reconstructing the 1D potential for the classical motion of a particle, given its trajectory. The simplest paradigm relating the two is

$$\frac{\Delta\alpha}{\alpha} = \kappa\zeta(\delta\phi)\,, \tag{3}$$

where $\kappa^2 = 8\pi G$. This reconstruction method only involves first derivatives of the data, and it will complement and extend traditional methods. A comparison of this and the standard method will yield a measurement of the scalar field coupling ζ, which can be compared to that coming from Equivalence Principle tests. In the E-ELT era, synergies will also exist with the Sandage-Loeb test [14].

Advantages of this method include the fact that it allows direct probes of Grand Unification and fundamental physics, and that it directly distinguishes a cosmological constant from a dynamical field (with no false positives). However, the key advantage is its huge redshift lever arm, probing the otherwise inaccessible redshift range where the field dynamics is expected to be fastest (that is, deep in the matter era). It is of course also much cheaper than putting a satellite in space: it is a ground-based method, and taking at face value the currently existing data one can show [1] that 100 good nights on a 10m-class telescope (such as the VLT, Keck or the LBT) could conceivably yield a five-sigma detection of dynamical dark energy.

6 Conclusions

Varying constants are a powerful, versatile and low-cost way to probe fundamental physics and dark energy. There is ample experimental evidence showing that fundamental couplings run with energy, and many particle physics and cosmology models suggest that they also roll with time. There is therefore every incentive to search for these, and there's no better place than in the early universe. Current measurements restrict any such relative variations to be below the 10^{-5} level, which is already a very significant constraint.

The coming years will bring big gains in sensitivity and also dedicated experiments, but doing things right is tough: we need customized observation procedures, laser frequency comb calibration, purpose-built data reduction pipelines, and further astrophysical probes to complement the existing ones. One must also keep in mind the dark energy lesson: when measurements from type Ia supernovae first suggested an accelerating universe these were largely dismissed until such evidence also emerged through independent methods (CMB, lensing, large-scale structure and so on). It is this quest for redundancy that this field must now pursue, and laboratory measurements (with atomic clocks), Equivalence Principle and temperature-redshift tests will be crucial in the next decade.

In addition to its direct impact, these studies have a unique role to play in shedding light on the enigma of dark energy. The early universe is an ideal fundamental physics laboratory, allowing us to carry out tests that one will never be able to do in terrestrial laboratories. Recent technological developments now provide us with tools to accurately search for varying constants and explore its impacts elsewhere, and this opportunity must be taken. The fact that something as fundamental (and abstract) as string theory may one day be confirmed using something as mundane as spectroscopy is an opportunity that neither astrophysicists nor particle physicists can afford to miss.

Acknowledgements I acknowledge discussions with a number of collaborators and colleagues—Silvia Galli, Gemma Luzzi, João Magueijo, Elisabetta Majerotto, Gianpiero Mangano, Alessandro Melchiorri, Eloisa Menegoni, Paolo Molaro, Michael Murphy, Nelson Nunes, Pedro Pedrosa, Patrick Petitjean, Georg Robbers, Rodger Thompson and Wim Ubachs—which have shaped my views on this subject. This work is funded by a Ciência2007 Research Contract, supported by FSE and POPH-QREN funds. Further support came from Fundação para a Ciência e a Tecnologia (FCT), Portugal, through grant PTDC/CTE-AST/098604/2008.

References

1. P.P. Avelino, C.J.A.P. Martins, N.J. Nunes and K.A. Olive, Phys. Rev. D74 (2006) 083508.
2. E.S. Battistelli et al., Astrophys. J. 580 (2002) L101.
3. J. Brinchmann et al., AIP Conf. Proc. 736 (2005) 117.
4. S.M. Carroll, Phys. Rev. Lett. 81 (1998) 3067.
5. M.J. Duff, L.B. Okun and G. Veneziano, JHEP 03 (2002) 023.
6. I. Maor, R. Brustein, J. McMahon and P.J. Steinhardt, Phys. Rev. D65 (2002) 123003.
7. C.J.A.P. Martins, Phil. Trans. Roy. Soc. Lond. A360 (2002) 2681.
8. C.J.A.P. Martins et al., Phys. Lett. B585 (2004) 29.
9. M.T. Murphy, J.K. Webb and V.V.Flambaum, Mon. Not. Roy. Astron. Soc. 345 (2003) 609.
10. N.J. Nunes and J.E. Lidsey, Phys. Rev. D69 (2004) 123511.
11. G. Luzzi et al., Astrophys. J. 705 (2009) 1122.
12. E. Reinhold et al., Phys. Rev. Lett. 96 (2006) 151101.
13. T. Rosenband et al., Science 319 (2008) 1808.
14. A. Sandage, Astrophysical Journal 136 (1962) 319.
15. R. Srianand, P. Petitjean and C. Ledoux, Nature 408 (2000) 931.
16. R.I. Thompson, J. Bechtold, J.H. Black and C.J.A.P. Martins, New Astron. 14 (2009) 379.

Atomic Transition Frequencies, Isotope Shifts, and Sensitivity to Variation of the Fine Structure Constant for Studies of Quasar Absorption Spectra

J.C. Berengut, V.A. Dzuba, V.V. Flambaum, J.A. King, M.G. Kozlov, M.T. Murphy, and J.K. Webb

Abstract Theories unifying gravity with other interactions suggest spatial and temporal variation of fundamental "constants" in the Universe. A change in the fine structure constant, $\alpha = e^2/\hbar c$, could be detected via shifts in the frequencies of atomic transitions in quasar absorption systems. Recent studies using 140 absorption systems from the Keck telescope and 153 from the Very Large Telescope, suggest that α varies spatially [61]. That is, in one direction on the sky α seems to have been smaller at the time of absorption, while in the opposite direction it seems to have been larger.

To continue this study we need accurate laboratory measurements of atomic transition frequencies. The aim of this paper is to provide a compilation of transitions of importance to the search for α variation. They are E1 transitions to the ground state in several different atoms and ions, with wavelengths ranging from around 900–6000 Å, and require an accuracy of better than 10^{-4} Å. We discuss isotope shift measurements that are needed in order to resolve systematic effects in the study. The coefficients of sensitivity to α-variation (q) are also presented.

1 Introduction

Current theories that seek to unify gravity with the other fundamental interactions suggest that spatial and temporal variation of fundamental constants is a possibility, or even a necessity, in an expanding Universe (see, for example the review of [57]). Several studies have tried to probe the values of constants at earlier stages in the

---

J.C. Berengut, V.A. Dzuba, V.V. Flambaum, J.A. King, and J.K. Webb
School of Physics, University of New South Wales, Sydney, NSW 2052, Australia

M.G. Kozlov
Petersburg Nuclear Physics Institute, Gatchina, 188300, Russia

M.T. Murphy
Centre for Astrophysics and Supercomputing, Swinburne University of Technology, Victoria 3122, Australia

C. Martins and P. Molaro (eds.), *From Varying Couplings to Fundamental Physics*, Astrophysics and Space Science Proceedings, DOI 10.1007/978-3-642-19397-2_2,

evolution of the Universe, using tools such as big-bang nucleosynthesis, the Oklo natural nuclear reactor, quasar absorption spectra, and atomic clocks (see, e.g. [21]).

Comparison of atomic transition frequencies on Earth and in quasar (QSO) absorption spectra can be used to measure variation of the fine-structure constant $\alpha = e^2/\hbar c$ over the last 10 billion years or so. Early studies used the "alkali-doublet" method [53], taking advantage of the simple α-dependence of the separation of a fine-structure multiplet.

More recently we developed the "many-multiplet" method [17, 18] which improves sensitivity to variation in α by more than an order of magnitude compared to the alkali-doublet method. Enhancement comes from the use of transitions which are more sensitive to α than the fine-structure splitting is, for example the s-wave orbital has maximum relativistic corrections to energy but no spin-orbit splitting. In addition the α-dependence varies strongly between different atoms and transitions (for example s–p and s–d transitions can have different signs) and this helps to control instrumental and astrophysical systematics. The number of spectral lines available for study is quite large; this gives a statistical advantage.

The first analyses using the many-multiplet method and quasar absorption spectra obtained at the Keck telescope revealed hints that the fine structure constant was smaller in the early universe [37, 39, 40, 42, 58–60]. A very extensive search for possible systematic errors has shown that known systematic effects cannot explain the result [38].

Our method and calculations have been used by other groups to analyse a different data set from the Very Large Telescope (VLT) in Chile ([55]), and their results indicate no variation of α (see also [12]). It was noted later that there were sharp fluctuations in chi-squared vs. $\Delta\alpha/\alpha$ graphs of [12, 55] that indicate failings in the chi-squared minimisation routine [43], and it was shown that the errors were underestimated by a large factor [43, 44, 56].

A large scale analysis, combining the Keck data with a new sample of 153 measurements from the VLT, indicates a spatial variation in α at the 4.1σ level [61]. This gradient has a declination of around −60°, which explains why the Keck data, restricted mainly to the northern sky since the telescope is in Hawaii at a latitude of 20° N, originally suggested a time-varying α that was smaller in the past. The VLT is in Chile, at latitude 25° S, giving the new combined study much more complete sky coverage. The new results are entirely consistent with previous ones. Other results from other groups using single ions in single absorption systems [31–33, 51] are also consistent with the dipole result [9]. We note that individual sight-lines are inherently less useful than large samples, no matter what the signal-to-noise ratio of the single sight-line spectra, because some systematic errors that are present for single sight-lines often randomize over a large sample [38].

2 Laboratory Spectroscopy

To continue this work, several new transitions are being considered. In Table 1 we present a list of lines commonly observed in high-resolution QSO spectra. All of the lines marked 'A' (extremely important), 'B' (very important), or 'C' (less important) lack the high-accuracy laboratory measurements necessary for studies of α variation. All transitions are from the ground state of the ion, with the exception of the CII lines marked with an asterisk which are transitions from the metastable $2s^22p\,{}^2P^o_{3/2}$ level. Predominantly the wavelengths and oscillator strengths are taken from the compilations of [35, 36]. The wavelengths have errors of about 0.005 Å, although it is possible that some errors are closer to 0.05 Å. Note that the oscillator strengths presented are not as accurate as the wavelengths: these measurements are much more difficult. As a general rule, the lines are more important for α variation if they lie above 1215.67 Å (the Lyman-α line of hydrogen) due to the "Lyman-α forest" seen in QSO spectra.

Table 1 High-priority lines observed in QSO spectra. The need for precise wavelength measurement (or re-measurement) is indicated by an A (extremely important), B (very important) or C (less important) in the 'Status' column; existing precise measurements are referenced in the last column. In the 'I.S.' column the status of isotope structure measurement is indicated: a ✓ means it has been measured, and 'A' means that it is unknown and urgently needed. All transitions are from the ground state of the ion, with the exception of the CII lines marked with an asterisk which are transitions from the metastable $2s^22p\,{}^2P^o_{3/2}$ level

Atom/ Ion	Wavelength λ (Å)	Frequency ω_0 (cm^{-1})	Oscillator Strength	q value (cm^{-1})	Status ω_0	Status I.S.	Refs.
C I	945.188	105799.1	0.272600	130 (60)	C	✓	[30]
	1139.793	87735.30	0.013960	0 (100)	C		
	1155.809	86519.47	0.017250	0 (100)	C		
	1157.186	86416.55	0.549500	0 (100)	C		
	1157.910	86362.52	0.021780	0 (100)	C		
	1188.833	84116.09	0.016760	0 (100)	C		
	1193.031	83820.13	0.044470	0 (100)	C		
	1193.996	83752.41	0.009407	0 (100)	C		
	1260.736	79318.78	0.039370	30 (10)	B		
	1276.483	78340.28	0.004502	17 (10)	B		
	1277.245	78293.49	0.096650	−13 (10)	B		
	1280.135	78116.74	0.024320	−21 (10)	B		
	1328.833	75253.97	0.058040	117 (10)	B		
	1560.309	64089.85	0.080410	137 (10)	B		
	1656.928	60352.63	0.140500	−24 (10)	B		
C II	1036.337	96493.74	0.123000	168 (10)	B		
	1037.018*	96430.32	0.123000	105 (10)	B		
	1334.532	74932.62	0.127800	178 (10)	B		
	1335.662*	74869.20	0.012770	115 (10)	B		
	1335.707*	74866.68	0.114900	118 (10)	B		
C III	977.020	102352.0	0.762000	165 (10)	C		
C IV	1548.204	64590.99	0.190800	222 (2)	B		[23]
	1550.781	64483.65	0.095220	115 (2)	B		[23]
O I	1025.762	97488.53	0.020300	0 (20)	C		[27]
	1026.476	97420.72	0.002460	0 (20)	C		
	1039.230	96225.05	0.009197	0 (20)	C		
	1302.168	76794.98	0.048870	0 (20)	B		

(*Continued*)

Table 1 (Continued)

Atom/	Wavelength	Frequency	Oscillator	q value	Status		Refs.
Ion	λ (Å)	ω_0 (cm^{-1})	Strength	(cm^{-1})	ω_0	I.S.	
Na I	3303.320	30272.58	0.013400	57 (2)	C		
	3303.930	30266.99	0.006700	51 (2)	C		
	5891.583	16973.37	0.655000	62 (2)	C	✓	[26, 28, 46]
	5897.558	16956.17	0.327000	45 (2)	C	✓	[22, 28]
Mg I	2026.477	49346.73	0.112000	87 (7)	B	✓	[1, 25]
	2852.963	35051.27	0.181000	90 (10)	B	✓	[1, 11, 24, 47, 52]
Mg II	1239.925	80650.04	0.000267	192 (2)	C		
	2796.354	35760.85	0.612300	212 (2)	B	✓	[1, 3, 13, 47]
	2803.532	35669.30	0.305400	121 (2)	B	✓	[1, 3, 47]
Al II	1670.789	59851.97	1.880000	270 (30)	B	✓	[23]
Al III	1854.718	53916.54	0.539000	458 (6)	B	✓	[23]
	1862.791	53682.88	0.268000	224 (8)	B	✓	[23]
Si II	1190.416	84004.26	0.250200		C		
	1193.290	83801.95	0.499100		C		
	1260.422	79338.50	1.007000		B		
	1304.370	76665.35	0.094000		B		
	1526.707	65500.45	0.117094	50 (30)	B	A	[23]
	1808.013	55309.34	0.002010	520 (30)	B	A	[23]
Si IV	1393.760	71748.64	0.528000	823 (40)	B	A	[23]
	1402.773	71287.54	0.262000	361 (15)	B	A	[23]
S II	1250.583	79962.61	0.005350		B		
	1253.808	79756.83	0.010700		B		
	1259.518	79395.39	0.015900		B		
Ca II	3934.777	25414.40	0.688000	446 (6)	B	✓	[62]
	3969.591	25191.51	0.341000	222 (2)	B	✓	[62]
Ti II	1910.600	52339.58	0.202000	−1564 (150)	A	A	
	1910.938	52330.32	0.098000	−1783 (300)	A	A	
	3067.245	32602.55	0.041500	791 (50)	B	A	[1]
	3073.877	32532.21	0.104000	677 (50)	B	A	[1]
	3230.131	30958.50	0.057300	673 (50)	B	A	[1]
	3242.929	30836.32	0.183000	541 (50)	B	A	[1]
	3384.740	29544.37	0.282000	396 (50)	B	A	[1]
Cr II	2056.256	48632.06	0.105000	−1110 (150)	B	A	[1, 48]
	2062.236	48491.05	0.078000	−1280 (150)	B	A	[1, 48]
	2066.164	48398.87	0.051500	−1360 (150)	B	A	[1, 48]
Mn II	1197.184	83529.35	0.156600	−2556 (450)	C		
	1199.391	83375.65	0.105900	−2825 (450)	C		
	1201.118	83255.77	0.088090	−3033 (450)	C		
	2576.877	38806.66	0.288000	1276 (150)	B	A	[1, 10]
	2594.499	38543.08	0.223000	1030 (150)	B	A	[1, 10]
	2606.462	38366.18	0.158000	869 (150)	B	A	[1, 10]
Fe II	1063.176	94057.80	0.060000		C		
	1063.971	93987.52	0.003718		C		
	1096.877	91167.92	0.032400		C		
	1121.975	89128.55	0.020200		C		
	1125.448	88853.51	0.016000		C		

(*Continued*)

Table 1 (Continued)

Atom/ Ion	Wavelength λ (Å)	Frequency ω_0 (cm^{-1})	Oscillator Strength	q value (cm^{-1})	Status		Refs.
					ω_0	I.S.	
	1143.226	87471.77	0.017700		C		
	1144.939	87340.98	0.106000		C		
	1260.533	79331.52	0.025000		B		
	1608.450	62171.63	0.058000	−1165 (300)	A	A	[49]
	1611.200	62065.53	0.001360	1330 (300)	A	A	[49]
	2249.877	44446.88	0.001821		A	A	
	2260.780	44232.51	0.002440		A	A	[1]
	2344.212	42658.24	0.114000	1375 (300)	B	A	[1,45]
	2367.589	42237.06	0.000212	1904	B		
	2374.460	42114.83	0.031300	1625 (100)	B	A	[1,45]
	2382.764	41968.06	0.320000	1505 (100)	B	A	[1,45]
	2586.649	38660.05	0.069180	1515 (100)	B	A	[1,45]
	2600.172	38458.99	0.238780	1370 (100)	B	A	[1,45]
Ni II	1317.217	75917.64	0.146000		A		
	1370.132	72985.67	0.076900		A		
	1393.324	71770.82	0.022220		A		
	1454.842	68735.99	0.032300		A		
	1467.259	68154.29	0.009900		C		
	1467.756	68131.22	0.006300		C		
	1502.148	66571.34	0.006000		C		
	1703.412	58705.71	0.012240		A		[48]
	1709.604	58493.07	0.032400	−20 (250)	A	A	[48]
	1741.553	57420.01	0.042700	−1400 (250)	A	A	[48]
	1751.915	57080.37	0.027700	−700 (250)	A	A	[48]
Zn II	2026.137	49355.00	0.489000	2470 (25)	C	✓	[1,34,48]
	2062.660	48481.08	0.256000	1560 (25)	B	A	[1,48]
Ge II	1237.059	80836.880	0.870000	2236 (70)	A		
	1602.486	62403.028	0.130000	−664 (70)	B		

Isotope shift measurements for these transitions are also needed in order to resolve a possible source of systematic error in the variation of α studies: the isotope abundance ratios in the gas clouds sampled in the quasar absorption spectra may not match those on Earth [38,41]. Spurious observation of α-variation due to differences in isotope abundance of any one element has been ruled out (see, e.g. [40]), however an improbable "conspiracy" of changes in several elements could mimic an effect. On the other hand, it is difficult to see how such changes could lead to spurious observation of a spatial variation since the underlying mechanisms of chemical evolution would have to vary spatially. Nevertheless, the many-multiplet method uses different transitions of different atoms at different redshifts, so ignoring the isotopic structure of transitions may destroy the consistency between sub-samples occupying different redshift ranges.

Accurate measurements of the isotope shift are required to quantify these systematic effects. Additionally, if the isotope shifts are known then it is possible to simultaneously determine both any possible α-variation and the isotope abundances in the early universe directly [29]. This can be used to constrain models of chemical evolution of the Universe and test models of nuclear processes in stars [2, 20]. We have performed very complicated calculations of some isotope shifts [4, 6–8], however calculations in group $3d$ atoms and ions are difficult, and our accuracy may be low. Therefore measurements for at least some lines are needed to benchmark calculations in this regime. In Table 1 we indicate lines for which isotope shifts are known by a ✓ in the 'I.S.' column. Lines that were used in previous studies (and hence have precise wavelength measurements), but for which the isotopic structure has not been measured are marked with an 'A' in this column.

A similar systematic effect to that caused by isotope abundances can occur due to differential saturation of the hyperfine components. This can occur because of deviations from local thermal equilibrium (see, e.g. [40]). While we do not discuss this issue in this paper, we note that in some cases, such as Al III and Mn II, hyperfine structure can be as important as isotopic structure.

3 Sensitivity Coefficients

We previously calculated the relativistic energy shifts, or q-values, for many of the lines seen in quasar spectra [5–7, 15, 16, 19, 50, 54]. The difference between the transition frequencies in QSO spectra (ω) and in the laboratory (ω_0) depends on the relative values of α. The dependence of the frequencies on small changes in α is given by the formula

$$\omega = \omega_0 + qx \,, \tag{1}$$
$$x = (\alpha/\alpha_0)^2 - 1 \approx 2\frac{\alpha - \alpha_0}{\alpha_0} \,.$$

The q values are calculated using atomic physics codes. The atomic energy levels are calculated to a first approximation using relativistic Hartree-Fock (Dirac-Hartree-Fock). Higher order effects are taken into account using a combination of configuration interaction (for many-valence-electron systems) and many-body perturbation theory; this is known as the "CI+MBPT" method [14]. The value of α is varied in the computer codes and the energy levels are recalculated, and hence the transition frequencies. The q values are extracted as

$$q = \left.\frac{d\omega}{dx}\right|_{x=0}$$

We also account for complications due to level pseudo-crossing as described by [19]. In Table 1 we present our current best q-values for easy reference. Note that for Fe II lines, we present the arithmetic average of the independent calculations [19] and [50]. Uncertainties here are representative rather than statistical.

Acknowledgements The authors would like to thank D. Morton and W. Ubachs for useful comments and for pointing out some errors.

References

1. M. Aldenius et al., MNRAS 370 (2006) 444.
2. T.P. Ashenfelter, G.J. Mathews and K.A. Olive, Phys. Rev. Lett. 92 (2004) 041102.
3. V. Batteiger et al., Phys. Rev. A80 (2009) 022503.
4. J.C. Berengut et al., Phys. Rev. A68 (2003) 022502.
5. J.C. Berengut et al., Phys. Rev. A70 (2004) 064101.
6. J.C. Berengut et al., Phys. Rev. A72 (2005) 044501.
7. J.C. Berengut et al., Phys. Rev. A73 (2006) 012504.
8. J.C. Berengut et al., J. Phys. B 41 (2008) 235702.
9. J.C. Berengut and V.V. Flambaum, arXiv:1009.3693.
10. R.J. Blackwell-Whitehead et al., MNRAS 364 (2005) 705.
11. S.L. Boiteux et al., J. Phys. (France) 49 (1988) 885.
12. H. Chand et al., A&A 417 (2004) 853.
13. R.E. Drullinger et al., Appl. Phys. 22 (1980) 365.
14. V.A. Dzuba et al., Phys. Rev. A54 (1996) 3948.
15. V.A. Dzuba and V.V. Flambaum, Phys. Rev. A71 (2005) 052509.
16. V.A. Dzuba and W.R. Johnson, Phys. Rev. A76 (2007) 062510.
17. V.A. Dzuba et al., Phys. Rev. Lett. 82 (1999) 888.
18. V.A. Dzuba et al., Phys. Rev. A59 (1999) 230.
19. V.A. Dzuba et al., Phys. Rev. A66 (2002) 022501.
20. Y. Fenner et al., MNRAS 358 (2005) 468.
21. V.V. Flambaum and J.C. Berengut, Int. J. Mod. Phys. A 24 (2009) 3342.
22. Y.P. Gangrsky et al., Eur. Phys. J. A 3 (1998) 313.
23. U. Griesmann and R. Kling, ApJ 536 (2000) L113.
24. L. Hallstadius, Z. Phys. A 291 (1979) 203.
25. S. Hannemann et Phys. Rev. A74 (2006) 012505.
26. G. Huber et al., Phys. Rev. C18 (2382) 2342.
27. T.I. Ivanov et al., MNRAS 389 (2008) L4.
28. P. Juncar et al., Metrologia 17 (1981) 77.
29. M.G. Kozlov et al., Phys. Rev. A70 (2004) 062108.
30. I. Labazan et al., Phys. Rev. A71 (2005) 040501.
31. S.A. Levshakov et al., A&A 434 (2005) 827.
32. S.A. Levshakov et al., A&A 449 (2006) 879.
33. S.A. Levshakov et al., A&A 466 (2007) 1077.
34. K. Matsubara et al., Appl. Phys. B 76 (2003) 209.
35. D.C. Morton, Astrophys. J. Suppl. Ser. 77 (1991) 119.
36. D.C. Morton, Astrophys. J. Suppl. Ser. 149 (2003) 205.
37. M.T. Murphy et al., MNRAS 327 (2001) 1208.
38. M.T. Murphy et al., MNRAS 327 (2001) 1223.
39. M.T. Murphy et al., MNRAS 327 (2001) 1237.
40. M.T. Murphy et al., MNRAS 345 (2003) 609.
41. M.T. Murphy et al., Astrophys. Space Sci. 283 (2003) 577.
42. M.T. Murphy et al., Lect. Notes Phys. 648 (2004) 131.
43. M.T. Murphy et al., Phys. Rev. Lett. 99 (2007) 239001.
44. M.T. Murphy et al., MNRAS 384 (2008) 1053.
45. G. Nave et al., J. Opt. Soc. Am. B 8 (1991) 2028.
46. K. Pescht et al., Z. Phys. A 281 (1977) 199.
47. J.C. Pickering et al., MNRAS 300 (1998) 131.

48. J.C. Pickering et al., MNRAS 319 (2000) 163.
49. J.C. Pickering et al., A&A 396 (2002) 715.
50. S.G. Porsev et al., Phys Rev. A76 (2007) 052507.
51. R. Quast et al., A&A 415 (2004) L7.
52. E.J. Salumbides et al., MNRAS 373 (2006) L41.
53. M.P. Savedoff, Nature 178 (1956) 689.
54. I.M. Savukov and V.A. Dzuba, Phys. Rev A77 (2008) 042501.
55. R. Srianand et al., Phys. Rev. Lett. 92 (2004) 121302.
56. R. Srianand et al., Phys. Rev. Lett. 99 (2007) 239002.
57. J.-P. Uzan, Rev. Mod. Phys. 75 (2003) 403.
58. J.K. Webb et al., Phys. Rev. Lett. 82 (1999) 884.
59. J.K. Webb et al., Phys. Rev. Lett. 87 (2001) 091301.
60. J.K. Webb et al., Astrophys. Space Sci. 283 (2003) 565.
61. J.K. Webb et al., arXiv:1008.3907.
62. A.L. Wolf et al., Phys. Rev. A78 (2008) 032511.

String Theory, Dark Energy and Varying Couplings

Marco Zagermann

Abstract I review the difficulties of some recent attempts to find stabilized string theory vacua with positive cosmological constant at tree level. Whereas models with energy momentum tensors satisfying the null energy condition (NEC) and conformally Ricci-flat internal spaces are easily shown to admit at most short transient periods of accelerated expansion, the situation is more complex in the presence of NEC-violating sources such as orientifold planes and more general curved compact spaces. We also comment on some recent discussions in the context of varying fundamental couplings in some of these string compactifications.

1 Introduction

String theory is a general proposal for a unified quantum theory of all particles and interactions, including gravity. In its perturbative formulation, the apparently pointlike "fundamental" particles found in Nature are re-interpreted as different oscillatory modes of one and the same type of objects: tiny one-dimensional filaments called strings. The quantization of extended relativistic objects such as strings requires a number of consistency conditions to hold, some of the most intriguing being the necessity for extra spatial dimensions or, at a somewhat different level, the natural occurrence of supersymmetry in string theory.

In order to explain that the extra dimensions of string theory (six in each of the five perturbative superstring theories) have gone unnoticed so far, one usually assumes that the extra dimensions are curled up to form a small compact manifold, smaller, at least, than the spatial resolution of today's measurement devices.

Just as in conventional Kaluza-Klein theories, compactified extra dimensions are accompanied by a plethora of scalar fields in the resulting effective four-dimensional

---

M. Zagermann
Institute for Theoretical Physics & Center for Quantum Engineering and Spacetime Research (QUEST), Leibniz Universität Hannover, Appelstr. 2, D-30167 Hannover, Germany
e-mail: Marco.Zagermann@itp.uni-hannover.de

C. Martins and P. Molaro (eds.), *From Varying Couplings to Fundamental Physics*,
Astrophysics and Space Science Proceedings, DOI 10.1007/978-3-642-19397-2_3,

(4D) field theory. These scalar fields descend from the internal (i.e. the 6D) components of the original 10D fields in the string spectrum, including, in particular, the dilaton Φ (a scalar field already in 10D), the 10D metric tensor, g_{MN} $(M, N, \ldots = 0, \ldots, 9)$, and various types of antisymmetric tensor fields (p-form potentials) $C_{M_1,\ldots M_p}$. Most of these effective 4D scalar fields correspond to higher Kaluza-Klein modes or very massive string excitations and consequently have to be integrated out of the effective 4D Lagrangian and do not appear as dynamical fields at low energies. In compactifications that preserve at least some of the original 10D supersymmetry, however, several of the above scalar fields remain as massless (or very light) scalar fields in the 4D low energy spectrum. They are called the moduli of a string compactification, and their vacuum expectation values (vevs) parameterize deformations of the compactification background that cost no (or very little) energy, hence their vanishing (or very low) mass.

Moduli fields are usually not charged under the gauge interactions of the Standard Model and interact with ordinary matter only via interactions of gravitational strength (i.e. by gravity itself or via Planck mass suppressed contact interactions). Despite this very weak interaction with visible matter, the presence of light scalar fields can have important phenomenological consequences. For instance, if the vevs of the moduli are not dynamically fixed by a suitable potential, they may be (space-) time dependent, and as most couplings and mass parameters of the 4D effective action depend on the moduli vevs, this may induce (space-)time-dependent "fundamental constants" – the topic of this conference. On the other hand, light moduli fields as such may also cause a number of phenomenological problems. Depending on the mass scale of the moduli, these can e.g. be in conflict with constraints from fifth force experiments, Big Bang Nucleosynthesis (BBN) or overclosure bounds. A simple way to safely avoid all these types of problems would be to ensure that the moduli are sufficiently heavy, say of order 30 . . . 100 TeV or higher. This seems to be not so easy to achieve with mere supersymmetry breaking effects, as these would naturally induce moduli masses of order the gravitino mass (for an interesting exception and a recent discussion, see e.g., [6] and references therein), which, in many supersymmetry breaking scenarios would be below the above-mentioned energy regime.

A very efficient technical tool for giving many moduli a sufficiently large mass in string compactifications is the use of background fluxes for the field strengths of the above-mentioned p-form fields $C_{M_1,\ldots,M_p}$ (see e.g. [5, 18, 23, 29] for reviews). The moduli masses this induces are usually not connected to the gravitino mass and can easily be made sufficiently large to avoid all the above moduli problems. Another advantage of using background fluxes in the internal space for moduli stabilization is that their effects on the moduli potential is comparatively easy to compute, as its evaluation amounts to a rather straightforward dimensional reduction of the classical 10D supergravity action. In many of the most popular scenarios (see e.g. [3, 34]), however, the fluxes are not sufficient for the stabilization of all moduli, and additional quantum corrections, often non-perturbative, have to be invoked. These quantum corrections are, unfortunately, much harder to evaluate explicitly. It is an interesting question whether one can achieve successful moduli stabilization without quantum corrections (for an interesting set of models in this direction, see e.g. [21], where complete moduli stabilization with purely classical ingredients was discussed, as well as the works [7,28,43]).

An additional complication for the construction of semi-realistic string compactifications with stabilized moduli comes from the requirement that the vacuum energy in the minimum should be positive so as to mimic an effective positive cosmological constant. Using just tree-level contributions to the scalar potential (i.e. the classical 10D supergravity equations of motion supplemented by the lowest order effective actions of brane-like sources), it turns out to be surprisingly difficult to construct a stabilized vacuum with positive vacuum energy (i.e., a (meta-)stable de Sitter (dS) vacuum). The models of [21] for instance stabilize the moduli in an anti-de Sitter vacuum, i.e. with a negative vacuum energy. That classical de Sitter vacua are hard to build follows from a number of no-go theorems [19,26,36,40] that, under certain assumptions, exclude such a possibility. Among these assumptions is a positivity requirement for the energy momentum tensor, e.g. in the form of the null energy condition (NEC), which states that $T_{MN}n^N n^M \geq 0$ for all lightlike vectors n^M (see e.g. [40]). What these no-go theorems do allow, is a transient period of accelerated expansion [40,42] of an e-fold or so. In [41], it was suggested that models of this type may be falsifiable on the basis of the time variation of Newton's constant and the dark energy equation of state they would induce.

In the rest of this contribution, I will review some recent attempts to circumvent the above-mentioned no-go theorems against classical de Sitter vacua, including the problems these attempts face and comment on the proposal of [41].

2 Orientifold Planes and Negative Internal Curvature

While the assumption of the null energy condition is satisfied for ordinary types of matter, the type II string theories do contain natural NEC-violating objects. These objects are the orientifold p-planes (Op-planes) of type II string theory; they describe extended non-dynamical defects that arise as fixed point sets of discrete identifications involving the orientation reversal of a string and a geometric reflection symmetry. Their world volume is $(p+1)$-dimensional, and, most importantly, they can be shown to have a negative energy density violating the NEC.

What is surprising is that even though the inclusion of orientifold planes violates the assumptions of the simplest no-go theorems mentioned above, there exist even stronger no-go theorems that forbid the construction of dS vacua also in the presence of orientifold planes provided the curvature of the 6D internal manifold is not negative [32]. In essence the no-go theorem of [32] determines the 4D scalar potential as a function of two universal moduli, the dilaton and the volume modulus parameterizing the overall size of the compact space. The dependences of the potential on these two moduli is such that one can give a lower bound on the ϵ-parameter (see below), whenever the field configuration is at positive potential energy:

$$\epsilon \equiv \frac{g^{ij}\partial_i V \partial_j V}{2V^2} \geq \frac{27}{13}, \quad \text{whenever } V(\phi) > 0 \tag{1}$$

where $\partial_i V \equiv \frac{\partial V}{\partial \phi^i}$ and g^{ij} is the inverse of the metric on the field space of the moduli that appears in their kinetic term, $\mathscr{L}_{\text{kin}} = \frac{1}{2} g_{ij}(\phi)\partial_\mu \phi^i \partial^\mu \phi^j$. In other words, the potential is always very steep in at least one modulus direction whenever the potential is positive. However, the potential does allow for AdS vacua, the models of [21] providing many examples.

This no-go theorem might be evaded, if, in addition to the fluxes and O-planes, one also allows for a *negative* (integrated) curvature of the 6D internal space, $R^{(6)} < 0$. The reason is that the integral over the internal curvature enters the 4D effective theory as a contribution, V_{curv}, to the effective moduli potential, but with a minus sign,

$$V_{\text{curv}} \propto -\int_{M^{(6)}} \sqrt{g^{(6)}} R^{(6)}. \tag{2}$$

Hence, a negative integrated curvature acts as a new positive contribution to the scalar potential that could perhaps "uplift" the known AdS vacua to dS vacua. Attempts in this direction include [10, 11, 13–17, 22, 25, 30, 38, 39, 44].

2.1 Difficulties of This Approach

Trying to use internal spaces of negative curvature as sources for uplift potentials meets with at least two challenges.

The first one is a priori more of a computational issue and relates to the fact that much less is known on compactifications on spaces with negative curvature than for instance for compactifications on Ricci-flat spaces. A major problem here is the identification of the light scalar fields one should keep in the action, which is very well understood for compactifications on the (Ricci-flat) Calabi-Yau manifolds.

The second problem is that a negative curvature space is inconsistent with the Einstein equation unless there is a source of negative energy density[1] at every point where the curvature is supposed to be negative, as was pointed out in [24]. For fluxes this is not satisfied, but orientifold planes do have this property, so one might wonder whether the use of orientifold planes *together* with negative curvature spaces may actually be consistent. The problem with this naive expectation is that the negative energy density of an Op-plane is localised on its $(p+1)$-dimensional world volume. So an internal space that has constant negative curvature everywhere seems inconsistent with the Einstein equations. In [24], however, it was also pointed out that a warp factor[2] (which is in any case introduced by localized sources such as Op-planes) may help to relax this problem. Moreover, for the purposes of obtaining

---

[1] More precisely, certain trace combinations of the energy momentum tensor have to be negative, see [24] for details.

[2] A compactification metric of the form $ds_{10}^2 = e^{2A} ds_4^2 + ds_6^2$ with A being a function of the internal 6D coordinates, is called a warped compactification with warp factor e^{2A}.

an uplifting potential, the curvature does not have to be negative everywhere; it is sufficient that the properly integrated internal curvature is negative.

3 de Sitter Vacua with "Smeared" O-Planes

Finding explicit solutions to the 10D equations of motion in the presence of localised sources such as Op-planes (or Dp-branes for that matter) are notoriously difficult to find, because of the backreaction of these sources on the geometry. The BPS-type Minkowski solutions [27] provide a notable exception. For this reason one often discusses compactifications in the approximation that the effects of the localized sources are only taken into account in their integrated form. At the level of the 10D equations of motion this corresponds to effectively "smearing" the sources in the directions transverse to their worldvolume. Putting aside for the moment the worry that completely delocalizing a localized object may not be a very good approximation, one could try to find de Sitter vacua with smeared orientifold planes on negative curvature spaces. In fact, it is the smeared negative energy of the O-planes that might now support the negative curvature of the internal space in the first place. It then remains to find negative curvature spaces simple enough to allow for a sufficient understanding of its 4D effective field theory. Interestingly, there are manifolds of constant negative curvature where the dimensional reduction is under reasonable control [1, 8, 9, 31, 33, 43]. These are 6D coset or group manifolds that allow for an $SU(3)$ or $SU(2)$ structure so as to preserve some supersymmetry.

In a systematic study for most of these models it was found that, even though the no-go theorems of [32] no longer apply, more refined no-go theorems can be formulated [10, 11, 25] that rule out almost all cases based on a similar argument regarding the ϵ-parameter, albeit with slightly relaxed lower bounds than $27/13$ and by using different moduli directions for these estimates. Among the coset and group spaces based on semisimple and Abelian groups [35], only one candidate is not covered by these refined no-go theorems, namely the manifold $SU(2) \times SU(2)$. On this manifold, a de Sitter extremum of the potential can indeed be identified numerically both in type IIA and type IIB string theory contexts [10, 11]. Unfortunately, this extremum turns out to be only a saddle point [10, 11], i.e. there is a strongly tachyonic direction making this solution perturbatively unstable and also useless for slow roll inflation (the slow-roll parameter η is of order one). Similar features were found for twisted tori in [25], but one may still hope that an enlargement of the set of manifolds one considers could give rise to more successful models.

4 Smeared Versus Localized O-Planes

While the searches for dS vacua in the smeared limit have at least been partially successful, it is still unclear to what extent these are really good approximations to solutions with fully localized orientifold planes or other localized sources.

Furthermore, upon localization, the problems with the negative curvature raised in [24] reappear. We therefore studied the relation between solutions with smeared and localized sources (O-planes and/or D-branes) in more detail in the recent work [4]. One can show that for BPS-like (but not necessarily supersymmetric) solutions such as [27] and their T-dual analogues in other spacetime dimensions, the smearing procedure changes the solution only in a very mild and controlled way that, in particular, does not change the position of the moduli fixed by the fluxes. The underlying reason is that even though the individual (de)localization effects on various fields of the solution are large, the BPS-property relates them to one another such that their influence on e.g. the moduli vevs or the total vacuum energy precisely cancels out (see [4, 20]). What we could also show is that, at least for these BPS-type solutions, spaces with negative internal curvature in the smeared limit still give a negative *integrated* internal curvature in the sense that the curvature contribution to the 4D scalar potential remains positive upon localization of the O-planes. This is possible due to large warp factors that the localization entails and relaxes some of the problems found in [24], at least in the BPS Minkowski vacua studied in [4].

The situation appears to be quite different for non-BPS solutions though. Here a cancellation of the (de)localization effects does in general not take place and solutions that have been derived in the smeared limit may experience stronger deformations or even cease to exist upon localization [4]. As de Sitter vacua are in general not expected to be BPS-like, this casts some doubts on the validity of de Sitter solutions that were obtained in the limit of smeared sources such as orientifold planes. Further implications of these findings also for solutions involving quantum contributions or for solutions close to a BPS-solution are currently under study.[3]

5 Conclusions

As we have tried to convey, it is quite difficult (if not impossible?) to construct (meta-)stable de Sitter vacua in purely classical string compactifications. Even if one uses smeared orientifold planes and negatively curved internal spaces, most of the well understood models can be ruled out on the basis of refined no-go theorems, whereas the few surviving models have not yet resulted in vacua without tachyonic directions. Turning this around, what these models do seem to give quite naturally are transient periods of accelerated cosmic expansion of at most a few e-folds. Models of similar type, albeit without NEC-violating sources and with conformally Ricci-flat internal spaces, have recently been studied in the context of a possible time variation of Newton's constant, G, and the parameter, w, of the dark energy equation of state in [41]. There it was proposed that combinations of near future measurements of w and $\dot{G}/G$ might be useable to severely constrain or even

---

[3] J. Blaback, U. H. Danielsson, D. Junghans, T. Van Riet, T. Wrase and M. Zagermann, work in progress.

rule out classical string compactifications without NEC-violating sources and with conformally Ricci-flat internal spaces due to the merely transient periods of accelerated expansion these models may provide. Whether these simple models are not already ruled out by other constraints is another question, but what we have seen here is that the situation with NEC-violating sources and a departure from conformal Ricci-flatness looks more complex, and it is not yet entirely clear whether stabilized de Sitter vacua are possible here or not. One may hope that at least some of the problems that are encountered in the attempts to construct such models may also teach one something nontrivial about de Sitter vacua in compactifications in which string or quantum corrections play an important role.

Acknowledgements It is a pleasure to thank my collaborators for the stimulating joint work on refs. [4, 9–11, 44] on which this contribution is mainly based, as well as the Organizers of the JENAM 2010 Workshop for setting up this interesting meeting. This work was supported by the German Research Foundation (DFG) within the Emmy Noether Program (Grant number ZA 279/1-2) and the Cluster of Excellence "QUEST".

References

1. G. Aldazabal and A. Font, JHEP 0802 (2008) 086 [arXiv:0712.1021].
2. D. Andriot, E. Goi, R. Minasian and M. Petrini, arXiv:1003.3774.
3. V. Balasubramanian, P. Berglund, J.P. Conlon and F. Quevedo, JHEP 0503 (2005) 007 [arXiv: hep-th/0502058].
4. J. Blaback, U.H. Danielsson, D. Junghans, T. Van Riet, T. Wrase and M. Zagermann, arXiv:1009.1877.
5. R. Blumenhagen, B. Kors, D. Lust and S. Stieberger, Phys. Rept. 445 (2007) 1 [arXiv: hep-th/0610327].
6. C.P. Burgess, A. Maharana and F. Quevedo, arXiv:1005.1199.
7. P.G. Camara, A. Font and L.E. Ibanez, JHEP 0509 (2005) 013 [arXiv:hep-th/0506066].
8. D. Cassani and A.K. Kashani-Poor, Nucl. Phys. B817 (2009) 25 [arXiv:0901.4251].
9. C. Caviezel et al., Class. Quant. Grav. 26 (2009) 025014 [arXiv:0806.3458].
10. C. Caviezel et al., JHEP 0904 (2009) 010 [arXiv:0812.3551].
11. C. Caviezel, T. Wrase and M. Zagermann, JHEP 1004 (2010) 011 [arXiv:0912.3287].
12. L. Covi et al., JHEP 0806 (2008) 057 [arXiv:0804.1073].
13. G. Dall'Agata, G. Villadoro and F. Zwirner, JHEP 0908 (2009) 018 [arXiv:0906.0370].
14. U.H. Danielsson, S.S. Haque, G. Shiu and T. Van Riet, JHEP 0909 (2009) 114 [arXiv: 0907.2041].
15. U.H. Danielsson, P. Koerber and T. Van Riet, JHEP 1005 (2010) 090 [arXiv:1003.3590].
16. B. de Carlos, A. Guarino and J.M. Moreno, JHEP 1001 (2010) 012 [arXiv:0907.5580].
17. B. de Carlos, A. Guarino and J.M. Moreno, JHEP 1002 (2010) 076 [arXiv:0911.2876].
18. F. Denef, M.R. Douglas and S. Kachru, Ann. Rev. Nucl. Part. Sci. 57 (2007) 119 [arXiv: hep-th/0701050].
19. B. de Wit, D.J. Smit and N.D. Hari Dass, Nucl. Phys. B283 (1987) 165.
20. O. DeWolfe and S.B. Giddings, Phys. Rev. D67 (2003) 066008 [arXiv:hep-th/0208123].
21. O. DeWolfe, A. Giryavets, S. Kachru and W. Taylor, JHEP 0507 (2005) 066 [arXiv: hep-th/0505160].
22. G. Dibitetto, R. Linares and D. Roest, Phys. Lett. B688 (2010) 96 [arXiv:1001.3982].
23. M.R. Douglas and S. Kachru, Rev. Mod. Phys. 79 (2007) 733 [arXiv:hep-th/0610102].
24. M.R. Douglas and R. Kallosh, JHEP 1006 (2010) 004 [arXiv:1001.4008].

25. R. Flauger, S. Paban, D. Robbins and T. Wrase, Phys. Rev. D79 (2009) [arXiv:0812.3886].
26. G.W. Gibbons, Aspects of Supergravity Theories, Three lectures given at GIFT Seminar on Theoretical Physics, San Feliu de Guixols, Spain, Jun 4-11, 1984.
27. S.B. Giddings, S. Kachru and J. Polchinski, Phys. Rev. D66 (2002) 106006 [arXiv: hep-th/0105097].
28. T.W. Grimm and J. Louis, Nucl. Phys. B718 (2005) 153 [arXiv:hep-th/0412277].
29. M. Grana, Phys. Rept. 423 (2006) 91 [arXiv:hep-th/0509003].
30. S.S. Haque, G. Shiu, B. Underwood and T. Van Riet, Phys. Rev. D79 (2009) 086005 [arXiv:0810.5328].
31. T. House and E. Palti, Phys. Rev. D72 (2005) 026004 [arXiv:hep-th/0505177].
32. M.P. Hertzberg, S. Kachru, W. Taylor and M. Tegmark, JHEP 0712 (2007) 095 [arXiv: 0711.2512].
33. M. Ihl, D. Robbins and T. Wrase, JHEP 0708 (2007) 043 [arXiv:0705.3410].
34. S. Kachru, R. Kallosh, A.D. Linde and S.P. Trivedi, Phys. Rev. D68 (2003) 046005 [arXiv: hep-th/0301240].
35. P. Koerber, D. Lust and D. Tsimpis, JHEP 0807 (2008) 017 [arXiv:0804.0614].
36. J.M. Maldacena and C. Nunez, Int. J. Mod. Phys. A16 (2001) 822 [arXiv:hep-th/0007018].
37. S.L. Parameswaran, S. Ramos-Sanchez and I. Zavala, arXiv:1009.3931.
38. D. Roest and J. Rosseel, Phys. Lett. B685 (2010) 201 [arXiv:0912.4440].
39. E. Silverstein, Phys. Rev. D77 (2008) 106006 [arXiv:0712.1196].
40. P.J. Steinhardt and D. Wesley, Phys. Rev. D79 (2009) 104026 [arXiv:0811.1614].
41. P.J. Steinhardt and D. Wesley, arXiv:1003.2815.
42. P.K. Townsend and M.N.R. Wohlfarth, Phys. Rev. Lett. 91 (2003) 061302 [arXiv: hep-th/0303097].
43. G. Villadoro and F. Zwirner, JHEP 0506 (2005) 047 [arXiv:hep-th/0503169].
44. T. Wrase and M. Zagermann, Fortsch. Phys. 58 (2010) 906 [arXiv:1003.0029].

The Variation of G in a Negatively Curved Space-Time

J.P. Mimoso and F.S.N. Lobo

Abstract Scalar-tensor (ST) gravity theories provide an appropriate theoretical framework for the variation of Newton's fundamental constant, conveyed by the dynamics of a scalar-field non-minimally coupled to the space-time geometry. The experimental scrutiny of scalar-tensor gravity theories has led to a detailed analysis of their post-newtonian features, and is encapsulated into the so-called parametrised post-newtonian formalism (PPN). Of course this approach can only be applied whenever there is a newtonian limit, and the latter is related to the GR solution that is generalized by a given ST solution under consideration. This procedure thus assumes two hypothesis: On the one hand, that there should be a weak field limit of the GR solution; On the other hand that the latter corresponds to the limit case of given ST solution. In the present work we consider a ST solution with negative spatial curvature. It generalizes a general relativistic solution known as being of a degenerate class (A) for its unusual properties. In particular, the GR solution does not exhibit the usual weak field limit in the region where the gravitational field is static. The absence of a weak field limit for the hyperbolic GR solution means that such limit is also absent for comparison with the ST solution, and thus one cannot barely apply the PPN formalism. We therefore analyse the properties of the hyperbolic ST solution, and discuss the question o defining a generalised newtonian limit both for the GR solution and for the purpose of contrasting it with the ST solution. This contributes a basic framework to build up a parametrised pseudo-newtonian formalism adequate to test ST negatively curved space-times.

1 Introduction

The possibility that physics might differ in diverse epochs and/or places in the universe is a question of paramount importance to understand what are the limits of our present physical laws [4, 11, 18, 31]. This issue is at present very much at

---

J.P. Mimoso and F.S.N. Lobo
CAAUL/Departamento de Física, Faculdade de Ciências, Universidade de Lisboa, Campo Grande Ed. C8, 1749-016 Lisboa, Portugal
e-mail: jpmimoso@cii.fc.ul.pt, flobo@cii.fc.ul.pt

C. Martins and P. Molaro (eds.), *From Varying Couplings to Fundamental Physics*,
Astrophysics and Space Science Proceedings, DOI 10.1007/978-3-642-19397-2_4,

the forefront of the debate in gravitational physics and cosmology[1] as a result of the observations of a possible variation of the fine structure constant α_{em} at high redshifts ($z > 0.5$) by Webb et al [30]. These observations remind us that our physics is based on peculiar coupling constants that might also be evolutionary on the cosmological scale.

Variations of fundamental constants are a common feature in the generalizations of Einstein's theory of general relativity (GR) [31]. Extensions of GR have not only been claimed to be unavoidable when approaching the Planck scale of energies, since gravitation is expected to be unified with all the other fundamental interactions, but they have also been advocated as an explanation for the late time acceleration of the universe recently unveiled by cosmological observations [6, 15, 24, 26].

Scalar-tensor (ST) gravity theories, in particular, provide an appropriate theoretical framework for the variation of Newton's gravitational constant, which is induced by the dynamics of a scalar-field non-minimally coupled to the space-time geometry. The experimental scrutiny of scalar-tensor gravity theories requires a detailed analysis of their post-newtonian features, and is encapsulated into the so-called parametrised post-newtonian formalism (PPN) [7, 11, 18, 31]. This procedure assumes two hypothesis: On the one hand, that there should be a weak field limit of the GR solution; On the other hand that the latter corresponds to the limit case of a given ST solution.

In the present work we investigate the impact of a hyperbolic geometry on the possible variation of Newton's constant G. This question has been somewhat overlooked in the past, and, as we will show in the present work, raises a fundamental question regarding the physical interpretation of the results. To address this issue we derive a new scalar-tensor solution with an hyperbolic threading of the spatial hypersurfaces [16]. Our solution extends a general relativistic solution known as being of a degenerate class A2 for its unusual properties [13, 28]. The latter GR solution is characterised by a threading of the spatial hypersurfaces by means of pseudo-spheres instead of spheres. It does not exhibit the usual weak field limit in the region where the gravitational field is static, because the gravitational field has a repulsive character. This absence of a weak field limit for the hyperbolic GR solution means that such limit is also absent for comparison with the ST solution, and thus one cannot barely apply the PPN formalism. To address the latter question, we believe that one should look at the perturbations of the general relativistic limit rather than of the absent newtonian weak field. At least this enables us to assess the effects of the variation of G.

2 Scalar-Tensor Gravity Theories

In the Jordan-Fierz frame, scalar-tensor gravity theories can be derived from the action

---

[1] For various perspectives on this issue see the other contributions in this volume.

$$S = \int \sqrt{-g} \left\{ \left[\Phi R - \frac{\omega \Phi}{\Phi} \left(\nabla(\Phi) \right)^2 \right] + 16 \Pi G_N \mathscr{L}_m \right\} \tag{1}$$

where R is the usual Ricci curvature scalar of a spacetime endowed with the metric g_{ab}, Φ is a scalar field, $\omega(\Phi)$ is a dimensionless coupling function, $U(\Phi)$ is a cosmological potential for Φ, and $\mathscr{L}_m$ represents the Lagrangian for the matter fields[2] (note that in this work we shall use units that set $c = 1$). Since Φ is a dynamical field, the trademark of these theories is the variation of $G = \Phi^{-1}$ and the archetypal theory is Brans-Dicke theory in which $\omega(\Phi)$ is a constant [9].

In this frame the energy-momentum tensor of the matter $T^{ab} = 2/\sqrt{|g|}\, \delta S_m / \delta g_{ab}$ is conserved, i.e., $\nabla_a T^{ab} = 0$. This means that the matter test particles follow the geodesics of the spacetime metrics, and the scalar field feels the presence of matter and influences the spacetime curvature, and hence the metric. Therefore the notorious feature of this class of theories is the latter non-minimal coupling between the scalar field and the spacetime geometry, in a similar way to that of the dilaton of string theory. Due to this coupling, the gravitational physics is governed by this interaction and the derivation of exact solutions is considerably more difficult than in GR [5].

This transpires perhaps in a more transparent way if we recast the theory in the so-called Einstein frame by means of an appropriate conformal transformation. Following Damour and Nordvedt's notation [12], we rescale the original metric according to ($g_{ab} \to \tilde{g}_{ab} = A^{-2}(\varphi)\, g_{ab}$, where $A^{-2}(\varphi) = (\Phi/\Phi_*)$ with $\Phi_* = G^{-1}$ being a constant that we take to be the inverse of Newton's gravitational constant, and $\frac{\mathrm{d} \ln \Phi}{\mathrm{d}\varphi} = \sqrt{\frac{16\pi}{\Phi_*}}\, \alpha(\varphi)$). The action becomes

$$\mathscr{L}_\varphi = \tilde{R} - \tilde{g}^{ab} \varphi_{,a} \varphi^{,b} + 2U(\varphi) + 16\pi \tilde{\mathscr{L}}_m(\Psi_m, A^2(\varphi) \tilde{g}_{ab}). \tag{2}$$

Still as in Damour and Nordvedt [12] we introduce

$$\mathscr{A}(\varphi) = \ln A(\varphi), \qquad \alpha(\varphi) = \frac{\partial \mathscr{A}(\varphi)}{\partial \varphi}, \qquad \mathscr{K}(\varphi) = \frac{\partial \alpha(\varphi)}{\partial \varphi}. \tag{3}$$

Setting $U = 0$, the field equations read

$$\tilde{R}_{ab} = 2 \partial_a \varphi\, \partial_b \varphi + 8\pi G_N \left(\tilde{T}_{ab} - \frac{1}{2} \tilde{T}\, \tilde{g}_{ab} \right) \tag{4}$$

$$\nabla^a \nabla_a \varphi = -4\pi\, G_N\, \tilde{T}. \tag{5}$$

This frame has the advantage of decoupling the helicities of the linearised gravitational waves arising as metric perturbations from the massless excitations of the scalar field φ. Moreover, we can associate with the redefined scalar field the role of

---

[2] Alternatively we may cast the action as $L_\varphi = F(\varphi) R - \frac{1}{2}\, g^{ab} \varphi_{,a} \varphi^{,b} + 2U(\varphi) + 16\pi \mathscr{L}_m$ where the non-minimally coupled scalar field has a canonical kinetic energy term.

a matter source acting on the right-hand side of the field equations by introducing an adequate, effective energy-momentum tensor. The net result can be interpreted as field equations in the presence of two interacting sources: the redefined scalar field and the original matter fields. This mutual coupling between the two components is dependent on $\omega(\phi)$, and is thus, in general, time varying [21–23]. The only exception occurs when ω is constant, which corresponds to the BD case. Different scalar-tensor theories correspond to different couplings.

There are not many scalar-tensor solutions of negatively curved universes in the literature, and thus it is of considerable interest to derive and discuss a solution which to the best of our knowledge is new, albeit a vacuum one [25]. In what follows we address this question by first reviewing the general relativistic solution.

3 The General-Relativistic Vacuum Solution with Pseudo-Spherical Symmetry

We consider the metric given by

$$ds^2 = -e^{\mu(r)}\,\mathrm{d}t^2 + e^{\lambda(r)}\,\mathrm{d}r^2 + r^2\,(\mathrm{d}u^2 + \sinh^2 u\,\mathrm{d}v^2), \tag{6}$$

where the usual $2-d$ spheres are replaced by pseudo-spheres, $\mathrm{d}\sigma^2 = \mathrm{d}u^2 + \sinh^2 u\,\mathrm{d}v^2$, hence by surfaces of negative, constant curvature. These are still surfaces of revolution around an axis, and v represents the corresponding rotation angle. For the vacuum case we get

$$e^{\mu(r)} = e^{-\lambda(r)} = \left(\frac{2\mu}{r} - 1\right), \tag{7}$$

where μ is a constant [8, 28]. This vacuum solution is referred as degenerate solutions of class A [28], and being an axisymmetric solution it is a particular case of Weyl's class of solutions [8],

We immediately see that the static solution holds for $r < 2\mu$ and that there is a coordinate singularity at $r = 2\mu$ (note that $|g|$ neither vanishes nor becomes ∞ at $r = 2\mu$) [2, 16]. This is the complementary domain of the exterior Schwarzschild solution. In our opinion this metric can be seen as an anti-Schwarzschild in the same way the de Sitter model with negative curvature is an anti-de Sitter model. In the region $r > 2\mu$, likewise what happens in the latter solution, the g_{tt} and g_{rr} metric coefficients swap signs and the metric becomes cosmological.

Using pseudo-spherical coordinates

$$\{x = r\sinh u\cos v,\ y = r\sinh u\sin v,\ z = r\cosh u,\ w = b(r)\}, \tag{8}$$

the spatial part of the metric (6) can be related to the hyperboloid

$$w^2 + x^2 + y^2 - z^2 = \left(\frac{b^2}{r^2} - 1\right) r^2, \tag{9}$$

embedded in a 4-dimensional flat space. We then have

$$\mathrm{d}w^2 + \mathrm{d}x^2 + \mathrm{d}y^2 - \mathrm{d}z^2 = \left((b'(r))^2 - 1\right) \mathrm{d}r^2 + r^2 \left(\mathrm{d}u^2 + \sinh^2 u \, \mathrm{d}v^2\right), \tag{10}$$

where the prime stands for differentiation with respect to r, and

$$b(r) = \mp 2\sqrt{2\mu}\sqrt{2\mu - r}\,. \tag{11}$$

It is possible to write the line element as

$$\mathrm{d}s^2 = -\tan^2\left[\ln(\bar{r})^{\mp 1}\right] \mathrm{d}\tau^2 + \left(\frac{2\mu}{\bar{r}}\right)^2 \cos^4\left[\ln(\bar{r})^{\mp 1}\right] \times \\ \times \left[\mathrm{d}\bar{r}^2 + \bar{r}^2 \left(\mathrm{d}u^2 + \sinh^2 u \, \mathrm{d}\phi^2\right)\right], \tag{12}$$

which is the analogue of the isotropic form of the Schwarzschild solution. In the neighbourhood of $u = 0$, i.e., for $u \ll 1$, we can cast the metric of the 2-dimensional hyperbolic solid angle as

$$\mathrm{d}\sigma^2 \simeq \mathrm{d}u^2 + u^2 \mathrm{d}v^2 \tag{13}$$

so that it may be confused with the tangent space to the spherically symmetric S^2 surfaces in the neighborhood of the poles. The apparent arbitrariness of the locus $u = 0$, is overcome simply by transforming it to another location by means of a hyperbolic rotation, as it is done in case of the spherically symmetric case where the poles are defined up to a spherical rotation (SO(3) group). So, the spatial surfaces are conformally flat. However, we cannot recover the usual Newtonian weak-field limit for large r, because of the change of signature that takes place at $r = 2\mu$.

In what concerns light rays, fixing u and v we have

$$\frac{\mathrm{d}t}{\mathrm{d}r} = \pm\frac{r}{2\mu - r} \tag{14}$$

and we see that this ratio vanishes at $r = 0$, becomes equal to one at $r = \mu$ and diverges at $r = 2\mu$. This tells us that, similarly to the Schwarzschild solution, the light cones close themselves when they approach the $r = 2\mu$ event horizon, but otherwise behave exactly in the opposite way to what happens in the Schwarzschild exterior solution. Indeed the Schwarzschild's outgoing light rays now become ingoing, and conversely.

Analysing the "radial" motion of test particles, we have the following equation

$$\dot{r}^2 + \left(\frac{2\mu}{r} - 1\right)\left(1 + \frac{h^2}{r^2 \sinh^2 u_*}\right) = \epsilon^2, \tag{15}$$

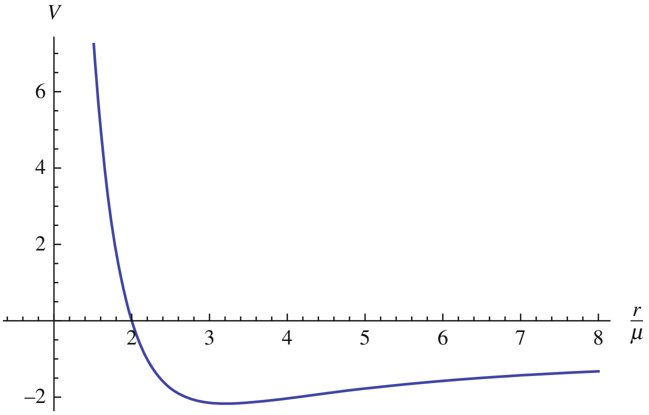

Fig. 1 Plot of the anti-Schwarzschild potential $V(r/2\mu)$

where ϵ and h are constants of motion defined by $\epsilon = \left(\frac{2\mu}{r} - 1\right) \dot{t} = \text{const}_\text{t}$ and $h^2 = r^2 \sinh^2 u_* \, \dot{v} = \text{const}_\text{v}$, for fixed $u = u_*$, and represent the energy and angular momentum per unit mass, respectively.

We may define the potential

$$2V(r) = \left(\frac{2\mu}{r} - 1\right) \left(1 + \frac{h^2}{r^2 \sinh^2 u_*}\right), \tag{16}$$

which we plot in Figure 1. This potential is manifestly repulsive, crosses the r-axis at $r = 2\mu$, and asymptotes to the negative value $V_\infty = -1$ as $r \to \infty$. It has a minimum at $r_\pm = (h^2 \mp \sqrt{h^4 - 12\mu^2 h^2})/(2\mu)$, provided the angular momentum per unit mass h takes a high enough value. However this minimum, when it exists, falls outside the $r = 2\mu$ divide. So we realise that a test particle is subject to a repulsive potential and its radial coordinate is ever increasing, inevitably crossing the event horizon at $r = 2\mu$. (A more complete discussion of the geodesics can be found in [2]). In [8] it is hinted that the non-existence of a clear newtonian limit is related to the existence of mass sources at ∞, but no definite conclusions were drawn.

4 The Scalar-Tensor Solution

In order to derive the scalar-tensor generalization of the metric (6), we apply a theorem by Buchdahl [10] establishing the reciprocity between any static solution of Einstein's vacuum field equations and a one-parameter family of solutions of Einstein's equations with a (massless) scalar field. The Einstein frame description of the scalar-tensor gravity theories fits into the conditions of the Buchdahl theorem.

Indeed in this frame, after the conformal transformation of the original metric, we have GR plus a massless scalar field which is now coupled to the matter fields. Therefore, in the absence of matter we can use Buchdahl's theorem and we are able to derive the scalar-tensor generalisation of the negatively curved metric we have been considering. Given the metric (6), we derive the corresponding scalar-tensor solution

$$\begin{aligned} \mathrm{d}s^2 = &-\left(\frac{2\mu}{r}-1\right)^{B}\mathrm{d}t^2+\left(\frac{2\mu}{r}-1\right)^{-B}\mathrm{d}r^2 \\ &+\left(\frac{2\mu}{r}-1\right)^{1-B} r^2\,(\mathrm{d}u^2+\sinh^2 u\,\mathrm{d}v^2), \end{aligned} \tag{17}$$

$$\varphi(r)=\sqrt{\frac{C^2(2\omega+3)}{16\pi}\varphi_0}\,\ln\left(\frac{2\mu}{r}-1\right), \tag{18}$$

where

$$C^2=\frac{1-B^2}{2\omega+3} \qquad -1\le B\le 1. \tag{19}$$

This clearly reduces to our anti-Schwarzschild metric (6) in the GR limit when $B=1$, and hence $C=0$ implying that $G=\Phi^{-1}$ is constant (we assume $(2\omega+3)>0$ throughout). On the other hand this also shows that the solution has two branches corresponding to $C=\pm\{(1-B^2)/(2\omega+3)\}^{1/2}$.

Notice that as pointed out by Agnese and La Camera [1], the $r=2\mu$ limit is no longer just a coordinate singularity, but rather a true singularity as it can be seen from the analysis of the curvature invariants. In the spherically symmetric case, Agnese and La Camera show that the singularity at $r=2\mu$ has the topology of a point, and hence the event horizon of the black hole shrinks to a point. In the Einstein frame this happens because the energy density of the scalar field diverges [29]. In the case under consideration the $r=2\mu$ condition now corresponds to the areal radius of the pseudo-spheres, $R=\left(\frac{2\mu}{r}-1\right)^{(1-B)/2} r$ becoming zero.

Reverting $\varphi=\int\sqrt{\Phi_0(2\omega+3)/(16\pi)}\,\mathrm{d}\ln(\Phi/\Phi_0)$, and the conformal transformation, $g_{ab}=(2\mu/r-1)^{-C}\,\tilde{g}_{ab}$, we can recast this solution in the original frame in which the scalar-field is coupled to the geometry and the content is vacuum, i.e. the Jordan frame. We derive

$$\Phi(r)=\Phi_0\left(\frac{2\mu}{r}-1\right)^{C}, \tag{20}$$

$$\begin{aligned} \mathrm{d}s^2 = &-\left(\frac{2\mu}{r}-1\right)^{B-C}\mathrm{d}t^2+\left(\frac{2\mu}{r}-1\right)^{-B-C}\mathrm{d}r^2 \\ &+\left(\frac{2\mu}{r}-1\right)^{1-B-C} r^2\,(\mathrm{d}u^2+\sinh^2 u\,\mathrm{d}v^2). \end{aligned} \tag{21}$$

This shows that the gravitational constant $G = \Phi^{-1}$ decays from an infinite value at $r = 0$ to a vanishing value at $r = 2\mu$ when $C > 0$, and conversely, grows from zero at $r = 0$ to become infinite at $r = 2\mu$, when $C > 0$. As we did for the general relativistic case we study the geodesic behaviour of test particles in the scalar-tensor spacetime. The quantities ϵ and h defined as the energy per unit mass and the angular momentum per unit mass, respectively, now become

$$\epsilon = \left(\frac{2\mu}{r} - 1\right)^{B-C} \dot{t}, \qquad h = \left(\frac{2\mu}{r} - 1\right)^{1-B-C} \left(r^2 \sinh^2 u_* \, \dot{v}\right), \tag{22}$$

and are once again first integrals of the motion of test particles. Therefore for the "radial" motion of test particles, we have the following equation

$$\left(\frac{2\mu}{r} - 1\right)^{-2C} \dot{r}^2 + \left(\frac{2\mu}{r} - 1\right)^{B-C} \left(1 + \frac{h^2}{\left(\frac{2\mu}{r} - 1\right)^{(1-B-C)} r^2 \sinh^2 u_*}\right) = \epsilon^2. \tag{23}$$

This is analogous to the equation of motion of a particle with variable mass under the potential $2V(r) = \left(\frac{2\mu}{r} - 1\right)^{B-C} \left(1 + \frac{h^2}{\left(\frac{2\mu}{r} - 1\right)^{(1-B-C)} r^2 \sinh^2 u_*}\right)$. The latter crucially depend on the signs of the exponents of the terms $\xi(r) = \left(\frac{2\mu}{r} - 1\right)$. If we recast Eq. (23) as

$$\dot{r}^2 + \xi^{B+C} \left(1 + \frac{h^2}{\xi^{(1-B-C)} r^2 \sinh^2 u_*}\right) - \epsilon^2 \xi^{2C} = 0, \tag{24}$$

we now have the motion of a test particle with vanishing effective energy under the self-interaction potential

$$2V_{eff}(r) = \xi^{B+C}(r) \left(1 + \frac{h_*^2}{r^2} \xi^{B+C-1}\right) - \epsilon^2 \xi^{2C}, \tag{25}$$

where $h_* = h \sinh u_*$. In Figures 2 and 3 we plot some possible cases, which help us draw some important conclusions. On the one hand, high values of ω imply more repulsive potentials, since the higher ω the closer we are to GR. Notice that high values of ω mean small C, i.e., smaller variation of G. It is though remarkable that for larger departures from GR (left plot of 2) $V(r)$ may exhibit a minimum in the range $0 < r < 2\mu$, leading to closed orbits, something which was not possible in the GR solution. On the other hand comparing the left plots of Figures 2 and 3, we realise that the increase in angular momentum renders the potential more repulsive, shifting the minimum beyond $r = 2\mu$.

Overall, what is most remarkable in what regards the vacuum ST solution derived here is that we are in the presence of a strong gravitational field. The absence of a

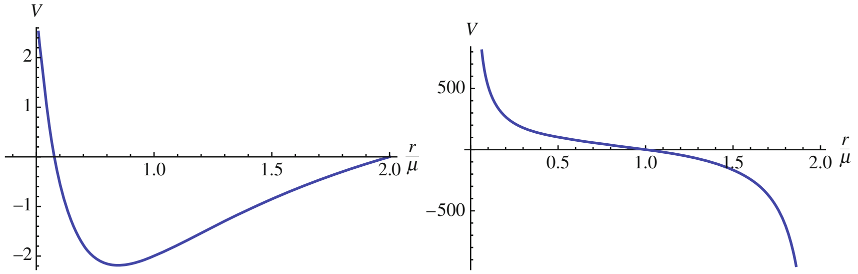

Fig. 2 In both plots $\omega = 0$, $B = 1/2$, $h_* = 1$, $\epsilon = 2$, but left one has $C = +1/2$, and right $C = -1/2$

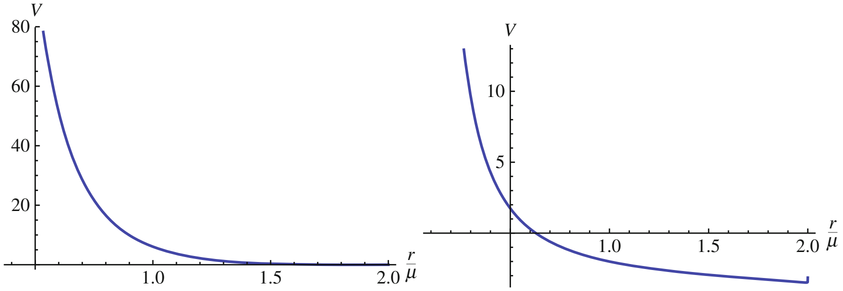

Fig. 3 Left plot: $\omega = 0$, $B = 1/2 = C$,$\epsilon = 2$, but $h_* = 2$, while right plot: $\omega = 10^4$, $B = 1/2$, $C = 1/200$, $\epsilon = 2$, $h_* = 1$

newtonian asymptotic limit at the GR level is the signature of this situation, and prevents us from performing the usual PPN multipolar expansion that permits to identify the departures from GR. Thus, if one wishes to ascertain how our ST solution departs from GR, we need to look at the perturbation of the GR solution itself (rather than that of the almost Minkowski weak field solution). The way to accomplish this is to generalise the formalism developed in a number of remarkable works for the Schwarzschild solution (see [17] and references therein). We have to trade the spherical symmetry of the latter by the pseudo-spherical symmetry of our solution. At present we are pursuing this task and we will report our results elsewhere. From the observational viewpoint what will be needed to test the admissibility of the negatively curved solutions under consideration (both the GR and the ST solutions) is to resort to test of strong fields requiring the detection of gravitational waves (for a discussion see [27])).

5 Discussion

We have considered a static solution with a pseudo-spherical foliation of space. We reviewed its exotic features, and derived the extended scalar-tensor solution. The fundamental feature of these solutions is the absence of a newtonian weak field limit. Indeed it is known that not all of the GR solutions allow a newtonian limit, and this is the situation here. However, assuming that the solutions of the Einstein field equations represent gravitational fields, albeit far from our common physical settings, it is possible to ascertain the implications of varying G in the strong fields by comparing the ST to their GR counterparts. From the viewpoint of observations this relies on the future detection of gravitational waves. We conclude with a quotation from John Barrow [3] which seems appropriate here

> *The miracle of general relativity is that a purely mathematical assembly of second-rank tensors should have anything to do with Newtonian gravity in any limit.*

Acknowledgements The authors are grateful to Carlos Martins and Paolo Molaro for organizing a very enjoyable symposium on VFC, and acknowledge the financial support of the grants PTDC/FIS/102742/2008 and CERN/FP/109381/2009 from FCT (Portugal).

References

1. A.G. Agnese and M. La Camera, Phys. Rev. D31 (1985) 1280.
2. L.A. Anchordoqui et al., arXiv:gr-qc/9509018.
3. J.D. Barrow, Lecture Notes in Physics 383 (1991) 1.
4. J.D. Barrow, Phil. Trans. Roy. Soc. Lond. A363 (2005) 2139 [astro-ph/0511440].
5. J.D. Barrow and J.P. Mimoso, Phys. Rev. D50 (1994) 3746.
6. O. Bertolami et al., Phys. Rev. D75 (2007) 104016 [arXiv:0704.1733].
7. C.G. Boehmer et al., Class. Quant. Grav. 27 (2010) 185013 [arXiv:0910.3800].
8. W.B. Bonnor and M-A.P. Martins, Classical and Quantum Gravity 8 (1991) 727.
9. C. Brans and R.H. Dicke, Phys. Rev. 124 (1961) 925.
10. H.A. Buchdahl, Phys. Rev. 115 (1959) 1325.
11. T. Damour, Astrophys. Space Sci. 283 (2003) 445 [gr-qc/0210059].
12. T. Damour, K. Nordtvedt, Phys. Rev. D48 (1993) 3436.
13. J. Ehlers and W. Kundt, in Gravitation: an introduction to current research (ed. L. Witten), Wiley, New York and London (1962).
14. G.W. Gibbons, Lecture Notes in Physics 383 (1991) 110.
15. F.S.N. Lobo, arXiv:0807.1640.
16. F.S.N. Lobo and J.P. Mimoso, Phys. Rev. D82 (2010) 044034 (2010) [arXiv:0907.3811].
17. K. Martel and E. Poisson, Phys. Rev. D71 (2005) 104003 [gr-qc/0502028].
18. C.J.A.P. Martins, Nucl. Phys. Proc. Suppl. 194 (2009) 96.
19. M.A.P. Martins, Gen. Rel. Grav. 28 (1996) 1309.
20. J.P. Mimoso, F.S.N. Lobo, and N. Montelongo, Dust solutions with pseudo-spherical symmetry, in preparation.
21. J.P. Mimoso and A.M. Nunes, Phys. Lett. A248 (1998) 325.
22. J.P. Mimoso and A. Nunes, Astrophys. and Space Sci., 283 (2003) 661.
23. J.P. Mimoso and D. Wands, Phys. Rev. D51 (1995) 477 [gr-qc/9405025].
24. N.J. Nunes, T. Dent, C.J.A.P. Martins and G. Robbers, arXiv:0910.4935.
25. J.O'Hanlon and B.O.J. Tupper, Il Nuovo Cimento 7 (1972) 305.
26. S. Nojiri and S.D. Odintsov, arXiv:1011.0544.
27. D. Psaltis, [arXiv:0806.1531].
28. H. Stephani et al., Exact solutions of Einstein's field equations, Cambridge, UK: Univ. Press (2003).
29. D. Wands, Phd thesis, pp. 20, University of Sussex, 1993.
30. J.K. Webb et al., Phys. Rev. Lett. 87 (2001) 091301.
31. C.M. Will, Living Rev. Rel. 9 (2005) 3 [gr-qc/0510072].

Beyond Bekenstein's Theory

L. Kraiselburd, M. Miller Bertolami, P. Sisterna, and H. Vucetich

Abstract There are several very different motivations for studying the variation of fundamental constants. They may provide a connection between cosmology and particle physics due to the coincidence of large dimensionless numbers arising from the combination of different physical constants. Bekenstein's variable charge model is very attractive because it is based on very general assumptions: covariance, gauge invariance, causality and time-reversal invariance of electromagnetism. The generality of its assumptions guarantee the applicability of the scheme to other gauge interactions such as the strong forces. Besides, it introduces a useful simplifying assumption; namely, that the gravitational sector is unaffected by the scalar field introduced to vary the coupling constant. That is why it is interesting to explore first this simplified model, before a similar exploration of more general theories.

1 Introduction

Since the proposal due to Gamow [11], the possible time variation of the fine structure constant has been analyzed by many authors. There are many publications

---

L. Kraiselburd
Grupo de Gravitación, Astrofísica y Cosmología, Facultad de Ciencias Astronómicas y Geofísicas, Universidad Nacional de La Plata, Paseo del Bosque s/n (1900) La Plata, Argentina
e-mail: lkrai@fcaglp.fcaglp.unlp.edu.ar

M.M. Bertolami
Grupo de Evolución estelar y pulsaciones, Facultad de Ciencias Astronómicas y Geofísicas, Universidad Nacional de La Plata, Paseo del Bosque s/n (1900) La Plata, Argentina
e-mail: mmiller@fcaglp.fcaglp.unlp.edu.ar

P. Sisterna
Facultad de Ciencias Exactas y Naturales, Universidad Nacional de Mar del Plata, Funes 3350 (7600) Mar del Plata, Argentina
e-mail: sisterna@mdp.edu.ar

H. Vucetich
Grupo de Gravitación, Astrofísica y Cosmología, Facultad de Ciencias Astronómicas y Geofísicas, Universidad Nacional de La Plata, Paseo del Bosque s/n (1900) La Plata, Argentina
e-mail: vucetich@fcaglp.fcaglp.unlp.edu.ar

C. Martins and P. Molaro (eds.), *From Varying Couplings to Fundamental Physics*, Astrophysics and Space Science Proceedings, DOI 10.1007/978-3-642-19397-2_5,

on observational upper bounds on its time variation as well as several theoretical frameworks (see [19,26] and references there in). It's very motivating to think about the possibility that alpha has had a different value to the current, although this is a subject of great debate and more research must be done about it [21].

Bekenstein's theory [1], resting on a number of minimal hypothesis based on highly accepted physical principles, is in a sense representative of many low energy theories inspired on grand unification schemes. In this work we will derive equations that govern the energy exchange between matter, the scalar field and the electromagnetic field. Although we do not analyze the precise mechanism of energy release, we assume that the work done by the scalar field is radiated away in an efficient way, as is the case in the rotochemical heating of neutron stars due to the spin down of the star [7,23].

In section 2 we make a brief review of Beckenstein's theoretical model. In section 3 we derive a generalized version of Poynting theorem for the electromagnetic field and we find how the energy flow of matter is modified by the scalar field. In section 4 we describe the magnetic energy of matter using "sum rules techniques". In section 5, we study the thermal history of the Earth in the presence of the scalar field. Finally in section 6 we present our conclusions.[1]

2 Bekenstein's Theory

Here we review Bekenstein's theory and its prediction for the cosmological time variation of α. Although we will consider galactic as well as terrestrial phenomena, we nevertheless can confidently assume that they track the cosmological evolution of α [25].

Bekenstein [1] modifies Maxwell's theory by introducing a field ϵ that dynamically describes the variation of α. The hypothesis are [1,19]

1. The theory must reduce to Maxwell's when $\alpha = \text{Cte}$.
2. The changes in α are dynamical (i.e. generated by a dynamical field) ϵ.
3. The dynamics of the electromagnetic field as well as ϵ's can be obtained from a variational principle.
4. The theory must be local gauge invariant.
5. The theory must preserve causality.
6. The action must be time reversal invariant.
7. Planck's scale ℓ_P is the smallest length available in the theory.
8. Einstein's equations describe gravitation.

String theories and the like in which there are other fundamental length scales, force us to set aside condition 7. These hypothesis uniquely lead to the following action:

$$S = S_{\text{em}} + S_\epsilon + S_m + S_G \tag{1}$$

---

[1] This contribution is a summary of our article "Energy production in varying α theories", which will be published in Astronomy and Astrophysics.

where

$$S_{\mathrm{em}} = -\frac{1}{16\pi}\int F^{\mu\nu}F_{\mu\nu}\sqrt{-g}d^4x, \tag{2}$$

$$S_{\epsilon} = -\frac{\hbar c}{2\ell_B}\int \frac{\epsilon^{,\mu}\epsilon_{,\mu}}{\epsilon^2}\sqrt{-g}d^4x, \tag{3}$$

S_m and S_G are the matter and gravitational field actions respectively, and the metric here is $(-1, 1, 1, 1)$.

Bekenstein modifies the connection between the vector potential and the electromagnetic field that comes from Maxwell's.

$$F_{\mu\nu} = \frac{1}{\epsilon}\left[(\epsilon A_\nu)_{,\mu} - (\epsilon A_\mu)_{,\nu}\right] \tag{4}$$

and the (second kind) local gauge invariance implies

$$\epsilon A'_\mu = \epsilon A_\mu + \chi_{,\mu} \tag{5}$$

$$\nabla_\mu = \partial_\mu - e_0\epsilon A_\mu \tag{6}$$

as the gauge transformation and covariant derivative of the theory respectively. The last equation defines the local value of the elementary electric charge (coupling constant)

$$e(\boldsymbol{r}, t) = e_0\epsilon(\boldsymbol{r}, t) \tag{7}$$

that is

$$\epsilon = \left(\frac{\alpha}{\alpha_0}\right)^{\frac{1}{2}} \tag{8}$$

In what follows we will neglect the small spatial variations of α and focus on the cosmological variation, as we will be interested on any secular energy injection of the scalar field on a planet such as the Earth. In our approximation it is also enough to work in flat space-time.

The field equations for the electromagnetic field and for ϵ are

$$\left(\frac{1}{\epsilon}F^{\mu\nu}\right)_{,\nu} = 4\pi j^\mu \tag{9a}$$

$$\begin{aligned}\Box \ln\epsilon &= \frac{\ell_B^2}{\hbar c}\left[\epsilon\frac{\partial\sigma}{\partial\epsilon} - \epsilon j^\mu A_\mu + \frac{1}{4\pi}\left(A_\mu F^{\mu\nu}\right)_{,\nu}\right] \\ &= \frac{\ell_B^2}{\hbar c}\left(\epsilon\frac{\partial\sigma}{\partial\epsilon} - \frac{F^{\mu\nu}F_{\mu\nu}}{8\pi}\right)\end{aligned} \tag{9b}$$

where $j^{\mu} = \sum(e_0/c\gamma)u^{\mu}(-g)^{-1/2}\delta^3[x^i - x^i(\tau)]$ and σ is the energy density of matter [1]. $\Box$ is the covariant flat d'Alambertian

$$\Box\phi = \phi^{,\mu}{}_{,\mu} = \eta^{\mu\nu}\phi_{,\mu,\nu}. \tag{10}$$

A note regarding the matter lagrangian is in order: in [1, 2] Bekenstein represents matter as an ensemble of classical particles. However, wherever quantum phenomena become important, as in white dwarfs or condensed matter physics, this is not a realistic description. It is neither a good picture at large energy scales (or small length scales) because fermions have a "natural length scale", the particle Compton wave length $\lambda_C = \hbar/mc$, that makes quite unrealistic any classical model at higher energies. In particular several conclusions of reference [2] have to be reconsidered.

In reference [1] it is shown that the cosmological equation of motion for ϵ is

$$\frac{d}{dt}\left(a^3\frac{\dot{\epsilon}}{\epsilon}\right) = -a^3\frac{\ell_B^2}{\hbar c}\left[\epsilon\frac{\partial\sigma}{\partial\epsilon} - \frac{1}{4\pi}\left(\mathbf{E}^2 - \mathbf{B}^2\right)\right]. \tag{11}$$

In the non relativistic regime $\mathbf{E}^2 \gg \mathbf{B}^2$ and $\sigma \propto \epsilon^2$, hence

$$\frac{d}{dt}\left(a^3\frac{\dot{\epsilon}}{\epsilon}\right) = -a^3\zeta_c\frac{\ell_B^2}{\hbar c}\rho_m c^2 \tag{12}$$

where ρ_m is the total rest mass density of electromagnetically interacting matter and ζ_c is a parameter describing its "electromagnetic content", which is essentially the ratio of the energy-momentum trace and the total mass. A first estimation is

$$\zeta_c \sim 1.2 \times 10^{-3}. \tag{13}$$

Following the standard cosmological model, we assume dark matter to be electromagnetically neutral.

Given that $\rho_m \propto a^{-3}$ we can integrate Eq. (12) and use the usual cosmological notation obtaining

$$\frac{\dot{\epsilon}}{\epsilon} = -\frac{3\zeta_c}{8\pi}\left(\frac{\ell_B}{\ell_P}\right)^2 H_0^2\Omega_B\left[\frac{a_0}{a(t)}\right]^3(t - t_c). \tag{14}$$

Primordial nucleosynthesis standard model tell us that the integration constant t_c must be very small in order not to spoil the agreement between theory and observation. Using WMAP values we obtain the following prediction for $(\dot{\alpha}/\alpha)_0$

$$\left(\frac{\dot{\alpha}}{H_0\alpha}\right)_0 = 1.3 \times 10^{-5}\left(\frac{\ell_B}{\ell_P}\right)^2. \tag{15}$$

Any measurement with a precision such as $\sigma(\dot{\alpha}/H_0\alpha) \sim 10^{-5}$ is difficult to achieve, so the comparison between theory and experiment is a difficult task.

The same arguments can be applied to many theories with varying α, such as Kaluza-Klein [19] or string inspired theories as Damour-Polyakov's [4, 5].

3 Energy Transfer in Bekenstein's Formalism

We will study how energy is injected and then released in varying α theories, in order to look for observable consequences in the emissions of astrophysical as well as geophysical systems. According to Bekenstein and using $c = 1$, the electromagnetic contribution has the same form as in Maxwell's theory

$$T^{\text{em}}_{\mu\nu} = \frac{1}{4\pi}\left[F_{\mu\lambda}F_{\nu}{}^{\lambda} - \frac{g_{\mu\nu}}{4}F_{\lambda\sigma}F^{\lambda\sigma}\right] \tag{16}$$

the difference lying in the connections between the vector potential and the field Eq. (4).

On the other hand, the energy-momentum tensor of the scalar field ϵ is:

$$T^{\mu\nu}_{\epsilon} = \frac{\hbar}{\ell_B^2}\left(\frac{\epsilon^{,\mu}\epsilon^{,\nu}}{\epsilon^2} - \frac{1}{2}g^{\mu\nu}\frac{\epsilon^{,\alpha}\epsilon_{,\alpha}}{\epsilon^2}\right). \tag{17}$$

In what follows we use the redefined field as $\psi = \ln\epsilon$. As we will consider local phenomena, we can work in a locally inertial coordinate system. We denote the "field part of the energy-momentum tensor" as the scalar plus electromagnetic energy momentum tensor:

$$T^{\mu\nu}_{\text{f}} = T^{\mu\nu}_{\text{em}} + T^{\mu\nu}_{\epsilon} \tag{18}$$

In terms of ψ and replacing $g^{\mu\nu}$ with $\eta^{\mu\nu}$, we obtain that the divergence of T_{f} is

$$\begin{aligned} T_{\text{f}}^{\mu\nu}{}_{,\nu} = {} & \frac{1}{4\pi}\left[F^{\mu\alpha}{}_{,\nu}F^{\nu}{}_{\alpha} + F^{\mu\alpha}F^{\nu}{}_{\alpha,\nu} - \frac{1}{2}\eta^{\mu\nu}F^{\alpha\beta}F_{\alpha\beta,\nu}\right] \\ & + \frac{\hbar}{\ell_B^2}\left(\psi^{,\mu}{}_{,\nu}\psi^{,\nu} + \psi^{,\mu}\psi^{,\nu}{}_{,\nu} - \eta^{\mu\nu}\psi_{,\alpha,\nu}\psi^{,\alpha}\right). \end{aligned} \tag{19}$$

Putting the equations of motion (9) inside Eq. (19) and simplifying the result using the homogeneous Maxwell equation, we obtain the following expression

$$T_{\text{f}}^{\mu\nu}{}_{,\nu} = -e^{\psi}j^{\alpha}F^{\mu}{}_{\alpha} + \psi_{,\nu}\left(\eta^{\mu\nu}\frac{\partial\sigma}{\partial\psi} + T^{\mu\nu}_{\text{em}} - \frac{1}{16\pi}\eta^{\mu\nu}F_{\alpha\beta}F^{\alpha\beta}\right). \tag{20}$$

Let us add to both sides of the equation the divergence of the energy momentum tensor of matter $T_{\text{m}}^{\mu\nu}{}_{,\nu}$ in order to find the energy transfer (according to hypothesis 8 we assume that Einstein's equations hold unmodified for the gravitational field and hence the total energy momentum tensor is conserved) $T_{\text{f}}^{\mu\nu}{}_{,\nu} + T_{\text{m}}^{\mu\nu}{}_{,\nu} = 0$. So, this equation explicitly shows the energy transfer from the field ψ to matter

$$T^{\mu\nu}_{\mathrm{m}\ \ ,\nu} = e^{\psi} j^{\alpha} F^{\mu}{}_{\alpha} - \psi_{,\nu} \left(\eta^{\mu\nu} \frac{\partial \sigma}{\partial \psi} + T^{\mu\nu}_{\mathrm{em}} - \frac{1}{16\pi} \eta^{\mu\nu} F_{\alpha\beta} F^{\alpha\beta} \right) \tag{21}$$

which is the source of any observable effect. From

$$\psi_{,\nu} = \frac{\epsilon_{,\nu}}{\epsilon} = \frac{1}{2} \frac{\alpha_{,\nu}}{\alpha} \tag{22}$$

we find the "machian" contribution to energy transfer

$$T^{\mu\nu}_{\mathrm{m}\ \ ,\nu}{}^{(machian)} = \frac{1}{2} \frac{\alpha_{,\nu}}{\alpha} \left(\eta^{\mu\nu} \frac{\partial \sigma}{\partial \psi} + T^{\mu\nu}_{\mathrm{em}} - \frac{1}{16\pi} \eta^{\mu\nu} F_{\alpha\beta} F^{\alpha\beta} \right) \tag{23}$$

We use Bekenstein's notation, that is, the time-space components of $e^{\psi} F^{\mu\nu}$ are identified with $\mathbf{E}$ while space-space components are identified with $\mathbf{B}$, and for us $\mathbf{S} = \frac{\mathbf{E}\times\mathbf{B}}{4\pi}$. Then, the component 0 of Eq. (21) reads

$$T^{0\nu}_{\mathrm{m}\ ,\nu} = \mathbf{j}.\mathbf{E} - e^{-2\psi} \frac{\mathbf{B}^2 \dot{\psi}}{4\pi} - e^{-2\psi} \nabla\psi.\mathbf{S} + \dot{\psi} \frac{\partial \sigma}{\partial \psi} \tag{24}$$

Implicit in our previous analysis and algebra stands the generalized Poynting theorem. In its standard version it involves only electromagnetic terms, while in our case it will also involve the interaction between the electromagnetic and scalar fields.

$${T_{em}}^{0\rho}{}_{,\rho} = \frac{\partial u_{em}}{\partial t} + \nabla . e^{-2\psi} \left(\frac{\mathbf{E}\times\mathbf{B}}{4\pi} \right) = -\mathbf{E}\cdot\mathbf{j} + \frac{e^{-2\psi}\mathbf{E}^2}{4\pi} \dot{\psi} + e^{-2\psi} \mathbf{S}.\nabla\psi \tag{25}$$

where ${T_{em}}^{00}{}_{,0} = (\partial u_{em})/\partial t$; the electromagnetic energy is $u_{em} = e^{-2\psi}(\mathbf{E}^2 + \mathbf{B}^2)/(8\pi)$ and ${T_{em}}^{0i}{}_{,i} = \nabla . e^{-2\psi}(\frac{\mathbf{E}\times\mathbf{B}}{4\pi}) = \nabla . e^{-2\psi}\mathbf{S}$; being $\mathbf{S}$ the Poynting vector. We note that this result is independent of the details of the gravitational and matter lagrangians, besides their interacting terms with the electromagnetic field. In particular it holds independently of the details of the interaction of matter with the scalar field. We recall that the usual interpretation of the first term in the right hand side of Eq. (25) is the work done by the electromagnetic field on matter. In the same fashion we may interpret the second and last term as the work done by the electromagnetic field on the scalar field. An analog phenomenon could be given by the work done by an increasing Newton constant G on a planet augmenting the pressure and thus compressing it [15].

Let us estimate the electrostatic contribution to the matter energy. In a non relativistic system such as a light atom or nuclei, the electromagnetic energy is given by the electrostatic field which satisfies the equation

$$\nabla \cdot \boldsymbol{E} e^{-2\psi} = 4\pi \rho^{0}_{\mathrm{em}} \tag{26}$$

where ρ^0_{em} is the reference charge density. In the limit when α varies only cosmologically the solution is

$$\boldsymbol{E} = e^{2\psi}\boldsymbol{E}_0 \tag{27}$$

where $\boldsymbol{E}_0$ is the electrostatic reference field defined for $e^{\psi} = 1$. The electromagnetic energy density results

$$u_{em} = e^{-2\psi}\frac{(\mathbf{B}^2 + \mathbf{E}^2)}{8\pi} = e^{2\psi}u^0_{em} \tag{28}$$

and the temporal variation

$$\dot{u}_{em} = 2\dot{\psi}u_{em} + e^{2\psi}\dot{u}^0_{em} = \frac{\dot{\alpha}}{\alpha}u_{em} + e^{2\psi}\dot{u}^0_{em}. \tag{29}$$

If there were no scalar injection of energy and $\dot{u}^0_{em} \approx 0$, the Poynting theorem Eq. (25) together with the expression for the energy variation Eq. (29) would lead to

$$\boldsymbol{j}\cdot\boldsymbol{E} = -\frac{\mathbf{B}^2}{4\pi}\dot{\psi}e^{-2\psi}. \tag{30}$$

As we will consider phenomena where the motion of matter is negligible, taking the first index as 0 is equivalent to project along the fluid four-velocity. Also the total time derivative $d/dt = \partial/\partial t + \mathbf{v}.\nabla$ will be equal to the partial time derivative $\partial/\partial t$. In the general case when there is viscosity and heat transfer, the right-hand side can be written, in the non relativistic limit, as

$$T^{0\nu}_{\mathrm{m}\ ,\nu} = \frac{\partial}{\partial t}(\frac{1}{2}\rho v^2 + u) + \nabla.[\rho\mathbf{v}(\frac{1}{2}v^2 + w) - \mathbf{v}.\sigma' + \mathbf{J}] \tag{31}$$

where w is the specific enthalpy, u is the internal energy density, $\mathbf{J}$ is the heat flux, which can generally be written as $-\kappa\nabla T$, being T the temperature and κ the thermal conductivity. Finally, $(\mathbf{v}.\sigma')_k$ stands for $v_i\sigma'_{ik}$, with σ' being the viscous stress tensor [18]. As we said above, we neglect the velocity of the fluid, so we obtain

$$T^{0\nu}_{\mathrm{m}\ ,\nu} = \frac{\partial u}{\partial t} + \nabla\mathbf{J} \tag{32}$$

A note of caution regarding the internal energy is in order. We understand, as usual, "internal energy" as the energy that can be exchanged by the system in the processes considered (heat exchange, radiative transfer, etc.), which will differ from what we understand by "rest mass", which is the "non convertible energy". If the scalar field can change the effective electric charge, then it can alter the electromagnetic contribution to the rest mass, and consequently, this contribution will be no longer "rest mass", but "internal energy".

The time variation of the internal energy u will have two contributions: one corresponding to the cooling process $\frac{\partial u}{\partial t}|_{cooling}$ and another one related to the interaction with the scalar field $\frac{\partial \sigma_\mu}{\partial t}$. This last term accounts for the dependence of the bulk of matter on the scalar field, which is mainly given by the electromagnetic contribution to the nuclear mass. Then equation (24) will finally read

$$\frac{\partial u}{\partial t}|_{cooling} + \frac{\partial \sigma_\mu}{\partial t} + \nabla \mathbf{J} = -\frac{\boldsymbol{B}^2}{4\pi}\dot{\psi} e^{-2\psi} - \frac{e^{-2\psi}\mathbf{B}^2\dot{\psi}}{4\pi} - e^{-2\psi}\nabla\psi.\mathbf{S} - \dot{\psi}\frac{\partial \sigma}{\partial \psi}. \quad (33)$$

Since the scalar field is space independent, and given that the electromagnetic energy of matter is mainly accounted by the nuclear content, we assume that the following condition $\frac{\partial \sigma}{\partial \psi} - \frac{\partial \sigma_\mu}{\partial \psi} \approx 0$ is fulfilled. Consequently, we obtain

$$\nabla \mathbf{J} = -\frac{e^{-2\psi}\mathbf{B}^2\dot{\psi}}{2\pi} - \frac{\partial u}{\partial t}|_{cooling}. \quad (34)$$

We define

$$\xi_a = 2\frac{e^{-2\psi}\mathbf{B}^2\dot{\psi}}{M_a 4\pi} \approx 2\frac{\dot{\alpha}}{\alpha}\frac{\mathbf{B}^2}{8\pi M_a} \quad (35)$$

as two times the energy production per mass unit of any material substance a (using the approximation, $e^{-2\psi} \to 1$ when $\psi << 1$).

Now follows our main physical assumption: *the cooling term is not modified by the scalar field*. The reasons for this assumption are two: 1) as we just showed, the electrostatic energy “injected” by the scalar field stays within the matter bulk (the cancellation of terms as seen in Eq. (34)) and 2) the thermal evolution should not change given the high thermal conductivity of the Earth and white dwarfs considered in this work. Thus we expect the magnetic energy excess to be radiated away, increasing the heat flux **J** as shown in Eq. (34).

4 The Electromagnetic Energy of Matter

As we have mentioned in the previous section, the only “input” we have is that which comes from the magnetic field. Stationary electric currents which are generated by charged particles and their static magnetic moments, and quantum fluctuations of the number density are the responsible of the generation of magnetic fields in quantum mechanics. Such contributions have been studied and calculated by [13, 28] from a minimal nuclear shell model using the following analysis (for more details see [16]).

The total magnetic energy of the nucleus can be written as,

$$E_m \simeq \frac{1}{2c^2}\sum_\alpha \int d\boldsymbol{x}d\boldsymbol{x}' \frac{\langle 0|\boldsymbol{j}(\boldsymbol{x}')\,|\alpha\rangle \cdot \langle \alpha|\boldsymbol{j}(\boldsymbol{x})\,|0\rangle}{|\boldsymbol{x}-\boldsymbol{x}'|}, \quad (36)$$

where α runs over a complete set of eigenstates of the nuclear hamiltonian H. We neglect the momentum dependence of the nuclear potential and assume a constant density within the nucleus. Making some calculations we finally obtain,

$$E_m = \int d^3x \frac{B^2}{8\pi} \simeq \frac{1}{2c^2} \int d^3x d^3x' \frac{\boldsymbol{j}(\boldsymbol{x}) \cdot \boldsymbol{j}(\boldsymbol{x}')}{\mid \boldsymbol{x} - \boldsymbol{x}' \mid} \simeq \frac{3}{20\pi} \frac{\bar{E}}{R(A)\hbar c} \int \sigma dE, \quad (37)$$

where $R(A)$ is the nuclear radius, A number of nucleons. These quantities have the following approximate representation

$$R(A) = 1.2A^{\frac{1}{3}}\ \mathrm{fm}, \qquad \int \sigma dE \simeq 1.6A\,\mathrm{MeV\ fm}^2. \quad (38)$$

Then, the fractional contribution of the magnetic energy to rest mass energy is

$$\zeta(A) \simeq \frac{E_{m_A}}{m_A c^2} \approx 8.60 \times 10^{-6} A^{-1/3} \quad (39)$$

5 The Earth Heat Flux

The contribution of $\dot{\alpha}/\alpha$ to the heat flux can be calculated using the global heat balance for the Earth [17], assuming that the *machian* contribution H_C is the only extra energy production,

$$M_E C_p \frac{dT_m}{dt} = -Q_{tot} + H_C + H_G \quad (40)$$

where M_E is the Earth's mass; $C_p \approx 1200\,\mathrm{J/Kg - K}$ is the average heat capacity of the planet and T_m is the mantle potential temperature. H_G represents the heat generated by radioactive isotopes. The total heat loss Q_{tot} can be written as the sum of two terms, one that comes from the loss of heat in the oceans Q_{oc}, and the other by continental heat loss Q_{cont}. Using the results obtained by Labrosse and Jaupart [17], we rewrite the total heat loss as $Q_{tot} \approx MC_p\lambda_G T_m$ where $\lambda_G \approx 0.1\,\mathrm{Gyr}^{-1}$ is the timescale constant for the secular Earth's cooling. Assuming that the most abundant elements of the Earth are oxygen, silica and iron $\bar{\zeta} \approx 2.75 \times 10^{-6}$ and using $H_0 \approx 2.5 \times 10^{-18}\,\mathrm{s}^{-1}$, the "extra" energy contribution can be written as,

$$H_C = \bar{\zeta} c^2 H_0 \frac{\dot{\alpha}}{\alpha H_0} \quad (41)$$

From (14), we can describe the extra contribution as a function of time, writing $\frac{a(t)}{a_0}$ as a power series [27],

$$\frac{a(t)}{a_0} \approx 1 + H_0 dt - \frac{q_0}{2}(H_0 dt)^2 + \frac{j_0}{6}(H_0 dt)^3 + \cdots \quad (42)$$

and then making a Taylor series expansion up to third order of H_C. Replacing this *machian* contribution in Eq. (40) and solving it, we find an expression for the cosmological perturbation of the mantle's temperature ΔT_m in terms of the time interval Δt and $\frac{\dot{\alpha}}{\alpha H_0}$.

$$\begin{aligned}\Delta T_m(t) =& 2.43 \times 10^5\, {}^{\mathrm{K}}/_{\mathrm{Gyr}} \frac{\dot{\alpha}}{H_0 \alpha} (\Delta t)^3 - 3.78 \times 10^6\, {}^{\mathrm{K}}/_{\mathrm{Gyr}} \frac{\dot{\alpha}}{H_0 \alpha} (\Delta t)^2 \\ &+ 3.05 \times 10^7\, {}^{\mathrm{K}}/_{\mathrm{Gyr}} \frac{\dot{\alpha}}{H_0 \alpha} \Delta t\end{aligned} \tag{43}$$

According to [17], *the total amount of cooling experienced by the Earth after an initial magma ocean phase cannot exceed* 200 K. So, in the last 2.5 Gyr, $\Delta T_m <$ 200 K. With these restrictions we obtain a bound for the time variation of α,

$$\left| \frac{\dot{\alpha}}{H_0 \alpha} \right|_0 < 1.93 \times 10^{-6} \tag{44}$$

Using this result into Eq.(15) we find that,

$$\left(\frac{\ell_B}{\ell_P} \right)^2 < 0.15 \qquad \frac{\ell_B}{\ell_P} < 0.39 \tag{45}$$

A different bound can be obtained observing that the total radiated power of the Earth Q_{tot} can be explained by radioactive decay within twenty per cent [17]. The most recent data was estimated from an adjustment made with 38347 measurements. The methodology was to use a half-space cooling approximation for hydrothermal circulation in young oceanic crust; and for the rest of the Earth surface, the average heat flow of various geological domains was estimated as defined by global digital maps of geology, and then made a global estimate by multiplying the total global area of the geological domain [6].

The result shows that $Q_{tot} \approx 47$ TW (see [6] fore more details). Therefore,

$$|Q_{mach}| = |M_E C_P \lambda_G T_m(t)| < 0.2 Q_{tot} \tag{46}$$

Then, in an interval of 2.5 Gyr we find

$$\left| \frac{\dot{\alpha}}{H_0 \alpha} \right|_0 < 3.98 \times 10^{-6} \tag{47}$$

and

$$\left(\frac{\ell_B}{\ell_P} \right)^2 < 0.31 \qquad \frac{\ell_B}{\ell_P} < 0.55 \tag{48}$$

6 Conclusions

The energy exchange with ordinary matter in alternative theories with new fields such as Beckenstein's theory is a delicate subject. Using the field equations and general hypothesis of the theory we derived the energy transfer between matter and fields. Hypothesis 8 is key, as states that the matter energy momentum tensor is the quantity that has to be added to the field sector in order to make the total tensor divergence free. We also assumed that dark matter is electrically neutral, neglected the motion of matter in the bodies considered, and found that the dynamical feature of the electric charge makes the atomic electromagnetic energy part of the internal energy of the system. Eq. (34) shows that there is an extra contribution to the heat current besides the cooling of matter, which is given by the time variation of the scalar field and by the magnetic content of matter. We also justified our assumption that the matter cooling rate is not modified by the scalar field. Finally using a minimal nuclear shell model we estimated the magnetic energy content of matter, thus permitting us to quantify the anomalous heat flux in terms of the fundamental parameters of the theory and the chemical composition of the body.

Our best bound was obtained analyzing the geothermal aspects of the Earth, as those are naturally the best understood and measured of our solar system, and the surface heat flux is very low. Our bounds ($1.52 \times 10^{-16}\,\text{yr}^{-1}$ and $3.14 \times 10^{-16}\,\text{yr}^{-1}$) are comparable with that obtained in laboratory combining measurements of the frequencies of Sr [1], Hg+ [9], Yb+ [22] and H [8] relative to Caesium ($(3.3 \pm 3.0) \times 10^{-16}\,\text{yr}^{-1}$) [20]; only one order of magnitude weaker than Oklo's ($(2.50 \pm 0.83) \times 10^{-17}\,\text{yr}^{-1}$) (the theory independent most stringent bound on α time variation up to date [10]) and another found from measurements of the ratio of Al+ and Hg+ optical clock frequencies over a period of a year ($(5.3 \pm 7.9) \times 10^{-17}\,\text{yr}^{-1}$) [20, 24]. The constraints we found depend on the cooling model of the Earth, but there is a general agreement on the mechanisms behind it [14]. The data set is redundant putting solid constraints on the theory. This analysis may be applied to other theories with extra fields that introduce extra "internal energies" to matter. We will report further work on future publications.

References

1. J.D. Bekenstein. Phys. Rev. D25 (1982) 1527.
2. J.D. Bekenstein, Phys. Rev. D66 (2002) 123514.
3. S. Blatt et al., Phys. Rev. Lett. 100 (2008) 140801.
4. T. Damour and A.M. Polyakov, Gen. Rel. Grav. 26 (1994) 1171.
5. T. Damour and A.M: Polyakov, Nucl. Phys. B423 (1994) 532.
6. J.H. Davies and R. Davies, Solid Earth 1 (2010) 5.
7. R. Fernandez and A. Reisenegger, Astrophys. J. 625 (2005) 291.
8. M. Fischer et al., Phys. Rev. Lett. 92 (2004) 230802.
9. T.M. Fortier et al., Phys. Rev. Lett. 98 (2007) 070801.
10. Y. Fujii et al., Nuc. Phys. B573 (2000) 377.
11. G. Gamow, Phys. Rev. Lett. 19 (1967) 759.s

12. D.E. Groom et al., Eur. Phys. J. C15 (2000) 191.
13. M.P. Haugan and C.M. Will, Phys. Rev. D15 (1977) 2711.
14. A.M. Jessop, Thermal geophysics, Elsevier, Amsterdam (1990)
15. P. Jofré, A. Reisenegger and R. Fernandez. Phys.Rev.Lett. 97 (2006) 131102.
16. L. Kraiselburd and H. Vucetich, Int. J. Mod. Phys. E20 (2011) 101.
17. S. Labrosse and C. Jaupart, Earth Planet. Sci. Lett. 260 (2007) 465.
18. L.D. Landau and E.M. Lifshitz, Fluid Mechanics, Elsevier, Oxford (1987).
19. S.J. Landau, La variación temporal y espacial de las constantes fundamentales: Cotejo entre teorías y datos geofísicos y astronómicos, Facultad de Ciencias Astronómicas y Geofsicas, Universidad Nacional de La Plata, Argentina (2002).
20. B. Li, D.F. Mota and J.D. Barrow, arxiv:1009.1396.
21. M.T. Murphy, J.K. Webb and V.V. Flambaum, Mon.Not.R.Astron.Soc. 345 (2003) 609.
22. E. Peik et al., Phys. Rev. Lett. 93 (2004) 170801.
23. A. Reisenegger, Astrophys. J. 442 (1995) 749.
24. T. Rosenband et al., Science 319 (2008) 1808.
25. D.J. Shaw and J.D. Barrow, Phys.Lett. B639 (2006) 596.
26. J.-P. Uzan, Rev. Mod. Phys. 75 (2003) 403.
27. S. Weinberg, Gravitation and cosmology, John Wiley and Sons, New York-USA (1972).
28. C.M. Will, Theory and Experiment in Gravitational Physics, C. U. P., Cambridge (1981).

The Cooling of White Dwarfs and a Varying Gravitational Constant

E. García–Berro, L.G. Althaus, S. Torres, P. Lorén–Aguilar, A.H. Córsico, and J. Isern

Abstract Within the theoretical framework of some modern unification theories the constants of nature are functions of cosmological time. Since white dwarfs are long-lived, compact objects, they offer the possibility of testing a possible variation of the gravitational constant and, thus, to place constraints to these theories. We present full white dwarf evolutionary calculations in the case in which the gravitational constant G decreases with time. White dwarf evolution is computed in a self-consistent way, including the most up-to-date physical inputs. The evolutionary sequences also consider accurate outer boundary conditions provided by non-gray model atmospheres and a detailed core chemical composition that results from the calculation of the full evolution of progenitor stars. We find that the mechanical structure and the energy balance of the white dwarf are strongly modified by the presence of a varying G. In particular, for a rate of change of G larger than $\dot{G}/G = -1 \times 10^{-12}\ \mathrm{yr}^{-1}$, the evolution of cool white dwarfs is markedly affected. The impact of a varying G is more notorious in the case of more massive white dwarfs.

E. García–Berro, S. Torres, and P. Lorén–Aguilar
Departament de Física Aplicada, Universitat Politècnica de Catalunya, c/Esteve Terrades, 5, 08860 Castelldefels, Spain
Institut d'Estudis Espacials de Catalunya, c/Gran Capità 2–4, Edif. Nexus 104, 08034 Barcelona, Spain,
e-mail: garcia,santi,loren@fa.upc.edu

L.G. Althaus and A.H. Córsico
Facultad de Ciencias Astronómicas y Geofísicas, Universidad Nacional de La Plata, Paseo del Bosque s/n, (1900) La Plata, Argentina
e-mail: althaus,acorsico@fcaglp.fcaglp.unlp.edu.ar

J. Isern
Institut de Ciències de l'Espai (CSIC), Campus UAB, 08193 Bellaterra, Spain
Institut d'Estudis Espacials de Catalunya, c/Gran Capità 2–4, Edif. Nexus 104, 08034 Barcelona, Spain
e-mail: isern@ieec.cat

C. Martins and P. Molaro (eds.), *From Varying Couplings to Fundamental Physics*,
Astrophysics and Space Science Proceedings, DOI 10.1007/978-3-642-19397-2_6,

1 Introduction

In several modern grand-unification theories, the constants of nature are supposed to be functions of low-mass dynamical scalar fields — see, for instance, Ref. [25] and references therein. If these theories are correct, we expect them to experience slow changes over cosmological timescales — see the review papers [35] and [16] for general descriptions of the theoretical approaches which can be used to formally describe the variation of fundamental constants and for recent revisions of the most stringent upper limits to their rate of change. This contradicts the fact that for most applications we assume that these constants are independent of time (and of space location). In fact, the statement about the constancy of the fundamental "constants" of nature is just a hypothesis, though quite an important one, which deserves to be explored. The issue of variation of the physical constants was first addressed by Dirac [12], who formulated it within the framework of his Large Number Hypothesis. In his pioneering work, he basically considered variations of the fine structure constant, α, which characterizes the strength of the electromagnetic interaction, and of G, which provides the strength of the gravitational interaction. Given that, as mentioned, the hypothetical variations of the fundamental constants are expected to occur over very large timescales, bounds obtained from astronomical observations are of the maximum interest to test the validity of these theories.

In recent years, several constraints have been placed on the variation of the fine structure constant [16,35]. This is a controversial issue, since there have been recent claims that for a range of redshifts ($0.5 < z < 3.5$) the results are consistent with a time-varying fine structure constant [29,37,38], whereas other authors have challenged these results [8,9,23,30,34], or, at least, have cast doubts on such a possible detection of a time-varying α [24]. In sharp contrast with the vivid debate about whether (or not) there is evidence for a varying fine structure constant, relatively few works have been devoted to study a hypothetical variation of the gravitational constant. The reason probably lies on the intrinsic difficulty of measuring the value of this constant [28]. Actually, the gravitational constant is the fundamental constant for which we have the less accurate determination, and the several measures of G differ considerably. Therefore, it is not surprising that many methods aimed to bound any hypothetical variation of G have been devised. At present, the most tight constrains are those obtained using Lunar Laser Ranging and Big Bang nucleosynthesis. The Lunar Laser Ranging experiments provide an upper bound $\dot{G}/G = (0.2 \pm 0.7) \times 10^{-12}\ \mathrm{yr}^{-1}$ [20], whereas Big Bang nucleosynthesis bounds are of the same order of magnitude $-0.3 \times 10^{-12}\ \mathrm{yr}^{-1} \lesssim \dot{G}/G \lesssim 0.4 \times 10^{-12}\ \mathrm{yr}^{-1}$ [3, 10]. Nevertheless, the difficulty of measuring G and the fact that its variation, if any, might had not been uniform in time recommend the use of alternative methods.

2 The Role of G in the Evolution of White Dwarfs

White dwarf stars provide an independent way of testing the possibility of any hypothetical variation of the gravitational constant. There are several reasons for this. First, white dwarfs are extremely long-lived stars. Thus, the effects of a varying gravitational constant can become prominent, even for very small secular rates of change. Second, white dwarfs are the end-point of stellar evolution for the vast majority of stars. Hence, the present Galactic populations contain substantial numbers of white dwarfs. Third, white dwarfs are rather compact objects. The pressure of degenerate electrons supports their mechanical structure, and this structure is very sensitive to the precise value of G. Finally, the evolution of white dwarfs is relatively well understood, and can be fairly described as a simple gravothermal process. Hence, for sufficiently low temperatures their luminosity is derived entirely from a close balance between the thermal and the gravitational energies. Consequently, a secularly varying G largely affects the gravothermal balance of white dwarfs and, thus, their luminosities.

One of the possible methods to constrain a variation of G using the structure and evolution of white dwarfs takes advantage of the dependence of the secular rate of change of the period of pulsation of variable white dwarfs on its cooling rate [5, 6]. In the case of a constant G the secular rate of change of the period not only depends on the cooling rate but also on the rate of change of the radius of the white dwarf [2, 39]:

$$\frac{\dot{\Pi}}{\Pi} \approx -a\frac{\dot{T}}{T} + b\frac{\dot{R}}{R} \tag{1}$$

In the case of a varying G, there is an additional term related to $\dot{G}/G$ that is partially counterbalanced by the second term in Eq. (1). This was shown in Ref. [5], who applied the method to the well studied variable white dwarf G117-B15A and obtained a rather loose bound, $-2.5 \times 10^{-10}\ \mathrm{yr}^{-1} \leq \dot{G}/G \leq 0$.

Another method to constrain a possible variation of G using white dwarfs is to use their luminosity function, that is the number of white dwarfs per unit bolometric magnitude and unit volume. This stems from the fact that the number counts of white dwarfs in each magnitude bin depends sensitively on the characteristic cooling time of white dwarfs in the corresponding luminosity interval. Furthermore, for a given age of the Galaxy, the white dwarf luminosity function presents a marked cut-off, which is an indicator of the age of the Galaxy. The position of this cut-off depends primarily on the white dwarf cooling times. Thus, since a varying G modifies the white dwarf evolutionary times its position depends sensitively on the adopted rate of change of G. The first studies in which dwarf number counts were considered to constrain a possible variation of the gravitational constant resulted to be non-conclusive [36]. This was due to both the lack of good observational data and of reliable cooling models. Later, a simplified treatment of cooling was used [15] to check which could be the effects of a slowly varying G in the white dwarf cooling ages and number counts. In this study it was assumed that $\dot{G}/G$ was small enough to ensure that white dwarfs have time to adjust its mechanical structure to the actual value of G in a timescale much shorter than that of the cooling timescale. Under such assumption, the white dwarf luminosity can be written as:

$$L + L_\nu = -\frac{dB}{dt} + \frac{\dot{G}}{G}\Omega. \tag{2}$$

where B is the binding energy of the white dwarf, $B = U + \Omega$, U is the total internal energy, Ω is the total gravitational energy and L_ν is the neutrino luminosity. The evolution of the luminosity was then obtained from a series of static models, not from fully evolutionary calculations, assuming a relationship between the luminosity and the core temperature obtained from fits to evolutionary calculations with constant G. Furthermore, it was assumed that the evolution of a $0.6\,M_\odot$ was representative of that of white dwarfs with very different masses. Despite this simplified treatment using the white dwarf luminosity function available at that time they were able to obtain an upper limit $\dot{G}/G \leq -(1.0 \pm 1.0) \times 10^{-11}$ yr^{-1}. This method was criticized in [6] who claimed that Eq. (2) could be further worked out, but their criticism does not apply to the results of [15] because the cancellation of the different terms was carefully taken into account in that work.

What neither the works of [15] nor [6] took into account is the fact that the relationship between the core temperature and the luminosity of white dwarfs also depends on the gravitational constant. For instance, adopting the simplified Mestel cooling law [27] it turns out that $L \propto G$. This means that a full stellar evolutionary code is needed if an accurate treatment of white dwarf cooling when G changes with time is to be done. To our knowledge, the only calculations of cooling white dwarfs with a time-varying G employing an up-to-date stellar evolutionary code are those of [4] but their analysis turned out to be flawed by a numerical artifact, and detailed calculations remain to be done. Moreover, none of the above mentioned works took into account that if G varies its value in the past differs from its present value, and all the calculations were done using the present value of G, thus neglecting a potentially important effect.

Yet there is another possible way to use white dwarfs to constrain any hypothetical variation of G. As it is well known, white dwarfs have a maximum mass, Chandrasekhar's mass. This limiting mass depends on the precise value of the gravitational constant. To be specific, it turns out that $M_{\rm Ch} \propto G^{-3/2}$. On the other hand Type Ia supernovae are supposed to be the result of the complete incineration of white dwarfs with masses close to Chandrasekhar's mass. This is the fundamental reason why Type Ia supernovae are supposed to be one of the best examples of standard (or, at least, calibrable) candles. As a matter of fact, it turns out that, although the nature of their progenitors and the detailed mechanism of explosion are still the subject of a strong debate, their observational light curves are relatively well understood and characterized and, consequently, their individual intrinsic differences can be easily accounted for. Thus, a change in the Chandrasekhar mass affects the intrinsic brightness of thermonuclear supernovae, and thus their distance determination. Consequently, using the Hubble diagram of high-redshift supernovae consistent upper limits on the rate of variation of G can be posed [18].

Given all the previous discussion it is quite evident that the evolution and structure of white dwarfs is sensitive to the past value of G and to its rate of variation. However, all previous studies have clear shortcomings, and have not considered the evolution of cooling white dwarfs when a varying G is adopted with enough degree of detail to set reliable upper bounds to the variation of G. Thus fully evolutionary calculations with a large degree of realism are highly desirable. In this work we aim at closing this gap. We focus exclusively on the role of a varying G in the cooling of white dwarfs, and for the moment being, we neglect other effects that may have a considerable impact in the cooling times, such a possible different chemical composition of the white dwarf cores, or the initial-to-final mass relationship. This effects will be explored in a future and will be presented elsewhere.

3 Updated Cooling Sequences with a Varying *G*

In the interest of simplicity, for the evolutionary calculations presented here we have assumed that $\dot{G}/G$ remains constant with time. Such calculations have been done using the LPCODE [1] stellar evolutionary code — see [31] for recent applications of this stellar evolutionary code, and for a detailed description of the physical inputs included in our cooling sequences. For the purpose of the present work it is sufficient to say that our cooling sequences include the most modern and appropriate physical inputs. However, let us mention that among such inputs we include the most modern prescriptions for neutrino emission rates [19,22], conductive [7] and radiative opacities [21], element diffusion [1], carbon-oxygen phase separation upon crystallization [14], ^{22}Ne gravitational sedimentation [1, 13, 17], non-gray model atmospheres [32] and a reliable equation of state [26, 33].

Given that our aim is to compute self-consistently the cooling of white dwarfs in the presence of a varying G, we write the local luminosity equation as

$$\frac{\partial L_r}{\partial m} = -\epsilon_\nu - \frac{\partial u}{\partial t} + \frac{P}{\varrho^2}\frac{\partial \varrho}{\partial t}. \tag{3}$$

and we allow G to vary. This is a fair approach and has been adopted in previous studies of this kind [11]. Using the equation of hydrostatic equilibrium the density of each of the layers of the white dwarf now varies not only because the white dwarf cools, but also because G varies. In passing we note that the models of Ref. [15] were a sequence of static models in which although both contributions were taken into account, this was not done in a self-consistent way, since for these static models the present value of G was adopted, which is not the case of the present work. Naturally, this influences the cooling of white dwarfs. In this work, we assume that G decreases with time. Thus, since energy will be absorbed to expand the star in response to a decreasing G, we expect to find that white dwarfs cool faster [15].

4 Evolutionary Results

We have computed the full evolution of white dwarf model sequences of masses 0.525, 0.609 and 1.0 $M_\odot$, for three values of the rate of change of G, namely $\dot{G}/G = -5\times10^{-11}$ yr^{-1}, $\dot{G}/G = -1\times10^{-11}$ yr^{-1}, and $\dot{G}/G = -1\times10^{-12}$ yr^{-1}.

Table 1 White dwarf evolutionary sequences computed in this work. We list the white dwarf stellar mass (in solar units) and, for each value of the rate of change of the gravitational constant, $\dot{G}/G$ (in units of yr^{-1}), the initial value of G at the beginning of the white dwarf cooling phase, G_i/G_0, being G_0 the actual value of G. The numbers in brackets give the stellar luminosity. $\log(L/L_\odot)$, at which $G = G_0$ occurs

$M_{\mathrm{WD}}/M_\odot$	G_i/G_0		
	$\dot{G}/G = -5 \times 10^{-11}$	$\dot{G}/G = -1 \times 10^{-11}$	$\dot{G}/G = -1 \times 10^{-12}$
0.525	1.40 (−4.40)	1.10 (−4.37)	1.010 (−4.33)
0.525	1.30 (−4.20)	1.05 (−4.05)	1.005 (−4.00)
0.525	1.20 (−4.05)	1.02 (−3.66)	
0.525	1.10 (−3.77)		
0.609	1.50 (−4.83)	1.20 (< -5)	1.100 (< -5)
0.609	1.40 (−4.40)	1.10 (−4.30)	1.050 (< -5)
0.609	1.30 (−4.19)	1.05 (−4.02)	1.020 (< -5)
0.609	1.20 (−4.02)	1.02 (−3.60)	
0.609	1.10 (−3.68)		
1.000	1.24 (−4.64)	1.10 (−4.55)	1.020 (< -5)
1.000	1.20 (−4.12)	1.05 (−3.68)	1.010 (−4.30)
1.000	1.10 (−3.23)	1.02 (−3.10)	1.005 (−3.56)

Since the white dwarf evolution in the case of a varying G is strongly dependent on the initial value of G, we have computed for each value of $\dot{G}/G$ several evolutionary sequences with different values of G_i/G_0, where G_i stands for the value of G at the beginning of the cooling track at high effective temperature, and G_0 corresponds to the present value of G. All in all, we have computed 30 white dwarf evolutionary sequences. These sequences are listed in Table 1, which gives for each sequence the white dwarf stellar mass and the values of G_i/G_0 for each of the values of the rate of change of G adopted here. In addition, in this table we also list the surface luminosity (in solar units) for which $G = G_0$. Note that the election of the values of G_i has been made in such a way that the present value of the gravitational constant occurs at advanced stages of white dwarf evolution, mainly when the surface luminosity ranges from $\log(L/L_\odot) = -3$ to -5, the luminosities of the most typical white dwarfs.

The evolution of the central density and temperature for our $0.609\,M_\odot$ white dwarf model sequences for the case of a rate of change of G of $\dot{G}/G = -5 \times 10^{-11}$ yr^{-1} and for different initial values of G at the start of the cooling track is shown in Fig. 1. The standard case in which $G = G_0$ is adopted during the evolution is also depicted. This figure clearly emphasizes the marked dependence of the white dwarf structure on the actual value of G, an expected feature in view of the compact nature of these stars. Note in particular that the central density of our model white dwarf becomes considerably smaller as the gravitational constant decreases. Considering that the energy of cool white dwarfs is essentially of gravothermal origin, this has important implications for the evolution of old white dwarfs, since even a small change in G will alter the energy balance of the star, and thus its luminosity and the corresponding cooling times.

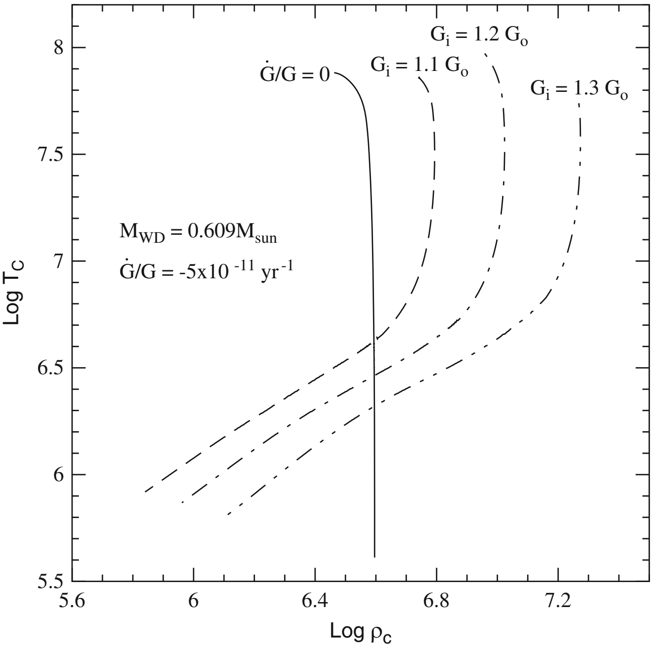

Fig. 1 Central temperature versus central density for the 0.609 $M_\odot$ white dwarf model sequences assuming $\dot{G}/G = -5 \times 10^{-11}$ yr^{-1} and for different initial values of the gravitational constant G at the start of the cooling phase. The standard case of a constant value of G during the entire evolution is also shown for the sake of comparison

The impact of the initial value of G and of its rate of change on the cooling times can be assessed inspecting Fig. 2. This figure shows the temporal evolution of the surface luminosity for different 0.609 $M_\odot$ white dwarf cooling sequences. The curve labeled as $G_i = G_0$ displays the standard evolution in which the gravitational constant is set to the present value of G during the entire evolution. The curve labeled as "$G_i = 1.4G_0$ (constant)" shows the evolution for the situation in which a constant value of G is adopted, but for the (unrealistic, but illustrative) case in which $G = 1.4G_0$. In this case, the change in the slope of the cooling curve at $\log(L/L_\odot) \approx -2.7$ and the subsequent decrease in the cooling rate reflects in large part the onset of core crystallization (which occurs earlier than in the standard case) and the associated energy release. This cooling curve should be compared with the cooling sequence labeled as $G = 1.4G_0$ which displays the cooling sequence for the same sequence but now assuming that G decreases at the rate $\dot{G}/G = -5 \times 10^{-11}$ yr^{-1}. It is clear from this figure that when G is allowed to vary the energy balance of the star results strongly modified. Indeed, note that the cooling rate is strongly accelerated. This fact reflects the energetic demand required for the star to expand against gravity in response to a decreasing G. As a result, by the time the gravitational constant has reached the present value — which for this

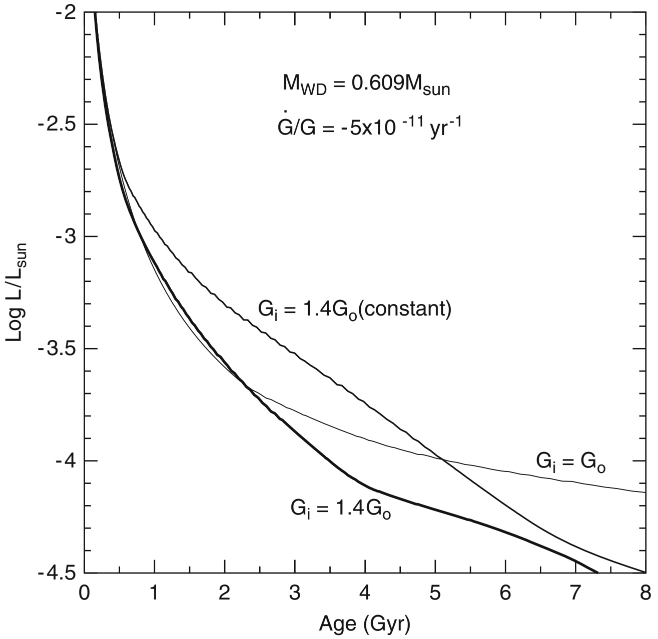

Fig. 2 Surface luminosity versus age for different $0.609\,M_\odot$ white dwarf sequences. The line labeled as $G_i = 1.4G_0$ corresponds to the case of a constant value of G, which we have chosen to be $1.4G_0$, during the entire white dwarf evolution. The line labeled as $G_i = G_0$ displays the evolution for the standard case. Finally the curve labeled as $G_i = 1.4G_0$ shows the evolution assuming $\dot{G}/G = -5 \times 10^{-11}$ yr^{-1} and an initial value of G at the start of the cooling phase of $G_i = 1.4G_0$

sequence occurs at $\log(L/L_\odot) \approx -4.4$ — the cooling process has been strongly accelerated.

From the previous discussion it is rather evident that the white dwarf cooling rate depends sensitively both on the adopted initial value of G and on the rate of change of G. To disentangle both effects we have computed a set of cooling sequences for which the present value of G occurs for $\log(L/L_\odot) \approx -4.0$, which is the most typical luminosity of field white dwarfs. This set of cooling sequences is shown in Fig. 3 for an otherwise typical white dwarf of mass $\sim 0.609\,M_\odot$. We have adopted several secular rates of change of the gravitational constant, namely $\dot{G}/G = -1 \times 10^{-12}$ yr^{-1}, -1×10^{-11} yr^{-1}, and -5×10^{-11} yr^{-1}. It is worth noting that there is a marked dependence of the white dwarf evolutionary timescales on the assumed rate of change of G. In passing we note that this dependence is more notorious in the case of more massive white dwarfs, because their structure is more compact, but we do not show here the results for the sake of conciseness. However, it is evident from Fig. 3 that for the case in which $\dot{G}/G = -1 \times 10^{-12}$ yr^{-1} the evolutionary cooling times are almost indistinguishable from those of the standard case, in which a constant G is adopted (shown in this figure as a dashed line). This value of $\dot{G}/G$

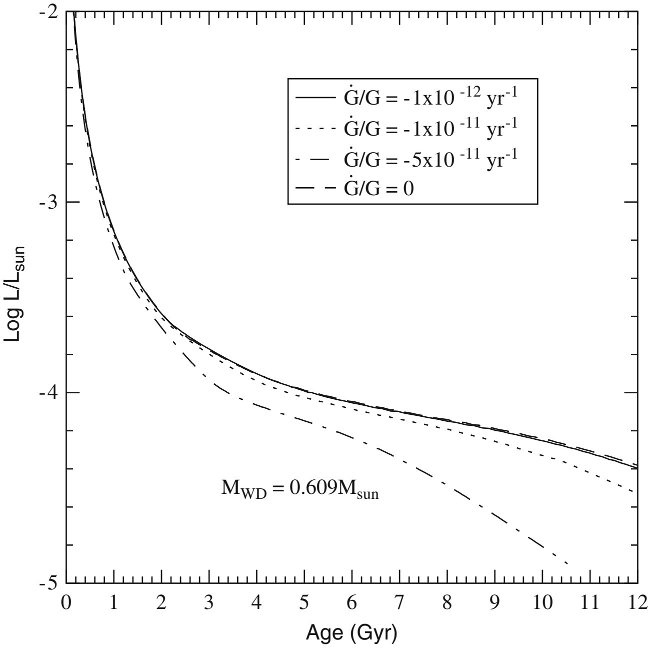

Fig. 3 Surface luminosity versus age for several 0.609 $M_{\odot}$ white dwarf model sequences, adopting different values of $\dot{G}/G$ (solid lines). From top to bottom, curves correspond to $\dot{G}/G = -1 \times 10^{-12}$ yr^{-1}, -1×10^{-11} yr^{-1}, and -5×10^{-11} yr^{-1}. The present value of the gravitational constant occurs when $\log(L/L_{\odot}) \approx -4.0$. The dashed line corresponds to the standard case of a constant G

provides a lower limit for the rate of change of G above which we expect that the evolution of white dwarfs will be influenced in a noticeable way by a secularly varying G.

5 Conclusions

The variation of the fundamental constants of nature is a controversial topic that deserves further study. In recent years several studies have been devoted to investigate the variation of the fine structure constant, α, but very few investigations have been carried out to set upper bounds on a hypothetical variation of the gravitational constant, G. There are several reasons for this, but perhaps the most important one is that the relative error on the determination of the value of G is the largest one when all the fundamental constants of nature are considered. Additionally, the most stringent upper limits on the rate of variation of G come from the Earth-Moon system, or from cosmological determinations, namely Big Bang nucleosynthesis and the cosmic microwave background, whereas very few constraints at a Galactic scale have been derived so far. White dwarfs provide us with an unique opportunity to confirm or discard a variation of G at such scales. The reason is that white dwarfs are strong-gravity and slowly-evolving objects, with very long evolutionary timescales, and moreover the physics governing their evolution is relatively well understood. In a step forward to do this, in this work we have computed a new set of white dwarf evolutionary sequences in which we allow G to vary. In the interests of simplicity, we have assumed that $\dot{G}/G$ remains constant with time. Specifically, we have followed the evolution of white dwarf model sequences of masses 0.525, 0.609 and $1.0\,M_{\odot}$ considering three values for the rate of change of G, namely $\dot{G}/G = -5\times10^{-11}\,\mathrm{yr}^{-1}$, $\dot{G}/G = -1\times10^{-11}\,\mathrm{yr}^{-1}$, and $\dot{G}/G = -1\times10^{-12}\,\mathrm{yr}^{-1}$, and different initial values of G. These sequences have been computed taking into account the core chemical composition predicted by the evolution of progenitor stars with different stellar masses as well as the state-of-the art input physics relevant for white dwarf stars. We find that the mechanical structure of cool white dwarfs is strongly modified when a slowly varying G is adopted. Specifically, we have found that a varying G alters the hydrostatic balance, and hence the balance between the gravitational energy and total internal energy (electronic, ionic and Coulomb energies). Naturally, this influences the cooling of the white dwarfs. Since we have assumed that the rate of change of G is negative, the cooling process is accelerated in all cases, since energy is absorbed to expand the star. Moreover, we have found that these effects are more noticeable for massive white dwarfs, owing to their larger gravities. Finally, we find that for and otherwise typical white dwarf of $\sim 0.6\,M_{\odot}$ when the rate of change of G larger than $\dot{G}/G = -1 \times 10^{-12}\,\mathrm{yr}^{-1}$ the evolution at sufficiently low luminosities is markedly affected. Last but not least, we mention that the calculations to study other effects that may have a considerable impact in the cooling times, such a possible different chemical composition of the white dwarf cores, or the effect of a varying G in the initial-to-final mass relationship, are currently under way, and will be presented elsewhere.

Acknowledgements This research was supported by AGAUR, by MCINN grants AYA2008–04211–C02–01 and AYA08-1839/ESP, by the ESF EUROCORES Program EuroGENESIS (MICINN grant EUI2009-04170), by the European Union FEDER funds, by AGENCIA: Programa de Modernización Tecnológica BID 1728/OC-AR, and by PIP 2008-00940 from CONICET. LGA also acknowledges a PIV grant of the AGAUR of the Generalitat de Catalunya.

References

1. L.G. Althaus et al., Astrophys. J, 719 (2010) 612.
2. A. Baglin and J. Heyvaerts, Nature 222 (1969) 1258.
3. C. Bambi, M. Giannotti and F.L. Villante, Phys. Rev. D71 (2005) 123524.
4. O.G. Benvenuto, L.G. Althaus and D.F. Torres, M.N.R.A.S. 305 (1999) 905.
5. O.G. Benvenuto, E. García–Berro and J. Isern, Phys. Rev. D69 (2004) 082002.
6. M. Biesiada and B. Malec, M.N.R.A.S. 350 (2004) 644.
7. S. Cassisi et al., Astrophys. J. 661 (2007) 1094.
8. H. Chand et al., A&A417 (2004) 853.
9. H. Chand,et al., A&A 451 (2006) 45.

10. C.J. Copi, A.N. Davis and L.M. Krauss,, Phys. Rev. Lett. 92 (2004) 171301.
11. S. degl'Innocenti et al., A&A 312 (1996) 345.
12. P.A.M. Dirac, Proc. R. Soc. London, Ser. A. 165 (1938) 199.
13. E. García–Berro, L.G. Althaus, A.H. Córsico and J. Isern, Astrophys. J. 677 (2008) 473.
14. E. García–Berro, M. Hernanz, J. Isern and R. Mochkovitch, Nature 333 (1988) 642.
15. E. García–Berro, M. Hernanz, J. Isern and R. Mochkovitch, M.N.R.A.S. 277 (1995) 801.
16. E. García–Berro, J. Isern and Y.A. Kubyshin, A&AR 14 (2007) 113.
17. E. García–Berro et al., Nature 465 (2010) 194.
18. E. Gaztañaga et al., Phys. Rev. D65 (2002) 023506.
19. M. Haft, G. Raffelt and A. Weiss, Astrophys. J, 425 (1994) 222.
20. F. Hofmann et al., in Proc. of the EGU General Assembly 2010, Vienna, Austria, 12 (2010) 2857.
21. C.A. Iglesias and F.J. Rogers, Astrophys. J. 464 (1996) 943.
22. N. Itoh et al., ApJS 102 (1996) 411.
23. N. Kanekar et al., Phys. Rev. Lett., 95 (2005) 261301.
24. N. Kanekar et al., Astrophys. J, 716 (2010) L23.
25. P. Lorén–Aguilar, E. García–Berro, J. Isern and Y.A. Kubyshin, Class. & Quantum Grav. 20 (2003) 3885.
26. G. Magni and I. Mazzitelli, A&A 72 (1979) 134.
27. L. Mestel, M.N.R.A.S. 112 (1952) 583.
28. P.J. Mohr, B.N Taylor and D.B. Newell, Rev. Mod. Phys, 80 (2008) 633.
29. M.T. Murphy et al., MNRAS345 (2003) 609.
30. R. Quast et al., A&A415 (2004) L7.
31. I. Renedo et al., Astrophys. J, 717 (2010) 183.
32. R.D. Rohrmann, L.G. Althaus and S.O. Kepler, A&A (2010) in press.
33. L. Segretain et al., Astrophys. J. 434 (1994) 641.
34. R. Srianand et al., Phys. Rev. Lett.92 (2004) 121302.
35. J.-P. Uzan, Rev. Mod. Phys. 75 (2003) 403
36. S.C. Vila, Astrophys. J, 206 (1976) 213.
37. J.K. Webb et al., Phys. Rev. Lett.82 (1999) 884.
38. J.K. Webb et al., Phys. Rev. Lett.87 (2001) 091301.
39. D. Winget et al., Nature 303 (1983) 781.

Testing the Variation of Fundamental Constants with the CMB

Silvia Galli, C.J.A.P. Martins, Alessandro Melchiorri, and Eloisa Menegoni

Abstract The high precision of current and future CMB data may allow the detection of numerous physical processes that might change the standard model of recombination, leaving recognizable imprints on the angular power spectra. We review some of the results obtained in constraining the variation of fundamental constants, in particular the effects of the gravitational constant G and of the fine structure constant α.

1 Introduction

The recent measurements of the Cosmic Microwave Background (CMB) flux provided by experiments such as the Wilkinson Microwave Anisotropy Probe (WMAP) mission (see [12, 16, 17], the ACBAR collaboration (see [29]) and many others have confirmed several aspects of the cosmological standard model and improved the constraints on several key parameters. These spectacular results, apart from the experimental improvements, have been possible due to the high precision of the CMB theoretical predictions that have now reached an accuracy close to 0.1% over a wide range of scales. A key ingredient in the CMB precision cosmology is the

---

S. Galli
Laboratoire APC 10, rue Alice Domon et Leonie Duquet 75205 Paris Cedex 13
Physics Department and INFN, Università di Roma “La Sapienza”, Ple Aldo Moro 2, 00185 Rome, Italy
e-mail: galli@apc.univ-paris7.fr

C.J.A.P. Martins
Centro de Astrofísica, Universidade do Porto, Rua das Estrelas, 4150-762 Porto, Portugal

A. Melchiorri
Physics Department and INFN, Università di Roma “La Sapienza”, Ple Aldo Moro 2, 00185 Rome, Italy

E. Menegoni
Physics Department and INFN, Università di Roma “La Sapienza”, Ple Aldo Moro 2, 00185 Rome, Italy

C. Martins and P. Molaro (eds.), *From Varying Couplings to Fundamental Physics*,
Astrophysics and Space Science Proceedings, DOI 10.1007/978-3-642-19397-2_7,

accurate computation of the recombination process. Since the seminal papers by Peebles and Zel'dovich (see [27, 40]) detailing the recombination process, further refinements to the standard scheme were developed [32] allowing predictions at the accuracy level found in data from the WMAP satellite and predicted for the Planck satellite [13, 34, 37].

While the attained accuracy on the recombination process is impressive, it should be noticed that these computations rely on the assumption of standard physics. Non-standard mechanisms such as (just to name a few) high redshift stars or active galactic nuclei, topological defects and dark matter decays or annihilation could produce extra sources of radiation or determine a variation of fundamental constants, therefore yielding a modification of the recombination process. With the WMAP results and the future Planck data, it therefore becomes conceivable that deviations from standard recombination may be detected.

Here we want to focus on how much current and future CMB data can constrain the variation of fundamental constants. The interest in this work relies in the fact that this analysis tests the value of the couplings at time and lenght scales that are comparable to the age/size of the universe, providing complementary constraints to the ones obtainable with laboratory experiments. In Sec. 2 we present the results obtained in constraining the Gravitational Constant, while in Sec. 3 we report the constraints for the fine structure constant. In Sec. 4, we consider the possibility that the Gravitational constant and the fine structure constant could vary together due to an underlying common mechanism.

Most of the work presented here is taken from [8, 9, 21, 23, 24]. We refer the reader to those papers for further details.

2 Newton's Gravitational Constant

The hypothesis that fundamental constants of physics could vary in space and time was probably first proposed by Dirac [7]. Since then, many authors have explored this possibility (see [38] for a detailed review), improving the accuracy on the value of these constants. Many different methods have been used to test the constancy of these quantities at different scales and epochs. Nevertheless, it is still difficult to determine some of them with very high precision. In particular, the gravitational constant G remains one of the most elusive constants in physics. The past two decades did not succeed in substantially improving our knowledge of its value from the precision of 0.05% reached in 1942 (see [11]). On the contrary, the variation between different measurements forced the CODATA committee[1], which determines the internationally accepted standard values, to temporarily increase the uncertainty from 0.013% for the value quoted in 1987 to the one order of magnitude larger uncertainty of 0.15% for the 1998 "official" value ([25]).

---

[1] See http://www.codata.org/

Measurements of the Cosmic Microwave Background temperature and polarization anisotropy have been suggested as a possible tool for determining the value of the gravitational constant G (see [39]).

In [8] we constrained the value of G using WMAP5 [12] and ACBAR [29] data and simulated data for the PLANCK satellite and for a hypothetical cosmic variance limited experiment.

We first determined the constraints on a constant value of G using current CMB data. We parameterized the deviations from the conventional value of the gravitational constant G_0 by introducing a dimensionless parameter λ_G such that $G = G_0\lambda_G^2$ following [39]. The effect of different values of λ_G on the angular power spectra is shown in Fig. 1.

We then allowed λ_G to vary in a modified version of the CAMB code ([19]) in the publicly available Markov Chain Monte Carlo package `cosmomc` ([18]), sampling the following set of parameters: the baryon and cold dark matter densities ω_b and ω_c, the Hubble constant H_0, the scalar spectral index n_s, the overall normalization of the spectrum A_s at $k = 0.05$ Mpc^{-1}, the optical depth to reionization, τ, the amplitude of the Sunyaev-Zel'dovich power spectrum and the gravitational constant $\lambda_G = \sqrt{(G/G_0)}$. Furthermore, we considered purely adiabatic initial conditions and we imposed spatial flatness.

Results for different sets of data are shown in table 1.

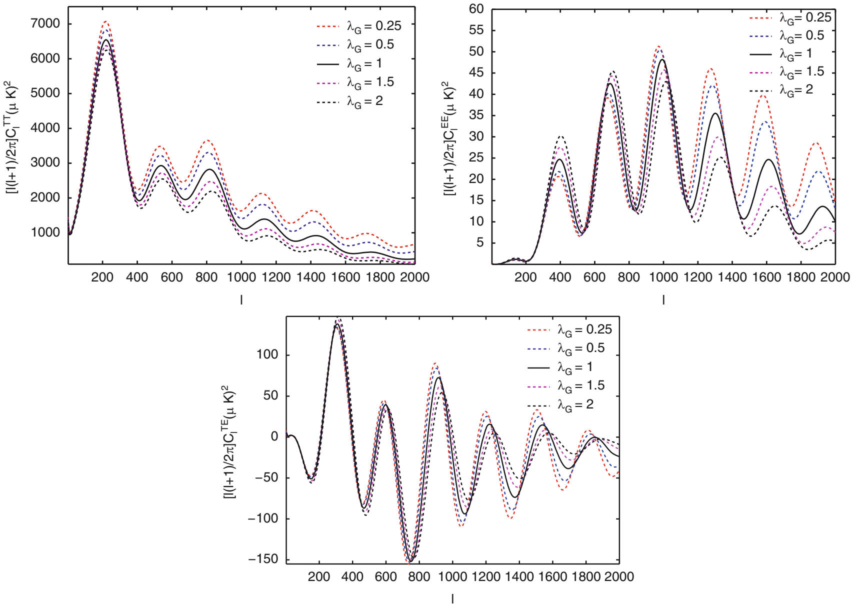

Fig. 1 Temperature, Polarization and cross Temperature-Polarization power spectra in function of variations in λ_G. Taken from [8]

Table 1 *Constraints on λ_G from current WMAP and ACBAR data and future constraints achievable from the Planck satellite mission and from a cosmic variance limited experiment (CVL). Taken from [8]*

Experiment	Constraints on λ_G at 68%cl
WMAP	1.01 ± 0.16
WMAP+POL	0.97 ± 0.13
WMAP+ACBAR	1.03 ± 0.11
PLANCK	1.01 ± 0.015
CVL	1.002 ± 0.004

CMB data can constrain a constant value of G with an accuracy of $\sim 10\%$ level at 68% c.l., therefore not being competitive with the accuracy quoted by the CODATA committee of 0.01% at 68% c.l. Only a cosmic variance limited experiment will be able to achieve a slightly more comparable precision, reaching an accuracy of $\sim 0.4\%$.

3 Fine Structure Constant

A time varying fine structure constant can leave an imprint on CMB anisotropies by changing the time of recombination and the size of the acoustic horizon at photon-electron decoupling, and the steadily improving CMB datasets have been extensively used to constrain it. Parameterizing a variation in the fine structure constant as $\Delta_\alpha = (\alpha - \alpha_0)/\alpha_0$, where $\alpha_0 = 1/137.03599907$ is the standard, local, value and α is the value during the recombination process, the authors of [22] used the first year WMAP data, finding the constraint $-0.06 < \Delta_\alpha < 0.01$ at 95% c.l. (see also [7]). This constraint was subsequently updated to $-0.039 < \Delta_\alpha < 0.01$ (see [36]) by combining the third year WMAP data with the Hubble Space Telescope key project constraint on the Hubble Constant. More recently, using the five-year observations from the WMAP satellite, the authors of [26] found the constraint $-0.05 < \Delta_\alpha < 0.042$. It is well known (see e.g. [36]) that a variation in the fine-structure constant is mostly degenerate with a variation in the Hubble constant $H_0 = 100\,\mathrm{hKm/s/Mpc}$. Combining CMB data with independent measurements of H_0 can indeed improve the constraint on α. Fig. 2 shows the effect of different values of α on the CMB power spectra.

In [23] we investigated the new constraints on α obtained by using substantial improvements reported both in measurements of CMB anisotropies and in the determination of the Hubble constant. The results from the ACBAR ([29]), QUAD ([3]) and BICEP ([4]) experiments, together with the WMAP data from the five-year survey, sample the CMB temperature angular spectrum with great accuracy down to arcminute angular scales and also provide clear evidence for acoustic oscillations in the polarization channel. We also included the older datasets from BOOMERanG ([15]) and CBI ([30]). Moreover, we included the improved constraint on the Hubble

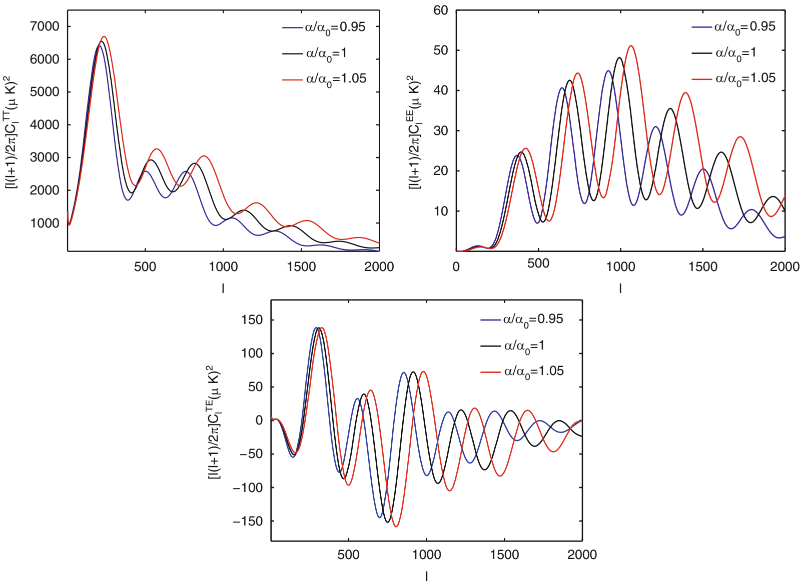

Fig. 2 Temperature, Polarization and cross Temperature-Polarization power spectra in function of variations of α/α_0

Table 2 Limits on α/α_0 from WMAP data only (first row), from a larger set of CMB experiments (second row), and from CMB plus the HST prior on the Hubble constant, $h = 0.748 \pm 0.036$ (third row). We report errors at 68% and 95% confidence level

Experiment	α/α_0	68% c.l.	95% c.l.
WMAP-5	0.998	±0.021	$^{+0.040}_{-0.041}$
All CMB	0.987	±0.012	±0.023
All CMB+HST	1.001	±0.007	±0.014

constant of $h = 0.747 \pm 0.036$ at 68% c.l., from the recent analysis of [31]. We analysed these data by means of the COSMOMC code.

We sampled the same set of cosmological parameters described in Sec. 2, with the fine structure constant in place of the gravitational constant.

In Table 2 we report the constraints on the α/α_0 parameter obtained from the COSMOMC analysis, using different combinations of datasets.

Clearly the new CMB data at arcminute angular scales provide a substantial improvement in the determination of α. The uncertainty on α is indeed halved when the data coming from the QUAD, BICEP and ACBAR experiments are included in the analysis. The increase in the precision is mainly due to the effects from modified recombination on the CMB anisotropy damping tail that is more accurately measured by the QUAD and ACBAR experiments.

In [24] we also showed that these constraints are relaxed by more than 50% when dark energy models different from a cosmological constant are considered.

4 Coupled Variation of the Couplings

The constraints presented in the previous sections assumed that only a single coupling, either G or α, is varied at the time, together with the 6 ΛCDM parameters and the amplitude of the Sunyaev-Zel'dovich power spectrum. Nevertheless, in any sensible theory where a coupling is rolling, one generically expects the others to do so as well, though possibly at fairly different rates. Since the rolling is expected to be due to the same underlying mechanism (the most natural of which will be a dynamical, fundamental scalar field), the rates of change of the various couplings will in fact be related in any given theory.

In [21] we used the CMB to constrain possible variations of α and Newton's constant G together, assuming them to be related by a phenomenological parameter whose value will be different in various fundamental physics scenarios.

Specifically, we considered that the variations of α and G are related by

$$\frac{\Delta\alpha}{\alpha} = Q\frac{\Delta G}{G} \tag{1}$$

with Q a free parameter that can be positive or negative, but not much larger than unity in absolute value (we conservatively assumed that $-10 < Q < 10$). As an illustration of the range of values allowed in some representative models, Kaluza-Klein-type theories typically have $1 < Q \leq 3$, Einstein-Yang-Mills has $Q = 1$, and Randall-Sundrum type models have very small positive Qs (say $Q \sim 0.01$). These examples are discussed in more detail in [10,20]—note that all of them have $Q > 0$. However, one can equally easily find models with $Q < 0$: for example string theory dilaton-type models have $Q \sim -1$ [6], while the BSBM-Brans-Dicke model has $Q = -1$ exactly [2].

We sampled the following ten-dimensional set of cosmological parameters, adopting flat priors on each of them: the baryon and cold dark matter densities $\omega_{\rm b}$ and $\omega_{\rm c}$, the Hubble constant H_0, the scalar spectral index n_s, the overall normalization of the spectrum A_s at $k = 0.05$ Mpc^{-1}, the optical depth to reionization, τ and, finally, the variations in the fine structure constant α/α_0 and in the Newton's constant λ_G. Furthermore, we considered purely adiabatic initial conditions and we impose spatial flatness.

Our basic data set is the five–year WMAP data [12, 16] (temperature and polarization), ACBAR ([29]), QUAD ([3]) and BICEP ([4]), as well as the older datasets from BOOMERanG ([15]) and CBI ([30]). For all these experiments we marginalized over a possible contamination from Sunyaev-Zel'dovich component, rescaling the WMAP template at the corresponding experimental frequencies.

We also combined the CMB data with the recent UNION catalog of supernovae type Ia luminosity distances and with the improved constraint on the Hubble constant of $h = 0.747 \pm 0.036$ at 68% c.l., from the analysis of [31].

We also computed the constraints on λ_G and α using standard BBN theoretical predictions as provided by the numerical code described in [28], which includes a full updating of all rates entering the nuclear chain based on the most recent

Table 3 Limits on α/α_0 and λ_G from CMB data only (first row), from CMB+SN-Ia (second row), from CMB plus the HST prior on the Hubble constant, $h = 0.748 \pm 0.036$ (third row), from CMB plus BBN (fourth row) and for simulated mock data for the Planck experiment. We report errors at 68% confidence level

Experiment	α/α_0	68% c.l.	λ_G	68% c.l.
All CMB	0.999	±0.017	1.04	±0.12
All CMB+SN-Ia	0.989	±0.012	1.04	±0.11
All CMB+HST	1.003	±0.008	1.13	±0.09
ALL CMB+BBN	0.985	±0.009	1.01	±0.01
Planck only	1.000	±0.015	1.02	±0.09

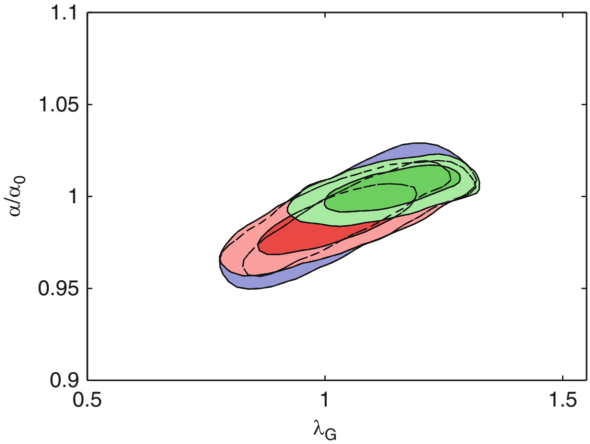

Fig. 3 68% and 95% c.l. constraints on the α/α_0 vs λ_G for different datasets. The contours regions come from CMB data (blue), CMB data and SN-Ia (red), and CMB+HST (green)

experimental results on nuclear cross sections. The BBN predictions were compared with the experimental determinations of the ^{4}He mass fraction Y_p and D/H abundance ratio, $Y_p = 0.250 \pm 0.003$ and D/H $= (2.87^{+0.22}_{-0.21}) \times 10^{-5}$, as discussed in [35]. In Table 3 we report the constraints on the α/α_0 and the λ_G parameters obtained from the COSMOMC analysis, using different combinations of datasets, and in Figure 3 we show the 68% and 95% c.l. constraints on the α/α_0 vs λ_G for the different datasets.

Comparing these with the results presented in the previous sections for the two individual parameters, we see only a mild change in the best fit and confidence intervals for α, while the changes are somewhat larger for G. Furthermore, the constraints partially improve when a prior is imposed on the value of H_0, as both the parameters are degenerate with the Hubble constant.

It is also interesting to notice that, due to the degeneracy between the two parameters, a future detection for a variation in α could be on the contrary due to a variation in G. It is therefore important to pursue a combined search for variations in the two constants since their effect on the CMB anisotropy are very similar. Nevertheless, due to this degeneracy the bounds obtained will be only marginally improved by Planck compared to current CMB data. On the contrary, stronger improvements can be obtained by combining the CMB data with a BBN analysis, if one assumes that α and G do not vary from BBN to recombination.

From the perspective of mode-building it is interesting to consider the behavior of the Q parameter, which in terms of our analysis pipeline is defined as $\frac{\alpha}{\alpha_0} - 1 = Q(\lambda_G^2 - 1)$.

Obviously, since the current data doesn't show any evidence for variations in G or α it is not possible to rule out any of the models discussed before, even though linearly fitting the apparent correlation between α and λ_G the data seem to prefer positive values of Q. In other words, if there are any variations at or around the percent level, then the variations of the two parameters must have the same sign.

Acknowledgements The work of C.M. is funded by a Ciência2007 Research Contract, supported by FSE and POPH-QREN funds.

References

1. P.P. Avelino et al., Phys. Rev. D64 (2001) 103505 [arXiv:astro-ph/0102144]; C.J.A.P. Martins et al., Phys. Rev. D66 (2002) 023505 [arXiv:astro-ph/0203149].
2. J.D. Barrow, J. Magueijo and H.B. Sandvik, Phys. Lett. B541 (2002) 201 [arXiv:astro-ph/0204357].
3. M.L. Brown et al. [QUaD collaboration], arXiv:0906.1003.
4. H.C. Chiang et al., arXiv:0906.1181.
5. T. Clifton, J.D. Barrow and R.J. Scherrer, Phys. Rev. D71 (2005) 123526. A. Liddle, A. Mazumdar and J.D. Barrow Phys. Rev. D58 (1998) 027302. F. Wu, L. Qiang, X. Wang, X. Chen, arXiv:0903.0384; F. Wu, L. Qiang, X. Wang, X. Chen, arXiv:0903.0385.
6. T. Damour, F. Piazza and G. Veneziano, Phys. Rev. D66 (2002) 046007 [arXiv:hep-th/0205111].
7. P.A.M. Dirac, Nature (London) 139 (1937) 323. P.A.M. Dirac, Proc. Roy. Soc. London A165 (1938) 198. P.A.M. Dirac, Proc. Roy. Soc. London A338 (1974) 439. P.A.M. Dirac, Proc. Roy. Soc. London A 365 (1979) 19.
8. S. Galli, A. Melchiorri, G.F. Smoot and O. Zahn, Phys. Rev. D80 (2009) 023508 [arXiv:0905.1808]
9. S. Galli et al., arXiv:1005.3808, Phys. Rev. D (2010) in press.
10. E. Garcia-Berro, J. Isern and Y. A. Kubyshin, Astron. Astrophys. Rev. 14 (2007) 113.
11. P.R. Heyl and P. Chrzanowski, J. Res. Natl. Bur. Std. U.S. 29 (1942) 1.
12. G. Hinshaw et al. [WMAP Collaboration], arXiv:0803.0732.
13. W. Hu, D. Scott, N. Sugiyama and M. White, *Phys. Rev.* D52 (1998) 5498.
14. K. Ichikawa, T. Kanzaki and M. Kawasaki, Phys. Rev. D74 (2006) 023515 [arXiv:astro-ph/0602577].
15. W. C. Jones et al., arXiv:astro-ph/0507494; F. Piacentini et al., arXiv:astro-ph/0507507; arXiv:astro-ph/0507514.
16. E. Komatsu et al., arXiv:0803.0547.
17. E. Komatsu et al., arXiv:1001.4538.
18. A. Lewis and S. Bridle, Phys. Rev. D66 (2002) 103511, available from `http://cosmologist.info`.
19. A. Lewis, A. Challinor and A. Lasenby, Astrophys. J. 538 (2000) 473 [arXiv:astro-ph/9911177].

20. P. Loren-Aguilar, E. Garcia-Berro, J. Isern and Yu. A. Kubyshin, Class. Quant. Grav. 20 (2003) 3885 [arXiv:astro-ph/0309722].
21. C.J.A.P. Martins, E. Menegoni, S. Galli, G. Mangano and A. Melchiorri, Phys. Rev. D82 (2010) 023532.
22. C.J.A.P. Martins et al., Phys. Lett. B585 (2004) 29 [arXiv:astro-ph/0302295]; G. Rocha et al., Mon. Not. Roy. Astron. Soc. 352 (2004) 20.
23. E. Menegoni, S.Galli, J. Bartlett, C.J.A.P. Martins and A. Melchiorri, Phys. Rev. D80 (2009) 087302.
24. E. Menegoni et al., I.J.M.P. D19 (2010) 507.
25. P.J. Mohr and B.N. Taylor, Rev. Mod. Phys., 72 (2000) 351.
26. M. Nakashima, R. Nagata and J. Yokoyama, Prog. Theor. Phys. 120 (2008) 1207 [arXiv:0810.1098].
27. P.J.E. Peebles, *Astrophys. J.* 153 (1968) 1.
28. O. Pisanti et al., Comput. Phys. Commun. 178 (2008) 956 [arXiv:0705.0290].
29. C.L. Reichardt et al., [arXiv:0801.1491].
30. A.C.S. Readhead et al., Astrophys. J. 609 (2004) 498.
31. A.G. Riess et al., Astrophys. J. Suppl. 183 (2009) 109 [arXiv:0905.0697].
32. S. Seager, D.D. Sasselov and D. Scott, *Astrophys. J.* 523 (1999) 1, astro-ph/9909275.
33. S. Seager, D.D. Sasselov and D. Scott, Astrophys. J. Suppl. 128 (2000) 407 [arXiv:astro-ph/9912182].
34. U. Seljak, N. Sugiyama, M. White and M. Zaldarriaga, astro-ph/0306052
35. P.D. Serpico et al., JCAP 0412 (2004) 010 [astro-ph/0408076].
36. P. Stefanescu, New Astron. 12 (2007) 635 [arXiv:0707.0190].
37. E.R. Switzer and C.M. Hirata, Phys. Rev. D77 (2008) 083006 [arXiv:astro-ph/0702143]; C.M. Hirata and E.R. Switzer, Phys. Rev. D77 (2008) 083007 [arXiv:astro-ph/0702144].
38. J.-P. Uzan, Reviews of Modern Physics, 75 (2003) 403; J.-P. Uzan, arXiv:1009.5514
39. O. Zahn and M. Zaldarriaga, Phys. Rev. D67 (2003) 063002 [arXiv:astro-ph/0212360].
40. Ya. B. Zel'dovich, V.G. Kurt and R.A. Sunyaev, Zh. Eksp. Teoret. Fiz. 55 (1968) 278, English translation: Sov. Phys. JETP. 28 (1969) 146.

The Value of the Fine Structure Constant Over Cosmological Times

Carlos M. Gutiérrez and Martín López-Corredoira

Abstract The optical spectra of objects classified as QSOs in the SDSS DR6 are analyzed with the aim of determining the value of the fine structure constant in the past and then check for possible changes in the constant over cosmological timescales. The analysis is done by measuring the position of the fine structure lines of the [OIII] doublet ($\lambda\lambda 4959$ and $\lambda\lambda 5008$) in QSO nebular emission. From the sample of QSOs at redshifts $z < 0.8$ a sub sample was selected on the basis of the amplitude and width of the [OIII] lines. Two different method were used to determine the position of the lines of the [OIII] doublet, both giving similar results. Using a clean sample containing 1568 of such spectra, a value of $\Delta\alpha/\alpha = (+2.4 \pm 2.5) \times 10^{-5}$ (in the range of redshifts $z \sim 0 - 0.8$) was determined. The use of a larger number of spectra allows a factor ~ 5 improvement on previous constraints based on the same method. On the whole, we find no evidence of changes in α on such cosmological timescales. The mean variation compatible with our results is $1/ < t > \Delta\alpha/\alpha = (+0.7 \pm 0.7) \times 10^{-14}$ yr^{-1}.

1 Introduction

In some theories that try to unify all the fundamental interactions, the constants of nature are functions of a low mass dynamical scalar field, which slowly changes over cosmological timescales [15]. Astrophysics offers a possible test to constrain the parameters of such theories by directly measuring the values of such constants through the comparison of properties of objects at different evolutionary epochs of the Universe [8, 9]. In particular, several methods have been developed to measure the value of the fine structure constant (α) based on the analysis of cosmic microwave background data [14], Big Bang nucleosynthesis [7], and the

---

C.M. Gutiérrez and M. López-Corredoira
Instituto de Astrofísica de Canarias, 38205 La Laguna, Tenerife, Spain
e-mail: cgc@iac.es

C. Martins and P. Molaro (eds.), *From Varying Couplings to Fundamental Physics*,
Astrophysics and Space Science Proceedings, DOI 10.1007/978-3-642-19397-2_8,

fine splitting of several atomic lines in QSO spectra (see below). A review on the techniques and observational constraints can be found in [5].

Here, we mention only those methods based on fine structure splitting. The splitting ratio $(\lambda_2 - \lambda_1)/(\lambda_2 + \lambda_1)$ at two different epochs gives the relative difference in α between these two epochs. It is shown [15] that

$$\frac{\Delta\alpha}{\alpha}(z) = \frac{1}{2}\left\{\frac{[(\lambda_2 - \lambda_1)/(\lambda_2 + \lambda_1)]_z}{[(\lambda_2 - \lambda_1)/(\lambda_2 + \lambda_1)]_0} - 1\right\}$$

where λ_2 and λ_1 are the wavelengths of the pairs of the doublet, and the subscripts z and 0 refer to the values at redshift z and local respectively.

The method has been employed to measure the relative separation of absorption lines in the spectra of QSOs, including the alkali doublet [2], and the many multiplet method (MML, [16]). The best constraints obtained using the alkali doublet method are those by Chand et al. [4] ($\delta\alpha/\alpha = (0.15 \pm 0.44) \times 10^{-5}$ over the range $1.59 \leq z \leq 2.32$). The MML is the only method that has resulted in claims for the detection of variation of α [13, 16] $\Delta\alpha/\alpha = (-0.574 \pm 0.102) \times 10^{-5}$ in the range $0.2 \leq z \leq 3.7$, although these results are controversial. Another group [10] has developed a slight modification of the MML method in which only one atomic ion (Fe II) is used, avoiding many of the assumptions and uncertainties inherent to the MML method. Their latest analysis [11, 12] determined $\Delta\alpha/\alpha = (-0.12 \pm 1.79) \times 10^{-6}$ at $z = 1.15$ and $\Delta\alpha/\alpha = (5.4 \pm 2.5) \times 10^{-6}$ at $z = 1.84$.

Here, we use the [OIII] nebular emission lines in QSOs to constrain past variations in α. The method was proposed by Bahcall and Salpeter [1], and was later applied by Bahcall et al.[3] and Grupe et al. [6]. Because the analysis is based on a pair of lines only, the constraints on $\Delta\alpha/\alpha$ are not as strong as those obtained with the other methods mentioned above, but has the advantage that it is more transparent and less subject to systematics. The method is based on the same element and level of ionization, and both lines originate in the same upper energy level, so the analysis is quite independent of the physical conditions of the gas where the [OIII] lines originate. It therefore represents a good alternative for determining the value of α on a firm basis. Bahcall et al. [3] analyzed the QSOs of the Early Data Release of SDSS and built a clean sample of 42 QSOs in the range $0.16 \leq z \leq 0.80$, from which they derived $\Delta\alpha/\alpha = (+0.7 \pm 1.4) \times 10^{-4}$. Here, we use the QSOs in the latest release of the SDSS to improve such constraints significantly.

2 Sample Selection and Methodology

The *SDSS-DR6 Catalog Archive Server*[1] contains 77 082 objects classified as QSOs. By SQL queries we downloaded the extracted 1d spectra of all of them. These spectra have a resolution ∼2000 and the range covered is ∼3400–9200 Å, which

---

[1] http://www.sdss.org/dr6/access/index.html#CAS

includes the [OIII] doublet up to redshift ∼0.85; this restriction in redshift automatically limits the sample to 28,860 spectra. The wavelength calibration was checked by measuring the position of the atmospheric OI line. From 1656 sky spectra we determined a mean position of 5578.885 Å and a standard deviation of 0.287 Å which agrees quite well with the theoretical value (5578.887 Å) and with expectations from the spectral resolution of the spectra. The selection of the final sample was done on the basis of the strength, shape and width of the [OIII] lines, reliability of the continuum estimation, and possible contribution due to the relative proximity of the Hβ line. The estimation of the spectral position of the [OIII] lines was done following two methods which are described below.

Method 1: To estimate the centroids of the lines, we first determined the FWHM of each line and averaged the flux of the pixels within the spectral range covered by that FWHM. We estimate the relative strength of the [OIII] lines with respect to the noise in the adjacent continuum. Such noise was estimated by measuring the continuum rms of each spectrum in the wavelength range 5040–5100 Å (rest frame). We select those objects that have strong ($SNR > 20$ in the peak) [OIII] lines. These restrictions provide us with a sub sample (which we refer to hereafter as the "raw sample") of 3739 objects. The contribution of the Hβ line could in principle produce a blueshift in the estimation of the centroids of the lines, particularly affecting the 4959 Å line. We checked that this contribution could be properly quantified by computing the level of the flux (after subtraction of the continuum) in a spectral region slightly bluer than the position of the [OIII] ($\lambda\lambda$4959) Å line. After many trials we chose the 4925–4935 Å (rest frame) wavelength range to estimate possible residuals of Hβ and remove from the sample those objects with fluxes in that interval above 0.05 the peak value of the [OIII] ($\lambda\lambda$4959) Å line. We also eliminated spectra with very wide or double peaked [OIII] lines. Figure 1 shows the different spectral regions used to calculate fluxes and centroids, and to assess potential $H\beta$ residual contamination and the continuum level. We do not impose any further restrictions based on the shape (the presence of asymmetries) of the [OIII] lines. After all these cuts, 1978 spectra remained to constitute our "clean 1" sample. Using this sample we obtain mean $\Delta\alpha/\alpha = (-0.9 \pm 2.6) \times 10^{-5}$. The results are very robust against

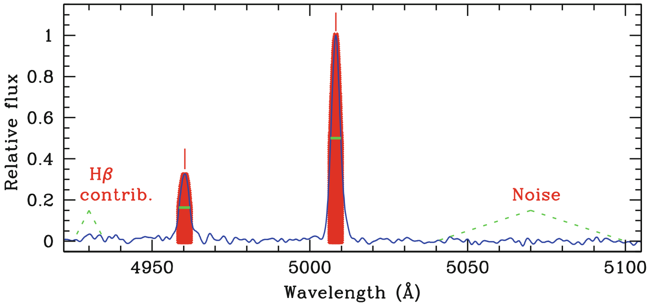

Fig. 1 Diagram showing the regions used to compute the centroids and relative fluxes, and the regions used to assess the $H\beta$ residual contamination and the noise in the continuum

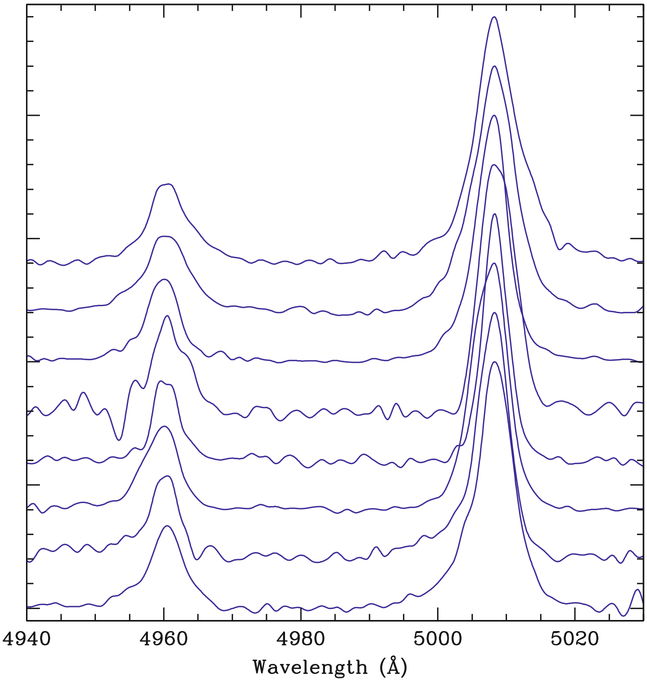

Fig. 2 The spectral region around the [OIII] doublet for some of the objects included in the clean sample (see the main text). The spectra have been normalized with respect to the peak of the main [OIII] line

the precise constraints; for instance selecting only those spectra with $SNR > 30$ in the peak of the [OIII] lines, we obtain mean $\Delta\alpha/\alpha = (1.9 \pm 2.6) \times 10^{-5}$. Figure 2 shows examples of the region centered around the [OIII] doublet of some spectra randomly chosen from this sample. The figure shows that for a given spectrum both lines are well above the noise level, and have similar shapes. A few of them show the presence of asymmetries probably related to the kinematics of the cloud or the presence of multiple clouds. The distributions of centroids of each member of the doublet show similar rms (0.78 Å); this indicates the absence of significant distortions in the estimation of the position of the 4959 Å line due to the relative proximity of the Hβ line. The distribution of the wavelength separation between the centroids of both lines has a rms of 0.11 Å; this indicates that the main factor broadening the distribution of the centroids of the [OIII] lines are absolute spectral shifts which mostly reflect the kinematics ($\leq$150 km s^{-1}) of the narrow line clouds where the [OIII] originates.

Method 2: The emission lines of OIII (4959 and 5008), and Hβ (narrow and broad components) were simultaneously modeled by a single Gaussian each. The wavelength position of each line of the [OIII] doublet was directly estimated as the central position of the corresponding Gaussian. In principle this seems a very simple description of the line profiles, and in many cases produces a poor fit to the data. However, in practice the method takes advantage of the expected similar shape for both lines of the doublet, and removes most of the contribution of Hβ in the spectral region of the [OIII] doublet. After removing the most extreme cases of poor fits, the results are quite consistent and robust. Selecting those spectra in which each of the [OIII] lines are described by Gaussian with peak amplitudes > 20 the level of the continuum noise, and σ within the range 1.4-3.0 Å (rest frame of the [OIII] 5008 line) there were 1568 spectra ('clean sample 2') from which we obtained $\Delta\alpha/\alpha = (+2.4 \pm 2.5) \times 10^{-5}$.

3 Results and Discussion

The results obtained by both methods are compatible and quite similar. Both estimations are also compatible with the local value.

To analyze the value of $\Delta\alpha/\alpha$ as a function of redshift (or look-back time) we compute the mean values in redshift interval. This is shown in Fig. 3 and Table 1. The bins in redshift have been built in order to include approximately the same number (175) of spectra each. Although none of the bins shows a statistical significant departure from zero, the largest deviation is at the 2.7σ level in the bin

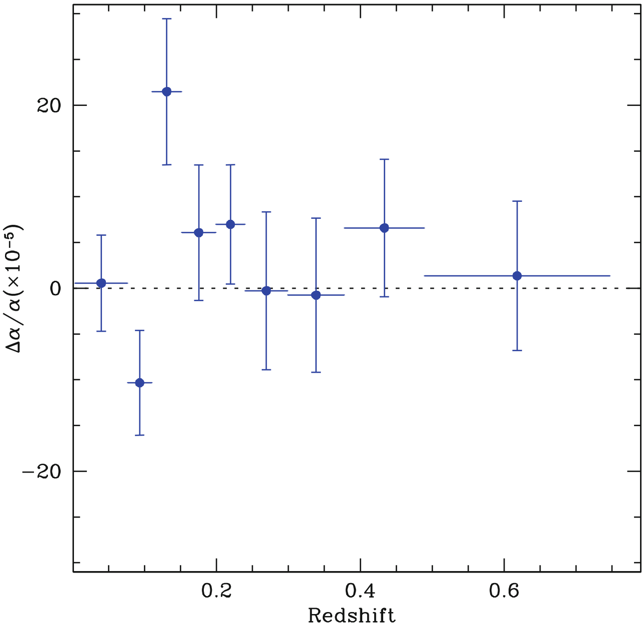

Fig. 3 $\Delta\alpha/\alpha$ vs. redshift. Each bin contains the contribution of ~175 spectra

Table 1 $\Delta\alpha/\alpha$ at different redshifts

Redshift	$\Delta\alpha/\alpha$ (10^{-5})	1-σ errors
$0.003 - 0.076$	$+0.6$	5.2
$0.076 - 0.110$	-10.3	5.7
$0.110 - 0.152$	$+21.5$	8.0
$0.152 - 0.199$	$+6.1$	7.4
$0.199 - 0.240$	$+7.0$	6.5
$0.240 - 0.300$	-0.3	8.6
$0.300 - 0.378$	-0.8	8.4
$0.378 - 0.490$	$+6.6$	7.5
$0.490 - 0.747$	$+1.4$	8.2

which corresponds to the range in redshift 0.110-0.152. That bin includes those cases in which one of the [OIII] lines lies near the spectral position of the atmospheric OI line. To check for the possible influence of some residual of the OI line in the estimation of the centroids of [OIII] in that range of redshift, we built a new sample excluding those spectra having redshifts in which any of the [OIII] lines is closer than 15 Å to the spectral position of the atmospheric OI line. This new constraint removes 59 spectra. The overall results on $\Delta\alpha/\alpha$ do not change much ($\Delta\alpha/\alpha = (+0.6 \pm 2.4) \times 10^{-5}$) using this new clean sample, but the significance of the departure from zero in the corresponding bin in redshift (0.107-0.161) is largely reduced ($\Delta\alpha/\alpha = (+7.0 \pm 5.8) \times 10^{-5}$).

The range in redshift spanned by our sample corresponds to a maximum look-back time of 6.6 Gyr, and a mean of 3.0 Gyr. Following Bahcall et al., the mean rate of possible changes is $1/ < t > \Delta\alpha/\alpha = (+0.7 \pm 0.7) \times 10^{-14}$ yr^{-1}. A linear fit of $\Delta\alpha/\alpha$ with respect to look-back time gives a slope of $(0.2 \pm 1.6) \times 10^{-14}$ yr^{-1}. All these numbers as a whole do not show any significant evidence of change in $\Delta\alpha/\alpha$ with redshift.

The analysis by Bahcall et al. [3] based on the Early Data Release of SDSS, comprised a sub sample of the sample analyzed in this paper, so it is worth making a comparison of both studies. There are 38(10) shared objects between the sample of these authors and our raw(clean) sample. The distribution of $\Delta\alpha/\alpha$ obtained from objects in common between our raw sample and the Bahcall et al. sample is similar, while the rms of $\Delta\alpha/\alpha$ from our clean sample is 0.5×10^{-3}, slightly better than the sample of Bahcall et al. (0.7×10^{-3}). So, although the method and criteria for selecting the samples are quite different from each other, both studies agree quite well. The much higher number of spectra used in this study (1568 in our clean sample) with respect to the 42 objects in the Bahcall et al. sample would allow us in principle to reduce the uncertainty by a factor $\sqrt{1568/42} = 6.1$. The result presented by Bahcall et al. is $(0.7 \pm 1.4) \times 10^{-4}$, and therefore our result ($\Delta\alpha/\alpha = (+2.4 \pm 2.5) \times 10^{-5}$) improves the sensitivity by a factor $\sim$5, which agrees with statistical expectations.

Acknowledgements We have used the following online databases: Sloan Digital Sky Survey (http://www.sdss.org/), the Atomic Line List (http://www.pa.uky.edu/~peter/atomic/), and NIST Atomic Spectra Database (http://physics.nist.gov/PhysRefData/ASD).

References

1. J.N. Bahcall and E.E. Salpeter, Astrophys. J. 142 (1965) 1677
2. J.N. Bahcall, W.L.W. Sargent and M. Schmidt, Astrophys. J, 149 (1967) 211
3. J.N. Bahcall, C.L. Steinhardt and D. Schlegel, Astrophys. J, 600 (2004) 520
4. H. Chand, et al., A&A 430 (2005) 47
5. E. García-Berro, J. Isern and Y.A. Kubyshin, A&AR, 14 (2007) 113
6. D. Grupe, A.K. Pradhan and S. Frank, AJ, 130 (2005) 355
7. K. Ichikawa and M. Kawasaki, Phys. Rev. D65 (2002) 123511
8. N. Kanekar et al., Mod. Phys. Lett. A23 (2008) 2711.
9. S.J. Landau and C. Simeone, 487 (2008) 857
10. S.A. Levshakov et al., A&A 434 (2005) 827
11. S.A. Levshakov et al., A&A, 466 (2007) 1077
12. P. Molaro et al., Eur. Phys. J. Special Topics 163 (2008) 173
13. M.T. Murphy, J.K. Webb and V.V. Flambaum, MNRAS 345 (2003) 609
14. M. Nakashima, R. Nagata and J. Yokoyama, P. Th. Ph. 120 (2008) 1207
15. J.-P. Uzan, Rev. Mod. Phys. 75 (2003) 403
16. J.K. Webb et al., Phys. Rev. Lett. 82 (1999) 884

Current State of $m_p/m_e = \mu$ Measurements Versus Cosmic Time

Rodger I. Thompson

Abstract This article reviews the current state of measurement of $\mu = M_P/M_e$ the ratio of the proton to electron mass in the early universe. Unlike the contribution in this volume by Webb et al. on the value of the fine structure constant α there is no current evidence for a different value of μ in the early universe at the one part in 10^5 level Astronomical observations provide a determination of this ratio in the early universe through observations of molecular absorption and emission lines in distant objects. Observations of molecular hydrogen in distant damped Lyman Alpha clouds provide a measurement of μ at a time when the universe was only 20% of its present age. The limit of $\Delta\mu/\mu \leq 10^{-5}$ produces a significant observational constraint on quintessence theories for the evolution of the universe and Super Symmetric theories of elementary particles. It is expected that future work will improve this limit even further. It would be very difficult to reconcile a constant value of μ with a varying value of α.

1 Introduction

In this article the measurements of $\mu = M_P/M_e$, the ratio of the proton to electron mass, in the early universe are discussed. As such, the extensive laboratory work on the values of the fundamental constants at the present time will not be reviewed. All of the measurements described here involve molecular spectra. It was pointed out 35 years ago [16] that molecular spectra are sensitive to the value of μ and could provide a measurement of that fundamental constant in the early universe.

R.I. Thompson
Steward Observatory, University of Arizona, Tucson, AZ 85721, USA
e-mail: rit@email.arizona.edu

C. Martins and P. Molaro (eds.), *From Varying Couplings to Fundamental Physics*,
Astrophysics and Space Science Proceedings, DOI 10.1007/978-3-642-19397-2_9,

2 How μ Affects Molecular Spectra

As first described in [16] the spectra of molecules are sensitive to the value of μ. In basic terms the rotational energy is directly proportional to μ through the moment of inertia and the vibrational energy is proportional to the square root of μ as in a classical harmonic oscillator. An interesting alternative derivation of the dependence is given in [15]. The dependence of the rotational and vibrational energies on the value of μ means that emission and absorption lines of molecules between different rotational and vibrational states will have different shifts that can not be mimiced by a redshift. [16] suggested that the absorption lines of molecular hydrogen observed in high redshift Damped Lyman Alpha (DLA) clouds would provide a measure of μ in the early universe. At that time, however, there were not large enough telescopes, sensitive enough spectrometers, and accurately enough measured line wavelengths to carry out the measurement. Currently all three requirements are present and a vigorous observation and analysis program is being carried out, primarily on the Lyman and Werner Bands of H_2.

Unfortunately the electronic energy levels of molecules are little affected by the value of μ therefore the shifts in energy of the rotational and vibrational levels is diluted by the much larger electronic energy levels that are observed in the Lyman and Werner bands that are redshifted from the ultraviolet into the optical bands. A much more sensitive measurement can be made on pure rotational transitions that for most molecules lie in the radio region. Even more sensitive are the inversion transitions of molecules like ammonia where the nitrogen nucleus passes through the plane of the three hydrogen atoms. There have been several programs to observe both the rotational and inversion spectra of molecules at radio frequencies as described later in this review. To date they have been limited to redshifts below 1 and have other difficulties as explained in the review of those observations.

3 Nature of the Lyman and Werner Bands

The transitions that are normally observed in molecular hydrogen for the measurement of μ are the Lyman and Werner band electronic transitions. Their rest wavelengths are in the 900 to 1000 angstrom region so they are only observable from the ground at redshifts above 2. The transitions are observed in absorption in the spectra of quasars with intervening DLAs containing molecular hydrogen. The absorptions are from the ground electronic and vibrational state from the first few low lying rotational states, usually from rotational quantum numbers $J = 0$-4. A schematic (not to scale) depiction of the energy level diagram for the Lyman and Werner bands is given in Fig. 1. Note that the selection rules for these transitions are that $\Delta J = -1,0,1$ for the rotational levels and that Δv can be any integer for the vibrational levels. All observed absorption lines from DLA systems are from the ground electronic and vibrational states with rotational energies usually of $J = 0$ through 4.

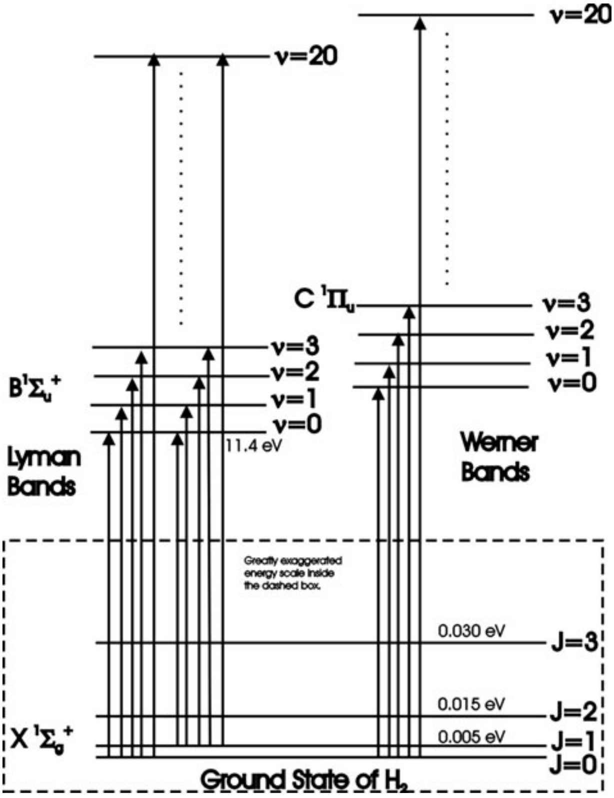

Fig. 1 The energy level diagram for the Lyman and Werner band of H_2. Note the overlap between low vibrational level Werner lines and high vibrational level Lyman lines

4 Sensitivity Constants

[19] were the first to formally introduce the sensitivity factor K_i for each line i which is defined as

$$K_i = \frac{d \ln \lambda_i}{d \ln \mu} = \frac{\mu}{\lambda_i}\frac{d\lambda_i}{d\mu} = -\frac{\mu}{\nu_i}\frac{d\nu_i}{d\mu} \tag{1}$$

With this definition the observed wavelength λ_i is related to the rest wavelength λ_0 by

$$\lambda_i/\lambda_0 = (1+z)(1+K_i\Delta\mu/\mu) \tag{2}$$

Since the signal to noise of the observed spectra are generally not high enough to fit the expected pattern of $\Delta\mu$ induced redshifts,traditionally data analysis has been carried out by linear fitting of the reduced redshift ζ of each line versus the sensitivity factor K_i for the lines. The reduced redshift ζ is defined by

$$\zeta = \frac{z_i - z_Q}{1+z_Q} = \Delta\mu/\mu K_i \tag{3}$$

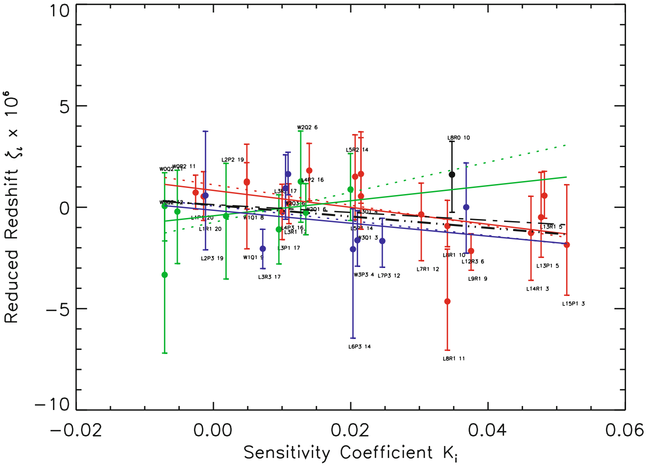

Fig. 2 The reduced redshift versus sensitivity factor plot for Q0347-383. The symbols are color coded according to the rotational level of the lower electronic state. J = 0(black), J = 1(red), J = 2(green), J = 3(blue). The solid line is the weighted fit and the dotted line is the unweighted fit to the individual J levels. The thick dash 3 dot line is the weighted fit and the thick dash dot line the unweighted fit to all J levels combined. The transitions are labeled with the last number being the order. The orders are the observed orders with the true order number being 126 minus the printed number

where z_i is the measured redshift of the individual lines and z_Q is the intrinsic redshift of the DLA system containing the H_2 lines. Figure 2 gives an example of such a plot taken from [17]. Note that the fitted slope in this type of plot is $\Delta\mu/\mu$. Also notice that the reduced redshift axis is multiplied by 10^6.

5 Advantages and Disadvantages of H_2 Observation to Determine μ

As might be expected there is a mix of advantages and disadvantages in using H_2 observations to determine the value of μ.

5.1 H_2 Advantages

A distinct advantage of using H_2 absorption lines to measure μ is that there are many different lines that have the same ground state. This reduces the possibility that different kinematics in areas of different excitation temperature can mimic changes in μ. In practice, however, lines from all of the ground rotational states are generally grouped into one data set to increase the signal to noise of the fitting. Since the sensitivity constants are not strongly dependent on the ground rotational state this should not produce a systematic affect. If μ is different than the present value the signal should be present in lines from all of the ground states and not present if there is no change in μ.

A second advantage of using H_2 is that the wavelengths of the transitions are known to high accuracy [10, 18]. Most of the lines have wavelengths determined to a few parts in 10^8 or better. This allows an accurate determination of the delta wavelength values of the observed lines from their rest wavelengths. Significant improvement over the present accuracy of measurement will, however, require even more accurate wavelength measurements.

A final advantage of H_2 is that the presence of two electronic transition systems, the Lyman and Werner bands, mixes together lines with high and low sensitivity constants. The superposition of the systems reduces the effect of wavelength errors. In principle it should be possible to use the low sensitivity constant lines as wavelength calibrators for the high sensitivity lines. Unfortunately the low number of observed lines has not allowed that exercise. At higher resolution, where the number of instrumental blends is reduced, this may be a viable method.

5.2 H_2 Disadvantages

A key disadvantage of H_2 is that very few DLAs contain sufficient H_2 densities to produce observable spectra. At this time only about a dozen systems have been examined. If a low resolution signature of DLAs likely to contain H_2 could be developed then the vast treasury of SDSS quasar spectra could be searched and candidates followed up a high spectral resolution. To date no reliable signature has been identified.

Unfortunately the Lyman and Werner H_2 bands lie in the Lyman alpha forest of atomic absorption lines. This means that most of the H_2 absorption lines are overlaid or blended with Lyman forest lines. Selection of lines suitable for analysis is a difficult and often subjective task. Different authors using the same data set usually make different selections of line for analysis which makes quantitative comparison of results difficult.

Finally since the observed transitions are electronic the large electronic energies dilute the changes in energy of the rotational and vibrational levels. Typical sensitivity constants are on the order of 10^{-2} as opposed to on the order of 1 for pure rotational transitions. This means that wavelength accuracies must exceed the desired accuracy in $\Delta\mu/\mu$ by a factor of 100. As mentioned above, this may be the ultimate limitation on the accuracy of the method.

6 Results to Date

There have been a relatively limited number of sources used to determine values for μ in the early universe. In some cases the same spectra have been analyzed by different groups using different data reduction and analysis techniques, which

Table 1 Listing of known μ measurements at high redshift

Object	Z_{abs}	$\Delta\mu/\mu$	Reference
Q0528−250	2.811	$\leq 2 \times 10^{-4}$	Foltz et al. (1988)
Q0528−250	2.811	$\leq 7 \times 10^{-4}$	Cowie & Songaila (1995)
Q0528−250	2.811	$\leq 2 \times 10^{-4}$	Potekhin et al. (1998)
Q0528−250	2.811	$1.4 \pm 3.9 \times 10^{-6}$	King et al. (2008)
Q1232+082	2.339	$1.44 \pm 1.14 \times 10^{-4}$	Ivanchik[a] et al. (2002)
Q1232+082	2.339	$1.32 \pm 0.74 \times 10^{-4}$	Ivanchik[a] et al. (2002)
Q0347−382	3.0249	$5.8 \pm 3.4 \times 10^{-5}$	Ivanchik[a] et al. (2002)
Q0347−382	3.0249	$1.22 \pm 0.73 \times 10^{-4}$	Ivanchik[a] et al. (2002)
Q0347−382	3.0249	$5.02 \pm 1.82 \times 10^{-5}$	Ivanchik et al. (2003)
Q0347−382	3.0249	$1.47 \pm 0.83 \times 10^{-5}$	Ivanchik et al. (2005)
Q0347−382	3.0249	$-0.5 \pm 3.6 \times 10^{-5}$	Ubachs & Reinhold (2004)
Q0347−382	3.0249	$2.06 \pm 0.79 \times 10^{-5}$	Reinhold et al. (2006)
Q0347−382	3.0249	$2.06 \pm 0.79 \times 10^{-5}$	Ubachs et al. (2006)
Q0347−382	3.0249	$0.82 \pm 0.74 \times 10^{-5}$	King et al. (2008)
Q0347−382	3.0249	$2.1 \pm 1.4 \times 10^{-5}$	Went & Reimers (2008)
Q0347−382	3.0249	$-2.8 \pm 1.6 \times 10^{-5}$	Thompson et al. (2009)
Q0405−443	2.5947	$2.78 \pm 0.88 \times 10^{-5}$	Ubachs et al. (2007)
Q0405−443	2.5947	$2.78 \pm 0.88 \times 10^{-5}$	Reinhold et al. (2006)
Q0405−443	2.5947	$2.11 \pm 1.39 \times 10^{-5}$	Ivanchik et al. (2005)
Q0405−443	2.5947	$1.01 \pm 0.62 \times 10^{-5}$	King et al. (2008)
Q0405−443	2.5947	$0.055 \pm 1.0 \times 10^{-5}$	Thompson et al. (2009)
J2123−0050	2.059	$0.56 \pm 0.62 \times 10^{-5}$	Malec et al. (2010)

[a] Ivanchik et al. (2002) used two different H_2 wavelength lists, hence the double listing for each source.

produced differing results. The single claim for a change in μ came from [14] based on spectra of Q0347-383 and Q0405-443 taken with UVES on the VLT. Subsequent analysis of the same data by [5], [21] and [17], however, found a null result. Ref. [17] attributed the positive claim by [14] as due to errors in the UVES pipeline wavelength calibration. These errors were removed in subsequent versions of the pipeline production process. The sources and results of the various μ measurements known to the author are compiled in 6. Note that most authors have combined the results from more than one source to produce limits on the change in μ that are somewhat smaller than the limits on individual sources. A consensus limit on the change in μ would appear to be $\Delta\mu/\mu \leq 10^{-5}$ although [5] claim a limit of $\Delta\mu/\mu = (2.6 \pm 3) \times 10^{-6}$ which is strongly influenced by their result for Q0528-250.

7 Systematic Errors

Precision measurements such as those required to evaluate the value of μ are very susceptible to systematic errors therefore an understanding of the sources of systematic error is extremely important in the study of fundamental constants. In the following section we review some of the possible systematic errors that could affect μ measurements.

7.1 Wavelength Calibration

A distinct advantage of using H_2 for μ measurements is that each line has a unique sensitivity constant and therefore a unique shift which can not be mimiced by an error in redshift. In practice, however, the data quality is not good enough to match the particular pattern of shifts. We therefore try to compute a slope in the reduced redshift versus sensitivity factor plot. The sensitivity factors increase with increasing vibrational quantum number of the upper state. The lower state is always in the ground vibrational state. As the upper level vibrational quantum number increases the energy of the upper state increases and the wavelength of the transition decreases. This produces a correlation between wavelength and sensitivity factor with the sensitivity factor increasing as the wavelength decreases. A systematic error in the wavelength scale will then mimic a change in μ. This is probably the source of the previously claimed positive detection of a change in μ.

7.1.1 Lyman and Werner Line Mix

The possibility of a linear wavelength error mimicing a change in μ is partially mitigated by the mixing of Lyman and Werner lines in the spectra. The higher electronic energy of the upper state of the Werner series produces shorter wavelength transitions with low vibrational quantum number and hence lower sensitivity factors at the same wavelengths as the high sensitivity lines of the Lyman series as shown in Figure 2. Mixtures of high sensitivity and low sensitivity lines can occur over short wavelength intervals where systematic wavelength calibration errors have a much smaller effect. A particular wavelength interval for Q0347-383 is shown in Figure 3.

In [17] the Werner lines were compared to their nearest Lyman lines in terms of wavelength and the histogram of the differences in redshift Δz was plotted. Both Q0347-383 and Q0405-443 have roughly an equal number of lines of positive and negative Δz values as shown in figure 4. This is the result of a new analysis that improves on the figure from [17] where all of the Q0347-383 values were negative.

7.2 Errors in Rest Wavelengths of H_2

Although the accuracy of the H_2 rest wavelengths from [18] exceeds our current accuracy of astronomical measurements, improvement by a factor of 10 to 1 part in 10^6 may require more accurate wavelength measurements. Typical sensitivity

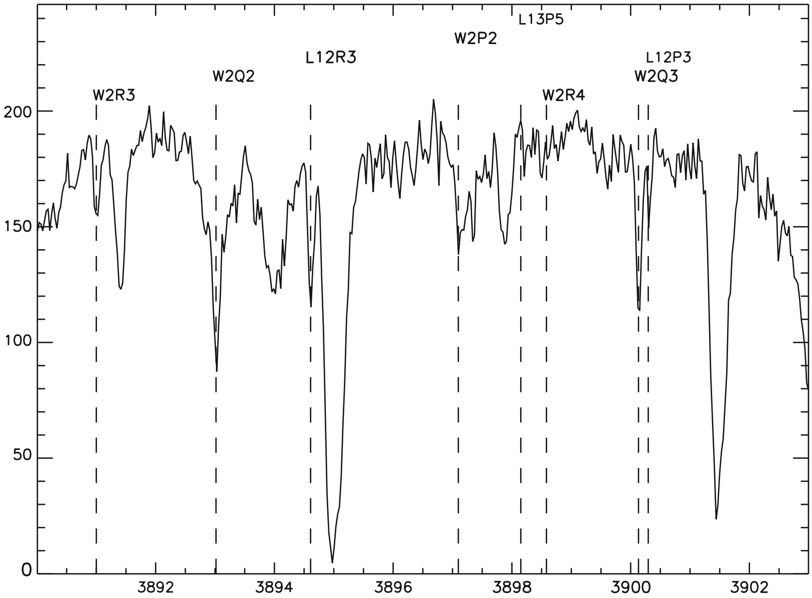

Fig. 3 A region of the spectrum of Q0347-383 that has a mixture of low sensitivity Werner (W) and high sensitivity Lyman lines (L). The number after the W or L designator is the vibrational quantum number of the upper state. Note that W2R3, L12R3, W2Q3 and L12P3 all have identical ground states

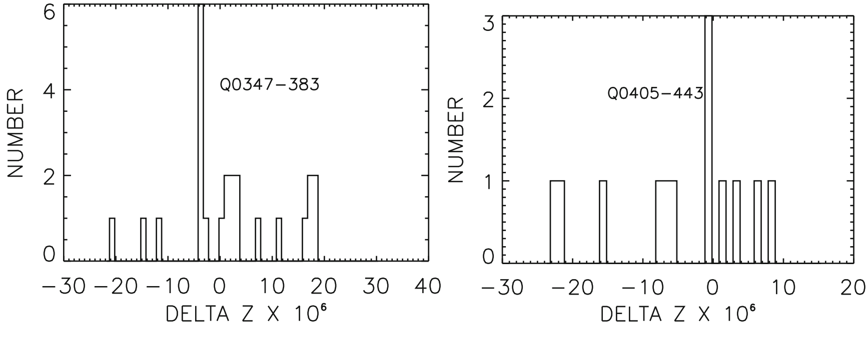

Fig. 4 Histogram of the delta redshift between each of the Werner band lines and their adjacent Lyman band lines for Q0347-383. A positive value means that the Lyman line had a higher redshift than the Werner line. Note that this is the delta redshift not the delta reduced redshift defined in Equation 3

constants have values on the order of 0.02 and the typical wavelength errors are about a few time 10^{-8}. Since the accuracy of measurements of $\Delta\mu/\mu$ scale as the wavelength error divided by the sensitivity factor, this leads to errors on the order of 10^{-6}, which leaves no room in the error budget for other sources of error.

7.3 *Errors in the Sensitivity Factor*

Errors in $\Delta\mu/\mu$ scale directly as errors in the sensitivity factors. If there is a systematic error in the sensitivity factors they will lead to the same order of error in $\Delta\mu/\mu$. A possibility is a systematic error in the sensitivity factor with increasing vibrational quantum number. This could lead to a false positive in the measurement. Since sensitivity factors are calculated from our knowledge of molecular physics a systematic error in the approximations used in the calculation could produce a systematic sensitivity factor error.

7.4 *Instrumental Errors*

In most spectrometers used to measure $\Delta\mu/\mu$ the light path of light from the observed object is not the same as the light path of the calibration lamp light. Differences in angle between the principal rays of the object and calibration light can introduce systematic wavelength differences even if the rest wavelengths of the calibration lines are accurately known. Similarly temporal instability on the time scale of the difference in time between object and calibration source observation can introduce errors.

8 Radio Measurements

Radio measurements of molecular radio rotational and inversion transitions have two important advantages over optical measurements of electronic transitions. The first is that the sensitivity factors for radio transitions are of the order of unity for rotational transitions and can be as high as 4 to 5 for inversion transitions. Inversion transitions are when one nucleus passes through the plane of the other nuclei. An example is when the nitrogen nucleus in ammonia passes through the plane defined by the three hydrogen nuclei. The sensitivity factor for this transition is 4.46. The second advantage is that the frequency measurement of the lines can be made to very high accuracy with $\Delta\nu/\nu \leq 10^{-7}$. Unfortunately there are also disadvantages with radio molecular spectroscopy. In general there are usually not multiple transitions from the same ground state to provide a comparison or reference value so that a shift in μ can be separated from the redshift. Commonly transitions of other molecules are used as the reference. This introduces the possibility that different kinematics between the two molecular species could mimic a change in μ. A second disadvantage is that to date all of the observations of radio transitions to measure μ have been at redshifts significantly less than 1. This provides a smaller time baseline and may invoke another problem. In some theories of dark energy than invoke a rolling scaler field coupled to the value of μ the values of the fundamental constants only roll in the matter dominated era [1] and become locked in to their present day value in the dark energy era of expansion. All of the radio μ measurements to date are in the dark energy dominated era.

8.1 Radio Results

[3] and [12] have observed the inversion spectrum of ammonia in B0218+357 with limits on $\Delta\mu/\mu$ of $(0.6 \pm 1.9) \times 10^{-6}$ and $< 1.8 \times 10^{-6}$ respectively at a redshift of 0.68466. In the first case CO molecular transitions provided the reference wavelengths and HCN and HCO^+ served as the reference transitions in the second case. There is no guarantee that the kinematics of these molecules are identical. However, the lack of a detected shift makes the result significantly more credible than the detection of a shift would have been.

A more controversial claim is that the value of μ varies spatially in our own galaxy [9, 11]. This claim is made based on the observation of the inversion transitions of ammonia along various sight lines in our galaxy. The reference transitions in this case are transitions in HC_3N and N_2H^+. The $\Delta\mu/\mu$ values found in this study are $(4-14) \times 10^{-8}$ which correspond to velocities on the order of 10 to a few 10s of km/sec. It is interesting to compare this reference with the recent claim [20] of a spatial variation of the fine structure constant α at high redshift.

9 The Future

Just as recent advances in telescopes and spectrometers have ushered in the age of serious measurements of the fundamental constants in the early universe it is expected that the next generation of telescopes and spectrometers will make similar advances. On the immediate horizon is the Potsdam Echell Polarimetric Spectroscopic Instrument (PEPSI) on the Large Binocular Telescope (LBT) at a resolution of 300,000. Also on the horizon is the CODEX spectrometer scheduled for the Extremely Large Telescope (ELT). Both of these instruments will significantly increase both the spectral resolution and the signal to noise of H_2 spectra at high redshift. To take advantage of this increased power we must also support laboratory measurements of molecular spectra in both the Ultra Violet, for redshifted optical observations, and radio transition frequencies for observations with radio telescopes. Recent breakthroughs of observations of radio molecular emission spectra at high redshift holds hope of observing radio absorption spectra in cold Damped Lyman Alpha systems at high redshift.

The constraints, and claimed shifts, on the values of the fundamental constants is having an impact on the parameter space available to theories of dark energy and alternatives, such as Super Symmetry, to the standard model of particle physics. It is important for these disciplines to work hand in hand for future progress in this exciting field. of elementary particles.

Acknowledgements The author would like to acknowledge partial support for attendance at the JENAM conference by the Centro de Astrofisica da Universidade do Porto. He would also like to thank his colleagues, Jill Bechtold, John Black, Daniel Eisenstein, Xiaohui Fan, Rob Kennicutt, Carlos Martins, Xavier Prochaska, Yancey Shirley and Wim Ubachs for their many contributions and discussions.

References

1. J.D. Barrow, H.B. Sandvik and J. Magueijo, Phys. Rev. D65 (2002) 063504.
2. L.L. Cowie and A. Songaila, Astrophys. J., 453 (1995) 596.
3. V.V. Flambaum and M.G. Kozlov, Phys. Rev. Lett. 98 (2007) 240801.
4. C.B. Foltz, F.H. Chaffee and J.H. Black, Astrophys. J. 324 (1988) 267.
5. J.A.King et al., Phys. Rev. Lett. 101 (2008) 251304.
6. A.V. Ivanchik et al., Astronomy Letters, 28 (2002) 423 (page 483 in Asttronomicheskii Zhurnal)
7. A.V. Ivanchik et al., APSS 283 (2003) 583.
8. A.V. Ivanchik, A. et al., A. Ap, 440 (2005) 45.
9. S.A. Levshakov, P. Molaro and M.G. Kozlov, arXiv:0808.0583v1
10. A.L. Malec et al., MNRAS 403 (2010) 1541.
11. P. Molaro, S.A. Levsahkov and M.G. Kozlov, Nuc. Phys. B (Proc. Suppl.) 194 (2009) 287.
12. M.T. Murphy et al., Science 320 (2008) 1611.
13. A.Y. Potekhin et al., Astrophys. J. 505 (1998) 523.
14. E. Reinhold et al., Phys. Rev. Lett. 96 (2006) 151101.
15. Shu, F.H. The Physics of Astrophysics Volume I Radiation, Mill Valley: University Science Books 1991, Chapt. 28.
16. R.I. Thompson, Astrophysical Letters 16 (1975) 3.
17. R.I. Thompson et al., Astrophys. J, 703 (2009) 1648.
18. W. Ubachs et al., Jour. Mol. Spec. 241 (2007) 155.
19. D. Varshalovich and D. Levshakov, JETP Letters 58 (1993) 231.
20. J.K. Webb et al., arXiv:1009.3907,v1
21. M. Wendt and D. Reimers, D. 2008, Eur. Phys. J. ST, 163 (2008) 197.

Robust Limit on a Varying Proton-to-Electron Mass Ratio from a Single H_2 System

M. Wendt and P. Molaro

Abstract The variation of the dimensionless fundamental physical constant $\mu = m_p/m_e$ can be checked through observation of Lyman and Werner lines of molecular hydrogen in the spectra of distant QSOs. Only few systems have been used for the purpose providing different results between the different authors. Our intention is to resolve the current controversy on variation of μ and devise explanations for the different findings. An analysis based on independent data sets of QSO 0347-383 is put forward and new approaches for some of the steps involved in the data analysis are introduced. Drawing on two independent observations of a single absorption system in QSO 0347-383 our detailed analysis yields $\Delta\mu/\mu = (15 \pm (9_{\mathrm{stat}} + 6_{\mathrm{sys}})) \times 10^{-6}$ at $z_{\mathrm{abs}} = 3.025$. Current analyses tend to underestimate the impact of systematic errors. This work presents alternative approaches to handle systematics and introduces methods required for precision analysis of QSO spectra available in the near future.

1 Introduction

The Standard Model of particle physics (SMPP) is very successful and its predictions are tested to high precision in laboratories around the world. SMPP needs several dimensionless fundamental constants, such as coupling constants and mass ratios, whose values cannot be predicted and must be established through experiment [5]. Our confidence in their constancy stems from laboratory experiments over human time-scales but variations might have occurred over the 14 billion-year history of the Universe while remaining undetectably small today. Indeed, in theoretical models seeking to unify the four forces of nature, the coupling constants vary naturally on cosmological scales.

M. Wendt
Hamburger Sternwarte, Universität Hamburg, Gojenbergsweg 112, 21029 Hamburg, Germany
e-mail: mwendt@hs.uni-hamburg.de

P. Molaro
INAF-Osservatorio Astronomico di Trieste, Via G. B. Tiepolo 11, 31143 Trieste, Italy

C. Martins and P. Molaro (eds.), *From Varying Couplings to Fundamental Physics*,
Astrophysics and Space Science Proceedings, DOI 10.1007/978-3-642-19397-2_10,

The proton-to-electron mass ratio, $\mu = m_p/m_e$ has been the subject of numerous studies. The mass ratio is sensitive primarily to the quantum chromodynamic scale. The Λ_{QCD} scale should vary considerably faster than that of quantum electrodynamics Λ_{QED}. As a consequence, the secular change in the proton-to-electron mass ratio, if any, should be larger than that of the fine structure constant. This makes μ a very interesting target to search for possible cosmological variations of the fundamental constants.

The present value of the proton-to-electron mass ratio is $\mu = 1836.15267261(85)$ [12]. Laboratory experiments by comparing the rates between clocks based on hyperfine transitions in atoms with a different dependence on μ restrict the time-dependence of μ at the level of $(\dot{\mu}/\mu)_{t_0} = (1.6 \pm 1.7) \cdot 10^{-15}\ \mathrm{yr}^{-1}$ [1].

A probe of the variation of μ is obtained by comparing rotational versus vibrational modes of molecules as first suggested by Thompson [19]. The method is based on the fact that the wavelengths of vibro-rotational lines of molecules depend on the reduced mass, M, of the molecule. The energy difference between two consecutive levels of the rotational spectrum of a diatomic molecule scales with the reduced mass M, whereas the energy difference between two adjacent levels of the vibrational spectrum is proportional to $(M)^{1/2}$:

$$\nu = c_e + \frac{c_v}{\mu^{1/2}} + \frac{c_r}{\mu}, \tag{1}$$

with c_e, c_v and c_r as constant factors for the electronic, vibrational and rotational contribution, respectively. Consequently, by studying the Lyman and Werner transitions of molecular hydrogen we may obtain information about a change in μ. The observed wavelength λ_{obs} of any given line in an absorption system at the redshift z differs from the local rest-frame wavelength λ_0 of the same line in the laboratory according to the relation

$$\lambda_{\mathrm{obs},i} = \lambda_{0,i}(1+z)(1+K_i\frac{\Delta\mu}{\mu}), \tag{2}$$

where K_i is the sensitivity coefficient of the ith component computed theoretically for the Lyman and Werner bands of the H_2 molecule. Using this expression, the cosmological redshift of a line can be distinguished from the shift due to a variation of μ.

This method was used to obtain upper bounds on the secular variation of the electron-to-proton mass ratio from observations of distant absorption systems in the spectra of quasars at several redshifts. The quasar absorption system towards QSO 0347-383 was first studied by us using high-resolution spectra obtained with the very large telescope/ultraviolet-visual echelle spectrograph (VLT[1]/UVES[2]) commissioning data we derived a first stringent bound at $(-1.8 \pm 3.8) \cdot 10^{-5}$ [9].

---

[1] Very Large Telescope at the European Southern Observatory (ESO).

[2] UV-Visual Echelle Spectrograph.

Subsequent measures of the quasar absorption systems of QSO 0347-382 and QSO 1232+082 provided hints for a variation $(2.4 \pm 0.6) \cdot 10^{-5}$, i.e. at 3.5 σ [7, 18, 21]. The new analysis used additional high-resolution spectra and updated laboratory data of the energy levels and of the rest frame wavelengths of the H_2 molecule.

However, more recently [8, 20, 22] re-evaluated data of the same system and report a result in agreement with no variation. The more stringent limits on $\Delta\mu/\mu$ have been found at $\Delta\mu/\mu = (2.6 \pm 3.0_{\mathrm{stat}}) \times 10^{-6}$ from the combination of three H_2 systems [8] and a fourth one have provided $\Delta\mu/\mu = (+5.6 \pm 5.5_{\mathrm{stat}} \pm 2.7_{\mathrm{sys}}) \times 10^{-6}$ [13].

This work is motivated on one side by the use of a new data set available in the ESO data archive and previously overlooked and by numerous findings of different groups that partially are in disagreement witch each other. A large part of these discrepancies reflect the different methods of handling systematic errors. Evidently systematics are not yet under control or fully understood. We try to emphasize the importance to take these errors, in particular calibration issues, into account and put forward some measures adapted to the problem.

In the following we will concentrate on the single H_2 system observed towards QSO 0347-383 to trace the proton-to-electron mass ration μ at high redshift ($z_{\mathrm{abs}} = 3.025$). We intend to reach a robust estimation of the achievable accuracy with current data by comparing independent observation runs.

2 Data

2.1 Observations

QSO 0347-383 is a bright quasar (V $\approx$ 17.3) with z_{em} 3.23, which shows a Damped Lyman α system at $z_{abs} = 3.0245$. The hydrogen column density is of N(H I) = $5 \cdot 10^{20}$ cm^{-2} with a rich absorption-line spectrum [9]. The $z_{abs} = 3.025$ DLA exhibits a multicomponent velocity structure. There are at least two gas components: a warm gas seen in lines of neutral atoms, H and low ions, and a hot gas where the resonance doublets of C IV and Si IV are formed. In correspondence of the cool component molecular hydrogen was first detected by [10] who identified 88 H_2 lines.

All works on QSO 0347-383 are based on the same UVES VLT observations[3] in January 2002 (see [7]). The data used therein were retrieved from the VLT archive along with the MIDAS based UVES pipeline reduction procedures. The slit width was 0.8″. The grating angle for the QSO 0347-383 observations had a central wavelength of 4300 Å. The images are 2×2 binned. The 9 spectra were recorded during 3 nights with an exposure time of 4500 seconds each. Additional observational parameters are described in [7]. The above mentioned data was recently

---

[3] Program ID 68.A-0106.

Table 1 Journal of the observations

Date	Time	λ	Exp(sec)	Seeing (arcsec)	airmass	S/N (mean)
2002-01-13	03:42:54	390	4800	1.7	1.5	20
2002-01-14	02:13:24	390	4800	1.0	1.2	28
2002-01-15	00:43:32	437	4800	0.96	1.0	67
2002-01-18	03:25:04	437	4800	1.63	1.4	49
2002-01-24	02:20:14	437	4800	1.07	1.7	29
2002-02-02	01:33:58	390	4800	0.5	1.2	37

carefully reduced again [20]. This work, however, is only in part based on this original reduced data.

Here we take into account additional observational data of QSO 0347-383 acquired in 2002 at the same telescope but not previously analyzed.[4]

The UVES observations comprised of 6 × 80 minutes-exposures of QSO 0347-383 on several nights, thus adding another 28.800 seconds of exposure time. The journal of these observations as well as additional information is reported in Table 1. Three UVES spectra were taken with the DIC1 and setting 390+580 nm and three spectra with DIC2 and setting 437+860, thus providing blue spectral ranges between 320-450 and 373-500 nm respectively. We note that QSO 0347-383 has no flux below 370 nm due to the Lyman discontinuity of the $z_{abs} = 3.023$ absorption system. The slit width was set to $1''$ for all observations providing a Resolving Power of $\approx 40\,000$. The different slit widths and hence different resolutions of the observation runs pose no problem since all data are analyzed separately during the fit. The seeing was varying in the range between $0.5''$ to $1.4''$ as measured by DIMM but generally is better than this at the telescope. The CCD pixels were binned by 2×2 providing an effective 0.027-0.030 Å pixel, or 2.25 km s^{-1} at 400 nm along dispersion direction.

2.2 Reduction

The standard UVES pipeline has been followed for the data reduction. This includes sky subtraction and optimal extraction of the spectrum. Typical residuals of the wavelength calibrations were of $\approx$0.5 mÅ or $\approx$40 m s^{-1} at 400 nm. The spectra were reduced to barycentric coordinates and air wavelengths have been transformed to vacuum by means of the dispersion formula [3]. Proper calibration and data reduction will be the key to detailed analysis of potential variation of fundamental constants. The influence of calibration issues on the data quality is hard to measure and the magnitude of the resulting systematic error is under discussion. The measurements rely on detecting a pattern of small relative wavelength shifts between different transitions spread throughout the spectrum. Normally, quasar spectra are

---

[4] Program ID 68.B-0115(A).

calibrated by comparison with spectra of a hollow cathode thorium lamp rich in unresolved spectral lines. However several factors are affecting the quality of the wavelength scale. The paths for ThAr light and quasar light through the spectrograph are not identical thus introducing small distortions between ThAr and quasar wavelength scales. In particular differences in the slit illuminations are not traced by the calibration lamp. Since source centering into the slit is varying from one exposure to another this induce an offset in the zero point of the scales of different frames which could be up to few hundred of m s^{-1}. In section 3.1 we provide an estimate of these offsets which result of a mean offset of 168 m s^{-1} as well as a procedure to avoid this problem. Laboratory wavelengths are know with limited precision which is varying from line to line from about 15 m s^{-1} of the better known lines to more than 100 m s^{-1} for the more poorly known lines [16, 20]. However, this is the error which is reflected in the size of the residuals of the wavelength calibration. Iodine cell based calibration cannot be applied directly in the case of QSO 0347-383 since at a redshift of $z \approx 3$ all observed lines lie outside the range of Iodine lines which cover about 5 000-6 000 Å. Additionally, at the given level of continuum contamination due to Lyman-α forest at such redshifts a super-imposed spectrum of the iodine cell is not desirable.

Effects of this kind have been investigated at the Keck/HIRES spectrograph by comparing the ThAr wavelength scale with one established from I2-cell observations of a bright quasar [6]. They found both absolute and relative wavelength offsets in the Keck data reduction pipeline which can be as large as 500 - 1 000 m s^{-1} for the observed wavelength range. Such errors would correspond to $\Delta\lambda \approx 10-20$ mÅ and exceed by one order of magnitude presently quoted errors [20]. Examination of the UVES spectrograph at the VLT carried out via solar spectra reflected on asteroids with known radial velocity showed no such dramatic offsets being less than $\approx$100 m s^{-1} [14] but systematic errors at the level of few hundred m s^{-1} have been revealed also in the UVES data by comparison of relative shifts of lines with comparable response to changes of fundamental constants [2]. These examples well show that current $\Delta\mu/\mu$-analysis based on quasar absorption spectra at the level of a few ppm enters the regime of calibration induced systematic errors. While awaiting a new generation of laser-comb-frequency calibration, today's efforts to investigate potential variation of fundamental physical constants require factual consideration of the strong systematics.

We note also that the additional observations considered here were taken for other purposes and the ThAr lamps are taken during daytime, which means several hours before the science exposures and likely under different thermal and pressure conditions. However, in the present work we bypass the possibility of different zero points of the different images via the seldom case of independent observations. Instead of co-adding all the spectra we compute first the global velocity shifts between the spectra with the procedure described in the following section and we also utilize the whole uncertainties coming from the wavelength accuracies as part of the analysis procedure.

3 Preprocessing

3.1 Relative Shifts of the 15 Spectra

Prior to further data processing the reduced spectra are reviewed in detail. The first data set (henceforward referred to as set A) consists of nine separate spectra observed between 7th and 9th of January in 2002. The second set of 6 spectra (B) was obtained between January 13th and February 2nd in 2002.

Due to slit illumination effects and grating motions the individual spectra are subject to small shifts – commonly on sub-pixel level – in wavelength. These shifts will be particularly crucial in the process of co-addition of several exposures. To estimate these shifts all spectra were interpolated by a polynomial using *Neville's algorithm* to conserve the local flux (see Fig. 1). The resulting pixel step on average is $1/20$ of the original data. Each spectrum was compared to the others. For every data point in a spectrum the pixel with the closest wavelength was taken from a second spectrum. Their deviation in flux was divided by the quadratic mean of their given errors in flux. This procedure was carried out for all pixels inside certain selected wavelength intervals resulting in a mean deviation of two spectra. The second spectrum is then shifted against the first one in steps of $\sim$1.5 mÅ. The run of the discrepancy of two spectra is of parabolic nature with a minimum at the relative shift with the best agreement. Fig. 2 shows the resulting curve with a parabolic fit. In this exemplary case the second spectrum shows a shift of 6.2 mÅ in relation to the reference spectrum. The clean parabolic shape verifies the approach. The offsets between the exposures are relevant with a peak to peak excursion up to almost 800 m s^{-1}. The average deviation is 2.3 mÅ or 170 m s^{-1} at 400 nm. For further

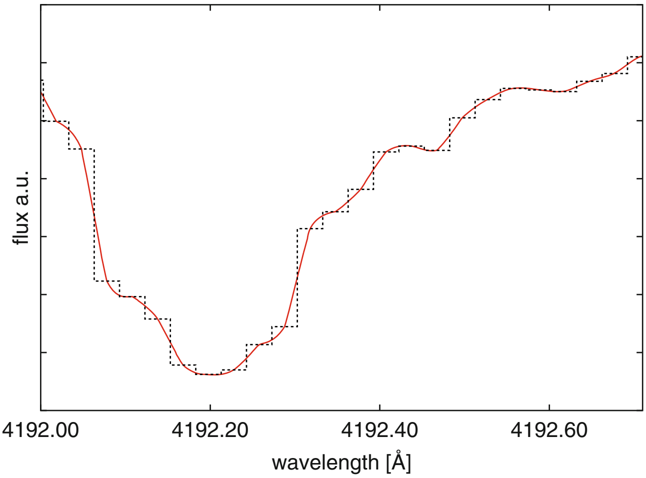

Fig. 1 Example region of the QSO 0347-383 spectrum showing the recorded flux (*red*) and its interpolation via a polynomial using *Neville's algorithm* to conserve the flux

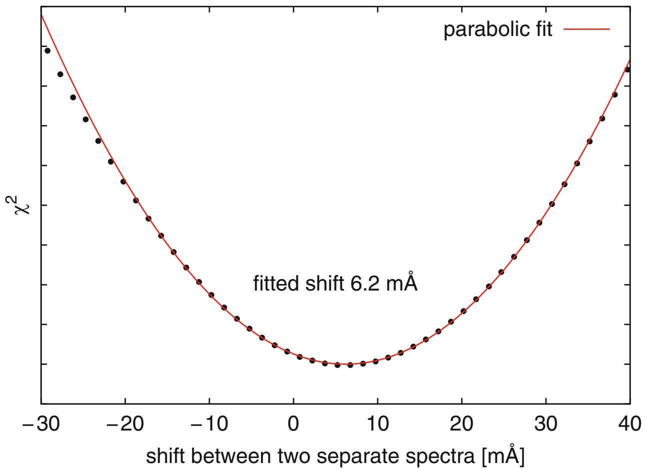

Fig. 2 Exemplary plot of the sub-pixel cross-correlation. The resulting shift is ascertained via parabolic fit. In this case the two spectra are in best agreement with a relative shift of 6.2 ± 0.5 mÅ

analysis in this paper all the 15 spectra are shifted to their common mean, which is taken as an arbitrary reference position. To avoid areas heavily influenced by cosmic events or areas close to overlapping orders only certain wavelength intervals were taken into account, namely the regions 3877-3886 Å, 3986-4027 Å, 4145-4175 Å and 4216-4240 Å.

3.2 Selection of Lines and Line Fitting

The selection of suitable H_2 features for the final analysis is rather subjective. As a matter of course all research groups cross-checked their choice of lines for unresolved blends or saturation effects. The decision whether a line was excluded due to continuum contamination or not, however, relied mainly on the expert knowledge of the researcher and was only partially reconfirmed by the ascertained uncertainty of the final fitting procedure. This work puts forward a more generic approach adapted to the fact that we have two distinct observations of the same object.

In this paper each H_2 signature is fitted with a single component. The surrounding flux is fit by a polynomial and the continuum is rectified accordingly. This approach is tested and verified in [22], however lines near saturated or steeply descending areas should be avoided. A selection of 52 (in comparison with 68 lines for that system in [8]) lines is fitted separately for each dataset of 9 (A) and 6 (B) exposures, respectively. In this selection merely blends readily identifiable or emerging from equivalent width analysis are excluded. Each rotational level is fitted with conjoined line parameters except for redshift naturally. A common column density

N and broadening parameter b corresponds to each of the observed rotational levels (in this case $J = 1, 2, 3$).

The data are not co-added but analyzed simultaneously via the fitting procedure introduced in [17]. In principle each set of parameters (line centroid, broadening parameter, column density, coefficients of the continuum polynomial) drawn from a large parameter space is tested in all individual spectra and judged by a weighted χ^2. The standard deviations of line positioning are provided by the diagonal elements of the scaled covariance matrix, a procedure described in detail in the above mentioned paper by Quast et al. and verified, i.e., in [22]. For each of the 52 lines there are two resulting fitted redshifts or observed wavelengths, respectively, with their error estimates. To avoid false confidence, the single lines are not judged by their error estimate but by their difference in wavelength between the two data sets in relation to the combined error estimate. Fig. 5 shows this dependency. The absolute offset $\Delta\lambda_{\text{effective}}$ to each other is expressed in relation to their combined error given by the fit:

$$\Delta\lambda_{\sigma\Sigma 1,2} = \frac{\Delta\lambda_{\text{effective}}}{\sqrt{\sigma_{\lambda_1}^2 + \sigma_{\lambda_2}^2}}. \tag{3}$$

Fig. 5 reveals notable discrepancies between the two datasets, the disagreement is partially exceeding the 5-σ level[5]. Since the fitting routine is known to provide proper error estimates [17, 22], the dominating source of error in the determination of line positions is due to systematic errors. This result indicates calibration issues of some significance at this level of precision. The comparison of two independent observation runs reveals a source of error that cannot be estimated by the statistical quality of the fit alone. For further analysis only lines that differ by less than 3 σ are taken into account. This criterion is met by 36 lines.

It is noteworthy that line selections of this absorption system by other groups diverge from each other by a large amount. King et al. processed a total of 68 lines [8]. By reconstructing the continuum flux with additionally fitted lines of atomic hydrogen they felt confident not to care about the relative position of the H_2 features next to the Lyman-α forrest. Fitting H_2 features as single lines, however, is affected by the surrounding flux and its nature as simulations have shown [22]. Thompson et al. [20] selected 36 lines for analysis of which differs from our semi-automatical choice of lines by almost 40%.

Hence, the different findings arise through in large parts independent analysis. Different approaches, line selections and in the end applied methods contribute to a more solid constraint on variation of fundamental constants. This variety is mandatory to understand contradicting findings, not only in case of the proton-to-electron mass ratio. Figure 3 plots the results of this paper, Ubachs et al. [21] and Thompson et al. [20], who published the individual fit parameters. The redshifts derived are of 3.0248969 (56), 3.0248988(29) and 3.0248987(61) for this paper, Ubachs et al.

---

[5] Lines fitted with seemingly high precision and thus a low error reach higher offsets than lines with a larger estimated error at the same discrepancy in λ_{obs}. Clearly the lower error estimates merely reflects the statistical quality of the fit, not the true value of the specific line position.

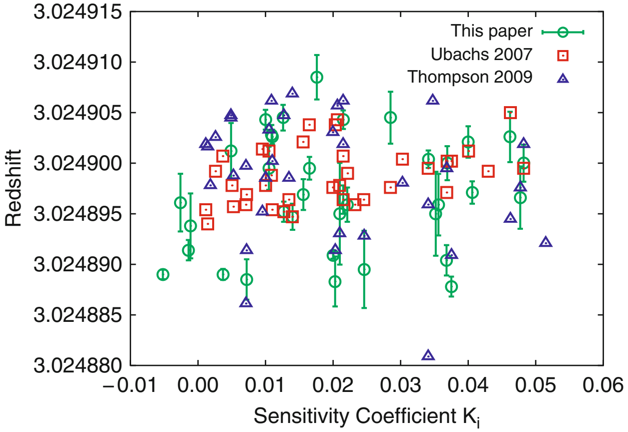

Fig. 3 2 Final results in redshift vs. sensitivity coefficient K_i for this paper (*circles*), Ubachs et al. [21] (*squares*) and Thompson et al. [20] (*triangles*)

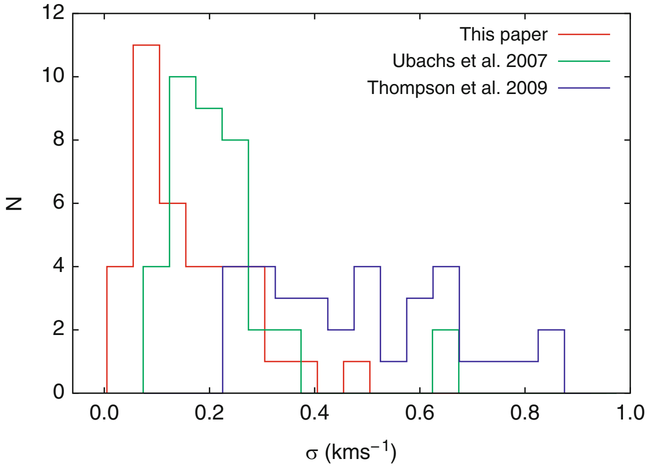

Fig. 4 Line positioning errors in km s^{-1} for this paper (*solid*), Ubachs et al. [21] (*red*) and Thompson et al. [20] (*blue*), binned to 50 m s^{-1}

(2007) and Thompson (2009) respectively, which is not surprising being based at least partially on the same data. All three analysis are based on the same source for sensitivity coefficients. The distribution of positioning errors for the mentioned works is illustrated in Figure 4. The three sets of measure show a significant scatter around the mean quite in excess of the error in line position which is suggestive of the presence of systematic errors.

The chosen $\Delta\lambda$ criterium for line selection permits evaluation of the self-consistency of a line positioning via fit for the involved data. While the availability

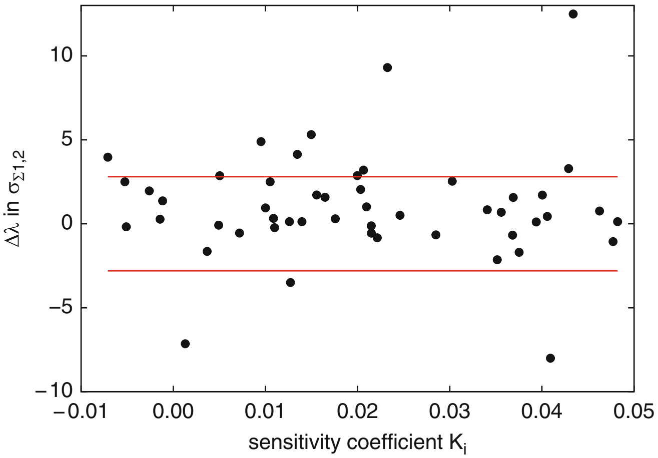

Fig. 5 Selection of 52 apparently reasonable lines to be fitted separately for each dataset of 9 and 6 exposures, respectively. Their absolute offset $\Delta\lambda_{\text{effective}}$ to each other is expressed in relation to their combined error given by the fit (see Eq. 1). The red lines border the 3σ domain

of two independent observations on short time scale is rather special, it illustrates one applicable modality to avoid relying on the fitting apparatus alone.

4 Results

For the final analysis the selected 36 lines are fitted in all 15 shifted, error-scaled spectra simultaneously. The result of an unweighted linear fit corresponds to $\Delta\mu/\mu = (15 \pm 16) \times 10^{-6}$ over the look-back time of ~ 11.5 Gyr for $z_{\text{abs}} = 3.025$. Fig. 6 shows the resulting plot.

The approach to apply an unweighted fit is a consequence of the unknown nature of the prominent systematics. The graphed scatter in redshift can not be explained by the given positioning errors alone. The likeliness of the data with the attributed error being linearly correlated is practically zero. The fit to the data is not self-consistent. For this work the calibration errors and the influence of unresolved blends are assumed to be dominant in comparison to individual fitting uncertainties per feature. For the following analysis the same error is adopted for each line. With an uncertainty in redshift of 1×10^{-6} we obtain: $\Delta\mu/\mu = (15 \pm 6) \times 10^{-6}$. However the goodness-of-fit is below 1 ppm and is not self consistent. The goodness of fit of a statistical model describes how well it fits a set of observations. A linear model with the given parameters does not represent the observed data sample very well. The apparent discrepancies between model and data including their errorbars shown in Figure 6 are extremely unlikely (below one part per million) to be chance fluctuations. Judging by that and Fig. 6, a reasonable error in observed redshift should at least be in the order of $4 - 5 \times 10^{-6}$. The weighted fit gives: $\Delta\mu/\mu = (15 \pm 14) \times 10^{-6}$.

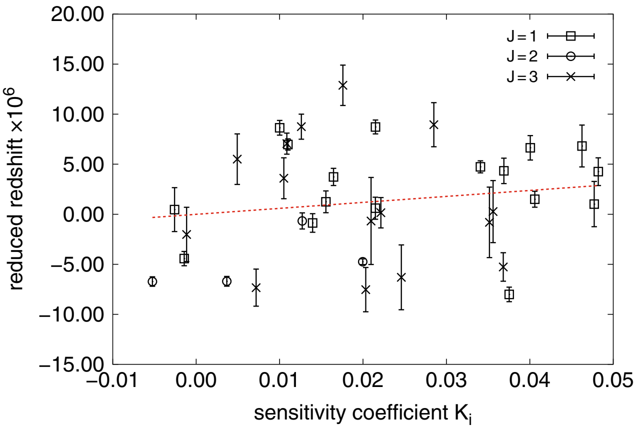

Fig. 6 The unweighted fit for QSO 0347-383 corresponds to $\Delta\mu/\mu = (15 \pm 16) \times 10^{-6}$. The error bars correspond merely to the fitting uncertainty in the order of 180 m s^{-1} on average. Note, that at such a high scatter $z_{Ki=0}$ differs from $\bar{z}$ by less than 1 σ_z

This approach is motivated by the goodness-of-fit test:
$Q(\chi^2|\nu)$ is the probability that the observed chi-square will exceed the value χ^2 by chance even for a correct model, ν is the number of degrees of freedom. Given in relation to the incomplete gamma function:

$$Q(\chi^2|\nu) = \Gamma\left(\frac{\nu}{2}, \frac{\chi^2}{2}\right). \tag{4}$$

Assuming a gaussian error distribution, Q gives a quantitative measure or the goodness-of-fit of the model. If Q is very small for some particular data set, then the apparent discrepancies are unlikely to be chance fluctuations that would be expected for a gaussian error distribution. Much more probably either the model is wrong or the size of the measurement errors is larger than stated. However, the chi-square probability Q does not directly measure the credibility of the assumption that the measurement errors are normally distributed. In general, models with $Q < 0.001$ can be considered unacceptable. In this case the model is given and hence the low probability is due to underestimated errors in the data. Solely for given errors of ≈300 m s^{-1}, corresponding to $\approx 4 \times 10^{-6}$ in redshift for QSO 0347-383 the goodness-of-fit parameter Q exceeds 0.001. The scale of the error appears to be ≈ 300 m $s^{-1}$to achieve a self-consistent fit to the data.

For the data on QSO 0347-383 this corresponds to an error in the observed wavelength of roughly 4mÅ, which is notably larger than the estimated errors for the individual line fits which ranges from 0.5 mÅ to 6.5 mÅ with an average of 2.5 mÅ (≈180 m s^{-1}). The systematic error contributes an uncertainty of about 2 mÅ on average. The immediate calibration errors are in the order of 50 m s^{-1} for set B and presumably slightly larger for set A.

The final result can be subdivided as: $\Delta\mu/\mu = \big(15 \pm (9_{\text{stat}} + 6_{\text{sys}})\big) \times 10^{-6}$.

The comparably high scatter in Figure 6 can partially be attributed to the approach to fit single H_2 components with a polynomial fit to the continuum. In special cases, contaminated flux bordering a H_2 signature can introduce additional uncertainty in positioning therefore checks for self-consistency and systematics are of utmost importance.

The determination of the different errors involved is on a par with the actual result.

We believe that this result represents the limit of accuracy that can be reached with the given data set and the applied methods for analysis. The presented method yields a null result. The recent work by Thompson et al. [20] stated $\Delta\mu/\mu = (-28 \pm 16) \times 10^{-6}$ for a weighted fit based on the same system in QSO 0347-383. The therein stated error reflects the statistical uncertainty alone.

Note, that the given systematics of 2.7ppm for Keck/HIRES data given in [13] are in first approximation estimated by the observed $\sim$500 m s^{-1} peak-to-peak intra-order value reduced according to the number of molecular transitions observed, i.e. $\sim$500m s$^{-1}/\sqrt{93} \approx 52$m s^{-1}.

This work proposes to take alternative approaches into account when operating that close to the limits of several involved systems. The presented method was applied to the known QSO 0347-383 data for two main reasons:

- As an example to put forward alternative strategies.
- A stand-alone determination of $\Delta\mu/\mu$ based on QSO 0347-383 to back up current null-results and consequential constraints.

4.1 Uncertainties in the Sensitivity Coefficients

At the current level of precision, the influence of uncertainties in the sensitivity coefficients K_i is minimal. It will be of increasing importance though when wavelength calibration can be improved by pedantic demands on future observations. Eventually Laser Frequency Comb calibration will allow for practically arbitrary precision and uncertainties in the calculations of sensitivities will play a role. Commonly the weighted fits neglects the error in K_i.

Effective analysis in the future involves consideration of the error budget of the sensitivity coefficients. The χ^2 merit function for the generic case of a straight-line fit with errors in both coordinates is given by:

$$\chi^2(a,b) = \sum_{i=0}^{N-1} \frac{(y_i - a - bx_i)^2}{\sigma_{yi}^2 + b^2\sigma_{xi}^2} \tag{5}$$

and can be solved numerically with valid approximations (Lybanon [11]).

At the current level even an error in K_i of about 10% merely has an impact on the error estimate in the order of a few 10^{-6}, as resulted from simulations. The factual errors are expected to be in the order of merely a few percent (see [21]), yet they might contribute to the precision of future analysis.

Alternatively the uncertainties in K_i can be translated into an uncertainty in redshift via the previously fitted slope:

$$\sigma_{z_i\,\text{total}} = \sigma_{z_i} + b \times \sigma_{K_i} \qquad \text{with} \qquad b = (1 + z_{\text{abs}})\frac{\Delta\mu}{\mu}. \tag{6}$$

The results of this ansatz are similar to the fit with errors in both coordinates and in general this is simpler to implement.

Another possibility is to apply a gaussian error to each sensitivity coefficient and redo the normal fit multiple times with alternating variations in K_i. Again, the influence on the error-estimate is in the order of 1 ppm. The different approaches to the fit allow to estimate its overall robustness as well.

4.2 Individual Line Pairs

$\Delta\mu/\mu$ can also be obtained by using merely two lines that show different sensitivity towards changes in the proton-to-electron mass ratio. Another criterion is their separation in the wavelength frame to avoid pairs of lines from different ends of the spectrum and hence in particular error-prone. Several tests showed that a separation of $\Delta\lambda \leq 110$ Å and a range of sensitivity coefficients $K_1 - K_2 \geq 0.02$ produces stable results that do not change any further with more stringent criteria. Pairs that cross two neighboring orders ($\sim$ 50Å) show no striking deviations either. Fig. 7 graphs the different values for $\Delta\mu/\mu$ derived from 52 line pairs that match the aforementioned criteria. Note, that a single observed line contributes to multiple pairs. The gain in statistical significance by this sorting is limited as pointed out by

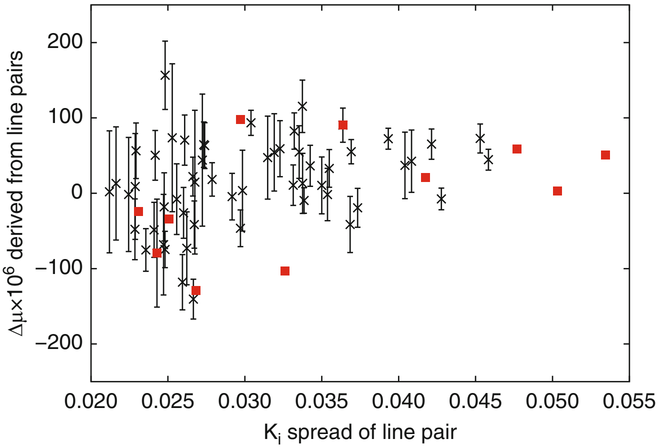

Fig. 7 $\Delta\mu/\mu$ derived from individual line pairs (52) which are separated by less than 110 Å and show a difference in sensitivity of more then 0.02. The errorbars reflect the combined positioning error of the two contributing lines. The weighted fit corresponds to $\Delta\mu/\mu = (6 \pm 12) \times 10^{-6}$. The *filled squares* graph 11 line pairs, selected to give the largest difference in sensitivity ($\geq$ 0.02) towards variation in μ

Molaro et al. [15]. Their average value yields $\Delta\mu/\mu = 6 \pm 12 \times 10^{-6}$. The scatter is then related to uncertainties in the wavelength determination which is mostly due to calibration errors. The standard error is 8×10^{-6}.

The approach to use each observed line only once in the analysis is plotted in Fig. 7 as filled squares. The pairs to derive $\Delta\mu/\mu$ from were constructed by grouping the line with the highest sensitivity value together with the line corresponding to the lowest value for K_i and so on with the remaining lines. The distance in wavelength space between the two lines was no criterium and it ranges from 20 Å to 590 Å. Without reutilization of lines, 11 pairs with a coverage in sensitivity of $\Delta\mathrm{K}_i \geq 0.02$ were found.

Evidently the usage of lines with comparably large distances in the spectrum has no influence on the results.

Acknowledgements We are thankful for the support from the Collaborative Research Centre 676 and for helpful discussions on this topic with D. Reimers, S.A. Levshakov, P. Petitjean and M.G. Kozlov.

References

1. S. Blatt et al., Phys. Rev. Lett.100 (2008) 14.
2. M. Centurión, P. Molaro, P. and S. Levshakov, arXiv 0910.4842.
3. B. Edlén, Metrologia 2 (1966) 71.
4. V.V. Flambaum and M.G. Kozlov, Phys. Rev. Lett.98 (2007) 24.
5. H. Fritzsch, arXiv:0902.2989
6. K. Griest et al., ApJ708 (2010) 158.
7. A. Ivanchik et al., ApJ440 (2005) 45.
8. J.A. King, J.K. Webb, M.T. Murphy and R.F. Carswell, Phys. Rev. Lett.101 (2008) 251304.
9. S.A. Levshakov, M. Dessauges-Zavadsky, S. D'Odorico and P. Molaro, MNRAS333 (2002) 373.
10. SS.A. Levshakov, M. Dessauges-Zavadsky, S. D'Odorico and P. Molaro, ApJ565 (2002) 696.
11. M. Lybanon, AJP 52 (1984) 22.
12. P.J. Mohr and B.N. Taylor, Rev. Mod. Phys. 72 (2000) 351.
13. A.L. Malec et al., arXiv: 1001.4080
14. P. Molaro et al., A&A481 (2008) 559.
15. P. Molaro, D. Reimers, I.I. Agafonova and S.A. Levshakov, EPJ 163 (2008) 173.
16. M.T. Murphy et al., MNRAS384 (2008) 1053.
17. R. Quast, R. Baade and D. Reimers, A&A431 (2005) 1167.
18. E. Reinhold et al. 2006, Phys. Rev. Lett. 96 (2006) 151101.
19. R.I. Thompson, Astrophys. Lett.16 (1975) 3.
20. R.I. Thompson et al., ApJ703 (2009) 1648.
21. W. Ubachs, R. Buning, K.S.E. Eikema and E. Reinhold, J. Molec. Spec. 241 (2007) 155.
22. M. Wendt and D. Reimers, EPJ 163 (2008) 197.

Searching for Chameleon-Like Scalar Fields

S.A. Levshakov, P. Molaro, M.G. Kozlov, A.V. Lapinov, Ch. Henkel, D. Reimers, T. Sakai, and I.I. Agafonova

Abstract Using the 32-m Medicina, 45-m Nobeyama, and 100-m Effelsberg telescopes we found a statistically significant velocity offset $\Delta V \approx 27 \pm 3$ m s^{-1} (1σ) between the inversion transition in NH_3(1,1) and low-J rotational transitions in N_2H^+(1-0) and HC_3N(2-1) arising in cold and dense molecular cores in the Milky Way. Systematic shifts of the line centers caused by turbulent motions and velocity gradients, possible non-thermal hyperfine structure populations, pressure and optical depth effects are shown to be lower than or about 1 m s^{-1} and thus can be neglected in the total error budget. The reproducibility of ΔV at the same facility (Effelsberg

---

S.A. Levshakov
Physical-Technical Institute, Polytekhnicheskaya Str. 26, 194021 St. Petersburg, Russia
e-mail: lev@astro.ioffe.rssu.ru

P. Molaro
INAF-Osservatorio Astronomico di Trieste, Via G. B. Tiepolo 11, 34143 Trieste, Italy
e-mail: molaro@oats.inaf.it

M.G. Kozlov
Petersburg Nuclear Physics Institute, 188300 Gatchina, Russia
e-mail: mgk@mf1309.spb.edu

A.V. Lapinov
Institute for Applied Physics, Uljanov Str. 46, 603950 Nizhny Novgorod, Russia
e-mail: lapinov@appl.sci-nnov.ru

Ch. Henkel
Max-Planck-Institut für Radioastronomie, Auf dem Hügel 69, D-53121 Bonn, Germany
e-mail: p220hen@mpifr-bonn.mpg.de

D. Reimers
Hamburger Sternwarte, Universität Hamburg, Gojenbergsweg 112, D-21029 Hamburg, Germany
e-mail: st2e101@hs.uni-hamburg.de

T. Sakai
Institute of Astronomy, The University of Tokyo, Osawa, Mitaka, Tokyo 181-0015, Japan
e-mail: sakai@ioa.s.u-tokyo.ac.jp

I.I. Agafonova
Physical-Technical Institute, Polytekhnicheskaya Str. 26, 194021 St. Petersburg, Russia
e-mail: ira@astro.ioffe.rssu.ru

C. Martins and P. Molaro (eds.), *From Varying Couplings to Fundamental Physics*,
Astrophysics and Space Science Proceedings, DOI 10.1007/978-3-642-19397-2_11,

telescope) on a year-to-year basis is found to be very good. Since the frequencies of the inversion and rotational transitions have different sensitivities to variations in $\mu \equiv m_{\rm e}/m_{\rm p}$, the revealed non-zero ΔV may imply that μ changes when measured at high (terrestrial) and low (interstellar) matter densities as predicted by chameleon-like scalar field models – candidates to the dark energy carrier. Thus we are testing whether scalar field models have chameleon-type interactions with ordinary matter. The measured velocity offset corresponds to the ratio $\Delta\mu/\mu \equiv (\mu_{\rm space} - \mu_{\rm lab})/\mu_{\rm lab}$ of $(26 \pm 3) \times 10^{-9}$ (1σ).

1 Introduction

This contribution sums up our results of differential measurements of the electron-to-proton mass ratio, $\mu = m_{\rm e}/m_{\rm p}$, carried out at the 32-m Medicina, 45-m Nobeyama, and 100-m Effelsberg telescopes [24–26, 29]. With high spectral resolution (FWHM $\sim$30-40 m s^{-1}), we observed narrow emission lines (FWHM < 200 m s^{-1}) of N-bearing molecules arising in cold and dense molecular cores of starless molecular clouds located in the Milky Way. The cores are characterized by low kinetic temperatures $T_{\rm kin} \sim 10$ K, gas densities $n \sim 10^4 - 10^5$ cm^{-3}, magnetic fields $B < 10$ μG, and ionization degrees $x_e \sim 10^{-9}$ [8]. The objective of this study is to probe the value of $\Delta\mu/\mu \equiv (\mu_{\rm space} - \mu_{\rm lab})/\mu_{\rm lab}$ which is predicted to be variable when measured at high (laboratory) and low (space) matter density environments [33].

A hypothetical variability of μ is thought to be due to the scalar fields – candidates to the dark energy carrier, – which are ultra-light in cosmic vacuum but possess an effectively large mass locally when they are coupled to ordinary matter by the so-called chameleon mechanism [16]. Several possibilities to detect chameleons were discussed in [2,7]. First laboratory experiments constraining these models have been recently carried out at Fermilab [42] and in the Lawrence Livermore National Laboratory [38].

A subclass of chameleon models considers the couplings of a scalar field to matter much stronger than gravitational and predicts that fundamental physical quantities such as elementary particle masses may depend on the local matter density, ρ, [33]. This means that a nonzero value of $\Delta\mu/\mu$ is to be expected for all interstellar clouds irrespective of their position and local matter density because the difference $\Delta\rho$ between the terrestrial environment in laboratory measurements and dense interstellar molecular clouds is extremely large, $\rho_\oplus/\rho_{\rm cloud} > 10^{10}$.

In the standard model (SM) of particle physics the dimensionless mass ratio $\mu = m_{\rm e}/m_{\rm p}$ defines the ratio of the electroweak scale to the strong scale since the mass of the electron $m_{\rm e}$ is proportional to the Higgs vacuum expectation value and the mass of the proton $m_{\rm p}$ is proportional to the quantum chromodynamics scale $\Lambda_{\rm QCD}$ [5]. The SM is extremely successful in explaining laboratory physics, but it has serious problems in astrophysics where it completely fails to explain dark matter and dark energy. There are many extensions of the SM including supersymmetry and different multidimensional theories which introduce new particles as possible candidates for the dark matter and additional scalar fields to describe the nature of dark energy.

A concept of dark energy with negative pressure appeared in physics long before the discovery of the accelerating universe through observations of nearby and distant Type Ia Supernovae [36, 37]. Early examples of dark energy in the form of a scalar field with a self-interaction potential can be found in reviews [3] and [35]. If masses of the elementary particles are affected by scalar fields, one can probe the dimensionless constant μ at different physical conditions by means of high precision spectral observations. Namely, since the inversion and rotational molecular transitions have different sensitivities to variations in μ [9], a nonzero $\Delta\mu/\mu$ causes an offset between the radial velocities ($\Delta V \equiv V_{\rm rot} - V_{\rm inv}$) of *co-spatially* distributed molecules, which, in turn, provide a measure of $\Delta\mu/\mu$. When the inversion line belongs to NH_3 we will herein call this procedure the ammonia method.

2 The Ammonia Method

NH_3 is a molecule whose inversion frequencies are very sensitive to changes of μ because of the quantum mechanical tunneling of the N atom through the plane of the H atoms. The inversion vibrational mode of NH_3 is described by a double-well potential, the first two vibrational levels lying below the barrier. The quantum mechanical tunneling splits these two levels into inversion doublets providing a transition frequency that falls into the microwave range [14].

The sensitivity coefficient to μ-variation of the NH_3 $(J, K) = (1, 1)$ inversion transition at 24 GHz is $Q_{\rm inv} = 4.46$ [9]. This means that the inversion frequency scales as

$$(\Delta\omega/\omega)_{\rm inv} \equiv (\tilde{\omega} - \omega)/\omega = 4.46(\Delta\mu/\mu), \tag{1}$$

where ω and $\tilde{\omega}$ are the frequencies corresponding to the laboratory value of μ and to an altered μ in a low-density environment, respectively. In other words, the inversion transition sensitivity to μ-variation is 4.46 times higher than that of molecular rotational transitions, where $Q_{\rm rot} = 1$ and thus,

$$(\Delta\omega/\omega)_{\rm rot} = \Delta\mu/\mu. \tag{2}$$

In astronomical spectra, any frequency shift $\Delta\omega$ is related to the radial velocity shift ΔV_r (V_r is the line-of-sight projection of the velocity vector)

$$\Delta V_r/c \equiv (V_r - V_0)/c = (\omega_{\rm lab} - \omega_{\rm obs})/\omega_{\rm lab}, \tag{3}$$

where V_0 is the reference radial velocity, c is the speed of light and $\omega_{\rm lab}$, $\omega_{\rm obs}$ are the laboratory and observed frequencies, respectively. Therefore, by comparing the apparent radial velocity $V_{\rm inv}$ for the NH_3 inversion transition with the apparent radial velocity $V_{\rm rot}$ for rotational lines originating in the same molecular cloud and moving with radial velocity V_0 with respect to the local standard of rest, one can find from Eqs. (1 – 3)

$$\Delta\mu/\mu = 0.289(V_{\rm rot} - V_{\rm inv})/c \equiv 0.289\Delta V/c. \qquad (4)$$

The velocity offset ΔV in Eq. (4) can be expressed as the sum of two components

$$\Delta V = \Delta V_\mu + \Delta V_n, \qquad (5)$$

where ΔV_μ is the shift due to μ-variation and ΔV_n is a random component caused by the inhomogeneous distribution of molecules, turbulent motions and velocity gradients, possible non-thermal hyperfine structure populations, pressure and optical depth effects, and instrumental imperfections (the so-called *Doppler noise*).

We will assume that the Doppler noise component has a zero mean, $\langle\Delta V_n\rangle =$ 0 km s^{-1}, and a finite variance, $Var(\Delta V_n) < \infty$. Then, the signal ΔV_μ can be estimated statistically by averaging over a data sample

$$\langle\Delta V\rangle = \langle\Delta V_\mu\rangle, \qquad (6)$$

and

$$Var(\Delta V) = Var(\Delta V_\mu) + Var(\Delta V_n). \qquad (7)$$

Equation (3) shows that the measurability of the signal $\langle\Delta V_\mu\rangle$ depends critically on the value of the Doppler noise, $Var(\Delta V_n)$. The Doppler noise can be reduced by the appropriate choice of molecular lines and molecular clouds.

To have similar Doppler velocity shifts the chosen molecular transitions should share as far as possible the same volume elements. NH_3 inversion transitions are usually detected in dense molecular cores ($n \sim 10^4 - 10^5$ cm^{-3}). Mapping of these cores in different molecular lines shows that there is a good correlation between the NH_3, N_2H^+, and HC_3N distributions [10, 15, 39, 41]. However, in some clouds NH_3 is not traced by HC_3N. The most striking case is the dark cloud TMC-1, where peaks of line emissions are offset by 7 arcmin [32]. Such a chemical differentiation together with velocity gradients within molecular cores is the main source of the unavoidable Doppler noise in Eq. (2). Additional scatter in the ΔV_n values may be caused by the different optical depths of the hyperfine structure transitions and by external electric and magnetic fields discussed below.

3 Selection of Targets

To minimize the Doppler noise component in Eq. (2), a preliminary selection of molecular cores suitable for the most precise measurements of the velocity offsets ΔV between rotational and inversion transitions is required. In general, molecular cores are not ideal spheres and when observed at high angular resolutions they frequently exhibit complex substructures. The line profiles may be asymmetric because of non-thermal bulk motions. Taking this into account, we formulate the following selection criteria:

1. The line profiles are symmetric and well described by a single-component Gaussian model. This selection increases the accuracy of the line center measurement. Multiple line components may shift the barycenter and affect the velocity difference between molecular transitions because, e.g., the ratio NH_3/HC_3N may vary from one component to another.
2. The line widths do not exceed greatly the Doppler width caused by the thermal motion of material, i.e., the non-thermal components (infall, outflow, tidal flow, turbulence) do not dominate the line broadening. This ensures that selected molecular lines correspond to the same kinetic temperature and arise co-spatially. For the molecules in question we require the ratio of the Doppler b-parameters to be $\beta = b(\mathrm{NH_3})/b(\mathrm{HC_3N})$ or $\beta = b(\mathrm{NH_3})/b(\mathrm{N_2H^+})$, be $\beta \geq 1$.
3. The spectral lines are sufficiently narrow ($b \sim 0.1-0.2$ km s^{-1}) for the hyperfine structure (hfs) components to be resolved. This allows us to validate the measured radial velocity by means of different hfs lines of the same molecular transition.
4. The spectral lines are not heavily saturated and their profiles are not affected by optical depth effects. The total optical depth of the NH_3 hf transitions is $\tau \leq 10$, i.e., the optical depth of the strongest hf component is $\lesssim 1$.

The kinetic temperature T_{kin}, and the nonthermal (turbulent) velocity dispersion, σ_{turb}, can be estimated from the line broadening Doppler parameters $b = \sqrt{2}\sigma_v$, of, e.g., the NH_3 (1,1) and HC_3N (2–1) lines. Here σ_v is the line of sight velocity dispersion of the molecular gas within a given cloud. If the two molecular transitions trace the same material and have the same nonthermal velocity component, σ_v is the quadrature sum of the thermal σ_{th} and turbulent σ_{turb} velocity dispersions. In this case a lighter molecule with a mass m_l should have a line width wider than with a heavier molecule with $m_h > m_l$.

For thermally dominated line widths ($\beta > 1$) and co-spatially distributed species we obtain the following relations (e.g., [10]):

$$T_{\mathrm{kin}} = m_l m_h(\sigma_l^2 - \sigma_h^2)/k(m_h - m_l), \tag{8}$$

and

$$\sigma_{\mathrm{turb}}^2 = (m_h\sigma_h^2 - m_l\sigma_l^2)/(m_h - m_l), \tag{9}$$

where k is Boltzmann's constant, and the thermal velocity dispersion σ_{th} is given by

$$\sigma_{\mathrm{th},i} = (kT_{\mathrm{kin}}/m_i)^{1/2}. \tag{10}$$

It should be noted that HC_3N is usually distributed in a volume of the molecular core larger than NH_3 since N-bearing molecules trace the inner core, whereas C-bearing molecules occupy the outer part [8]. Such a differentiation may cause a larger non-thermal component in the velocity distribution of HC_3N. If both molecules are shielded from external incident radiation, and the gas temperature mainly comes from heating by cosmic rays, then a formal application of Eqs. (5) and (9) to the apparent line widths provides a lower limit on $T_{\rm kin}$ and an upper limit on $\sigma_{\rm turb}$. In molecular cores where the only source of heating are the cosmic rays and the cooling comes from the line radiation mainly from CO, a lower bound on the kinetic temperature is about 8 K [11]. Thus, point 2 of the selection criteria requires $T_{\rm kin} \sim$ 8-10 K if both lighter and heavier molecules are distributed co-spatially.

4 Preliminary Results

In our preliminary single-pointing observations [25] we studied 41 molecular cores along 55 lines of sight. The $NH_3(1,1)$, $HC_3N(2\text{-}1)$, and $N_2H^+(1\text{-}0)$ transitions were observed with the 100-m Effelsberg, 32-m Medicina, and 45-m Nobeyama telescopes. The analysis of the total sample revealed large systematic shifts and 'heavy tails' of the ΔV probability distribution function resulting in a poor concordance between three mean values: the weighted mean $\langle \Delta V \rangle_{\rm W} = 27.4 \pm 4.4$ m s^{-1} (weights inversionally proportional to the variances), the robust redescending M-estimate $\langle \Delta V \rangle_{\rm M} = 14.1 \pm 4.0$ m s^{-1}, and the median $\Delta V_{\rm med} = 17$ m s^{-1}. The scatter in the ΔV values reflects effects related to the gas kinematics and the chemical segregation of one molecule with respect to the other (approximately 50% of the targets showed $\beta < 1$).

If we now consider molecular lines that fulfill the selection criteria, the sample size is $n = 23$, i.e. two times smaller than the total data set. Nevertheless, for this reduced sample we obtained better concordance: $\langle \Delta V \rangle_{\rm W} = 20.7 \pm 3.0$ m s^{-1}, $\langle \Delta V \rangle_{\rm M} = 21.5 \pm 2.8$ m s^{-1}, and $\Delta V_{\rm med} = 22$ m s^{-1}.

In this preliminary study we found 7 sources with thermally dominated motions which provide $\langle \Delta V \rangle_{\rm W} = 21.1 \pm 1.3$ m s^{-1}, $\langle \Delta V \rangle_{\rm M} = 21.2 \pm 1.8$ m s^{-1}, and $\Delta V_{\rm med} = 22$ m s^{-1}.

The most accurate result was obtained with the Effelsberg 100-m telescope: $\Delta V = 27 \pm 4_{\rm stat} \pm 3_{\rm sys}$ m s^{-1} (the value is slightly corrected in [26]). The systematic error in this estimate is due to uncertainties of the rest frequencies of the $HC_3N(2\text{-}1)$ hfs transitions since uncertainties of the $NH_3(1,1)$ hfs transitions are less than 1 m s^{-1} [21]. When interpreted in terms of the electron-to-proton mass ratio variation, this gives $\Delta\mu/\mu = (26 \pm 4_{\rm stat} \pm 3_{\rm sys}) \times 10^{-9}$.

Thus, for the first time we obtained an astronomical spectroscopic estimate of the relative change in the fundamental physical constant μ at the level of 10^{-9} which is 10^3 times more sensitive than the upper limits on $\Delta\mu/\mu$ obtained by the ammonia method from extragalactic observations [9, 13, 28, 30].

5 Mapping of Cold Molecular Cores in NH_3 and HC_3N Lines

In this section we report on new observations in which we measure ΔV at different positions across individual clouds in order to test the reproducibility of the velocity offsets in the presence of large-scale velocity gradients [26]. From the list of molecular cores observed with the Effelsberg 100-m telescope, we selected several objects with symmetric profiles of the $NH_3(1,1)$ and $HC_3N(2–1)$ hfs transitions. In these objects the line widths are thermally dominated, i.e., the parameter $\beta = \sigma_v(NH_3)/\sigma_v(HC_3N) \geq 1$. The chosen targets are the molecular cores L1498, L1512, L1517B, and L1400K, which have already been extensively studied in many molecular lines [1, 6, 22, 23, 40, 41].

The inversion line of ammonia $NH_3(1,1)$ at 23.694 GHz and the rotation line of cyanoacetylene $HC_3N(2–1)$ at 18.196 GHz were measured with a K-band HEMT (high electron mobility transistor) dual channel receiver, yielding spectra with an angular resolution of HPBW $\sim 40''$ in two orthogonally oriented linear polarizations. The measurements were carried out in frequency-switching mode using a frequency throw of 5 MHz. The backend was an FFTS (Fast Fourier Transform Spectrometer) operated with its minimum bandwidth of 20 MHz providing simultaneously 16 384 channels for each polarization. The resulting channel separations are 15.4 m s^{-1} for NH_3 and 20.1 m s^{-1} for HC_3N. We note, however, that the true velocity resolution is about two times lower, FWHM $\sim$ 30 m s^{-1} and 40 m s^{-1}, respectively [17]. The sky frequencies were reset at the onset of each scan and the Doppler tracking was used continuously to track Doppler shifts during the observations. Observations started by measuring the continuum emission of calibration sources and continued by performing pointing measurements toward a source close to the spectroscopic target. The calibration is estimated to be accurate to ±15% and the pointing accuracy to be higher than $10''$.

After corrections for the rounded frequencies, the individual exposures were co-added to increase the signal-to-noise ratio S/N. The spectra were folded to remove the effects of the frequency switch, and base lines were determined for each spectrum. The resolved hfs components show no kinematic substructure and consist of an apparently symmetric peak profile without broadened line wings or self-absorption features. The line parameters, such as the total optical depth in the transition τ (i.e., the peak optical depth if all hyperfine components were placed at the same velocity), the radial velocity V_{lsr}, the line broadening Doppler parameter b, and the amplitude A, were obtained through fitting of the *one-component* Gaussian model to the observed spectra:

$$T(v) = A \cdot [1 - \exp(-t(v))]\,, \tag{11}$$

with

$$t(v) = \tau \cdot \sum_{i=1}^{k} a_i \, \exp\left[-(v - v_i - V_{lsr})^2/b^2\right], \tag{12}$$

which transforms for optically thin transitions into

$$T(v) = A' \cdot \sum_{i=1}^{k} a_i \, \exp\left[-(v - v_i - V_{lsr})^2/b^2\right]. \tag{13}$$

The sum in (12) and (13) runs over the $k = 18$ and $k = 6$ hfs components of the $NH_3(1,1)$ and $HC_3N(2–1)$ transitions, respectively.

To test possible optical depth effects, we calculated two sets of the fitting parameters: (1) based on the analysis of only optically thin satellite lines with $\Delta F_1 \neq 0$, and (2) obtained from the fit to the entirety of the $NH_3(1,1)$ spectrum including the main transitions with $\Delta F_1 = 0$, which have optical depths $\tau \approx$ 1-2, as can be inferred from the relative intensities of the hfs components. The resulting V_{lsr} values for all targets were within the 1σ uncertainty intervals.

To control another source of errors caused by instrumental imperfections, we carried out *repeated* observations at 10 offset positions: two in L1498, L1517B, and L1400K, respectively, and four in L1512. The ΔV dispersion resulting from these repeated measurements is $\sigma(\Delta V) = 2.0$ m s^{-1}. This dispersion is lower than the calculated 1σ errors of the individual ΔV values, which ensures that we are not missing any significant instrumental errors at the level of a few m s^{-1}.

We also checked the velocity offsets ΔV obtained in our observations with the 100-m Effelsberg telescope in Feb 2009 and Jan 2010. The reproducibility of the velocity offsets at the same facility on a year-to-year base is very good for L1498, L1512 and L1517B (concordance within 1σ uncertainty intervals), except for L1400K where the central point is probably an outlier.

The comparison of the velocity dispersions determined from the $NH_3(1,1)$ and $HC_3N(2–1)$ lines did not show any significant variations with position within each molecular core. All data are consistent with thermally dominated line broadening. In particular, the following weighted mean values were determined: $\beta_{\rm L1498} = 1.24 \pm 0.03$, $\beta_{\rm L1512} = 1.32 \pm 0.05$, $\beta_{\rm L1517B} = 1.11 \pm 0.01$, and $\beta_{\rm L1400K} = 1.23 \pm 0.04$. The weighted mean values of the velocity dispersions for NH_3 range between $\sigma_{\rm L1512} = 78 \pm 1$ m s^{-1} and $\sigma_{\rm L1400K} = 86 \pm 1$ m s^{-1}, and for HC_3N between $\sigma_{\rm L1512} = 59 \pm 2$ m s^{-1} and $\sigma_{\rm L1517B} = 74 \pm 1$ m s^{-1}. This can be compared with the speed of sound inside a thermally dominated region of a cold molecular core that is defined as (e.g., [39])

$$v_s = (kT_{\rm kin}/m_0)^{1/2}\,, \tag{14}$$

where m_0 is the mean molecular mass. With $m_0 \approx 2.3$ amu for molecular clouds, one has $v_s \approx 60\sqrt{T_{\rm kin}}$ m s^{-1}, which shows that at the typical kinetic temperature of 10 K the nonthermal velocities are in general subsonic, and that the selected targets do represent the quiescent material at different distances from the core centers.

The gas temperature in the molecular cores was estimated from the apparent line widths using Eq. (5). For L1498 we obtained a lower limit on the kinetic temperature $T_{\rm kin} = 7.1 \pm 0.5$ K (average over 8 points), which is slightly lower than $T_{\rm kin} = 10$ K measured by a different method from the relative populations of the $(J, K) = (2, 2)$ and (1,1) levels of NH_3 described by the rotational temperature $T^{21}_{\rm R}$ [41]. For L1512 the temperature averaged over 11 points is $T_{\rm kin} = 9.6 \pm 0.6$ K, which is consistent with the value of 10 K. The kinetic temperatures in the L1517B core in all measured positions is well below 9.5 K – the value from [41], which means that the nonthermal velocity dispersions of NH_3 and HC_3N differ significantly and that both species *do not trace* the same material. The three scanned points in the L1400K core showed

$T_{\text{kin}} = 8.3 \pm 3.2$ K – close to the expected value of 10 K (measurements of the gas temperature in this core were not performed in previous studies).

We found that, in general, the spatial fluctuations of T_{kin} do not exceed a few kelvin implying uniform heating and absence of the localized heat sources. The kinetic temperature tends to rise with the distance from the core center, which is in line with the results from [41].

The radial velocity profiles along the different diagonal cuts toward the selected targets are shown in Figs. 3 and 4 in [26]. The diagonal cut in L1498 exhibits coherently changing velocities of $V_{lsr}(\text{HC}_3\text{N})$ and $V_{lsr}(\text{NH}_3)$ except one point at the core edge. The velocity gradient is small, $|\nabla V_{lsr}| \approx 0.5$ km s^{-1} pc^{-1}. This picture coincides with the previously obtained results based on observations of CO, CS, N_2H^+ and NH_3 in this core and was interpreted as an inward flow [22,41]. Taken together, all available observations classify L1498 as one of the most quiet molecular cores. Thus, we can expect that the Doppler noise (irregular random shifts in the radial velocities between different transitions) is minimal in this core.

In L1512, the $V_{lsr}(\text{NH}_3)$ and $V_{lsr}(\text{HC}_3\text{N})$ distributions are almost parallel (Fig. 1). The same kinematic picture was obtained for this core in [22] from observations of CS and NH_3 lines and interpreted as a simple rotation around the center. The velocity gradients derived from both NH_3 and HC_3N lines are similar, $\nabla V_{lsr} \approx 1.5$ km s^{-1} pc^{-1}, and consistent with the gradient based on N_2H^+ measurements in [4]. This means that NH_3, HC_3N, and N_2H^+ trace the same gas, so the Doppler shifts ΔV between them should be insignificant.

In the core L1517B, which is known to be very compact [22], we only observed the central $30'' \times 30''$ where the velocities of NH_3 and HC_3N along two perpendicular cuts do not change much: $\nabla V_{lsr}(\text{NH}_3) \approx 0.3$ km s^{-1} pc^{-1}, $\nabla V_{lsr}(\text{HC}_3\text{N}) \approx 0.8$ km s^{-1} pc^{-1}, and in the perpendicular direction $\nabla V_{lsr}(\text{NH}_3) \approx \nabla V_{lsr}(\text{HC}_3\text{N}) \approx -0.8$ km s^{-1} pc^{-1}. However, a wider area observation ($\approx 80'' \times 80''$) of this core

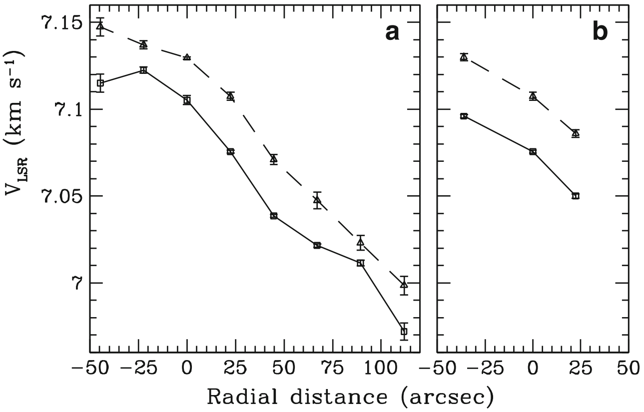

Fig. 1 Example of the line-of-sight velocities of NH_3 $(J, K) = (1, 1)$ (squares) and HC_3N $J = 2 - 1$ (triangles) at different radial distances along the main diagonal cut (panel **a**) and in the perpendicular direction (panel **b**) of the molecular core L1512. Shown are 1σ error bars. For more detail, see [26]

revealed an outward gas motion at the core periphery with a higher velocity gradient, $\nabla V_{lsr}(\mathrm{N_2H^+}) \approx 1.1$ km s^{-1} pc^{-1} [41], which is consistent with earlier results on NH_3 observations [12]. This can lead to an additional shift in the radial velocity of HC_3N line since, in general, the C-bearing molecules also trace a lower density gas component ($n < 10^4$ cm^{-3}) in the envelope of the molecular core. A higher nonthermal velocity dispersion of the HC_3N line than for NH_3 has already been mentioned above in regard to the temperature measurements in this core.

In L1400K we only observed three positions. Both molecules trace the same gradient of $\nabla V_{lsr} \approx 1.9$ km s^{-1} pc^{-1}, which is in line with $\nabla V_{lsr}(\mathrm{N_2H^+}) = 1.8 \pm 0.1$ km s^{-1} pc^{-1} derived in [4]. The mapping in different molecular lines in [41] revealed that L1400K deviates significantly from spherical symmetry and exhibits quite a complex kinematic structure. In particular, the distributions of N_2H^+ and NH_3 do not coincide: N_2H^+ has an additional component to the west of the center. This explains why [6] reported a blue-ward skewness for this core, $\theta = -0.42 \pm 0.10$, in the N_2H^+ (1–0) hfs profiles, whereas in our observations the $NH_3(1,1)$ hfs transitions are fully symmetric: at the central position the skewness of the resolved and single hfs component $F_1, F = 0, \frac{1}{2} \rightarrow 1, 1\frac{1}{2}$ of NH_3 is $\theta = -0.1 \pm 0.3$.

Our current measurements show very similar velocity shifts $\langle \Delta V \rangle_{\mathrm{M}} = 25.8 \pm 1.7$ m s^{-1} and 28.0 ± 1.8 m s^{-1} (M-estimates) for, respectively, the cores L1498 and L1512 where the Doppler noise reaches minimal levels. A higher shift $\langle \Delta V \rangle_{\mathrm{M}} = 46.9 \pm 3.3$ m s^{-1} is observed in the L1517B core – again in accord with its revealed kinematic structure, which allows us to expect a higher radial velocity for the HC_3N line. On the other hand, a lower value $\langle \Delta V \rangle_{\mathrm{M}} = 8.5 \pm 3.4$ m s^{-1} in L1400K may come from the irregular kinematic structure of the core center, which could increase the radial velocity of the NH_3 line.

Thus, as reference velocity offset we chose the most robust M-estimate of the mean value from the L1498 and L1512 cores: $\langle \Delta V \rangle_{\mathrm{M}} = 26.9 \pm 1.2_{\mathrm{stat}}$ m s^{-1}. Taking into account that the uncertainty of the HC_3N(2–1) rest frequency is about 3 m s^{-1}, whereas that of $NH_3(1,1)$ is less than 1 m s^{-1}, we finally have $\langle \Delta V \rangle_{\mathrm{M}} = 26.9 \pm 1.2_{\mathrm{stat}} \pm 3.0_{\mathrm{sys}}$ m s^{-1}. When it is interpreted in terms of the electron-to-proton mass ratio variation, as defined in Eq. (4), this velocity offset provides $\Delta\mu/\mu = (26 \pm 1_{\mathrm{stat}} \pm 3_{\mathrm{sys}}) \times 10^{-9}$.

6 Discussion and Conclusions

In two molecular cores with the lowest Doppler noise L1498 and L1512, we register very close values of the velocity offset $\Delta V \sim 27$ m s^{-1} between the rotational transition HC_3N(2–1) and the inversion transition $NH_3(1,1)$. These values coincide with the most accurate estimate obtained from the Effelsberg dataset on 12 molecular clouds in the Milky Way [25]. Two other cores, L1517B and L1400K, exhibit velocity shifts that are either higher (~ 47 m s^{-1} in L1517B) or lower (~ 9 m s^{-1} in L1400K) than the mean value, but the positive (L1517B) and negative (L1400K) deflections from the mean can be explained from the observed kinematics in these cores.

Of course, simultaneous observations of the $NH_3(1,1)$ inverse transition and rotational transitions of some N-bearing molecules, such as $N_2H^+(1\text{-}0)$ and $N_2D^+(1\text{-}0)$ would give a more accurate test. The main obstacle to this way is that the laboratory frequencies of N_2H^+ and N_2D^+ are known with accuracies not better than 14 m s^{-1} [25]. Using the N_2H^+ rest frequency from the Cologne Database for Molecular Spectroscopy (CDMS) [31] and observing with the Nobeyama 45-m telescope, we obtained a velocity shift between N_2H^+ and NH_3 of 23.0 ± 3.4 m s^{-1} in L1498, 24.5 ± 4.3 m s^{-1} in L1512, and 21.0 ± 5.1 m s^{-1} in L1517B [25]. We note that similar shifts are indicated for the central parts of L1498 and L1517B in Fig. 11 in [41], where these targets were observed with the 30-m IRAM telescope also using an N_2H^+ rest frequency which is very close to the CDMS value.

Obviously, for more definite conclusions, new laboratory measurements of the rest frequencies and new observations involving other targets and other molecular transitions with different sensitivity coefficients Q are required. It has already been suggested to measure Λ-doublet lines of the light diatomic molecules OH and CH [18], microwave inversion-rotational transitions in the partly deuterated ammonia NH_2D and ND_2H [19], low-laying rotational transitions in ^{13}CO and the fine-structure transitions in C I [27], and tunneling and rotation transitions in the hydronium ion H_3O^+ [20]. The fourth opportunity is of particular interest since the rest-frame frequencies of H_3O^+ transitions are very sensitive to the variation of μ, and their sensitivity coefficients have *different* signs. For example, the two lowest frequency transitions $J_K = 1_1^- \rightarrow 2_1^+$ and $J_K = 3_2^+ \rightarrow 2_2^-$ of para-H_3O^+ at, respectively, 307 and 364 GHz have $\Delta Q = Q_{307} - Q_{364} = 14.7$, which is 4 times larger than $\Delta Q = 3.46$ from the ammonia method. This means that the offset $\Delta V \sim 27$ m s^{-1}, detected with the ammonia method, should correspond to a relative velocity shift between these transitions, $\Delta V = V_{364} - V_{307}$, of about 100 m s^{-1} if $\Delta\mu/\mu \approx 26 \times 10^{-9}$. We consider the hydronium method [20] as an important independent test of the $\Delta\mu/\mu$ value in the Milky Way.

To conclude, we note that in cold molecular cores with low ionization degrees ($x_e \sim 10^{-8} - 10^{-9}$) frequency shifts caused by external electric and magnetic fields and by the cosmic black body radiation-induced Stark effect are less or about 1 m s^{-1} and cannot affect the revealed nonzero velocity offset between the rotational and inversion transitions in the ammonia method. Detailed calculations of these effects are given in [26].

Our current results tentatively support the hypothesis that the fundamental physical constant – the electron-to-proton mass ratio – may differ in low-density environments from its terrestrial value. This may be the consequence of the chameleon-like scalar field. However, new laboratory measurements of the molecular rest frequencies and new observations involving other molecular transitions and other targets are required to reach more definite conclusions.

Acknowledgements We are grateful to the staffs of the Medicina 32-m, Nobeyama 45-m, and Effelsberg 100-m radio telescope observatories for excellent support in our observations. We thank Gabriella Schiulaz for her kind assistance in preparing the text. The project has been supported in part by DFG Sonderforschungsbereich SFB 676 Teilprojekt C4, the RFBR grants No. 09-02-12223, 09-02-00352, and 08-02-92001, the Federal Agency for Science and Innovations grant NSh-3769.2010.2, the Program IV.12/2.5 of the Physical Department of the RAS.

References

1. P.J. Benson and P.C. Myers, Astrophys. J. S. 71 (1989) 89.
2. C. Burrage, A.-C. Davis and D.J. Shaw, Phys. Rev. D79 (2009) 044028.
3. R.R. Caldwell, R. Dave and P.J. Steinhardt, Phys. Rev. Lett. 80 (1998) 1582.
4. P. Caselli, P.J. Benson, P.C. Myers and M. Tafalla, Astrophys. J. 572 (2002) 238.
5. C., Chin, V.V. Flambaum and M.G. Kozlov, New J. Phys. 11 (2009) 055048.
6. A. Crapsi et al., Astrophys. J. 619 (2005) 379.
7. A. Davis, C.A.O. Schelpe and D.J. Shaw, Phys. Rev. D80 (2009) 064016.
8. J. Di Francesco et al., in Protostars and Planets. V. (eds. B. Reipurth et al.), Uni. Arizona Press, Tucson (2007).
9. V.V. Flambaum and M.G. Kozlov, Phys. Rev. Lett. 98 (2007) 240801.
10. G.A. Fuller and P. C. Myers, Astrophys. J. 418 (2009) 273.
11. P.F. Goldsmith and W.D. Langer, Astrophys. J. 222 (1978) 881.
12. A.A. Goodman, P.J. Benson, G.A. Fuller and P.C. Myers, Astrophys. J. 406 (1993) 528.
13. C. Henkel et al., A&A 500 (2009) 725.
14. P.T.P. Ho and C.H. Townes, ARA&A 21 (1983) 239.
15. S. Hotzel, J. Harju and C.M. Walmsley, A&A 415 (2004) 1065.
16. J. Khoury and A. Weltman, Phys. Rev. Lett. 93 (2004) 171104.
17. B. Klein et al., Proc. of the SPIE 6275 (2006) 627511.
18. M.G. Kozlov, Phys. Rev. A80 (2009) 022118.
19. M.G. Kozlov, A.V. Lapinov and S.A. Levshakov, J. Phys. B43 (2010) 074003.
20. M.G. Kozlov and S.A. Levshakov, Astrophys. J. (2010) in press.
21. S.G. Kukolich, Phys. Rev. 156 (1967) 83.
22. C.W. Lee, P.C. Myers and M. Tafalla, Astrophys. J. S. 136 (2001) 703.
23. J.-E. Lee, N.J. Evans II, Y.L. Shirley and K. Tatematsu, Astrophys. J. 583 (2003) 789.
24. S.A. Levshakov, P. Molaro and M.G. Kozlov, arXiv:0808.0583.
25. S.A. Levshakov et al., A&A 512 (2010) 44.
26. S.A. Levshakov et al., A&A (2010) in press.
27. S.A. Levshakov, P. Molaro and D. Reimers, A&A 516 (2010) 113.
28. K.M. Menten et al., A&A 492 (2008) 725.
29. P. Molaro, S.A. Levshakov and M.G. Kozlov, Nuc. Phys. B Proceed. Suppl. 194 (2009) 287.
30. M.T. Murphy, V.V. Flambaum, S. Muller and C. Henkel, Science 320 (2008) 1611.
31. H.S.P. Müller, F. Schlöder, J. Stutzki and G. Winnewisser, J. Mol. Struct. 742 (2005) 215.
32. C.A. Olano, C.M. Walmsley and T.L. Wilson, A&A 196 (1988) 194.
33. K.A. Olive and M. Pospelov, Phys. Rev. D77 (2008) 043524.
34. L. Pagani, F. Daniel and M.-L. Dubernet, A&A 494 (2009) 719.
35. P.J.E. Peebles and B. Ratra, Rev. Mod. Phys. 75 (2003) 559.
36. S. Perlmutter et al., Nature 391 (1998) 51.
37. A.G. Riess et al., Astron. J. 116 (1998) 1009.
38. G. Rybka et al., Phys. Rev. Lett. 105 (2010) 051801.
39. F.H. Shu, Astrophys. J. 214 (1977) 488.
40. M. Tafalla et al., A&A 455 (2006) 577.
41. M. Tafalla, P.C. Myers, P. Caselli and C.M. Walmsley, A&A 16 (2004) 191.
42. A. Upadhye, J.H. Steffen and A. Weltman, Phys. Rev. D81 (2010) 015013.

In Search of the Ideal Systems to Constrain the Variation of Fundamental Constants

Patrick Petitjean, Ragunathan Srianand, Pasquier Noterdaeme, Cédric Ledoux, and Neeraj Gupta

Abstract It has been realised in the last few years that strong constraints on the time-variations of dimensionless fundamental constants of physics can be derived at any redshift from QSO absorption line systems. Variations of the fine structure constant, α, the proton-to-electron mass ratio, μ, or the combination, $x = \alpha^2 g_\mathrm{p}/\mu$, where g_p is the proton gyromagnetic factor, have been constrained. However, except for α, the number of lines of sight where these measurements can be performed is limited. In particular the number of known molecular and 21 cm absorbers is small. Our group has started several surveys to search for these systems. We present here a summary of the results obtained till now. In the course of these surveys, we discovered a $z \sim 3$ system towards J133724.69+315254.55 which is close to "ideal" to constrain the variation of fundamental constants as several constants can be constrained using the same system, namely μ and $x = \alpha^2 G_\mathrm{p}/\mu$. In particular

---

P. Petitjean
Institut d'Astrophysique de Paris, Université Paris 6 & CNRS, UMR7095, 98bis Boulevard Arago, 75014, Paris, France
e-mail: petitjean@iap.fr

R. Srianand
IUCAA, Post Bag 4, Ganeshkhind, Pune 411 007, India
e-mail: anand@iucaa.ernet.in

P. Noterdaeme
Departamento de Astronomía, Universidad de Chile, Casilla 36-D, Santiago, Chile
e-mail: pasquier@das.uchile.cl

C. Ledoux
European Southern Observatory, Alonso de Córdova 3107, Casilla 19001, Vitacura, Santiago, Chile
e-mail: cledoux@eso.org

N. Gupta
ASTRON, Oude Hoogeveensedijk 4, 7991 PD, Dwingeloo, The Netherlands
e-mail: gupta@astron.nl

C. Martins and P. Molaro (eds.), *From Varying Couplings to Fundamental Physics*,
Astrophysics and Space Science Proceedings, DOI 10.1007/978-3-642-19397-2_12,

the constraint on x is particularly strong with $\Delta x/x = -(1.9 \pm 1.5) \times 10^{-6}$. If combined with the constraint on μ derived recently, this yields a 3σ upper limit on the variation of α at $z \sim 3$ of $\Delta\alpha/\alpha < 2.2\times10^{-6}$. We note that the quasar happens to be located in the northern part of the sky. Therefore the variations along the so-called "Australian dipole", if any, seem to be restricted to a very specific direction in the universe.

1 Introduction

Current laboratory constraints exclude any significant time variation of the dimensionless constants of physics in the low-energy regime. However, it is not impossible that these constants could have varied over cosmological time-scales. Savedoff [31] first pointed out the possibility of using redshifted atomic lines from distant objects to test the evolution of dimensionless physical constants. The idea is to compare the wavelengths of the same transitions measured in the laboratory on earth and in the remote universe. This basic principle has been first applied to QSO absorption lines by Bahcall et al. [1].

The field has been given tremendous interest recently with the advent of 10 m class telescopes. To make a long story short it is not yet certain that the variation of α claimed by Webb et al. [37] is confirmed or not because some people have claimed (unreasonably in our opinion) that everybody is wrong [2, 3, 18, 29, 32] except Murphy et al. [21]. In addition, the recent claims by Webb et al. [38] of the detection of a dipole, e.g. a directional space variation of α still waits confirmation. Future will tell us the truth! On the other hand, other constants (in particular μ) are till now claimed not to vary at the limit of the experiments [8–12, 30, 36, 39, 40].

Since the amount of observing time required by the study of one absorption system is quite large (typically 10 to 20 hours of 10 m class telescopes per quasar), the systems have to be selected carefully. In particular for μ and x, the small number of suitable systems may prevent the development of the field. We therefore have embarked on several surveys to find these systems. We search for molecular hydrogen at the VLT and 21 cm systems at GMRT.

2 How to Find Molecules

Molecular hydrogen is not conspicuous in Damped Lyman-α systems at high redshift contrary to what is seen in the Galaxy and, for a long time, only the DLA towards Q 0528−2505 was known to contain H_2 molecules [17]. H_2-bearing DLAs are nevertheless crucial to understand the physical properties of the interstellar medium of high-z galaxies [4, 7, 23, 34].

2.1 VLT/UVES Survey for Molecular Hydrogen

The first systematic search for molecular hydrogen in high-redshift ($z_{\rm abs} > 1.8$) DLAs was carried out using the Ultraviolet and Visual Echelle Spectrograph (UVES) at the Very Large Telescope (VLT, [14], see also [26]).

More recently we gathered a total sample of 77 DLAs/strong sub-DLAs, with $\log N(\text{H I}) \geq 20$ and $z_{\rm abs} > 1.8$, for which the wavelength range where corresponding H_2 Lyman and/or Werner-band absorption lines are expected to be redshifted is covered by UVES observations of the quasars [19].

H_2 is detected in thirteen of the systems with molecular fractions as low as $f \simeq 5 \times 10^{-7}$ up to $f \simeq 0.1$, with $f = 2N(H_2)/(2N(H_2) + N(\text{H I}))$ in the redshift range $1.8 < z_{\rm abs} \leq 4.2$ [15]. Upper limits are measured for the remaining 64 systems with detection limits of typically $\log N(H_2) \sim 14.3$, corresponding to $\log f < -5$. We find that about 35% of the DLAs with metallicities relative to solar $[\text{X/H}] > -1.3$ (i.e., 1/20th solar) with X = Zn, S or Si, have molecular fractions $\log f > -4.5$, while H_2 is detected – regardless of the molecular fraction – in $\sim$ 50% of them. On the contrary, only about 4% of the $[\text{X/H}] < -1.3$ DLAs have $\log f > -4.5$. We show that the presence of H_2 does not strongly depend on the total neutral hydrogen column density, although the probability of finding $\log f > -4.5$ is higher for $\log N(\text{H I}) \geq 20.8$ than below this limit (19% and 7% respectively). The overall H_2 detection rate in $\log N(\text{H I}) \geq 20$ DLAs is found to be about 16% (10% considering only $\log f > -4.5$ detections) after correcting for a slight bias towards large $N(\text{H I})$. There is a strong preference for H_2-bearing DLAs to have significant depletion factors, $[\text{X/Fe}] > 0.4$. In addition, all H_2-bearing DLAs have column densities of iron into dust larger than $\log N(\text{Fe})_{\rm dust} \sim 14.7$, and about 40% of the DLAs above this limit have detected H_2 lines. This demonstrates the importance of dust in governing the detectability of H_2 in DLAs. There is no evolution with redshift of the fraction of H_2-bearing DLAs nor of the molecular fraction in systems with detected H_2 over the redshift range $1.8 < z_{\rm abs} < 4.3$.

2.2 A Few Characteristics of the H_2 Bearing DLAs

An blind survey like the one described above is useful to derive information on the overall population of DLA systems. When it comes to select systems where H_2 can be detected and thus to increase the detection efficiency, a few characteristics can be used:

(i) There is no strong correlation between the presence of H_2 and the H I column density (Fig. 1) and molecules are seen at any $\log N(\text{H I})$.
(ii) There is a definite tendency for molecules to be more frequent at high metallicity (Fig. 2; see also [25]).
(iii) Dust is an important ingredient for the formation of H_2 and molecules are predominantly found in dusty systems (Fig. 3; see also [16]).

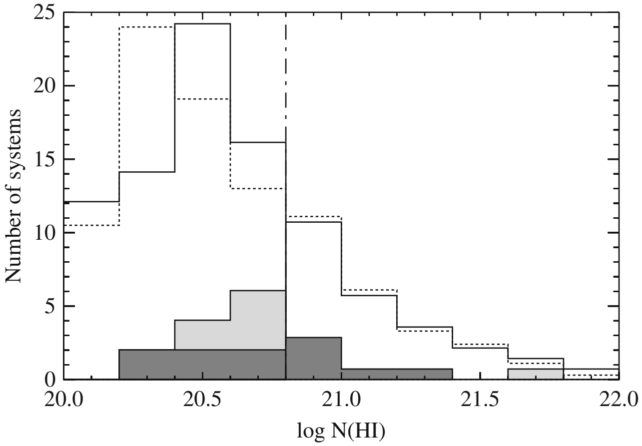

Fig. 1 Total neutral hydrogen column density (corrected) distributions of DLAs in the overall UVES sample (solid line), the sub-sample of H_2-bearing systems (grey), and that of the systems with molecular fraction $\log f > -4.5$ (dark grey). The distribution from the SDSS-DR5 DLA sample (dotted line; Prochaska et al. [27], Noterdaeme et al. [20]) is represented with a different scaling so that the area of both histograms are the same. H_2 is found at any H I column density

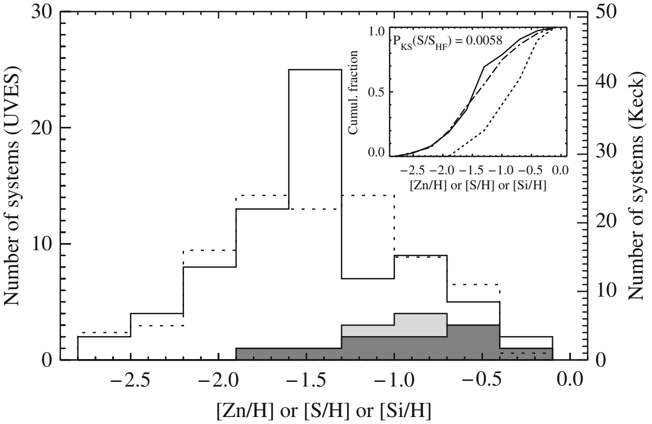

Fig. 2 The metallicity distribution of DLAs in the overall UVES sample (solid line) is compared to that from the Keck sample (dotted; Prochaska et al. [28]), adequately scaled (right axis) so that the area of both histograms are the same. The distributions are similar. Distributions from the sub-sample of H_2-bearing systems (grey), and that of the systems with molecular fraction $\log f > -4.5$ (dark grey) are also shown. It is clear from the figure and the Kolmogorov-Smirnov test probability (inset) that the distribution from H_2-bearing systems are skewed towards high metallicities

2.3 Other Molecules

Using refined selection criteria it was possible to increase the efficiency of the selection of H_2-bearing systems to about 30%. This gave us the possibility to discover

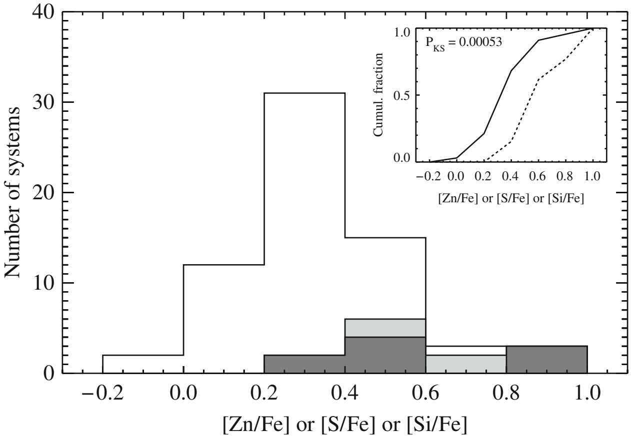

Fig. 3 Distribution of depletion factors from the overall UVES sample (solid line), the sub-sample of H_2-bearing systems (grey), and that of the systems with molecular fraction $\log f > -4.5$ (dark grey) It is clear from these histograms that the distribution of depletion factors for H_2-bearing systems is different from that of the overall sample. This shows clearly that H_2-bearing DLAs are more dusty than the overall DLA population. The probability that the two samples are drawn from the same parent population is indeed very small: $P_{\rm KS}$(SHI/SH2P) $\approx 10^{-3}$ (inset)

the first CO absorber together with several HD absorbers [22, 24, 33]. This opens up the exciting possibility to study astro-chemistry at high redshift.

3 Radio 21 cm Absorbers

We have also embarked on a large survey to search for 21 cm absorbers at intermediate and high redshifts. For this we first selected strong Mg II systems ($W_{\rm r} > 1$ Å) from the Sloan Digital Sky Survey in the redshift range suitable for a follow-up with the Giant Meterwave Telescope (GMRT), $1.10 < z_{\rm abs} < 1.45$. We then cross-correlated the ~3000 SDSS systems we found with the FIRST radio survey to select the background sources having at least a $S_{1.4\rm GHz} > 50$ mJy bright component coincident with the optical QSO. There are only 73 sources fulfilling these criteria out of which we observed 35 over ~400 hours of GMRT observing time [6].

We detected 9 new 21 cm absorption systems [5, 6]. This is by far the largest number of 21-cm detections from any single survey. Prior to our survey no intervening 21-cm system was known in the above redshift range and only one system was known in the redshift range $0.7 \le z \le 1.5$ (see Fig. 4). Our GMRT survey thus provides systems in a narrow redshift range where variations of x can be constrained. For this, high resolution and high signal-to-noise ratio observations of the absorbers must be performed to detect the UV absorption lines that will provide the anchor

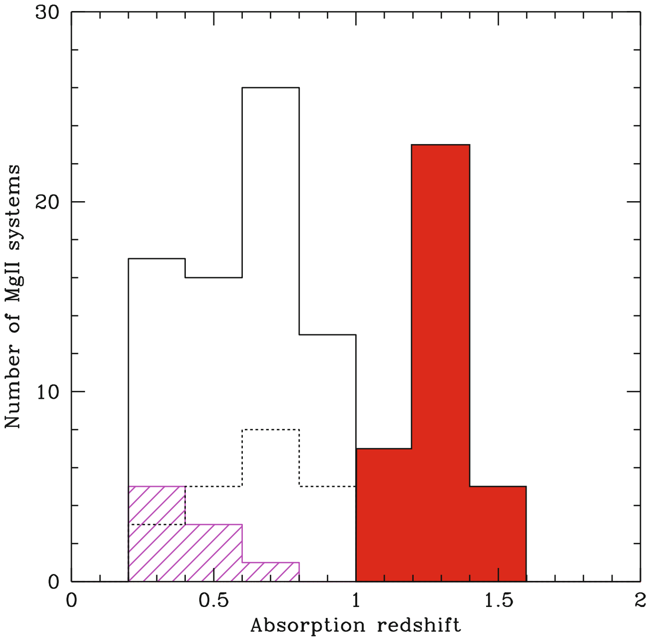

Fig. 4 Redshift distribution of Mg II systems that were searched for 21-cm absorption. The filled histogram is the GMRT sample of 35 Mg II systems presented in Gupta et al. [6] (33 of these absorption systems have W_r(Mg IIλ2796) $>$ 1Å). The solid line histogram is for the sample of Lane [13]. The distribution for the W_r(Mg IIλ2796) $\geq$ 1Å sub-set of these systems is given by the dashed line histogram and the hatched histogram corresponds to 21-cm detections among them

to fix the exact redshift, the variations of x being subsequently constrained by the position of the 21 cm absorption line.

Future capabilities (ASKAP, MeerKAT) will boost this field.

4 The Absorber at z_{abs} = 3.1744 Towards SDSS J133724.69+315254.55

We have reported recently the discovery of a system which is close to be "ideal" to constrain the variation of fundamental constants as several constants can be constrained using the same system, namely μ and $x = \alpha^2 G_p/\mu$ (see Fig. 5).

Indeed, we detected 21-cm and molecular hydrogen absorptions in the same damped Lyman-α system (with log N(H I) = 21.36±0.10) at z_{abs} = 3.1744 towards J133724.69+315254.55 (z_{em} ∼ 3.174, see [35]). We estimate the spin temperature of the gas to be, $T_S = 597^{+118}_{-100}$ K, intermediate between the expected values for cold and warm neutral media. This suggests that the H I absorption originates from a mixture of different phases. The total H_2 molecular fraction is low,

$f_{H2} = 10^{-7}$, and H_2 rotational level populations do not provide any constraint on the kinetic temperature of the gas. The average metallicity of the α-elements is, [S/H] $= -1.45 \pm 0.22$ ([O/S]$\sim +0.47 \pm 0.33$). Nitrogen is found underabundant with respect to α-elements by $\sim$1.0 dex and iron is depleted by $\sim$0.5 dex probably onto dust. Using photoionization models we derive the average density of the gas to be $\sim$2.5 cm^{-3} and the gas to be located more than 240 kpc away from the QSO.

While the 21-cm absorption line is located well within the H_2 velocity profile, its centroid is shifted by $\sim 2.9 \pm 0.4$ km/s with respect to the redshift measured from the H_2 lines. However, the position of the strongest metal absorption component matches the position of the 21-cm absorption line within 0.4 km/s. From this, we constrain the variation of the combination of fundamental constants $x = \alpha^2 G_{\rm p}/\mu$, $\Delta x/x = -(1.9 \pm 1.5) \times 10^{-6}$. We can place a constraint on μ in the same system. In this regard the system studied here is unique. However, as the H_2 column density is weak, only Werner band absorption lines are seen and, unfortunately, the range of sensitivity coefficients is too narrow to provide a stringent constraint: $\Delta\mu/\mu \leq 4.0 \times 10^{-4}$.

If we combine the constraint we obtain on x in this system with the constraint on μ obtained by King et al. [12] and Thompson et al. [36], $\Delta\mu/\mu = 2.6 \pm 3.0 \times 10^{-6}$, we obtain a 3σ upper limit on the variation of α at $z \sim 3$ of $\Delta\alpha/\alpha < 2.2{\times}10^{-6}$. We note that the quasar happens to be located in the northern part of the sky. Therefore the variations along the so-called “Australian dipole”, if any, seems to be restricted to a specific direction in the universe.

5 Conclusion

Since the amount of observing time required to constrain fundamental constants in one absorption system is quite large (typically 10 to 20 hours of 10 m class telescopes per quasar), the targeted systems have to be selected carefully. In particular for μ and x, the small number of suitable systems may prevent the development of the field. We therefore have embarked on several surveys to find these systems. We search for molecular hydrogen at the VLT and 21 cm systems at GMRT.

Systems where H_2 is to be expected can be selected based on the following observations:

(i) There is no strong correlation between the presence of H_2 and the H I column density and molecules are seen at any log N(H I).
(ii) There is a definite tendency for molecules to be more frequent at high metallicity.
(iii) Dust is an important ingredient for the formation of H_2 and molecules are predominantly found in dusty systems.

We have detected 9 new 21-cm absorption systems [5,6]. This is by far the largest number of 21-cm detections from any single survey. Prior to our survey no intervening 21-cm system was known in the above redshift range and only one system was

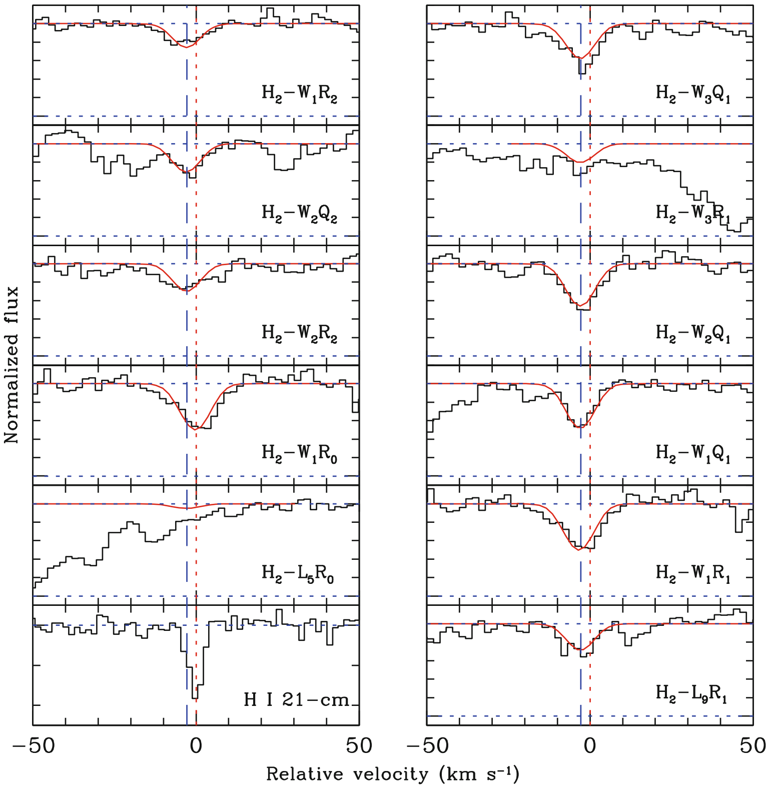

Fig. 5 Voigt profile fits to H_2 Lyman and Werner band absorption lines in the DLA towards SDSS J133724.69+315254.55. The vertical dotted and dashed lines mark the locations of the 21 cm and H_2 absorption lines, respectively. The apparent velocity shift between the two lines is ~2.7 km s^{-1}. The zero of the velocity scale is defined with respect to the redshift of the H_2 lines, $z_{abs} = 3.174441(5)$

known in the redshift range $0.7 \leq z \leq 1.5$ (see Fig. 4). Our GMRT survey thus provides systems in a narrow redshift range where variations of x can be constrained. For this, high resolution and high signal-to-noise ratio observations of the absorbers must be performed to detect the UV absorption lines that will provide the anchor to fix the exact redshift, the variations of x being subsequently constrained by the position of the 21-cm absorption line.

It would be highly interesting to find places where several constants can be constrained. We have reported recently the discovery of a system which is close to be "ideal" to constrain the variation of fundamental constants as several constants can be constrain in the same system, namely μ and $x = \alpha^2 G_p/\mu$. Indeed, we detected 21-cm and molecular hydrogen absorptions in the damped Lyman-α system at $z_{abs} = 3.1744$ towards J 133724.69+315254.55.

If we combine the constraint we obtain on x in this system with the constraint on μ obtained by King et al. [12] and Thompson et al. [36], $\Delta\mu/\mu = 2.6 \pm 3.0 \times 10^{-6}$, we obtain a 3σ upper limit on the variation of α at $z \sim 3$ of $\Delta\alpha/\alpha < 2.2\times10^{-6}$. We note that the quasar happens to be located in the northern part of the sky. Therefore the variations along the so-called “Australian dipole”, if any, seems to be restricted to a very specific direction in the universe.

Future radio capabilities such as ASKAP and MeerKAT, but also ALMA, in addition to the forthcoming VLT instrument CODEX, will boost this field, providing numerous places in the sky where to constrain the fundamental constants from molecular and 21-cm absorption lines.

Acknowledgements PN is supported by a CONICYT/CNRS fellowship. RS and PPJ gratefully acknowledge support from the Indo-French Centre for the Promotion of Advanced Research (Centre Franco-Indien pour la Promotion de la Recherche Avancée) under contract No. 4304-2.

References

1. J.N. Bahcall, W.L.W. Sargent and M. Schmidt, Astrophys. J, 149 (1967) L11.
2. H. Chand, R. Srianand, P. Petitjean and B. Aracil, A&A 417 (2004) 853.
3. H. Chand et al., A&A 451 (2006) 45.
4. J. Cui, J. Bechtold, J. Ge and D.M. Meyer, Astrohpys. J. 633 (2005) 649.
5. N. Gupta et al., Astrophys. J. 654 (2007) L111.
6. N. Gupta et al., MNRAS 398 (2009) 201.
7. H. Hirashita and A. Ferrara, MNRAS 356 (2005) 1529.
8. A.V. Ivanchik, P. Petitjean, E. Rodriguez and D.A. Varshalovich, Ap&SS 283 (2003) 583.
9. A.V. Ivanchik, E. Rodriguez, P. Petitjean and D.A. Varshalovich, Astron. Lett. 28 (2002) 423.
10. A.V. Ivanchik et al., A&A 440 (2005) 45.
11. N. Kanekar et al. Phys. Rev. Lett. 95 (2005) 261301.
12. J.A. King, J.K. Webb, M.T. Murphy and R.F. Carswell, Phys. Rev. Lett. 101 (2008) 251304.
13. W. Lane, PhD thesis, University of Gröningen (2000).
14. C. Ledoux, P. Petitjean and R. Srianand, MNRAS 346 (2003) 209.
15. C. Ledoux, P. Petitjean and R. Srianand, Astrophys. J. 640 (2006) L25.
16. C. Ledoux, R. Srianand and P. Petitjean, A&A 392 (2002) 781.
17. S.A. Levshakov and D.A. Varshalovich, MNRAS 212 (1985) 517.
18. S.A. Levshakov et al., A&A 434 (2005) 827.
19. P. Noterdaeme, C. Ledoux, P. Petitjean and R. Srianand, A&A 481 (2008) 327.
20. P. Noterdaeme, P. Petitjean, C. Ledoux and R. Srianand, A&A 505 (2009) 1087.
21. M.T. Murphy, J.K. Webb and V.V. Flambaum, MNRAS 345 (2003) 609.
22. P. Noterdaeme et al., A&A, 503 (2009) 765.
23. P. Noterdaeme et al., A&A 469 (2007) 425.
24. P. Noterdaeme et al., arXiv:1008.0637
25. P. Petitjean, C. Ledoux, P. Noterdaeme and R. Srianand, A&A 456 (2006) L9.
26. P. Petitjean, R. Srianand, C. Ledoux, A&A 364 (2000) L26.
27. J.X. Prochaska, S. Herbert-Fort and A.M. Wolfe, Astrophys. J, 635 (2005) 123.
28. J.X. Prochaska et al., Astrophys. J. S. 171 (2007) 29.
29. R. Quast, D. Reimers and S.A. Levshakov, A&A 415 (2004) L7.
30. E. Reinhold et al., Phys. Rev. Lett. 96 (2006) 151101.
31. M. Savedoff, Nature 178 (1956) 688.
32. R. Srianand, H. Chand, P. Petitjean and B. Aracil, Phys. Rev. Lett. 92 (2004) 121302.

33. R. Srianand, P. Noterdaeme, C. Ledoux, P. Petitjean, A&A 482 (2008) L39.
34. R. Srianand et al., MNRAS 362 (2005) 549.
35. R. Srianand, et al., MNRAS 405 (2010) 1888.
36. R. Thompson et al., Astrohys. J. 703 (2009) 1648.
37. J.K. Webb et al., Phys. Rev. Lett. 87 (1999) 884.
38. J.K. Webb et al., arXiv:1008.3907.
39. M. Wendt and P. Molaro, arXiv:1009.3133.
40. M. Wendt and D. Reimers, Eur. Phys. J ST, 163 (2008) 197.

Search for Cosmological μ-Variation from High-Redshift H_2 Absorption; A Status Report

Wim Ubachs, Julija Bagdonaite, Michael T. Murphy, Ruth Buning, and Lex Kaper

Abstract Observations of H_2 spectra in the line-of-sight of distant quasars may reveal a variation of the proton-electron mass ratio $\mu = m_p/m_e$ at high redshift, typically for $z > 2$. Currently four high-quality systems (Q0347-383, Q0405-443, Q0528-250 and J2123-050) have been analyzed returning a constraint $\Delta\mu/\mu < 1 \times 10^{-5}$. We present data and a μ-variation analysis of another system, Q2348–011 at redshift $z_{abs} = 2.42$, delivering $\Delta\mu/\mu = (-1.5 \pm 1.6) \times 10^{-5}$. In addition to observational data the status of the laboratory measurements is reviewed. The future possibilities of deriving a competitive constraint on $\Delta\mu/\mu$ from the known high-redshift H_2 absorbers is investigated, resulting in the identification of a number of potentially useful systems for detecting μ-variation.

W. Ubachs
Institute for Lasers, Life and Biophotonics, VU University Amsterdam, de Boelelaan 1081, 1081 HV Amsterdam, The Netherlands
e-mail: wimu@nat.vu.nl

J. Bagdonaite
Department of Astronomy, Vilnius University, Vilnius, Lithuania, and Institute for Lasers, Life and Biophotonics, VU University Amsterdam, de Boelelaan 1081, 1081 HV Amsterdam, The Netherlands
e-mail: julija.bagdonaite@ff.stud.vu.lt

M.T. Murphy
Centre for Astrophysics and Supercomputing, Swinburne University of Technology, Melbourne, Victoria 3122, Australia
e-mail: mmurphy@swin.edu.au

R. Buning
Institute for Lasers, Life and Biophotonics, VU University Amsterdam, de Boelelaan 1081, 1081 HV Amsterdam, The Netherlands. Present address: Leiden Institute of Physics, Leiden University, The Netherlands
e-mail: buning@physics.leidenuniv.nl

L. Kaper
Astronomical Institute Anton Pannekoek, Universiteit van Amsterdam, 1098 SJ Amsterdam, The Netherlands, and Institute for Lasers, Life and Biophotonics, VU University Amsterdam, de Boelelaan 1081, 1081 HV Amsterdam, The Netherlands
e-mail: l.kaper@uva.nl

C. Martins and P. Molaro (eds.), *From Varying Couplings to Fundamental Physics*, Astrophysics and Space Science Proceedings, DOI 10.1007/978-3-642-19397-2_13,

1 Cosmological μ Variation and the Laboratory Database

The proton-electron mass ratio $\mu = m_p/m_e$ is one of the constants suitable for targeting a possible variation of a physical constant on a cosmological time scale. Although μ is a dimensionless constant, lending itself for an observational approach, it is not a *fundamental* constant in a strict sense, like the fine-structure constant α, because μ involves all the binding physics of the quarks inside the proton. However, its close connection to m_e/Λ_{QCD} makes it the parameter determining the measure of the strong force with respect to the electroweak sector, and is therewith of fundamental importance. Variation of μ can be straightforwardly derived from a comparison between spectral lines observed at vastly differing redshifts. Values of wavelengths at high redshift λ_z^i are compared to laboratory wavelengths λ_0^i for as many as possible H_2 lines [40] using sensitivity coefficients for each individual spectral line $K_i = d \ln \lambda_i / d \ln \mu$. These K_i are calculable to the 1% accuracy level [43].

The laboratory wavelengths of the spectral lines in the Lyman and Werner bands of H_2 have been investigated at ever improved accuracy using tunable vacuum ultraviolet (VUV) lasers since over a decade [11, 13, 17, 35, 37, 44], also including spectra of HD [12, 16]. In addition the novel Fourier-transform spectrometer in the VUV range at the Soleil synchrotron was used to perform direct absorption spectra focusing on HD to cover the entire range of Lyman and Werner bands for this deuterated molecule [15]. The most accurate wavelength positions are obtained from a third indirect spectroscopic method based on the highly accurate determination of level energies for certain anchor levels [9], where the determination of Lyman and Werner wavelengths results from an independent measurement of spacings between excited states [38]. The full set of recommended wavelengths is reported in Bailly *et al.* [4]. Another compilation of these data, both for H_2 and HD is given in the appendix of Malec *et al.* [24], also including a listing of K_i sensitivity coefficients [15, 43], oscillator strengths of the absorption lines [2], and of damping coefficients [1].

A quasar absorption spectrum can be treated in different ways to detect a possible $\Delta\mu/\mu$. A straightforward method is to derive line positions by fitting H_2 resonances, and thereupon compare the results with the laboratory wavelengths; by deriving reduced redshifts $\zeta_i = (z_i - z_A)/(1 + z_A)$ with z_i the redshift determined for each line ($z_i = (\lambda_z^i/\lambda_z^0) - 1$) and z_A the redshift of the absorber, such a method gives a graphical insight into a possible variation of μ [37, 43]. In contrast to this line-by-line fitting method a *comprehensive* fitting method has advantages. There, an H_2 spectrum is generated, based on the available molecular parameters (wavelengths [4, 24], oscillator strengths [2], and damping parameters [1]). The value for $\Delta\mu/\mu$ is then a single fitting parameter comparing the observed spectrum with a model spectrum; this is accomplished via least squares fitting with the VPFIT software [47]. Each line is convolved with the instrumental profile (pertaining to the spectral resolving power $R = \lambda/\Delta\lambda$ of the spectrometer), a natural linewidth Γ, and a Doppler parameter b. The main advantage of the method is that a composite velocity structure can be addressed. The column densities $N(J)$ for each rotational state can be tied between velocity components or left independent. Further details

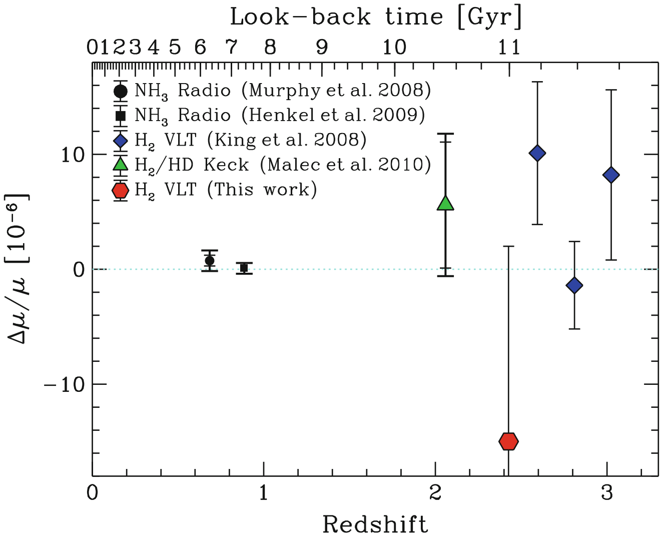

Fig. 1 Current result on cosmological μ-variation based on the five available high-quality H_2 absorption systems as a function of redshift: *diamonds* relate to Q0347–383, Q0405–443 and Q0528–250 [19], *triangle* is the result from J2123–005 [24], while the black points relate to the ammonia data [10, 25] for redshifts $z < 1$. The hexagonal point represents the result of the present analysis of Q2348–011

and advantages of the comprehensive fitting method are discussed in Refs. [19, 24]. By this means the spectral information on overlapping lines and of saturated lines can be included. In the example of the analysis of the Keck-HIRES spectrum of the quasar J2123–005 it is shown how the velocity structure can be investigated in much detail in terms of computed *composite residuals* which demonstrate a complex velocity structure that should be accounted for [24]. These optimized comprehensive fitting methods were also implemented in the analyses of the three systems Q0347–383, Q0405–443 and Q0528–250 by King *et al.* [19].

The resulting constraints on $\Delta\mu/\mu$ for the four systems mentioned are shown in Fig. 1. The figure also includes the result of the Q2348–011 analysis, details of which will be presented in the next section. The tighter constraints stemming from radio-astronomical observations of NH_3 at redshifts $z < 1$ are shown as well [10, 25]. The data show the present status of a possible variation of the proton-electron mass ratio to be $\Delta\mu/\mu < 1 \times 10^{-5}$ at redshifts $z = 2 - 3.5$.

2 VLT-UVES Observation of Q2348–011

H_2 absorption features associated with the Damped Lyman-α (DLA) system at $z = 2.42$ along the sightline of Q2348–011 (SDSS J235057.88–005209.8, $z_{em} \simeq 3.02$) were first reported by Petitjean *et al.* [32]. Since then this system has been the subject of several investigations but none of them focused on μ-variation (e.g. Ledoux *et al.* [20], Noterdaeme *et al.* [31]), but rather on the molecular column densities, the metallicity and the physical conditions of the gas contained in this DLA-system. For an investigation of μ-variation new observations of well-calibrated spectra of Q2348–011 were recorded, and will be presented here.

2.1 Data

The absorption spectrum of the quasar Q2348–011 was obtained with the Ultraviolet and Visual Echelle Spectrograph (UVES) at the Very Large Telescope (VLT) of the European Southern Observatory (ESO) in Paranal, Chile. Observations were carried out in visitor mode on four consecutive nights (2007 August 18-21). Q2348–011 is not a particularly bright object ($R_{mag} = 18.31$) so long exposures were needed. An overall of 15 spectra were recorded with an exposure time between 3600 and 4800 seconds each; they make up for a combined total of 19.25 hours of observation. The slit widths were set to $0.''8 - 1.''0$ and $0.''7 - 0.''8$ in, respectively, blue and red ranges. They were kept constant for all exposures irrespective of the noticeably varying seeing conditions, which were on average $1.''2$. These settings yield a resolution of R $\sim$ 51700 (in the blue-UV range where all H_2 lines are observed) and 55300 (in the red). This corresponds to a resolution element of 2.46 and 2.31 km s^{-1} in terms of velocity units, respectively. For optimum wavelength calibration the 15 science exposures were each attached with a ThAr calibration frame, obtained immediately after each science exposure. Special care was taken to use pre-selected Th-Ar reference lines following optimization procedures [26]. The final spectrum of Q2348–011 covers (vacuum-heliocentric) wavelengths 3572-9467 Å, with gaps at 4520-4621 and 7505-7665 Å. Parts of the spectrum are displayed in Fig. 2.

2.2 Analysis

The wavelength range covered by the VLT-UVES spectrum provides 58 H_2 transitions for rotational levels $J = 0 - 5$. The H_2 features fall in the wavelength range between 3580 and 3860 Å for this absorber at $z = 2.42$. This part of the combined spectrum has a signal-to-noise ratio (S/N) of 25. Note that no associated HD spectral features have been detected at a significant level. All the transitions observed arise from the Lyman band. Molecular hydrogen is present in 7 velocity features (the two left-most are blended together but they count at least as two), so in principle this spectrum would provide a sample of 58 × 7 absorption lines. However, besides the DLA at $z = 2.42$ (neutral content $\log N(\mathrm{H\,I}) = 20.50 \pm 0.10$, [20]), which contains molecular hydrogen, there is an additional DLA at $z = 2.62$, which has a larger column density of neutral hydrogen ($\log N(\mathrm{H\,I}) = 21.30 \pm 0.08$ [31]), but no signs of molecular hydrogen. The strong Lyman-β feature of the second DLA ($z = 2.62$) at

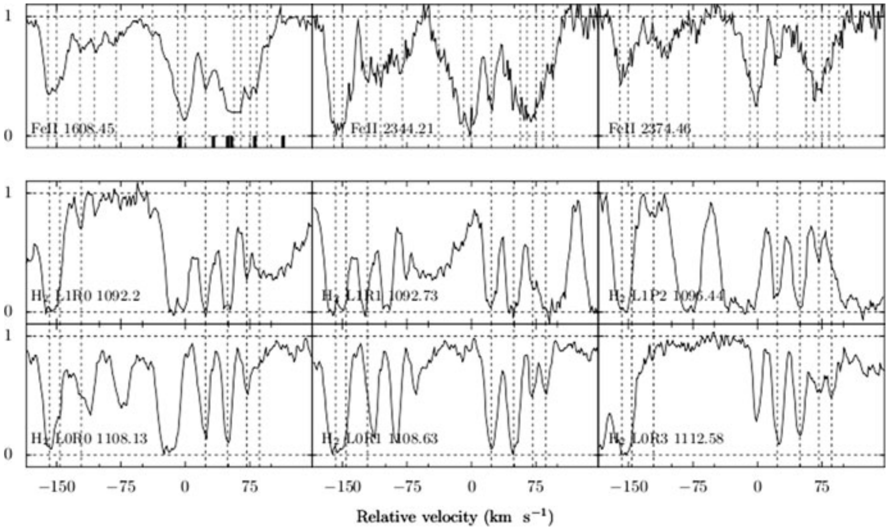

Fig. 2 Lower panel: H_2 velocity structure in the Q2348–011 DLA system at $z = 2.42$; upper panel: Fe II velocity structure of the same absorber. The positions of 7 different velocity features of H_2 are indicated by the blue dashed lines, and the positions of 14 velocity components of Fe II are indicated by the dashed lines. Note that the strongest velocity component in Fe II absorption profile (at 0 km s^{-1}) does not have an associated H_2 component. The cleanest Fe II transition (1608.45 Å) is blended with Si IV (1402.77 Å) of an additional absorber at $z = 2.93$. The ticks in the Fe II panel indicate positions of the overlapping Si IV lines

3710 Å obscures 4 H_2 transitions (24 velocity components) and damps some others (see Fig. 3), while also the Lyman-γ blends 4 H_2 lines (28 velocity components). This DLA gives rise to a cutoff in the absorption spectrum at 3580 Å, which makes this DLA an unfortunate coincidence along the sightline of Q2348–011. In addition there exist strong H I absorbers, almost at the column densities of sub-DLA's, at $z = 2.73$ and $z = 2.93$ obscuring several H_2 lines.

Another distinctive feature of this spectrum is self-blending of H_2: since the velocity structure of H_2 consists of numerous components spread over $\sim$ 300 km s^{-1}, nearby lying lines exhibit mutual overlap of velocity components. For example, velocity components 4-7 of H_2 L0R1 lie in the same region as velocity components 1-3 of H_2 L1P5. This kind of overlapping can be disentangled using the comprehensive fitting method, if a sufficient number of non-overlapping lines is available. However, the non-overlapping lines are blended in addition with the absorbers of the Lyman-α forest, and the overall amount of clear features is strongly reduced.

Some of the molecular hydrogen features are contaminated by metal lines associated with the two DLAs, namely, L2R0 with Si II (1020.69 Å) at $z = 2.62$, and L3R1, L3P1, L1P2, L1R3, L0P2, L0R3 are blended with various Fe II lines associated with the $z = 2.42$ DLA. Further, L1R5 and L1P4 may be blended with an additional C IV system at $z = 1.44$ but this is difficult to reconstruct unambiguously.

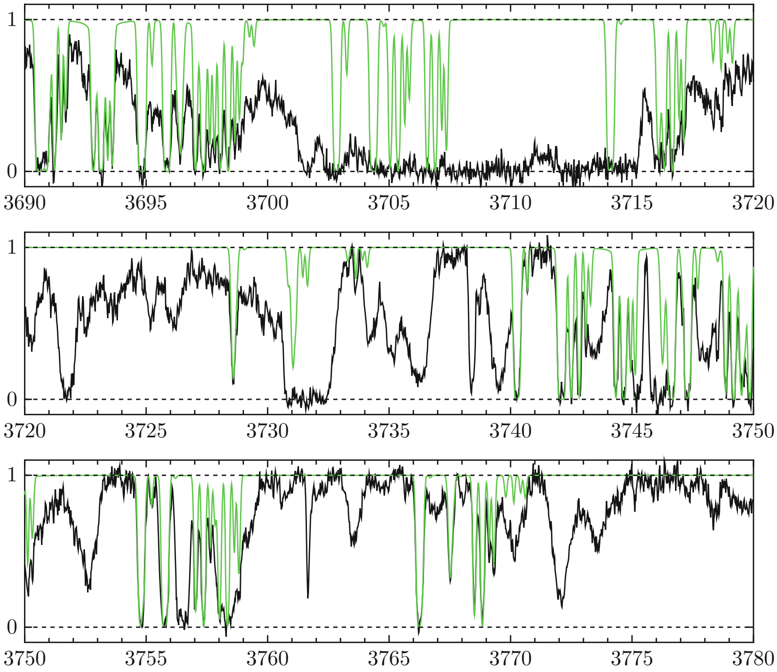

Fig. 3 H_2 absorption model superimposed on a portion of the Q2348–011 spectrum. The strong feature centered at 3710 Å is Lyman-β of the DLA at $z = 2.62$

Generally, the sightline towards the quasar Q2348–011 is rich in interesting absorbers: besides the two DLAs there are other strong metal absorbers at $z = 2.97$, 2.93, 2.72, 2.58 (C IV, Si IV, N V), and at $z = 0.86$, 0.77 (Mg II). The latter is remarkable in having numerous components spread over 750 km s^{-1}. Noteworthy coincidence is that the cleanest Fe II transition (1608.45 Å) associated with $z = 2.42$ is blended with Si IV (1402.77 Å) of the absorber at $z = 2.93$ (see Fig. 2). Also note that the most prominent velocity component in metal transitions does not have an associated H_2 component.

For the final fit deriving $\Delta\mu/\mu$ 35 regions with 36 different molecular hydrogen transitions have been selected. Each line is modeled as a Voigt profile. In the comprehensive fitting method the parameters (column density N, Doppler parameter b, and position z) are connected for different lines. Each J-level for H_2 has a different ground state population, so all transitions from the same J-level have the same value for N, b, and z. It is also assumed that a given velocity component has the same z and b value in all J-levels; physically this can be interpreted that the molecular hydrogen of all states resides in the same absorbing cloud. The value for $\Delta\mu/\mu$ is a single fitting parameter for all molecular hydrogen transitions. The absorption model is optimized to fit data by using the VPFIT software.

As analyzed by Malec *et al.* in the example of the J2123–005 quasar system, more than one velocity component can underlie a molecular absorption feature as distinguishable by inspection. Their presence can be confirmed or rejected relying on goodness-of-fit and by inspecting *composite residuals* [24]. As the two left-most features of H_2 absorption are blended, more components could in principle be present close to or between the two blended features. A fit with 7+1 velocity components (VC) instead of 7, where the additional VC was included between the two left-most VCs, has improved the χ^2_ν per degree-of-freedom by several hundredths, but the additional velocity component was rejected as unnecessary in transitions from $J = 4$ and $J = 5$ rotational levels. The 7+1 VC model is regarded as the fiducial result, because it gives the best match with the observed spectrum, i.e. it is statistically preferred as it returns the smallest χ^2_ν. A more detailed analysis will be presented in an upcoming paper [3].

3 Results

The fiducial absorption model led to the following result: $(\Delta\mu/\mu)_{7+1VC} = (-1.5 \pm 1.6) \times 10^{-5}$. Table 1 provides molecular cloud properties with their statistical uncertainties as derived from the final fitting attempt when $\Delta\mu/\mu$ was set as a free parameter.

The analysis of H_2 absorption in the Q2348–011 spectrum yields a competitive result on $\Delta\mu/\mu$, but it is three times less tight compared to the constraints from previous analyses (see Fig. 1). One of the major causes that led to the relatively large uncertainty is the low S/N of the spectrum. The second cause is that the spectrum is obscured by the neutral hydrogen features of the additional strong DLA at $z = 2.62$. The H_2 transitions falling at the shortest wavelengths covered by the spectrum are especially useful in μ-variation analysis, since they exhibit the larger K-coefficients (transitions in the Lyman band with higher vibration excitation). In the spectrum of Q2348–011 they are not detected due to the H I absorption produced by the additional DLA. Although the total number of H_2 transitions available in this spectrum is reduced, it is at least partially compensated by the presence of numerous velocity components associated with each transition. Altogether, each transition contributes a higher information content when it is imprinted in several velocity components. The complex absorption structure was successfully modelled by means of the comprehensive fitting method.

4 Potential High-Redshift H_2 Absorbers for Future Detection of μ-Variation

Detection of cosmological μ-variation, or putting strong constraints on the variation, should preferably be based on large numbers of high redshift H_2 absorbing systems. For comparison the recent study on a possible spatial dipole for the fine structure constant α relies on the analysis of almost 300 absorbing systems [48].

Table 1 Parameters and 1-σ statistical uncertainties pertaining to the 7 + 1 VC fiducial fit model for the molecular hydrogen absorption in the Q2348–011 spectrum. The 8 velocity components are at redshifts z and have Doppler widths b. The second row gives the velocity relative to $z = 2.426318$ in units of km s^{-1}

VC	z	b	log $N(H_2)$ [cm^{-2}]					
	Δv [km s^{-1}]	[km s^{-1}]	J = 0	J = 1	J = 2	J = 3	J = 4	J = 5
1a	2.424509(1) -158	6.73 ± 0.15	15.27 ± 0.15	16.45 ± 0.05	15.50 ± 0.14	15.92 ± 0.07	15.30 ± 0.03	15.12 ± 0.02
1b	2.424546(4) -155	9.94 ± 0.29	15.45 ± 0.08	15.53 ± 0.40	15.79 ± 0.07	15.67 ± 0.10	–	–
2	2.424652(2) -146	1.25 ± 0.24	14.97 ± 0.12	16.98 ± 0.50	14.37 ± 0.27	14.77 ± 0.21	14.20 ± 0.06	13.62 ± 0.13
3	2.424929(2) -122	4.15 ± 0.33	14.29 ± 0.03	14.47 ± 0.05	14.51 ± 0.03	13.67 ± 0.34	12.95 ± 1.00	–
4	2.426582(1) +23	4.56 ± 0.13	15.66 ± 0.02	15.84 ± 0.10	15.60 ± 0.03	15.62 ± 0.04	14.29 ± 0.04	13.81 ± 0.11
5	2.426883(1) +50	2.97 ± 0.08	16.24 ± 0.08	17.98 ± 0.04	17.27 ± 0.10	16.99 ± 0.13	14.31 ± 0.08	14.08 ± 0.07
6	2.427136(1) +72	3.10 ± 0.12	14.72 ± 0.05	15.22 ± 0.03	14.93 ± 0.04	14.86 ± 0.06	14.09 ± 0.06	13.67 ± 0.16
7	2.427310(1) +87	4.36 ± 0.22	14.45 ± 0.05	15.27 ± 0.03	14.75 ± 0.05	15.09 ± 0.05	14.29 ± 0.04	13.89 ± 0.16

However, for H_2, up to now only five systems (Q0347–383, Q0405–443, Q0528–250, J2123–050 and Q2348–011) of sufficient quality are found, and the results obtained in comprehensive fitting procedures are summarized in Fig. 1. We note that alternative line-by-line fitting procedures on the Q0347–383 and Q0405–443 systems have recently been reported [41, 49, 50]. Taking the weighted mean of the H_2 results of Fig. 1 yields $\Delta\mu/\mu = (2.9 \pm 2.6) \times 10^{-6}$ for redshift ranges between $z = 2.0 - 3.1$, which may be considered as the status by September 2010. The data provide firm evidence that μ-variation is below the 10^{-5} level for look-back times in the range of 10-12 Gyrs.

A recent analysis of the J1337+315 spectrum by Srianand *et al.* [31] yielded a constraint only at the 10^{-4} level. This is due to the combination of low brightness of the quasar ($R_{mag} = 18.08$) and low H_2 content at the absorbing cloud ($\log_{10} N(H_2) = 14.1$). The present analysis of the Q2348–011 H_2 absorption system demonstrate, that even when the S/N of a spectrum is low, a competitive constraint on $\Delta\mu/\mu$ can still be delivered if other circumstances are favorable. In case of Q2348–011 the low S/N is compensated by the presence of at least 7 sufficiently strong velocity components. However, in this regard the Q2348–011 absorbing system is rather an exception than a rule. In other known DLAs H_2 absorption is usually detected in no more than three visually distinguishable spectral features.

This raises the question how many of the thousands of quasar systems on the sky (see Fig. 4 and [46]), of which there are some 1000 identified as DLAs could produce a competitive result, i.e. at the level $\delta(\Delta\mu/\mu) \leq 5 \times 10^{-6}$.

Based on our experience in analyzing spectra, we postulate that high quality H_2 absorption systems should obey the following conditions:

- An apparent magnitude of $V_{mag} < 18$ of the quasar background source for providing a SNR of about 50 after a reasonable amount of data collection (15–20 h).
- A column density of $N(H_2)$ preferably in the range between 10^{14} and 10^{18} cm^{-2} yielding sufficient but not too saturated H_2 absorption.
- An H_2 absorption system at redshift $z > 2$; only then a sufficient number of lines will shift into the atmospherically transparent window and the throughput

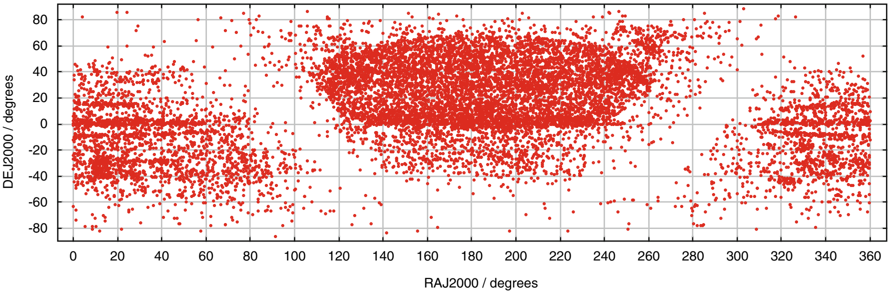

Fig. 4 Known quasars with magnitude $V < 18$ as obtained from [46]

window of Keck-HIRES and VLT-UVES; preferably some Werner lines should be observed for dealing with systematics [24].

- No occurrence of additional DLA's and only a limited amount of metal absorption systems along the same line of sight; the Q2348-011 absorber is an example of an unfavorable situation with an additional strong DLA and a few very strong HI absorbers, as well as several metal bearing systems.
- In principle, a firm constraint on the velocity structure of the H_2 absorber is only possible with the comprehensive fitting method. The present example of Q2348–011 demonstrates the applicability of this method in case of a complex structure with 7 velocity components. For line-by-line fitting methods the H_2 spectrum should preferably exhibit a single absorber; that a, e.g. two-component model, is statistically worse than a single component model should be demonstrated.

We have inspected the existing literature on high-redshift H_2 absorbers in order to identify possibly useful systems that may be targeted in future for μ-variation. In Table 2 all systems in which H_2 has been detected so far are listed. Relevant details for all systems, such as absorption and emission redshifts, their position on the sky,

Table 2 Listing of known high redshift H_2 absorption systems with some relevant parameters. Bessel R photographic magnitude taken from the SuperCOSMOS Sky Survey [8]. The five high-quality systems analyzed so far are offset. The column densities $N(\mathrm{H_2})$, $N(\mathrm{HD})$ and $N(\mathrm{H\,I})$ are given on a $\log_{10}$ scale in [cm^{-2}]

Quasars	z_{abs}	z_{em}	RA(J2000)	Decl.(J2000)	$N(\mathrm{H_2})$	$N(\mathrm{HD})$	$N(\mathrm{H\,I})$	R_{mag}	Ref.
Q0347−383	3.02	3.21	03:49:43.64	−38:10:30.6	14.5		20.6	17.48	[19,37]
Q0405−443	2.59	3.00	04:07:18.08	−44:10:13.9	18.2		20.9	17.34	[19,37]
Q0528−250	2.81	2.81	05:30:07.95	−25:03:29.7	18.2	[a]	21.1	17.37	[19]
J2123−005	2.06	2.26	21:23:29.46	−00:50:52.9	17.6	13.8	19.2	15.83	[24]
Q2348−011[b]	2.42	3.02	23:50:57.87	−00:52:09.9	18.4		20.5	18.31	[20,31][c]
Q0013−004	1.97	2.09	00:16:02.40	−00:12:25.0	18.9		20.8	17.89	[34]
HE0027−184	2.42	2.55	00:30:23.62	−18:19:56.0	17.3		21.7	17.37	[27]
Q0551−366	1.96	2.32	05:52:46.18	−36:37:27.5	17.4		20.5	17.79	[23]
Q0642−506	2.66	3.09	06:43:26.99	−50:41:12.7	18.4		21.0	18.06	[28]
FJ0812+320	2.63	2.70	08:12:40.68	+32:08:08.6	19.9	15.4	21.4	17.88	[5,42]
Q0841+129	2.37	2.48	08:44:24.24	+12:45:46.5	14.5		20.6	17.64	[33]
Q1232+082	2.34	2.57	12:34:37.58	+07:58:43.6	19.7	15.5	20.9	18.40	[14,45]
J1237+064	2.69	2.78	12:37:14.60	+06:47:59.5	19.2[d]	14.5	20.0	18.21	[29]
Q1331+170[e]	1.78	1.78	13:33:35.81	+16:49:03.7	19.7	14.8	21.2	16.26	[5,6]
Q1337+315	3.17	3.17	13:37:24.69	+31:52:54.6	14.1		21.4	18.08	[39]
Q1439+113	2.42	2.58	14:39:12.04	+11:17:40.5	19.4	14.9	20.1	18.07	[30]
Q1443+272	4.22	4.42	14:43:31.18	+27:24:36.4	18.3		21.0	18.81	[22]
Q1444+014	2.08	2.21	14:46:53.04	+01:13:56.0	18.3		20.1	18.10	[21]
Q2318−111	1.99	2.56	23:21:28.69	−10:51:22.5	15.5		20.7	17.67	[27]
Q2343+125	2.43	2.52	23:46:25.42	+12:47:43.9	13.7		20.4	20.18	[7,32]

[a] A recent re-analysis has shown that this system contains HD [18].

[b] Multiple DLAs in this system.

[c] Studied in this work for μ-variation.

the obtained column densities for H_2, HD and H I, and the magnitude are listed as well. Inspection of these systems leads to a quality assessment of the known H_2 absorber systems. Some of the systems can be discarded based on their low redshift (Q0551 − 366, Q2318 − 111, Q0013 − 004 and Q1331 + 170), on their low H_2 column density (Q2343 + 125 and Q1337 + 315), too low brightness, or combinations thereof. It should be noted that this assessment is linked to the status of present day technology. Future larger telescopes, or space-based telescopes equipped with high resolution spectrometers ($R > 50\,000$) may alter this view.

Based on the considerations given we have identified five quasar systems that have the potential to achieve a constraint at the $\delta(\Delta\mu/\mu) \leq 5 \times 10^{-6}$ level. These systems have been investigated to some extent, but larger numbers of exposures yielding better S/N, and ThAr attached calibration frames will be needed to reach the desired accuracy. Of the five systems, four have been observed with VLT-UVES, while one (FJ0812+320) has been studied with Keck-HIRES.

- **Q0642−506** with redshift $z_{abs} = 2.66$ provides a good number of H_2 lines with a high column density giving rise to saturation of only the strongest lines. The occurrence of only a single velocity components renders the spectrum relatively simple, also accessible for a line-by-line treatment. Spectra are shown in [28].
- **HE0027−184** is of similar good quality. It has a favorable magnitude and a molecular column density which allows for observation of a large number of lines to be observed. Indeed in the archived spectra with data observed in 2004 many lines are found, possible even up to $J = 6$ [27].
- **FJ0812+320** has a strong saturated H_2 component, which makes it less ideal. The system has been studied in particular for its abundant presence of the widest variety of metal lines [36] and of HD [5,42]. The system is nevertheless of importance because it is the only system of reasonable quality at northern declination, except for the special $z = 4.22$ system discussed below.
- **J1237+064** at $z_{abs} = 2.69$ shares some of the disadvantages of the previous system, in particular the very high column density giving rise to saturation. However, the velocity structure exhibits two weaker components, such that high-J lines can be obtained in the strong components, and the low-J lines in the weak components; HD is abundantly present and can be included in the analysis. This makes J1237+064 a target with a high potential. Further details on the system in [29].
- **Q1443+272** is a special case, and its unusually high redshift ($z_{abs} = 4.22$) alters some of the arguments. The system has a very low brightness, but that is partly compensated because the H_2 lines shift further into the visible, where scattering is less and CCD’s are more sensitive. In addition the high redshift shifts many more H_2 lines into the observable range. However, for these high redshift objects the Lyman-α forest becomes denser, which is a disadvantage. In summary this system has a good potential, if sufficient observation time is made available. Further details on the system in [22].

5 Conclusion

We have reviewed the status of investigations into variation of the proton-electron mass ratio from analyses of highly redshifted H_2 absorption systems. As of now five results have been obtained putting a tight constraint at the $\Delta\mu/\mu < 1 \times 10^{-5}$ level. We present spectroscopic data on the fifth H_2 absorption system, Q2348–011, and have show how a complex velocity structure can be unraveled using the comprehensive fitting method. An attempt is made to list in full all relevant quasar systems where H_2 has been observed so far, followed by an assessment as to which systems could produce a competitive result on $\Delta\mu/\mu$, provided that high-quality well-calibrated observations are performed.

Acknowledgements This work is based on observations carried out at the European Southern Observatory (ESO) under program ID 79.A-0404 (PI Ubachs), with the UVES spectrograph installed at the VLT Kueyen UT2 on Cerro Paranal, Chile. The authors wish to thank John Webb, Julian King and Steve Curran (Sydney), Adrian Malec (Melbourne) and Freek van Weerdenburg (Amsterdam) for fruitful discussions.

References

1. H. Abgrall, E. Roueff and I. Drira, Astron. Astrophys. Suppl. 141 (2000) 297.
2. H. Abgrall, E. Roueff, F. Launay and J.-Y. Roncin, Can. J. Phys. 72 (1994) 856.
3. J. Bagdonaite, M.T. Murphy, R. Buning, L. Kaper, W. Ubachs, to be published.
4. D. Bailly, E.J. Salumbides, M. Vervloet and W. Ubachs, Mol. Phys. 108 (2010) 827.
5. S.A. Balashev, A.V. Ivanchik and D.A. Varshalovich, Astron. Lett. 36 (2010) 761.
6. J. Cui, J. Bechtold, J. Ge and D.M. Meyer, Astrophys. J. 633 (2005) 649.
7. M. Dessauges-Zavadsky et al., Astron. Astroph. 416 (2004) 79.
8. N.C. Hambly et al., MNRAS 326 (2001) 1279.
9. S. Hannemann et al., Phys. Rev. A74 (2006) 062514.
10. C. Henkel et al., Astron. Astroph. 500 (2009) 725.
11. P.C. Hinnen, W. Hogervorst, S. Stolte and W. Ubachs, Can. J. Phys. 72 (1994) 1032.
12. P.C. Hinnen et al., Phys. Rev. A52 (1995) 4425.
13. U. Hollenstein, E. Reinhold, C. A. de Lange and W. Ubachs, J. Phys. B39 (2006) L195.
14. A.V. Ivanchik et al., MNRAS 404 (2010) 1583.
15. T.I. Ivanov et al., Mol. Phys 108 (2010) 771.
16. T.I. Ivanov et al., Phys. Rev. Lett. 100 (2008) 093007.
17. T.I. Ivanov, M.O. Vieitez, C.A. de Lange and W. Ubachs, J. Phys. B41 (2008) 035702.
18. J.A. King et al., to be published.
19. J.A. King, J.K. Webb, M.T. Murphy and R.F. Carswell, Phys. Rev. Lett. 101 (2008) 251304.
20. C. Ledoux et al., Astron. Astroph. 457 (2006) 71.
21. C. Ledoux, P. Petitjean and R. Srianand, MNRAS 346 (2003) 209.
22. C. Ledoux, P. Petitjean and R. Srianand, Astroph. J. Lett. 640 (2006) L25.
23. C. Ledoux, R. Srianand, P. Petitjean, Astron. Astroph. 392 (2002) 781.
24. A.L. Malec et al., MNRAS 403 (2010) 1541.
25. M.T. Murphy, V.V. Flambaum, S. Muller and C. Henkel, Science 320 (2008) 1611.
26. M.T. Murphy, P. Tzanavaris, J.K. Webb and C. Lovis, MNRAS 378 (2007) 221.
27. P. Noterdaeme et al., Astron. Astroph. 474 (2007) 393.
28. P. Noterdaeme, C. Ledoux, P. Petitjean and R. Srianand, Astron. Astroph. 481 (2008) 327.
29. P. Noterdaeme, P. Petitjean, C. Ledoux, S. Lopez, *et al.*, Astron. Astroph. **523**, A80 (2010).

30. P. Noterdaeme et al., Astron. Astroph. 491 (2008) 397.
31. P. Noterdaeme et al., Astron. Astroph. 469 (2007) 425.
32. P. Petitjean, C. Ledoux, P. Noterdaeme and R. Srianand, Astron. Astroph. 456 (2006) L9.
33. P. Petitjean, R. Srianand and C. Ledoux, Astron Astroph. 364 (2000) L26.
34. P. Petitjean, R. Srianand and C. Ledoux, MNRAS 332 (2002) 383.
35. J. Philip et al., Can. J. Chem. 82 (2004) 713.
36. J.X. Prochaska, J.C. Howk and A.M. Wolfe, Nature 423 (2003) 57.
37. E. Reinhold et al., Phys. Rev. Lett. 96 (2006) 151101.
38. E.J. Salumbides et al., Phys. Rev. Lett. 101 (2008) 223001.
39. R. Srianand et al., MNRAS 405 (2010) 1888.
40. R. Thompson, Astroph. Lett. 16 (1975) 3.
41. R.I. Thompson et al., Astroph. J. 703 (2009) 1648.
42. J. Tumlinson et al., Astroph. J. Lett. 718 (2010) L156.
43. W. Ubachs. R. Buning, K.S.E. Eikema and E. Reinhold, J. Mol. Spectr. 241 (2007) 155.
44. W. Ubachs and E. Reinhold, Phys. Rev. Lett. 92 (2004) 101302.
45. D.A. Varshalovich et al., Astron. Lett. 27 (2001) 683.
46. M.-P. Véron-Cetty and P. Véron, Astron. Astroph. 518 (2010) A10.
47. VPFIT software developed by R.F. Carswell; see http://www.ast.cam.ac.uk/~rfc/vpfit.html
48. J.K. Webb et al., arXiv:1008.3907.
49. M. Wendt, P. Molaro, Astron. Astroph. **526**, A96 (2010).
50. M. Wendt and D. Reimers, Eur. J. Phys. D Spec. Top. 163 (2008) 197.

Cosmological Birefringence: An Astrophysical Test of Fundamental Physics

Sperello di Serego Alighieri

Abstract We review the methods used to test for the existence of cosmological birefringence, i.e. a rotation of the plane of linear polarization for electromagnetic radiation traveling over cosmological distances, which might arise in a number of important contexts involving the violation of fundamental physical principles. The main methods use: (1) the radio polarization of radio galaxies and quasars, (2) the ultraviolet polarization of radio galaxies, and (3) the cosmic microwave background polarization. We discuss the main results obtained so far, the advantages and disadvantages of each method, and future prospects.

1 Introduction

Cosmological birefringence (CB)[1] deals with the possibility of a rotation of the plane of linear polarization for electromagnetic radiation traveling over large distances in the universe. This possibility arises in a variety of important contexts, like the presence of a cosmological pseudo-scalar condensate, Lorentz invariance violation and CPT violation, neutrino number asymmetry, the Einstein Equivalence Principle (EEP) violation. We refer the reader to [36, 37] for comprehensive reviews of these fundamental physical contexts and discuss here, in chronological order, the astrophysical methods that have been used to test for the existence of CB.

In general, what is needed to test for CB is a distant source of linearly polarized radiation, for which the orientation of the plane of polarization at the emission is known, and can therefore be compared with the one observed on Earth to see if it

---

[1] Reference [37] has argued that one should rather use the term optical activity, since birefringence refers to the two different directions of propagation that a given incident ray can take in a medium, depending on the direction of polarization. Although we agree with his comment in principle, we keep here the term that has been commonly adopted for the cosmological polarization rotation.

S. di Serego Alighieri
INAF – Osservatorio Astrofisico di Arcetri, Largo E. Fermi 5, Firenze, Italy
e-mail: sperello@arcetri.astro.it

C. Martins and P. Molaro (eds.), *From Varying Couplings to Fundamental Physics*,
Astrophysics and Space Science Proceedings, DOI 10.1007/978-3-642-19397-2_14,

has rotated during its journey. Since CB, if it exists, presumably increases with the distance traveled by the radiation, tests should use the most distant sources.

2 Radio Polarization of Radio Galaxies and Quasars

Reference [6] was the first to suggest to use the polarization at radio wavelengths of radio galaxies and quasars to test for CB[2]. It has used the fact that extended radio sources, in particular the more strongly polarized ones, tend to have their plane of integrated radio polarization, corrected for Faraday rotation, usually perpendicular and occasionally parallel to the radio source axis [11], to put a limit of 6.0^o at the 95% confidence to any rotation of the plane of polarization for the radiation coming from these sources in the redshift interval $0.4 < z < 1.5$.

Reanalyzing the same data, [38] claimed to have found a rotation of the plane of polarization, independent of the Faraday one, and correlated with the angular positions and distances to the sources. Such rotation would be as much as 3.0 rad for the most distant sources. However, several authors have independently and convincingly rejected this claim, both for problems with the statistical methods [7, 17, 31], and by showing that the claimed rotation is not observed for the optical/UV polarization of 2 radio galaxies (see the next section) and for the radio polarization of several newly observed radio galaxies and quasars [44].

In fact, the analysis of [44] is important also because it introduces a significant improvement to the radio polarization method for the CB test. The problem with this method is to estimate the direction of the polarization at the emission. Since the radio emission in radio galaxies and quasars is due to synchrotron radiation, the alignment of its polarization with the radio axis implies an alignment of the magnetic field. Theory and MHD simulations foresee that the projected magnetic field should be perpendicular to strong gradients in the total radio intensity [2, 40]. For example, for a jet of relativistic electrons the magnetic field should be perpendicular to the local jet direction at the edges of the jet and parallel to it where the jet intensity changes [4]. However such alignments are much less clear for the *integrated* polarization, because of bends in the jets and because intensity gradients can have any direction in the radio lobes, which emit a large fraction of the polarized radiation in many sources. In fact it is well known that the peaks at 90^o and 0^o in the distribution of the angle between the direction of the radio polarization and that of the radio axis are very broad and the alignments hold only statistically, but not necessarily for individual sources (see e.g. fig. 1 of [6]) . More stringent tests can be carried out using high resolution data and the local magnetic field's alignment for individual sources [44], although to our knowledge only once [29] this method has been used to put quantitative limits on the polarization rotation. For example, using

---

[2] Reference [3] had earlier claimed a substantial anisotropy in the angle between the direction of the radio axis and the direction of linear radio polarization in a sample of high-luminosity classical double radio sources, but used it to infer a rotation of the Universe, not to test for CB.

the data on the 10 radio galaxies of [29], reference [8] obtains an average constraint on any CB rotation of $\theta = -0.6^o \pm 1.5^o$ at the mean redshift $\langle z \rangle = 0.78$. However the comment by [29] remained unpublished and does not explain convincingly how the angle between the direction of the local intensity gradient and that of the polarization is derived. For example for 3C9, the source with the best accuracy, [29] refers to [28], who however do not give any measure of local gradients.

3 Ultraviolet Polarization of Radio Galaxies

Another test for CB uses the perpendicularity between the direction of the elongated structure in the ultraviolet (UV)[3] and the direction of linear UV polarization in distant powerful radio galaxies. The test was first performed by [10, 15], who obtained that any rotation of the plane of linear polarization for a radio galaxy at $z = 2.63$ is smaller than 10^o.

Although this UV test has sometimes been confused with the one described in the previous section, probably because they both use radio galaxies polarization, it is a completely different and independent test, which hinges on the well established unification scheme for powerful radio-loud AGN [1]. This scheme foresees that powerful radio sources do not emit isotropically, but their strong optical/UV radiation is emitted in two opposite cones, because the bright nucleus is surrounded by an obscuring torus: if our line of sight is within the cones, we see a quasar, otherwise we see a radio galaxy. Therefore powerful radio galaxies have a quasar in their nuclei, whose light can only be seen as light scattered by the interstellar medium of the galaxy. Often, particularly in the UV, this scattered light dominates the extended radiation from radio galaxies, which then appear elongated in the direction of the cones and strongly polarized in the perpendicular direction [14]. The axis of the UV elongation must be perpendicular to the direction of linear polarization, because of the scattering mechanism which produces the polarization. Therefore this method can be applied to any single case of distant radio galaxy, which is strongly polarized in the UV, allowing CB tests in many different directions. Another advantage of this method is that it does not require any correction for Faraday rotation, which is considerable at radio wavelengths, but negligible in the UV.

The method can be applied also to the polarization measured locally at any position in the elongated structures around radio galaxies, which has to be perpendicular to the vector joining the observed position with the nucleus. Using the polarization map in the V-band ($\sim$ 3000 Å rest-frame) of 3C 265, a radio galaxy at $z = 0.811$ [42], reference [44] obtain that the mean deviation of the 53 polarization vectors plotted in the map from the perpendicular to a line joining each to the nucleus is $-1.4^o \pm 1.1^o$. However usually distant radio galaxies are so faint that only the

---

[3] When a distant radio galaxy ($z > 0.7$) is observed at optical wavelengths ($\lambda_{obs.} \sim 5000$ Å), these correspond to the UV in the rest frame ($\lambda_{em.} \leq 3000$ Å).

integrated polarization can be measured: strict perpendicularity is expected also in this case, if the emission is dominated by the scattered radiation, as is the case in the UV for the strongly polarized radio galaxies [43].

Recently the available data on all radio galaxies with redshift larger than 2 and with the measured degree of linear polarization larger than 5% in the UV (at $\sim$ 1300 Å) have been re-examined, and no rotation within a few degrees in the polarization for any of these 8 radio galaxies has been found [16]. Also, assuming that the CB rotation should be the same in every direction, an average constraint on this rotation $\theta = -0.8^o \pm 2.2^o$ (1σ) at the mean redshift $\langle z \rangle = 2.80$ has been obtained [16]. The same data [16] have been used by [23] to set a CB constraint in case of a non-uniform polarization rotation, i.e. a rotation which is not the same in every direction: in this case the variance of any rotation must be $\left\langle \theta^2 \right\rangle \leq (3.7^o)^2$. It has also been noticed [33] that the CB test using the UV polarization has advantages over the other tests at radio or CMB wavelengths, if CB effects grow with photon energy (the contrary of Faraday rotation), as in a formalism where Lorentz invariance is violated but CPT is conserved [25, 26].

4 Cosmic Microwave Background Polarization

The most recent method to test for the existence of CB is the one that uses the Cosmic Microwave Background (CMB) polarization, which is induced by the last Thomson scattering of a decoupling photon at $z \sim 1100$, resulting in a correlation between temperature gradients and polarization [30]. After the first detection of CMB polarization anisotropies by DASI [27], there have been several CB tests using the CMB polarization pattern. Only the most recent ones are summarized here. The BOOMERanG collaboration, revisiting the limit set from their 2003 flight, find a CB rotation $\theta = -4.3^o \pm 4.1^o$ (68% CL), assuming uniformity over the whole sky [39]. The QUaD collaboration finds $\theta = 0.64^o \pm 0.50^o$ (stat.) $\pm 0.50^o$ (syst.) (68% CL) [5], while using two years of BICEP data one gets $\theta = -2.6^o \pm 1.0^o$ (stat.) $\pm 0.7^o$ (syst.) (68% CL) [9,41,45]. Combining 7 years of WMAP data and assuming uniformity, a limit to CB rotation $\theta = -1.1^o \pm 1.3^o$ (stat.) $\pm 1.5^o$ (syst.) (68% CL) has been set, or $-5.0^o < \theta < 2.8^o$ (95% CL), adding in quadrature statistical and systematic errors [24]. Therefore, although some have claimed to have detected a rotation [45], the CMB polarization data appear well consistent with a null CB. In principle the CMB polarization pattern can be used to test CB in specific directions. However, because of the extremely small anisotropies in the CMB temperature and polarization, these tests have so far used all-sky averages, assuming uniformity.

5 Other Methods

Observations of nearby polarized galactic objects could contribute to the CB test, in particular for those cases where polarization measurements can be made with high accuracy and at very high frequencies (useful if CB effects grow with photon energy). Pulsars and supernova remnants emit polarized radiation in a very broad frequency range. For example, hard X-ray polarization observations of the Crab Nebula [13] have been used to set a limit to CB rotation $\theta = -1^o \pm 11^o$ [32]. However this limit is not particularly stringent, both because of the low accuracy of the X-ray polarization measurement, and because of the limited distance to the source. Future more precise X-ray polarization experiments, such as POLARIX [12], could much improve the situation.

For an issue related to CB, reference [20] provides evidence that the directions of linear polarization at optical wavelengths for a sample of 355 quasars ($0 \leq z \leq 2.4$) are non-uniformly distributed, being systematically different near the North and South Galactic Poles, particularly in some redshift ranges. Such behaviour could not be caused by CB, since a rotation of randomly distributed directions of polarization could produce the observed alignments only with a very contrived distribution of rotations as a function of distance and position in the sky. Moreover the claim by [20] has not been confirmed by the radio polarization directions on a much larger sample of 4290 flat-spectrum radio sources [22].

The rotation of the plane of linear polarization can be seen as different propagation speeds for right and left circularly-polarized photons ($\Delta c/c$). The sharpness of the pulses of pulsars in all Stokes parameters can be used to set limits corresponding to $\Delta c/c \leq 10^{-17}$. Similarly the very short duration of gamma ray bursts (GRB) gives limits of the order of $\Delta c/c \leq 10^{-21}$. However the lack of linear polarization rotation discussed in the previous sections can be used to set much tighter limits ($\Delta c/c \leq 10^{-32}$, see ref. [19]).

In a complementary way to the astrophysical tests described in the previous sections, also laboratory experiments can be used to search for a rotation of the plane of linear polarization. These are outside the scope of this review. For example the PVLAS collaboration has found a polarization rotation in the presence of a transverse magnetic field [46]. However this claim has later been refuted by the same group, attributing the rotation to an instrumental artifact [47].

6 Comparison of the CB Test Methods

Table 1 summarizes the most important limits set on CB rotation with the various methods examined in the previous sections. Only the best and most recent results obtained with each method are listed. For uniformity, all the results for the CB rotation are listed at the 68% CL (1σ), except for the first one, which is at the 95% CL, as given in the original reference [6]. In general all the results are consistent with each other and with a null CB rotation. Even the CMB measurement by BICEP, which apparently shows a non-zero rotation at the 2σ level, cannot be taken as a firm CB detection, since it has not been confirmed by other more accurate measurements. Nevertheless we cannot but notice that most CB rotations have a negative value, although the most accurate measurement by QUAD has a positive one.

Table 1 Comparison of CB test methods

Method	CB rotation	Distance	Direction	Ref.
RG radio pol.	$\|\theta\| < 6^o$	$0.4 < z < 1.5$	all-sky (uniformity ass.)	[6]
RG radio pol.	$\theta = -0.6^o \pm 1.5^o$	$\langle z \rangle = 0.78$	all-sky (uniformity ass.)	[8,29]
RG UV pol.	$\theta = -1.4^o \pm 1.1^o$	z = 0.811	RA : 176.37^o, *Dec:* 31.56^o	[44]
RG UV pol.	$\theta = -0.8^o \pm 2.2^o$	$\langle z \rangle = 2.80$	all-sky (uniformity ass.)	[16]
RG UV pol.	$\langle \theta^2 \rangle \leq (3.7^o)^2$	$\langle z \rangle = 2.80$	all-sky (stoch. var.)	[16,23]
CMB pol. BOOMERanG	$\theta = -4.3^o \pm 4.1^o$	$z \sim 1100$	all-sky (uniformity ass.)	[39]
CMB pol. QUAD	$\theta = 0.64^o \pm 0.71^o$	$z \sim 1100$	all-sky (uniformity ass.)	[5]
CMB pol. BICEP	$\theta = -2.6^o \pm 1.2^o$	$z \sim 1100$	all-sky (uniformity ass.)	[9,41,45]
CMB pol. WMAP7	$\theta = -1.1^o \pm 2.0^o$	$z \sim 1100$	all-sky (uniformity ass.)	[24]

In practice all CB test methods have reached so far an accuracy of the order of 1^o and 3σ upper limits to any rotation of a few degrees. It has been however useful to use different methods since they are complementary in many ways. They cover different wavelength ranges, and, although most CB effects are wavelength independent, the methods at shorter wavelength have an advantage, if CB effects grow with photon energy. They also reach different distances, and the CMB method is unbeatable in this respect. However the relative difference in light travel time between $z = 3$ and $z = 1100$ is only 16%. The radio polarization method, when it uses the integrated polarization, has the disadvantage of not relying on a firm prediction of the polarization orientation at the source, which the other methods have. Also the radio method requires correction for Faraday rotation. All methods can potentially test for a rotation which is not uniform in all directions, although this possibility has not yet been exploited by the CMB method, which also cannot see how an eventual rotation depends on distance.

In the future improvements can be expected for all methods, e.g. by better targeted high resolution radio polarization measurements, by more accurate UV polarization measurements with the coming generation of giant optical telescopes [18,21,35], and by future CMB polarimeters such as PLANCK and POLARBEAR [34].

Acknowledgements I would like to thank Jan Browne for a useful discussion.

References

1. S. Antonucci, Ann. Rev. Astron. Astrophys. 31 (1993) 473.
2. M.C. Begelman, R. Blandford and M.J. Rees, Rev. Mod. Phys. 56 (1984) 255.
3. P. Birch, Nature 298 (1982) 451.
4. A.H. Bridle and R.A. Perley, Ann. Rev. Astron. Astrophys. 22 (1984) 319.
5. M.L. Brown et al., Astrophys. J. 705 (2009) 978.
6. S.M. Carroll, G.B. Field and R. Jackiw, Phys. Rev. D41 (1990) 1231.

7. S.M. Carroll and G.B. Field,, Phys. Rev. Lett. 79 (1997) 2394.
8. S.M. Carroll, Phys. Rev. Lett. 81 (1998) 3067.
9. H.C. Chiang et al., Astrophys. J. 711 (2010) 1123.
10. A. Cimatti, S. di Serego Alighieri, G.B. Field and R.A.E. Fosbury, Astrophys. J. 422 (194) 562.
11. J.N. Clarke, P.P Kronberg and M. Simard-Normandin, M.N.R.A.S. 190 (1980) 205.
12. E. Costa et al., Exp. Astron. 28 (2010) 137.
13. A.J. Dean et al., Science 321 (2008) 1183.
14. S. di Serego Alighieri, A. Cimatti and R.A.E. Fosbury, Astrophys. J. 431 (1994) 123.
15. S. di Serego Alighieri, G.B. Field and A. Cimatti, ASP Conf. Series 80 (1995) 276.
16. S. di Serego Alighieri, F. Finelli and M. Galaverni, Astrophys. J. 715 (2010) 33.
17. D.J. Eisenstein and E.F. Bunn, Phys. Rev. Lett. 79 (1997) 1957.
18. R. Gilmozzi and J. Spyromilio, Proc. of SPIE 7012 (2008) 701219.
19. M. Goldhaber and V. Trimble, J. Astrophys. Astr. 17 (1996) 17.
20. D. Hutsemekers et al.,, A& A 441 (2005) 915.
21. M. Johns, Proc. of SPIE 7012 (2008) 70121B.
22. S.A. Joshi et al., MNRAS 380 (2007) 162.
23. M. Kamionkowski, Phys. Rev. D82 (2010) 047302.
24. E. Komatsu et al., arXiv:1001.4538.
25. V.A. Kostelecký and M. Mewes, Phys. Rev. Lett. 87 (2001) 251304.
26. V.A. Kostelecký and M. Mewes, Phys. Rev. D66 (2002) 056005.
27. J.M. Kovac et al., Nature 420 (2002) 722.
28. P.P. Kronberg, C.C. Dyer and H.-J. Röser, Astrophys. J. 472 (1996) 115.
29. J.P. Leahy, astro-ph/9704285.
30. N.F. Lepora, arXiv:gr-qc/9812077.
31. T.J. Loredo, E.E. Flanagan and I.M. Wasserman, Phys. Rev. D56 (1997) 7507.
32. L. Maccione et al., Phys. Rev. D78 (2008) 103003.
33. M. Mewes (2010) priv. comm.
34. N.J. Miller, M. Shimon and B.G. Keating, Phys. Rev. D79 (2009) 103002.
35. J. Nelson and G.H. Sanders, Proc. of SPIE 7012 (2008) 70121A.
36. W.T. Ni, Prog. Theor. Phys. Suppl. 172 (2008) 49.
37. W.T. Ni, Rep. Prog. Phys. 73 (2010) 056901.
38. B. Nodland and J.P. Ralston, Phys. Rev. Lett. 78 (1997) 3043.
39. L. Pagano et al., Phys. Rev. D80 (2009) 043522.
40. D.J. Saikia and C.J. Salter, Ann. Rev. Astron. Asstrophys. 26 (1988) 93.
41. Y.D. Takahashi et al., Astrophys. J. 711 (2010) 1141.
42. H.D. Tran et al.,, Astrophys. J. 500 (1998) 660.
43. J. Vernetet al., A& A 366 (2001) 7.
44. J.F.C. Wardle, R.A. Perley and M.H. Cohen, Phys. Rev. Lett. 79 (1997) 1801.
45. J.-Q.Xia, H. Li and X. Zhang, Phys. Lett. , B687 (2010) 129.
46. E. Zavattini et al., Phys. Rev. Lett. 96 (2006) 110406.
47. E. Zavattini et al., Phys. Rev. D77 (2007) 032006.

ESO Future Facilities to Probe Fundamental Physical Constants

Paolo Molaro and Jochen Liske

Abstract Following HARPS, two ESO projects are aimed at the ambitious goal of trying to reach the highest possible precision in measuring the radial velocity of astronomical sources. ESPRESSO spectrograph, located at the incoherent combined 4VLT focus, but able to work either with one or all VLT units, and CODEX for E-ELT will mark ESO roadmap towards the cm s^{-1} level of precision and possibly to an unlimited temporal baseline. By providing photon noise limited measures their promise is to improve the present limits in the variability of fundamental physical constants by one and two orders of magnitude, respectively, thus allowing for instance to verify the claim discussed at this conference by John Webb of a possible spatial dipole in the variation of the fine structure constant.

1 Introduction

The variation of fundamental physical constants such as the fine structure and the proton-to-electron mass ratio is foreseen by several theories beyond the standard model of physics. Their variation could be due to some coupling of matter with scalar fields and implies a violation of the Equivalence Principle (Uzan, 2010). A most effective way to 3 measure a variability of the fine structure constant α or of the electron-to-proton ratio μ is by means of absorption lines in quasar spectra mainly in the optical range. However, variations are necessarily very tiny and would produce very small line shifts in the spectral lines whose detection is challenging presently available astronomical facilities.

P. Molaro
INAF-Osservatorio Astronomico di Trieste, Via G.B. Tiepolo 11 Trieste, Italy
e-mail: molaro@oats.inaf.it

J. Liske
ESO Karl-Schwarchild Strasse Munich, Germany
e-mail: jliske@eso.org

C. Martins and P. Molaro (eds.), *From Varying Couplings to Fundamental Physics*, Astrophysics and Space Science Proceedings, DOI 10.1007/978-3-642-19397-2_15,

Changes of one part per million in α or μ induce shifts of sensitive lines of about 20 m s^{-1}, which are somewhat ≈ 0.01 of the pixel sizes of high resolution spectrographs such as UVES or HIRES (Murphy et al. 2003, Thompson et al. 2009). It is well known that the positioning error of a simple gaussian line decreases with signal-to-noise, and with increasing spectrograph resolving power until the intrinsic line width is resolved. Landman et al. (1982) provided a convenient expression for the photon error in determining the centre of a gaussian line:

$$\sigma_0 = \frac{1}{(2\pi \ln 2)^{1/4}} \frac{1}{S/N} \sqrt{\Delta_{\rm pixel} {\rm FWHM}}.$$

Following HARPS, two projects have set the ambitious goal of trying to reach the highest possible precision in the radial velocity of astronomical sources. ESPRESSO for the VLT and CODEX for E-ELT will mark the ESO roadmap towards the cm s^{-1} level of precision and possibly to an unlimited temporal baseline as illustrated in Fig. 1.

In addition to photon noise there are errors of instrumental origin and other coming from the wavelength calibration. In particular, the latter could have been underestimated so far.

ThAr wavelength lines used in the present calibration system are known with a precision of 15 to 150 m s^{-1} thus setting an ultimate precision. There have been some claims that systematic errors can be of the order of 50–100 m s^{-1}, thus becoming the limiting factor dominant source of uncertainty for measures of $\frac{\Delta\alpha}{\alpha}$ with the ambition to reach the 1 ppm (parts-per-million) level accuracy (cfr Molaro 2010, these proceedings). Centurion et al. (2009) tested the presence of possible local wavelength calibration errors from the comparison of Fe II lines with almost identical sensitivity to fine structure constant changes. They found that deviations

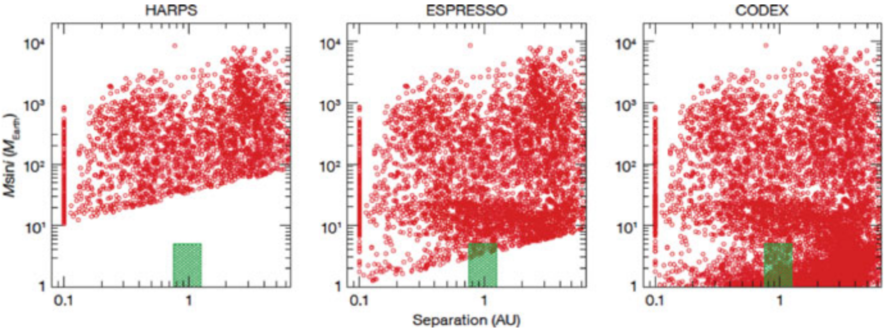

Fig. 1 Expected planet population at separations of 1 AU to be detected by Doppler spectroscopy with HARPS (precision 1 m s^{-1}), ESPRESSO/VLT (0.1 m s^{-1}) and CODEX/E-ELT (1 cm^{-1}) spectrographs. The figures are based on the predictions of the planet formation models for solar-mass stars by the Bern group. Note that stellar noise was considered to be reduced below instrumental noise. Spectrographs like ESPRESSO and CODEX are required to detect Earth-like planets in the habitable zone of solar-type stars (colored square area)

reaching 200 m s^{-1} or higher are present, which would correspond to a $\delta\alpha/\alpha$ of the order of $\geq 10^{-5}$. Griest et al. (2009) compared HIRES-Keck observations calibrated with ThAr with similar ones with a I_2 self-calibration spectrum and found significant and not reproducible deviations up to several hundreds m s^{-1} and similar, although somewhat smaller, deviations have been found in UVES by Whitman et al. (2010) by the same technique.

2 Laser Comb

A novel concept for wavelength calibration makes use of frequency laser comb. An IR laser produces a train of femtoseconds pulses synchronized with an atomic clock laser providing a series of uniformly spaced, very narrow lines whose absolute positions are known a priori with a relative precision of $\sim 10^{-12}$ (Murphy et al. 2007). The technical implementation is a joint collaboration between ESO and MPQ and a first prototype is expected around 2011. A first Laser Comb Wavelength calibration test was performed on HARPS at La Silla, ESO Chile, in January 2009 and a second one in June 2010.

The first test was limited onto one single order only (order N. 42) and showed wavelength calibration residuals with a particular structure as shown in Fig. 2. Sudden jumps are present every 512 pixels, which are likely originated by the 512 pixel mask used in the CCD manufacturing process (Wilken et al. 2010). Every 512 pixel, slightly smaller pixels occur and the ThAr wavelength calibration adapts to these defects by becoming locally unreliable with local departures up to 100 m s^{-1} within

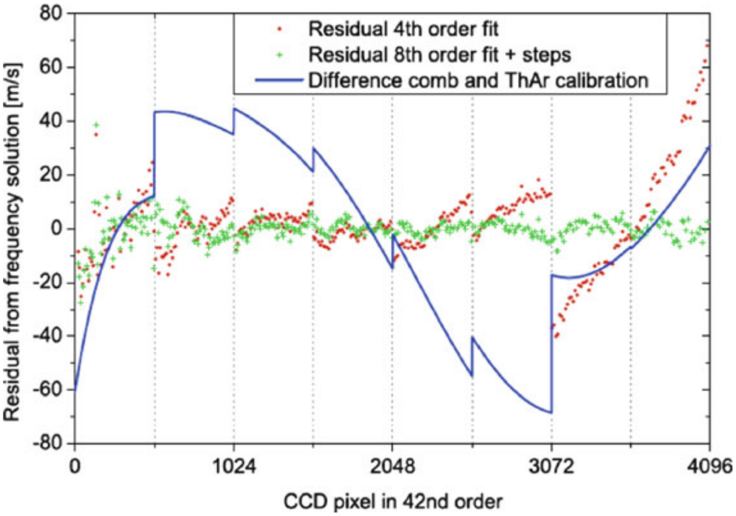

Fig. 2 Laser-Comb versus ThAr revealing large deviations in HARPS (rom Wilken et al. 2010)

one order range. It has to be noted that this occurs in a spectrograph which is delivering an overall accuracy of 1 m $s^{-1}$when using the whole spectrum. Considering that CCDs are manufactured in similar ways it is quite possible that similar problems are affecting also UVES and HIRES accounting for what observed by Griest et al. (2010) or Whitman et al. (2010). A deviation of 100 m s^{-1}would correspond to $\delta\alpha/\alpha \approx\ 7 \cdot 10^{-6}$ for a Fe II-Mg II pair. These results suggest that wavelength calibration issues are more serious than generally considered. In June 2010 a significant widening of the comb was achieved covering 23 orders from 470 to 580 nm providing about 11000 useful lines and a global overall photon noise in the radial velocity of 4 cm s^{-1}. Since the laser frequency comb provides an absolute wavelength calibration it will enable direct inter-instrument data comparisons, including future instruments, thus opening up the time domain beyond the life-time of a single instrument. The implementation of a locally reliable wavelength calibration tool such as the Laser Comb will revolutionise this field of research.

2.1 Espresso

The Echelle SPectrograph for Rocky Exoplanets and Stable Spectroscopic Observations (ESPRESSO) is a project for a high-resolution, fiber-fed spectrograph of high mechanical and thermal stability which can be operated with one or up to 4 UTs of the ESO VLT. With the formal endorsement by ESO Council in June 2010 the project, started in 2007, is now under a post phase A study. The consortium is lead by Francesco Pepe, Observatoire of Geneve, in a collaboration with the INAF-Observatories of Trieste and Milano, the Instituto de Astrofisica de Canarias, the Universities of Porto and Lisbon and ESO. ESPRESSO will adopt several of the properties of HARPS design which proved crucial in order to deliver accurate radial velocities, namely the spectrograph will be fiber-fed, the location inside a stable environment, enclosed inside a vacuum tank under temperature and pressure controlled with no human access.

ESPRESSO will be located in the Combined-Coudé laboratory of the VLT (cfr Fig. 3) and it will be the first instrument able to use a 16-m equivalent telescope, even though such a possibility was originally conceived back in the 70's. As such, the 4-UT mode is expected to offer a gain of about 1.2-1.5 mag compared to UVES and will make science which today is prevented by the readout-limited regime. In the 1-UT mode, ESPRESSO can be fed by any of the four UTs which extend the operational flexibility and optimize the use of VLT.

A Coudé train brings the light from the B Nasmyth platform of each VLT unit to the combined Coudé room, where a front-end unit can combine the light from up to 4 VLT units (cfr Fig. 4). The distances from each telescope to the combined focus are considerable, from 48 m of UT2 to the 69 m of UT1, and several options are presently considered from full optical components or long fibres or even hybrid solutions with transmission efficiencies of about 80% along most of the optical range.

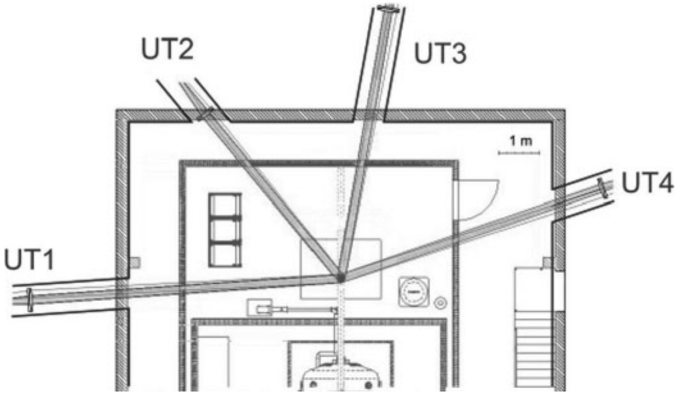

Fig. 3 Incoherent Coudé laboratory with the four beams arriving from the 4 VLT units. ESPRESSO will be the first instrument able to use a 16-m equivalent telescope

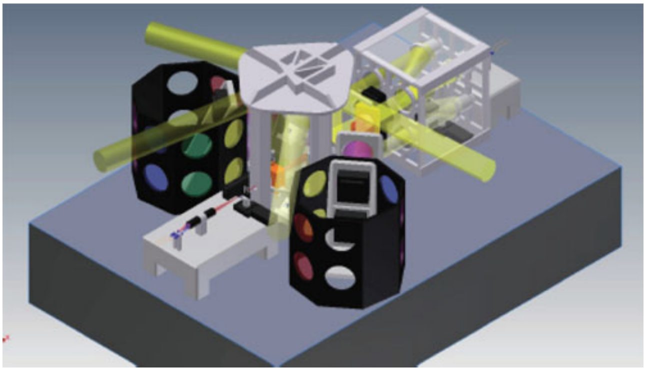

Fig. 4 Front-end unit which combine the light from up to 4 VLT units

The instrument acquisition and guide system collect it into a fiber which then feeds the spectrograph.

A possible spectrograph basic concept is a cross dispersed echelle with two arms, blue and red respectively, which are optimized for image quality and optical efficiency as shown in Fig. 5. At the entrance of the spectrograph an anamorphic pupil slicing unit compresses the beam in the cross-dispersion direction but not in the dispersion direction to provide high resolving power. The beam is then sliced and superimposed onto the echelle grating to minimize its size. In this way a compact design is obtained, and a 20 cm optical beam and a 20 × 160 cm echelle provide the resolving power of an un-sliced 40 cm beam spectrograph. The rectangular white pupil is the re-imaged and compressed onto 2 large 90 × 90 mm CCDs. The design allows a dual fiber system: while one fiber is on source, the second one can be used either to record the sky or a calibration source to monitor spectrograph shifts.

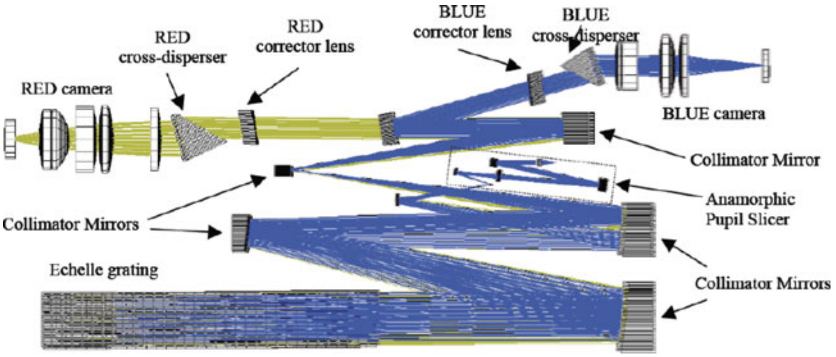

Fig. 5 ESPRESSO Optical two arm design, both optimized for image quality and optical efficiency

One critical item is the light input system, which must scramble the signal to ensure that the variability at the fiber input does not degrade the stability of the spectrograph, still keeping an excellent transmission. A stabilization system in the fiber head will compensate for seeing and tracking instabilities to ensure that a photon's position on the CCD only depends on its wavelength but not on its position on the entrance aperture. This component is rather critical, because at a resolution of 150 000 a typical pointing accuracy of $\sim$ 0.05 arcsec corresponds to an error of 100 m s^{-1} which requires a scrambling gain of $\sim$ 5000 in order to reach 2 cm s^{-1} accuracy. In particular, octagonal fibers show better properties than conventional round ones. In the 4-UT case there are 4 independent pupils and scrambling will occur after combining the light from the sub-pupils.

A recent realization of precision measurements is that CCD are alive and *breath*: HARPS shows radial velocity variations with changes of detector temperature due to the expansion of the detector along the attachments of the mosaic of CCDs to their support. CCD differential movements in the detector are of the order of 0.02 pixel/K or 0.10 m s^{-1} for 10 mK. These effects require a new temperature control of the CCD and a new super stable cryostat which are under study.

Opto-mechanical stability is obtained through a controlled environment in vacuum, avoiding movable components and containing the instrument volume and the size of optics. In UVES a thermal change of 0.1K or 0.1 mBar induces a radial velocity shift of about 20 m s^{-1} which depends on the settings, so that the required stability is of the order of 10^{-3} K or mBar. Simulations of both pre-assembled and assembled spectrograph are shown in Figs. 6 and 7.

With all these innovative solutions for the investigation of variability of fundamental constants ESPRESSO will be a limited photon noise instrument. The expected efficiencies are shown in Fig. 8. In the 1-UT mode a SNR of 30 is obtained with 1 exposure of 1 hour on a V $=$ 16 mag QSO. This will give a precision of about 30 m s^{-1} or a sensitivity of $\delta\alpha/\alpha \approx 1 \cdot 10^{-6}$. In the 4 UT mode with a binning of 4x2 and Resolution of 60000 a SNR of 50 will be obtained for a V $=$ 17.5 mag QSO

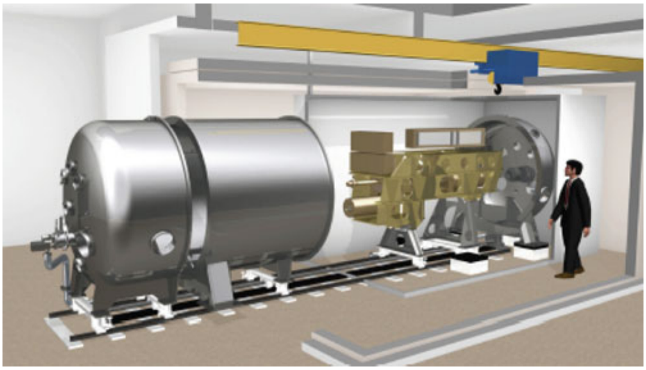

Fig. 6 ESPRESSO size and dimensions when open in the pre-assembly phase

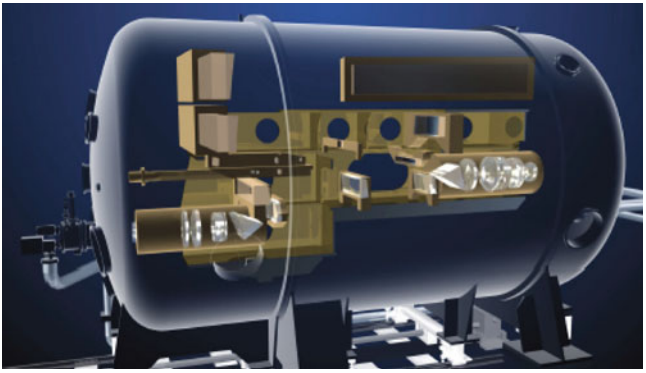

Fig. 7 ESPRESSO after assembling. The opto-mechanical stability is obtained through a controlled vacuum environment, avoiding movable components and minimizing the volume and size of the optics

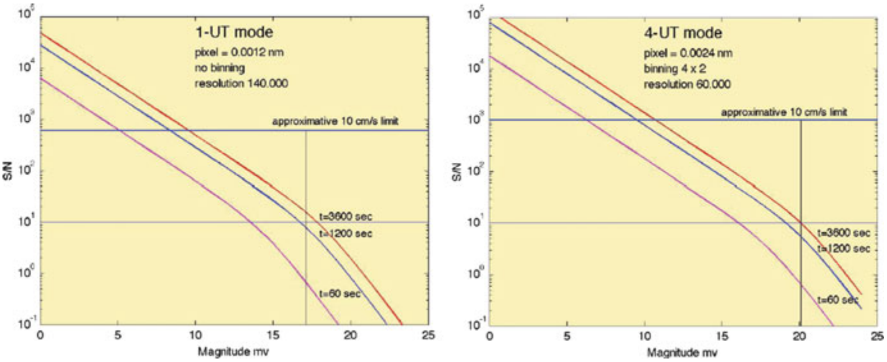

Fig. 8 Estimated performances of ESPRESSO in the 1-UT mode and in the 4-UT mode with a binning of 4x2. The 10 cm s^{-1} limit is shown for reference

providing almost the same precision of 30 m $s^{-1}$and thus allowing he observation of a significant sample of systems with the same precision.

3 Codex

CODEX, COsmic Dynamics EXperiment, is a concept for an extremely stable, high-resolution optical spectrograph for the European Extremely Large Telescope (E-ELT), a nasmyth telescope with a Coudé and a segmented primary mirror composed of 984 segments of 1.4 m to produce a 42 m diameter (Pasquini et al. 2005). The science case for CODEX encompasses a wide range of topics, including the search for exo-planets down to earth-like masses, for primordial nucleosynthesis and include the possible variation of fundamental constants. However, its prime science driver is the exploration of the universal expansion history by detecting and measuring the cosmological redshift drift using QSO absorption lines as foreseen by Allan Sandage (1962).

In order to achieve its science goals CODEX will have to deliver an exceptional radial velocity accuracy and stability, i.e. 2 cm s^{-1} over a timescale of $\sim$ 20 yr. Thus the spectrograph will certainly produce valuable results for searching changes of fundamental constant values. CODEX will represent a major development of high-resolution optical spectrographs compared to existing instruments such as UVES and HARPS.

Although the basic design concepts are already in place, several of the subsystems needed to achieve these requirements do not currently exist. Some of them will be implemented for the first time in ESPRESSO, which is a sort of CODEX precursor instrument that will allow us to test and gain experience with the novel aspects of these instruments. The spectrograph design contains several novel concepts, and makes use of pupil splitting and anamorphism in order to keep the dimensions of the optics and of the echelle grating reasonable. The diameter of the largest camera lens is 35 cm and the echelle grating is only twice the UVES size: 20 × 160 cm. The two arm design was chosen to optimize the efficiency and to keep each detector 's size limited; for the same purpose slanted VPHs are used as cross-dispersers, and they produce an anamorphism of a factor 1.5 to 2.5 perpendicular to the main dispersion.

In the E-ELT Coudé focus the light is collected by a fairly complex fibre interface, guiding and a tip-tilt correcting system, which accurately centers the object into the 500 μm fibre core. There is only one 500 microns at F/3 fibre entering the spectrograph and a second one dedicated to record the sky. This system is also containing the ADC instrument and the interface to the calibration system. The light in the fibre is scrambled, to allow the output signal to be independent of any input variation. Then the light is brought by the fibres into the spectrograph vessel, where no active functions are present. In the spectrograph, the pupil is made highly anamorphic and is sliced in 6 parts, which pass through the echelle spectrograph and collimating system to be divided into two separate paths (Blue and Red), each

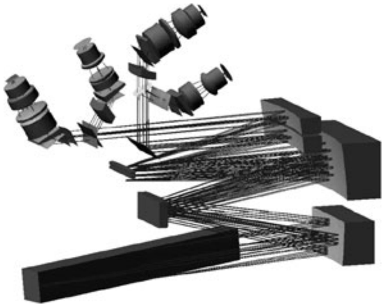

Fig. 9 CODEX spectrograph optical concept

imaged onto two separate cameras and to 9 cm × 9 cm monolithic detectors. Fig. 9 shows the optical concept. The pupil has an anamorphism by a factor 12, and it is split in 6 parts, grouped in 2 slits. Each of the two slits is separated by a dichroic into a red and a blue spectrum, after cross-dispersion obtained with a slanted VPH. With anamorphosis by a factor 2 the image is collected by an F/2.2 camera. The mechanical concept extrapolates from the HARPS experience: it obtains the highest mechanical and thermal stability to minimize the effects to be corrected for, and a spectrograph in a mild vacuum. Our analysis claims for a thermal environment which gets progressively more stable, to reach the 10 mK within the spectrograph, and 1 mK in the CCD. No movable parts are allowed in the spectrograph vessel. Special care is taken about the design of the detector head to keep it very stable, both thermally and mechanically, for instance by using continuous flow of nitrogen to cool the CCD. The optics is mounted on three optical benches, and special care is taken to select the material and its process, which is always the same to avoid differential thermal expansion. Fig. 10 shows a picture of the spectrograph vessel. The dimensions of the whole spectrograph are less than 4(l) × 2(w) × 3(h) meters. This design has some very attractive parts. In particular it is compact and of reasonable costs, and is the preferred one at the moment.

4 Conclusions

The current measurements of α and μ are performed in the best cases at the limit of few $\delta\alpha/\alpha \approx 10^{-6}$ with the limit coming by systematic errors in the measure. In particular, uncertainties originated in the wavelength calibration process and the use of slit spectrographs with their unavoidable slit off-centering leading to radial velocity shifts seem the most important ones. The new calibration technique based on the Laser Comb when available will significantly improve the understanding of this systematic. Laser comb and specifically designed fiber-fed HARPS-like spectrographs should thereby enable photon noise-limited measurements.

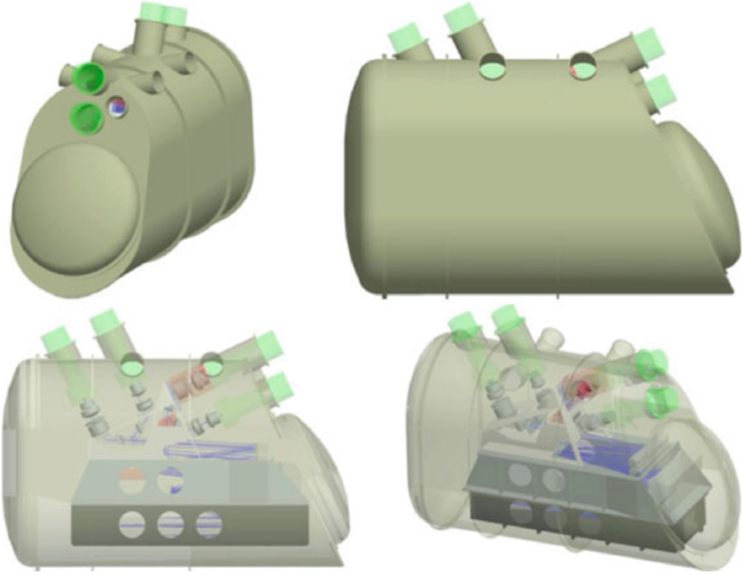

Fig. 10 CODEX vacuum vessel. Dimensions are 4(l)x2(w)x3(h) m

The large collecting power of the combined VLT, at first, and of the E-ELT, later on, will thus reduce the photon noise of these measurements allowing to break present limits by one or two orders of magnitude, respectively, unless astronomical limits related to the astronomical sources do not arise before. CODEX at E-ELT should enter in a new and so far unexplored regime, possibly disclosing other tiny and puzzling effects imprinted in the fundamental constant values.

Acknowledgements I am grateful to both the ESPRESSO and CODEX collaborations for the excellent work done and for allowing me to present some results before publication. The ESPRESSO team is composed by Francesco A. Pepe (PI), Stefano Cristiani, Rafael Rebolo Lopez, Nuno C. Santos, Antonio Amorim, Gerardo Avila, Willy Benz, Piercarlo Bonifacio, Alexandre Cabral, Pedro Carvas, Roberto Cirami, João Coelho, Maurizio Comari, Igor Coretti, Vincenzo De Caprio, Hans Dekker, Bernard Delabre, Paolo Di Marcantonio, Valentina D'Odorico, Michel Fleury, Ramón Garcia López, José Miguel Herreros Linares, Ian Hughes, Olaf Iwert, Jorge Lima, Jochen Liske, Jean-Louis Lizon, Gaspare Lo Curto, Christophe Lovis, Antonio Manescau, Carlos Martins, Denis Mégevand, André Moitinho, Paolo Molaro, Mario Monteiro, Manuel Monteiro, Christoph Mordasini, Luca Pasquini, Didier Queloz, José Luis Rasilla, Jose Manuel Rebordão, Samuel Santana Tschudi, Paolo Santin, Danuta Sosnowska, Paolo Spanó, Fabio Tenegi, Stéphane Udry, Eros Vanzella, Matteo Viel, Maria Rosa Zapatero Osorio, Filippo Zerbi.

The CODEX team is composed by Luca Pasquini (PI), Stefano Cristiani, Ramón Garcia-Lopez, Martin Haehnelt, Michel Mayor, Gerardo Avila, George Becker, Piercarlo Bonifacio, Bob Carswell, Roberto Cirami, Maurizio Comari, Igor Coretti, Gaspare Lo Curto, Hans Dekker, Bernard Delabre, Miroslava Dessauges, Paolo di Marcantonio, Valentina D'Odorico, Artemio Herrero, Garik Israelian, Olaf Iwert, Jochen Liske, Christophe Lovis, Antonio Manescau, Denis Mégevand, Paolo Molaro, Dominique Naef, Maria Rosa Zapatero Osorio, Francesco Pepe, Rafael Rebolo, Marco Riva, Paolo Santin, Paolo Spanó, Fabio Tenegi, Stéphane Udry, Eros Vanzella, Matteo Viel, Filippo Maria Zerbi. It is a pleasure to acknowledge Sergei Levshakov for many helpful discussions on the topic.

When we were writing these proceedings, we received the news that Allan Sandage passed away. We would like to recall that during his whole life spent inspiring research, it was Allan who set the idea of the direct measure of cosmic expansion. With CODEX we hope to realize in the next decades what he envisaged almost half a century ago.

References

1. Centurión, M.; Molaro P., Levshakov, S. A. Memorie SAIt 80, 929 (2009)
2. Griest, K., Whitmore, J.B., Wolf, A. M., Prochaska, J. X., Howk, J. et al.. 2009, arXiv:0904.4725
3. Murphy, M. T.; Webb, J. K.; Flambaum, V. V. 2003, MNRAS 345,609
4. Wilken, T., Lovis, C., Manescau, A., Steinmetz, T., Holzwarth, R., Paquini, L., Lo Curto, G., Hansch, T.W., Udem, Th. 2010, MNRAS 405, 16
5. Landman, D. A., Roussel-Dupre, R., & Tanigawa, G., Astrophys. J., 261, 732 (1982).
6. Murphy, M.T. Webb, J.K., Flambaum, V. V. astro-ph/0612407(2007)
7. Pasquini, L., et al. 2005, The Messenger 122
8. Sandage, A. 1962 Ap.J. 136, 319
9. Thompson, R. I., Bechtold, J., Black, J. H., Martins, C. J. A. P. New Astronomy, 14, 379 2009
10. Whitmore, J., B., Murphy, M., T., Griest, K., 2010 ApJ 723, 89
11. Uzan, J. P., 2010 arXiv:1009.5514

Starless Cores as Fundamental Physics Labs

Arturo Mignano, Paolo Molaro, Sergei Levshakov, Miriam Centurión, Giuseppe Maccaferri, and Alexander Lapinov

Abstract We present high resolution observations in the starless dense molecular core L1512 performed with the Medicina 32m radio telescope. The resolved hfs components of HC_3N and NH_3 show no kinematic sub-structure and consist of an apparently symmetric peak profile without broadened line wings or self-absorption features suggesting that they sample the same material. The velocity dispersion is $101(\pm 1)$ m $s^{-1}$for NH_3 and $85(\pm 2)$ m s^{-1} for HC_3N. The kinetic temperature of the cloud is estimated at 9.2 (± 1.2) K and the turbulence is of 76 m s^{-1}in a subsonic regime. This places L1512 among the most quiescent dark cores and makes it an ideal laboratory to study variations of the electron-to-proton mass ratio, $\mu = m_e/m_p$ by means of observations of inversion lines of NH_3 combined with rotational lines of other molecular species.

A. Mignano
INAF-Istituto di Radio Astronomia, Via P. Gobetti 101, Bologna, Italy
e-mail: amignano@ira.inaf.it

P. Molaro
INAF-Osservatorio Astronomico di Trieste, Via G.B. Tiepolo 11 Trieste, Italy
e-mail: molaro@oats.inaf.it

S. Levshakov
Ioffe Institute Politekhnicheskaya Str. 26, 194021St. Petersburg, Russia
e-mail: lev.astro@mail.ioffe.ru

M. Centurión
INAF-Osservatorio Astronomico di Trieste, Via G.B. Tiepolo 11 Trieste, Italy
e-mail: centurion@oats.inaf.it

G. Maccaferri
INAF-Istituto di Radio Astronomia, Via P. Gobetti 101, Bologna, Italy
e-mail: maccaferri@ira.inaf.it

A. Lapinov
Institute for Applied Physcis, Ulianov Str. 46, 603950 Nizhny Novgorog, Russia
e-mail: lapinov@appl.sci-nnov.ru

C. Martins and P. Molaro (eds.), *From Varying Couplings to Fundamental Physics*,
Astrophysics and Space Science Proceedings, DOI 10.1007/978-3-642-19397-2_16,

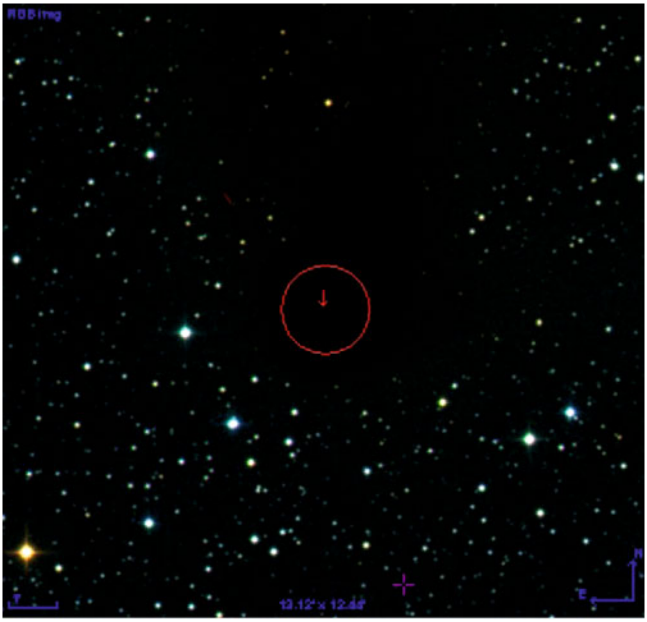

Fig. 1 The roundish silhouette of L1512 against the background Galactic starlight. Red circle shows the half-power beam width at 23 GHz

1 Introduction

Hier ist wahrhaftig ein Loch im Himmel! exclaimed William Herschel when discovering the Ophiuchus cloud as it is recorded in the observation notebook by Caroline, who was taking notes of her brother's observations in 1784.

Indeed some dense molecular cores are starless, and are not associated with any young stellar object, and show outstanding simple physical properties. They are still approaching the point of gravitational instability that leads to the formation of a low-mass star and lie at the bottom of the hierarchy of physical complexity. The kinetic temperature is $T_{\rm kin} \sim 10$ K, the gas number density $n_{\rm H_2} \sim 10^5$ cm^{-3}, the total mass is of 0.5-5 M$_{sun}$ and sizes between 0.03-0.2 pc. In the central region (5000-1000 AU) the cores have close-to-constant density of $\sim 10^5$ cm^{-3}. In contrast with their relatively simple physical structure, the dense cores show a complex chemical composition. Several molecules such as NH_3, CO, N_2H^+, N_2D^+, HC_3N, etc. are detected.

Observations of inversion lines of NH_3 combined with rotational lines of other molecular species offer the means to probe changes of the electron-to-proton mass ratio, $\mu = m_{\rm e}/m_{\rm p}$ (Flambaum & Kozlov 2007). A quantum tunneling effect makes the ammonia inversion spectrum very sensitive to the molecular mass and to the μ ratio. The masses of the elementary particles such as the electron $m_{\rm e}$ and the quarks

m_q are proportional to the Higgs VEV, and the mass of the composite particle proton m_p is mainly proportional to Λ_{QCD}. Thus by measuring NH_3 inversion frequencies in dark clouds it is possible to probe the ratio of the electroweak-to-strong scale in remarkably different physical conditions from Earth laboratories.

In a series of papers (Levshakov *et al.* 2008; Molaro *et al.* 2009; Levshakov *et al.* 2010a) we performed this experiment and, rather surprisingly, we found a possible change of $\Delta\mu/\mu = 26 \pm 1_{stat} \pm 3_{sys} \times 10^{-9}$. The signal could be interpreted as evidence of the presence of a light scalar field coupling with matter. However, the coupling is strong and requires a Chameleon mechanism to evade the conflict with Earth laboratory bounds. In chameleon theories the range of scalar fields depends onto the ambient density and the dense cores provide an accessible environment with the largest difference of local densities from those on earth and terrestrial laboratories. The local density in the dense cores is $\rho_{\rm space} \approx 3 \times 10^{-19}$ g cm^{-3}. Vacuum spectrographs in the laboratories usually operate with pressures of 1-10 mtorr and temperatures of $T_{\rm kin} \sim 10 - 40$ K giving $\rho_{\rm lab} \approx 3 \times 10^{-9}$ g cm^{-3} (H_2 chamber $T_{\rm kin} = 10$ K, $P = 1$ mtorr). Thus the ratio is of $\rho_{\rm lab}/\rho_{\rm space} \geq 10^{10}$. Moreover, the vacuum chambers are rather small with typical sizes of $\sim$ 10 cm. The chamber walls are made of heavy materials originating a gravitational field quite differently from the dark clouds, since chameleon fields are sensitive to the high density boundaries of the chamber and experimental apparatus (Khoury and Weltman 2004).

Here we show extremely high resolution radio observations for a study of the physical conditions of the dark core L1512 showing that it is one of the most quiescent dark clouds.

2 Observations and Data Reduction

The L1512 dark cloud (shown in Fig. 1) lies in the Taurus-Auriga-Perseus molecular complex, approximately located 140 pc away. The ammonia peak position is at $\alpha_{1950} = 5^h0^m54^s$, $\delta_{1950} = 32°29'0''$ (Meyers and Benson, 1983). The mean LSR velocity of L1512 is 7.1 Km s^{-1}. L1512 was selected because of the presence of narrow and sufficiently strong molecular lines showing hyperfine transitions, thus suggesting low kinetic temperatures.

We performed radio observations at the Medicina 32-m telescope in February 2010, by using the digital spectrometer ARCOS (ARcetri COrrelation Spectrometer). We observed NH_3(1-1) with a channel separation of 5 kHz, corresponding to 60 m s^{-1} at the ammonia inversion transition (23.694 GHz) and in high resolution mode with channels of 1.25 kHz corresponding to 20 ms^{-1} for the rotational HC_3N (2–1) line (18.196 GHz). The Medicina 32-m angular resolution is $\sim 1.6'$ at 23 GHz and $\sim 2.1'$ at 18 GHz.

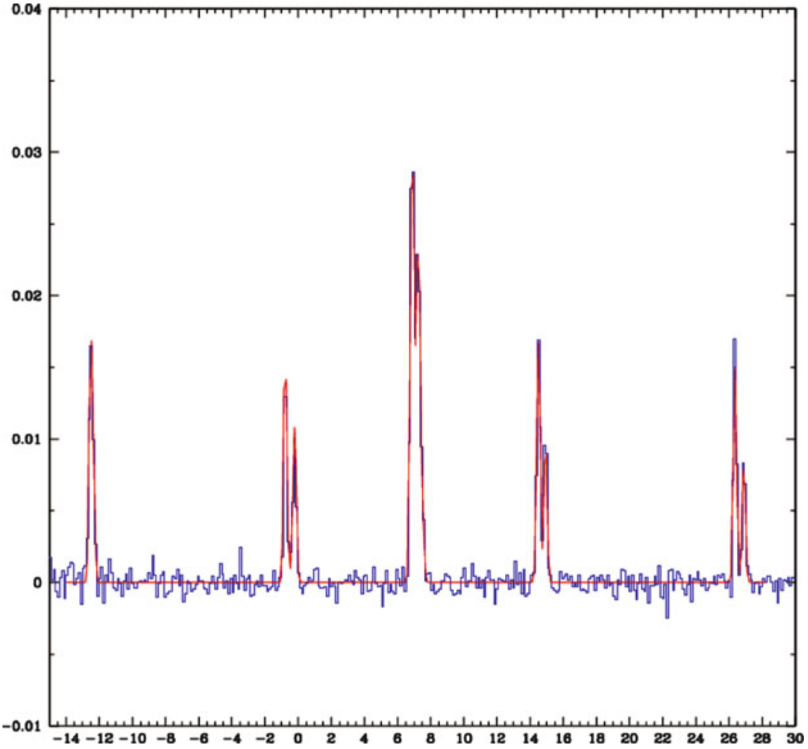

Fig. 2 Low resolution spectrum of NH_3 showing the whole comb spectrum with 18 hyperfine structure components partially resolved. The red continuous line is the model fitting

3 The Spectra

We used the CLASS reduction package[1] for standard data reduction. After corrections for the rounded frequencies, the individual exposures were co-added to increase the signal-to-noise ratio, S/N. In Fig. 2 we present a low resolution $NH_3(1,1)$ spectrum, while in Fig. 3 a high resolution HC_3Nspectrum is shown.

The resolved hfs components show no kinematic sub-structure and consist of an apparently symmetric peak profile without broadened line wings or self-absorption features, as shown in Fig. 4.

4 Temperature and Turbulence

Starless cores should be coupled to the surrounding gas in the region, and hence their motion should reflect the motion of the ambient material. In general, N-bearing molecules trace the inner core, whereas C-bearing molecules occupy the outer part,

---

[1] http://www.iram.fr/IRAMFR/GILDAS

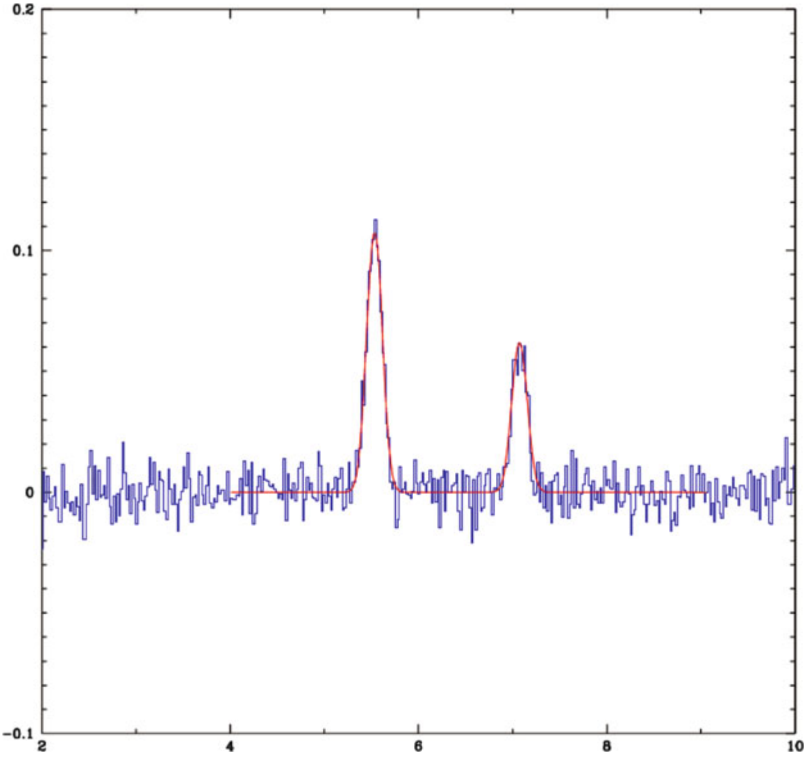

Fig. 3 High resolution spectrum of HC_3N

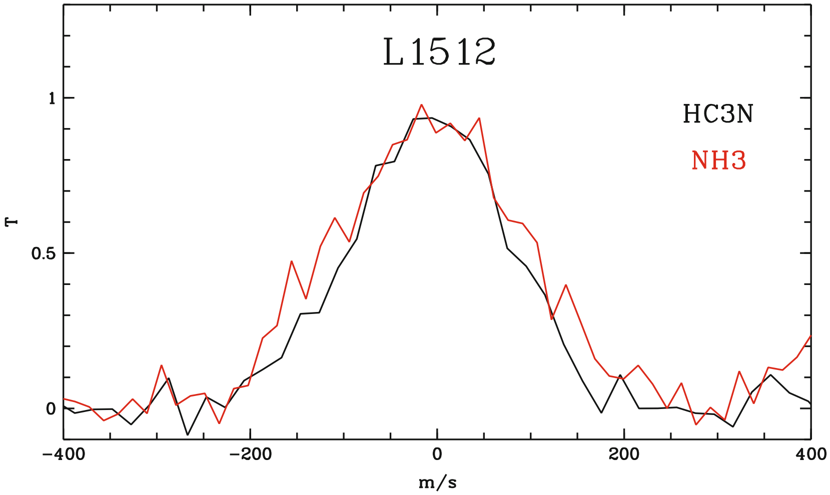

Fig. 4 L1512, HC_3N and NH_3 line profiles overlaid. The two lines have been re-normalized in intensity and shifted in radial velocity for display purposes

thus HC_3N is usually distributed in a larger volume of the molecular core as compared with NH_3. Such a chemical differentiation and velocity gradients within the core may cause a larger non-thermal component in the velocity distribution of HC_3N. If dense cores move ballistically, the differences in the line-centre velocities between the cores and envelopes are expected to be significant (Walsh *et al.* 2004), but this is not observed in L1512.

The kinematic state of the core gas can be deduced from the spectral line width from molecules present in the core. The gas temperature in a molecular cloud is determined by the balance between heating and cooling. If the cloud is shielded from the external incident radiation, the gas temperature is mainly due to the heating by cosmic rays and to the cooling of CO line radiation. In these conditions a lower bound on the kinetic temperature is about 8 K (Goldsmith & Langer 1978, Goldsmith 2001).

The thermal and the turbulent velocity dispersions can be estimated from the observed line broadening parameters, $b = \sqrt{2}\sigma_v$, of the NH_3 (1,1) and HC_3N (2–1) lines. The line of sight velocity dispersion $(b/\sqrt{2})$ of the molecular gas within the cloud σ_v $(\sigma = \mathrm{FWHM}/2\sqrt{2 \cdot ln2})$ is:

$$\sigma_v = \sqrt{\sigma_{\mathrm{th}}^2 + \sigma_{\mathrm{turb}}^2} \tag{1}$$

In L1512 the measured velocity dispersions are $\sigma = 101(\pm 1)$ m s^{-1} for NH_3 and $\sigma = 85(\pm 2)$ m s^{-1} for HC_3N.

If the two molecular transitions are thermally broadened and trace the same material, then the lighter molecule NH_3 (1,1) has a wider line width when compared with the heavier molecule HC_3N. This is precisely what is measured here and is shown in Fig. 4, where the lighter NH_3 of L1512 shows a wider profile than the HC_3N. Thus the radio-observations of L1512 are consistent with thermally dominated line broadening with the two species sampling the same gas.

For thermally dominated lines and co-spatially species the kinetic temperature of the gas is:

$$T_{\mathrm{kin}} = \frac{m_l m_h}{k(m_h - m_l)}(\sigma_l^2 - \sigma_h^2)\,, \tag{2}$$

The value of T_{kin} measured in the L1512 core is 9.2 (± 1.2) K. The σ_{th} is given by

$$\sigma_{\mathrm{th},i} = (k_B T_{\mathrm{kin}}/m_i)^{1/2}\,. \tag{3}$$

where k_B is Boltzmann's constant and the corresponding broadenings are 67 m s^{-1}for $NH_3$and 38 m s^{-1}for HC_3N. The turbulence is then given by:

$$\sigma_{\mathrm{turb}}^2 = \frac{m_h \sigma_h^2 - m_l \sigma_l^2}{m_h - m_l}\,, \tag{4}$$

and has a value of 76 m s^{-1}in L1512. Thus assuming that NH_3 traces the inner and denser gas while HC_3N the external envelope, the core L1512 does not move ballistically in the sense that the difference between the two molecules ($\approx$26 m s^{-1}) is smaller than the velocity width of the HC_3N line. Small relative motions between cores and envelopes indicate quiescence and suggest that dense cores do not gain significant mass by sweeping up material as they move through the cloud.

The speed of sound inside a thermally dominated region of a cold molecular core is

$$v_s = (kT_{\text{kin}}/m_0)^{1/2}\,, \tag{5}$$

With the mean molecular mass for molecular clouds of $m_0 \approx 2.3$ amu, the sound velocity $v_s \approx 60\sqrt{T_{\text{kin}}} = 182$ m s^{-1}. This shows that at the kinetic temperature of 9.2 K the non-thermal velocities are largely subsonic.

Thus, L1512 does indeed represent a very quiescent material at different distances from the core centers. This dense core is probably one of the best laboratories for investigating changes of the electron-to-proton mass ratio, $\mu = m_{\text{e}}/m_{\text{p}}$ by means of observations of inversion lines of NH_3 combined with rotational lines of other molecular species. As Thomas Hardy wrote in his 1882 *Two on a Tower* novel, the dark nebulae are indeed *deep wells for the human mind to let itself down into*.

References

1. Flambaum, V. V. & Kozlov, M. G.; Phys. Rev. Lett., 98, 240801; *2007*
2. Goldsmith, P. F.& Langer, W. D.; ApJ, 222, 881; *1978*
3. Goldsmith, P. F.; ApJ, 557, 736; *2001*
4. Khoury, J., & Weltman, A., 2004, Phys. Rev. Lett, 93, 171104
5. Levshakov, S. A.; Molaro, P.; Kozlov, M. G.; arXiv0808.0583; *2008*
6. Levshakov, S. A.; Molaro, P.; Lapinov, A. V. *et al.*; A&A512,44; *2010a*
7. Levshakov, S. A.; Lapinov, A. V., Henkel, C., Molaro, P., *et al.*; arXiv1008,1160; *2010b*
8. Molaro, P.; Levshakov, S. A.& Kozlov, M. G.; NuPhS, 194, 287; *2009*
9. Walsh AJ, Myers PC, Burton MG., Ap. J. 614:194; *2004*

Spectrographs, Asteroids and Constants

Paolo Molaro, Miriam Centurión, Sergio Monai, and Sergei Levshakov

Abstract Astronomical search for a variation of fundamental constants deals with accurate radial velocity measurements and needs reliable astronomical standards to calibrate the spectrographs to assess possible systematics. We show that the sunlight reflected by Asteroids provide a radial velocity standard of high precision. Preliminary we needed to produce a solar Atlas with a higher precision factor of one order of magnitude, i.e. down to about 10 m s^{-1}at a specific wavelength. The asteroid-based technique is used here to study radial velocity deviations in UVES as claimed recently. Preliminary results suggest the presence of systematics at the level of $\approx$80 m s^{-1}, i.e. of $\approx 4 \times 10^{-6}$ in $\delta\alpha/\alpha$.

1 Introduction

In the last years there has been increasing interest in better radial velocity measurements of astronomical sources. The reasons are manyfold and range from the intensive search for extra solar planets of lower and lower mass to astronomical checks of changes in the coupling fundamental constants, to projects aimed at measuring the change in the expansion velocity of the Universe Correspondingly in a number of papers the limitations of spectrographs in delivering accurate radial velocity has been deeply analyzed. By comparing spectra of the same QSO calibrated by adopting either the I_2 cell or the ThAr calibration lamp, Griest et al. (2009) and Whitmore et al. (2010) observed an offset up to 1 km s^{-1}between different observations and a modulation of about 300 m s^{-1}or about 200 m s^{-1}within a single spectral order in HIRES and UVES respectively. Centurión et al. (2009)

P. Molaro, M. Centurión, and S. Monai
INAF-Osservatorio Astronomico di Trieste, Via G.B. Tiepolo 11 Trieste, Italy
e-mail: molaro@oats.inaf.it, centurion@oats.inaf.it, monai@oats.inaf.it

S. Levshakov
Ioffe Institute Politekhnicheskaya Str. 26, 194021St. Petersburg, Russia
e-mail: lev.astro@mail.ioffe.ru

C. Martins and P. Molaro (eds.), *From Varying Couplings to Fundamental Physics*,
Astrophysics and Space Science Proceedings, DOI 10.1007/978-3-642-19397-2_17,

by comparing QSO absorption transitions of FeII with similar sensitivities to a change in α concluded that systematic errors of the order of 100 m $s^{-1}$are quite common in UVES spectra. These deviations are much larger than typical errors in the wavelength calibration as estimated from the mean wavelength-pixel residuals of the polynomial best solution. Thus, residuals in the wavelength calibration likely underestimate the wavelength calibration errors.

2 Asteroids as RV Calibrators

A practical way to move from relative to absolute radial velocities is to use standard radial velocity sources. However, best stellar standards provide radial velocities with accuracy in the range of $100 - 300$ m s^{-1}due to the presence of convective motions, stellar activity and spots, stellar cycles and photospheric granulation. Asteroids reflect sunlight without substantial modification of the solar spectrum and their velocity component with respect to the observer can be predicted with very high accuracy reaching the m s^{-1} level (Molaro et al. 2008). The reflected sunlight is shifted by the heliocentric radial velocity of the asteroid with respect to the Sun at the time t_1 when the photons left the asteroid and were shifted by the component of Earth rotation towards the asteroid at the time t_2, when the photons reach the Earth. The latter is the projection along the line-of-sight of the asteroid motion with respect to the observer at the observatory site adjusted for aberration, and comprises both the radial velocity of the asteroid and the component due to Earth rotation towards the line of sight. These motions can be computed quite precisely and therefore asteroids provide a standard of unique precision for radial velocity. The reflected sunlight can be used also for local wavelength calibration provided that:

- Solar line positions do not change with solar activity or solar cycle
- Solar line positions are known accurately

The first assumption is still to be verified while (quite surprisingly) we have only a poor knowledge of the absolute position of solar atmospheric lines. In available solar line atlases this is of $\approx$150 m s^{-1}or lower. Thus, on the first place we used HARPS observations of asteroids to construct a new solar atlas with precise solar line positions.

3 A New Solar Atlas

Any photospheric line is built up of many contributions from a variety of temporally variable inhomogeneities across the stellar surface. In particular the solar lines should reveal a variation connected to solar activity, which effectively suppresses the granulation cells. These displacements in a peak to peak modulation are ≤ 30 m s^{-1} over the 11 years solar activity period with the positions more redshifted in correspondence of the activity maximum. The highest quality solar spectra in the optical domain are the solar flux and disc-center atlas obtained on the McMath Solar Telescope at Kitt Peak National Observatory with the Fourier transform spectrometer (FTS) by Kurucz et al. (1984) and Brault and Neckel (1987). These atlases comprise a set of wavelength scans each made of several observations to produce an integrated solar disk flux. The whole spectrum covers the spectral region from 296 and 1300 nm and achieve a signal-to-noise ratio of ≈ 2500 with a resolving power of R$\approx$ 400,000. However, even neighboring scans were taken through different atmospheric conditions with different amounts of water vapor and ozone. Allende Prieto and Garcia Lopez (1998a,b) used these atlases to measure the central wavelength for a considerable number of lines and produced the most precise atlas of solar lines presently available. Allende Prieto and Garcia Lopez (1998a,b) line positions have a precision of the order of $\approx$150 m s^{-1}. We used HARPS observations of the asteroid Ceres to improve the solar atlas.

3.1 Ceres

The observations were performed with the spectrograph HARPS at the European Southern Observatorys 3.6-m telescope at La Silla, Chile, on July 16, 2006 and downloaded from ESO HARPS public archive. Ceres has a spherical shape with radius of 476.2 km. The rotational period is 9.075 h with a rotational velocity of $\approx$91 m s^{-1}, i.e. much lower then the solar one and therefore not causing extra broadening to the atmospheric solar lines. On 16 July Ceres was 99% illuminated and had an angular dimensions in the sky of 0.63 arcsec producing a constant reflectance of sunlight. Variation of reflectance with wavelength or presence of regolith developed by meteoroid impact on the asteroid do not affect the high resolution spectrum.

From the analysis of a 1800 s exposure solar spectrum reflected by Ceres we constructed a new solar atlas of 491 lines in the range 540-691 nm and of 220 lines in the 394-410 nm range. Lines were measured by means of the NGAUSS routine in STSDAS. The new Atlas agree with the solar atlas of Allende Prieto and García López (1998) (see Fig. 1 but the Internal precision of line position is of $\approx$ 45 m s^{-1}, i.e. improved by a factor 3 as shown in Fig. 2. An even more precise ATLAS is under construction based on new HARPS high signal-to-noise observations of the sun taken at twilight (Molaro et al. 2011). These new atlas will provide solar line position for more than 5000 lines with a precision of lines of $\approx$ 10 m s^{-1}locally but depending on the HARPS precision. The atlas can be usefully used to calibrate existing spectrographs at any wavelength in the covered range. For instance it can be used to check the systematic deviations observed in HIRES spectra by Griest et al. (2009) and in UVES spectra by Whitmore et al. (2010). By comparing spectra of the same source calibrated by adopting either the I_2 cell or the ThAr calibration lamp, they observed offsets up to 1 km s^{-1}between different observations and a modulation of about 300 m s^{-1}or about 200 m s^{-1}within a single spectral order in HIRES and UVES, respectively.

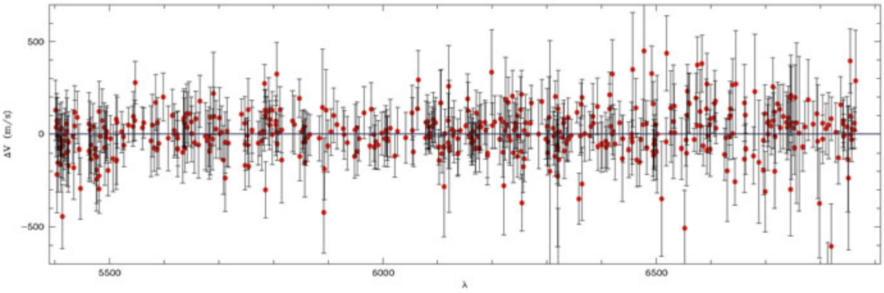

Fig. 1 Velocity difference between the position lines provided here and those of the solar flux by Allende Prieto and García López, (1998)

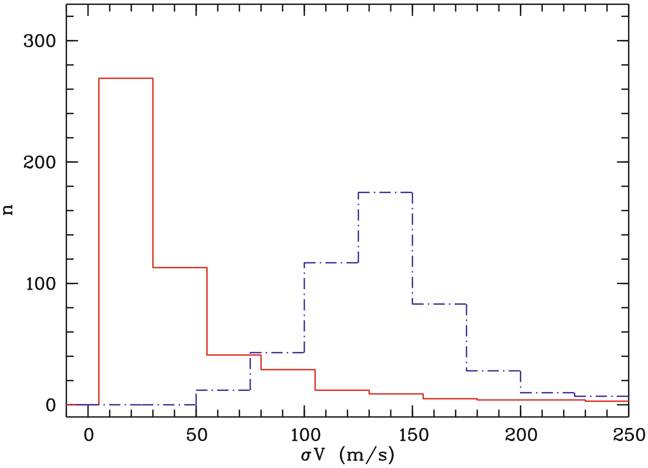

Fig. 2 Line positional error histogram for the lines measured here and the one of Allende Prieto and Garcia Lopez, (1998) for the same lines. The continuous red line our errors, dotted blue line the errors reported in Allende Prieto and García López, (1998)

4 Application: UVES

The available solar atlas can be used to calibrate other existing spectrographs such UVES and at any wavelength. For this purpose UVES observations of the asteroid Iris were taken on Sep 2009 with a resolving power R $\approx=$ 85000. Fig. 3 shows HARPS solar spectrum and UVES Iris spectrum. The figure shows how the solar spectrum recorded by two different spectrographs is pretty much similar. The differences of the positions in the UVES spectrum and the absolute positions of the solar atlas for 238 solar lines in the region between 500-530 nm (Orders 121 to 116). are shown in Fig. 4. The schematic saw-teeth pattern detected by Whitmore et al. (2010) is also sketched in the figure.

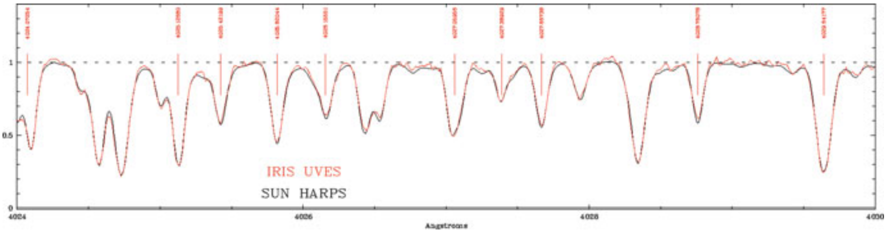

Fig. 3 UVES spectrum of asteroid Iris of Sept 2009 (red line), corrected to the observer's system of reference, and HARPS solar spectrum (black line) used for the new solar atlas

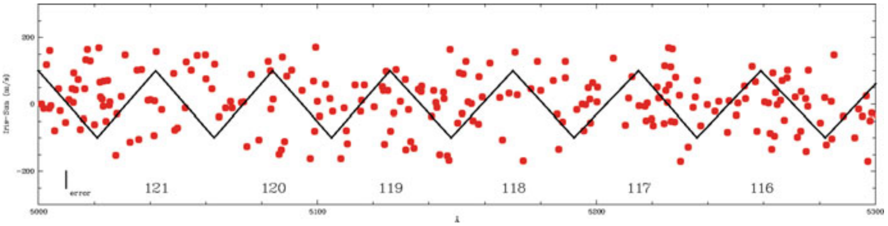

Fig. 4 Radial velocity shifts of individual lines of the IRIS-UVES spectrum relatively to the solar atlas of absolute line positions of Molaro et al. (2011)

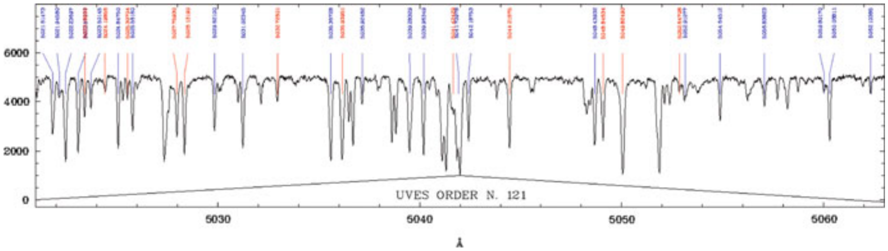

Fig. 5 Order N. 121 of the Iris UVES spectrum. Lines with positive deviations with respect to the solar atlas positions are marked in blue; negative deviations are in red

The observed dispersion is of 82 m s^{-1}. Since the typical error in the measurement of lines in the UVES Iris spectrum is of ≈ 50 m $s^{-1}$and wavelength calibration residuals are of 25 m s^{-1}, there is an excess in the observed dispersion which suggests the presence of local deviations in the UVES spectrum. The saw-teeth pattern detected by Whitmore et al. (2010) is not revealed by our test. However, deviations look as going up and down with characteristic length of 5-10 Å as shown in Fig. 5 suggesting a stretching of the relative scales of UVES and HARPS. It should be noted that absorption lines complexes span for similar wavelength ranges. Thus they likely persist when considering different components of the same absorber.

References

1. Allende Prieto C., & García López R.J. 1998, A&AS 131, 131
2. Centurión, M.; Molaro P., Levshakov, S. A. Memorie SAIt 80, 929 (2009)
3. Griest, K., Whitmore, J.B., Wolf, A. M., Prochaska, J. X., Howk, J. et al. 2009, arXiv:0904.4725
4. Molaro, P., Levshakov, S. A. et al. 2008, A&A 481, 559
5. Molaro, P., Centurión M. 2010 A&A in press
6. Molaro, P., Monai, et al. 2011, in preparation
7. Murphy, M. T.; Webb, J. K.; Flambaum, V. V. 2003, MNRAS 345,609
8. Wilken, T., Lovis, C., Manescau, A., Steinmetz, T., Holzwarth, R., Paquini, L., Lo Curto, G., Hansch, T.W., Udem, Th. 2010, MNRAS 405, 16
9. Whitmore, J., B., Murphy, M., T., Griest, K., 2010 ApJ 723, 89